The Committee Certification

We certify that we have read this dissertation, entitled **“Aerodynamic Performance of Gas Turbine Blades Due to Excitation of Vibration Effect"** and as an examining committee, examined the student **" Mushtaq Faisal Abd Alsadaa "** in its content and that in our opinion it meets the standard of dissertation for the Degree of Doctorate of Philosophy in Mechanical Engineering.

K. Alshamari
Zena
Prof. Dr.
Zena Khalefa Kadhim
Title: Member
Date: 27/ 6 /2022

Qasim H. Bader
Prof. Dr.
Qasim Hassen Bader
Title: Member
Date: 26 / 6 / 2022

Prof. Dr.
Ahmed Hashim Yousif
Title: Member
Date: 26/ 6 / 2022

Ahmedhaleel
Assist Prof. Dr.
Ahmed Hameed Kaleel
Title: Member
Date: 27/6 / 2022

Dhirg
Prof. Dr.
Dhirgham Alkhafaji
Title: First Supervisor
Date: 26/ 6 /2022

Riyadh S. Al-Turaih
Prof. Dr.
Riyadh S. Al-Turaih
Title: Second Supervisor
Date: 26/ 6 /2022

A. Rasool
Prof. Dr.
Adnan A. Abdulrasool
Title: Chairman
Date: 28/ 6 / 2022

Approval of the Mechanical Engineering Department
Head of the Mechanical Engineering Department

Assist. Prof. Dr.
Samer M. Abdul Haleem
Date: / /

Approval of the College of Engineering
Dean of the College of Engineering

Prof. Dr.
Hatem H. Obeid
Date: / /

SUPERVISOR CERTIFICATION

We certify that the preparation of this Dissertation, entitled "Aerodynamic **Performance of Gas Turbine Blades Due to Excitation of Vibration Effect**"

has been prepared by " **Mushtaq Faisal Abd Alsadaa**" under our supervision at the Department of mechanical Engineering, College of Engineering, University of Babylon, as a partial fulfillment of the requirements for Degree of Doctorate of Philosophy in Mechanical Engineering (Power).

Dhirgh

Signature:

Prof. Dr. Dhirgham Alkhafaji

(First supervisor)

26/ 6 /2022

Riyadh S. Al-Turaihi

Signature:

Prof. Dr. Riyadh S. Al-Turaihi

(Second supervisor)

26 / 6 /2022

ACKNOWLEDGEMENTS

Praise first to Allah for the guidance that has enabled me to complete my research.

I would like to express my deepest thanks and sincere gratitude to my supervisors, **Prof. Dr. Dhirgham Alkhafaji** and **Prof. Dr. Riyadh S. Al-Turaihi**, for their supervision, support, understanding, and encouragement.

I wish to express my thanks to head of mechanical department,

Asst. Prof. Dr. Samer Mohammad Abd - Alhalim, and to my friends and all the staff members of mechanical engineering department. I would like to thank my colleague Dr. Salwan Khafaji for his support.

I would like to thank everyone, who helped me in this study.

Signature:

Mushtaq Faisal Abd Alsadaa

29 /06 /2022

Appendix [A]

To calculate the uncertainty of the experimental results the following parameter is concerned:

1) The mean value of the variable x calculated as: $\bar{x}_{mean} = \frac{\sum_1^n x_i}{n}$
2) The standard deviation of x, given by: $\sigma = \sqrt{\frac{\sum_1^n (x_i-\bar{x})^2}{n-1}}$
3) The standard error is given by: $\sigma_m = \frac{\sigma}{\sqrt{n}}$
4) The uncertainty of variable x given by: $x = \bar{x} \pm \sigma_m$

While the variables which are measured their uncertainty are the pressure coefficient (C_p); the calculation shown in the

Table (A-1) where the value of x2 is the adopted value in this study.

No	The variable	The tested values	$\bar{x}_{mean}$	σ	σ_m	x	Uncertainty
Cp for first level and without vibration.							
1	x1	-0.9690					
2	x2	-0.9071	-0.8696	0.0938	0.0542	-0.8155	0.0664
3	x3	-0.8207				-0.9238	-0.0586
4	x4	-0.8210					
5	x5	-0.8302					
Cp for second level without vibration.							
1	x1	-0.9322					
2	x2	-0.9514	-0.8894	0.0884	0.0510	-0.8384	0.0609
3	x3	-0.7901				-0.9405	-0.0543
4	x4	-0.8931					
5	x5	-0.8803					
Cp for third level without vibration							
1	x1	-0.7403					
2	x2	-0.7555	-0.7309	0.0757	0.0437	-0.6872	0.0636
3	x3	-0.7701				-0.7746	-0.0565
4	x4	-0.7515					
5	x5	-0.6370					

CHAPTER ONE

INTRODUCTION

1. Background

Gas turbines have strong impact on human life since its introduction in the twentieth century. It has been used mainly for power generation and later on in aircraft propulsion. After more than half a century of creative development, it is still a challenge for engineers of all disciplines to achieve the ever increasing and more demanding design requirements. Focusing on the design of gas turbines, aerodynamic charactersitcs, structural integrity, vibrational aspects, combustion, cooling, acoustics and environmental effects are the subject of active research and development[1].

The gas turbines are typically designed by first deciding on the specifications of the blades according to the required performance, and then considering the strength issues. Conventionally, the consideration of blade strength was limited to the investigation of static centrifugal and steady bending stresses and avoiding dynamic resonances. Flow in turbomachinery is generally considered to be steady with the exception of phenomena such as rotating stalls and surging. However, rotating cascades are subjected to a relatively unsteady flow field due to the wake from preceding stators and struts or the inlet distortion from inlet conditions. As a result, fluctuating fluid forces act on the cascades and induce vibrations and these external forces are periodic. Even a small fluctuating fluid force may result in large vibration stresses on the blades, and long-term operation may cause fatigue failure[2]

The component efficiencies of gas turbines nowadays offer only small margins for improvement because of the high technical standard achieved so far. Therefore, other parameters to reduce the costs of gas turbine engines become important:

In aircraft propulsion, the weight-to-thrust ratio of the engine is an important parameter with a direct influence on the specific fuel consumption and air pollution, which enforces the design of lighter and more compact engines. This involves both the use of new materials and composite structures and the minimization of the structural integrity margins of the components. For example a necessary thickness of rotor trailing edges by 0.1 mm (to ensure an endurance limit) leads to 0.1 % specific fuel consumption penalty [1]. Other constructive measures to reduce weight are the decrease of the number of stages and the number of blades in a blade row, leading to increased loads of the individual blades. Also axial distances between engine components are minimized, which on the other hand leads to increased levels of dangerous aerodynamic interactions.

In stationary applications competition drives the turbine designers to increase load and performance of the engines and to optimize material use to be cost efficient. The lifetime of engine components is an important cost factor and reducing maintenance efforts for the engine is a major goal for gas-turbine manufacturers to be competitive. For aircraft engines the guaranteed lifetime of engine components is of special importance because of the safety requirement of such engines. The development costs of new gas turbines are enormous. Major savings can be made when replacing extensive tests. Prototypes of the largest stationary gas turbines are usually tested first when installed in the power plant. A failure detected at this stage is very expensive. The development and validation of numerical tools to calculate structural and aerodynamic behavior is a key factor to replace semi-empirical methods in the design process, so that new and unconventional designs can be proved fast and cheap without the need of testing. The present research work is motivated by the study of the effect of vibration on fluid flow around the blade for turbine engines, some of the major actual driving forces for new developments have been listed in this chapter. The novelty of this thesis that it deals with the effect of the vibration generated by the blade resulting from an imbalance in the rotating cascade of the gas turbine or from the turbine shaft bearings on the dynamics of the fluid surrounding the blade and to show the extent to which vibration affects the pressure and velocity distribution of the flowing fluid.

1.1. Gas Turbine Vibration Problems

Most components in a gas turbine engine are exposed to vibrations caused by unsteady forces due to relative motions of rotating and non-rotating parts. Currently, related research work focuses on four broad, sometimes overlapping, and areas: vibrations related to combustion instability, acoustically relevant vibrations, rotor instability and vibrations from blades, the latter one is subject of the present thesis. Beside other impacts the vibrations of gas-turbine-engine parts [3].

Various mechanisms are commonly defined describing the vibrations of turbomachinery blades, usually classified according to the origin of the excitation. These can be of mechanical thermal or aerodynamic nature. Mechanical excitations include blade tip casing contact or damage; aerodynamic excitations include blade row interaction (forced response), self-excitation (flutter), impact of cooling jets, compressor surge and rotating stall as well as turbulence [3].

1.1.1. Self-Excited Vibrations

When the vibrations are self-excited (flutter) the vibration motion of the blade itself causes an unsteady pressure field around the blade sustaining the vibration. Such behavior is usually started by small aerodynamic or mechanical disturbances above a It can lead to drastically increasing blade vibration amplitudes and rapid blade failure if the mechanical damping is too low to dissipate the aerodynamic energy put on the blade. Long and slender structures are more prone to flutter, i.e. the fan blades and 1st stage compressor blades, but also low-pressure turbine blades. Flutter is not a problem in high-pressure turbine [4].

1.1.2. Forced Vibrations

Forced vibrations (forced response) are characterized by aerodynamic excitation sources, which are flow disturbances acting periodically on the blades and originate from upstream and/or downstream obstacles. The most common forced vibrations are due to inlet distortions originating at the air intake (inlet struts, crosswinds), blade row interactions and hot streaks originating from the burners. Also, the burner cans themselves cause circumferential variations in the burner exit flow. The time-periodic excitation is in all cases caused by the relative rotational motion of excitation source and the excited structure, which leads to excitation frequencies multiples of the rotation frequency[4].

1.2. Flow Induced Vibration

Vibration problems due to fluid flow occur in many industrial plants. This obstructs smooth plant operation and in serious cases can lead to significant maintenance and repair costs and costly losses in productivity. These flow-related vibration phenomena are generally known as ‘flow-induced vibrations’ (FIV). The term ‘flow-induced vibration and noise’ (FIVN) is used when flow-induced noise is present. It is fairly evident that the fluid force acting on an obstacle in flow will vary due to the flow unsteadiness and that the varying force, in turn, may cause vibration of the obstacle. In the case of piping connected to reciprocating fluid machines, for example, it is well-known that the oscillating (fluctuating) flow in the piping generates excitation forces causing piping vibration. However, even for steady flow conditions, vibration problems may be caused by vortex shedding behind obstacles or by other phenomena. Flow-induced acoustic noise is also an important problem in industry [2].

1.3. Gas Turbine Functional Description

While the gas turbine, as shown in figure 1-1, is running, filtered ambient air is drawn through the inlet plenum assembly, then compressed in the axial flow compressor. Compressed air from the compressor flows into the annular space surrounding the 14 combustion chambers, from which it flows into the spaces between the outer combustion casings and the combustion liners, and enters the combustion zone through metering holes in each of the combustion liners [5].

The fuel nozzles introduce the fuel into each of the fourteen combustion chambers where it mixes with the combustion air and burns. The hot gases from the combustion chambers expand into the fourteen separate transition pieces attached to the downstream end of the combustion chamber liners and flow from there to the three-stage turbine section of the machine. Each stage consists of a row of fixed nozzles followed by a row of turbine buckets. In each nozzle row, the kinetic energy of the jet is increased, with an associated pressure drop, and in each following row of moving buckets, a portion of the kinetic energy of the jet is absorbed as useful work on the turbine rotor.

After passing through the 3rd-stage buckets, the exhaust gases are directed into the exhaust casing and diffuser, which contains a series of turning vanes to turn the gases from an axial direction to a radial direction, thereby minimizing exhaust hood losses. Then, the gases pass into the exhaust plenum and are discharged to atmosphere through the exhaust stack. The resultant shaft rotation turns the generator rotor to generate electrical power or to drive a centrifugal compressor in industrial power applications and drives the auxiliaries through the accessory gearbox[5].

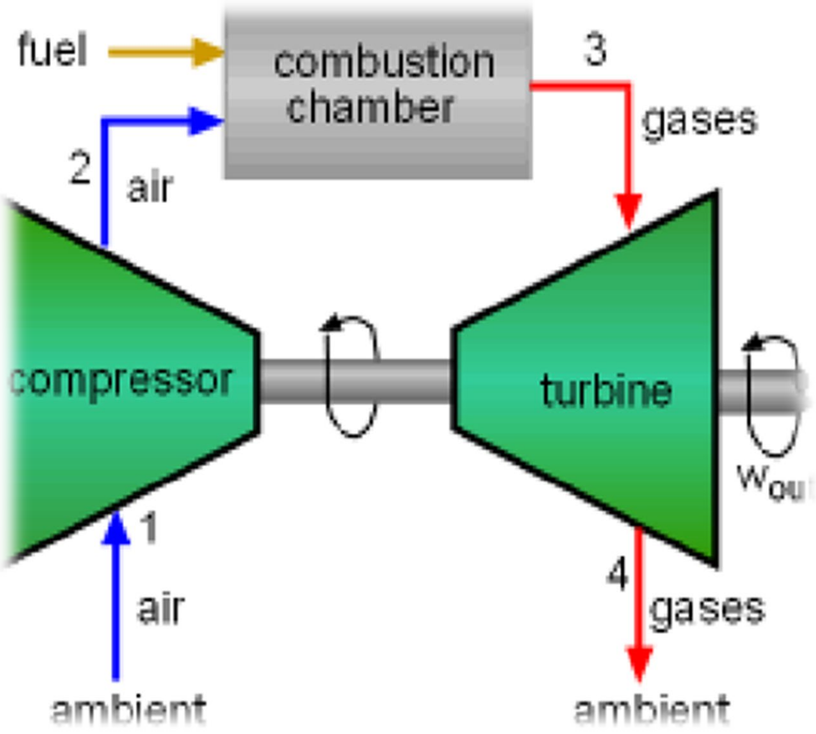

Fig. 1-1: Gas turbine engine (GE frame)

1.4. Types of Airflow in Cascade Blades

The aerodynamics of the flow in a two-dimensional/three-dimensional turbine cascade is still a focus of many on-going research activities in the gas turbine community. A detailed description of the turbine blade aerodynamics in two-dimensional and three-dimensional vane cascade can be found in Lakshminarayana (2000) [5] and in Acharya and Mahmood (2006) [6]. Vortex structures are a major source of the pressure or aerodynamic losses across the vane/blade passage. Because they entrain the hot fluid from the mainstream flow and enhance the convective turbulent transport in the endwall region as well as on the blade surface; this also causes a high local thermal loading on the turbine passage wall. Historically, the loss was categorized as “profile loss”, “endwall loss” and “leakage loss”, although it is clearly found that the loss mechanisms are seldom independent of each other. The relative magnitudes of these losses depend on the type of machine, blade aspect ratio and tip clearance. For many machines, each loss shares 1/3 of the total loss[5].

The Langston model, on the other hand, shows a general picture Fig. 1-2: Secondary flow vortex model of the generation and development of the two legs of a horseshoe (HS) vortex and the passage vortex (PV). It combines Hawthrone’s classical secondary flow model with the effects of the LE flow and the flow in the passage between the blades. The boundary layer separates at the saddle points forming a well-known HS vortex at the endwall of the cascade with the suction side (SS) and pressure side (PS) leg. The PS horseshoe vortex becomes a strong PV due to the passage pressure gradient. The SS leg is drawn into an adjacent passage and rotates in the opposite direction to the larger PV. This smaller vortex is known as counter vortex, and can be thought of as a “planet” rotating around the axis of the PV (the “sun”) [6]. When the PS leg of the HS vortex enters into the channel, it continuously sucks in the main flow and the boundary layers on the endwall move from the pressure surface to the suction surface. Since the PS leg has the same sense of rotation as the PV, this PS leg can be regarded as part of the PV. This vortex is gradually lifted away from the endwall and shifts towards the suction surface downstream from the blade channel. The SS leg of the HS vortex stays under the PS leg and leaves the blade channel along with it. Comparing the streamlines in figure.1-2 with those in the mid-span regions in Figure.1-3, it is clear that the turning of the streamlines inside the blade passage and around the leading edge is much greater near the endwall region which causes the cross-flow here to be stronger.

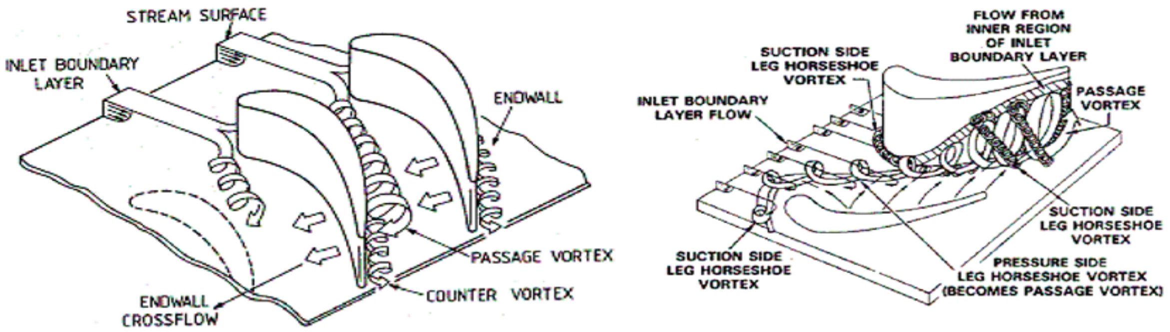

Langston (1980)

Sharma and Butler (1987)

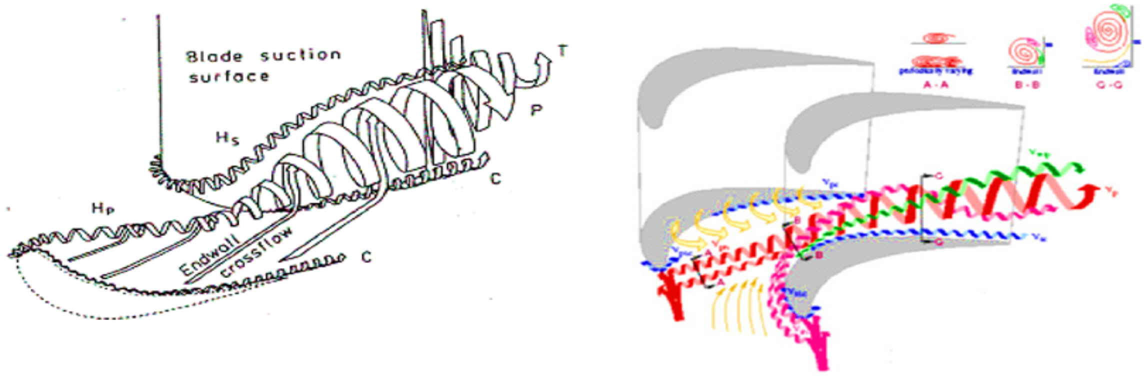

Kawai et al. (1990)

Wang et al. (1995)

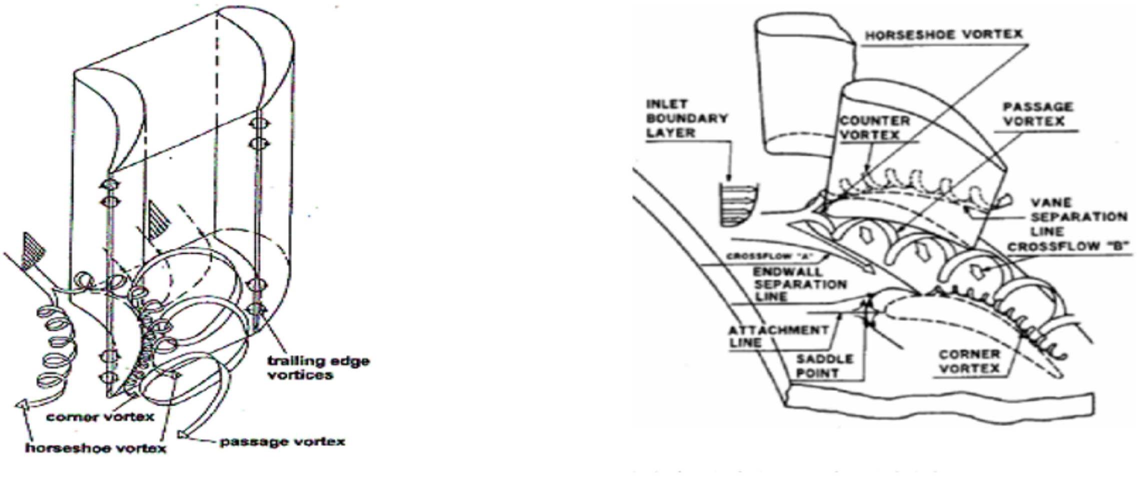

Sauer (1997)

Tekeishi et al. (1989)

Fig. 1-2: Secondary flow vortex model

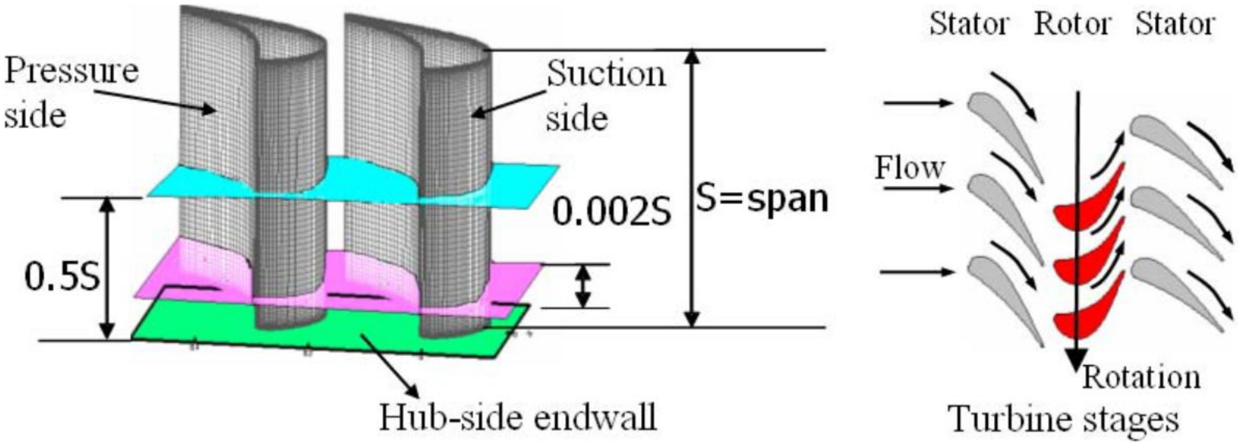

Fig. 1-3: Streamlines and static pressure distribution in the mid-span plane along blade.

1.5. The Aim of Study

The proposed study aims to investigate the effect of vibration levels on the flow in rotary turbine cascade blades for gas turbine experimentally and simulate this study numerically by COMSOL Multiphysics 5.6.

1.6. The Scope of This Study

There is no doubt that the rotation or movement of equipment and mechanical parts accompanied by vibration causing serious damage to the equipment, therefore many researchers around the world have studied vibration behavior, some have studied ways of controlling it and the other study the flow induced vibration. In the course of deep research, According to a research information , it found that most researchers have studied the vibration resulting from the flow, but little has been used for forced vibration which applies on some parts such as plate, cylinder etc. The scope of the study contains the following parts:

1.6.1. Experiment Study

a) Design and manufacture a vibration shaker and estimating the frequency and amplitude by using LabVIEW program.

b) Establish experimental set up to study the effect of forced vibration on the cascade turbine blades.

c) Perform a comparison to the velocity, and pressure profile with/without vibration.

d) Perform a comparison between experimental and numerical results.

1.6.2. Numerical Study

Accomplishment a theoretical study by using COMSOL Multiphysics 5.6 unsteady state to choose the effective frequency of the blade.

Utilization the COMSOL Multiphysics 5.6 program to conduct the structural conditions (vibration).

Simulate the study of the influence of vibration on the flow in the cascade turbine blades from the signal simple harmonic motion by using COMSOL Multiphysics 5.6 software.

CHAPTER TWO

LITERATURE REVIEW

2 Introduction

Gas turbine have continuous increasing usage in primary and secondary aerospace, aircraft structures, and electric power generation owing to their superior output power and high mechanical torque. One form of these types of the gas turbine being used in current study is that used for electric power generation. Due to the wide range of applications of the gas turbine, its aerodynamic characteristics have attracted many researchers and have been considerably improved to achieve realistic results.

The present review covers three aspects. The first includes the previous work about vibration induced by the fluid flow throughout the gas turbine. The second one is concerned with the developments of some theoretical modelling for better representation for the aerodynamic characteristics (pressure, velocity, and stream lines) and the traditional tools used for this purpose. The third aspect is concerned about the experimental work done regarding aerodynamic characteristics of several types of gas turbines.

2.1 Theoretical Analysis and Numerical Simulation

Gerolymos, 1988 [7]developed an algorithm for numerically integrating the Euler equations in blade-to-blade surface formulation. The method simulated all the inter-blade channels of an annular cascade. The equations were discretized in a grid that moves in order to follow the vibration of the blades. The equations were integrated using the explicit MacCormack scheme in finite-difference formulation. Mistuned vibration as well as standing-, traveling-, or influence-wave modes may be readily simulated. Also, two other faster methods were developed, simulating traveling and influence waves, respectively. A number of numerical results showed the aptitude of the method to simulate both started and unstated supersonic flow in vibrating cascades. A first comparison with available wind-tunnel data corroborates the validity of the approach to predict supersonic flutter of fans and compressors.

Chiang and Kielb, 1992[8] presented a comprehensive study based on past experience to determine the acceptability of a blade design. A new analysis system was developed to predict blade forced response. The system provided a design tool, over and above the standard Campbell diagram approach, for predicting potential forced response problems. The incoming excitation sources were modeled using a semi-empirical rotor wake/vortex model for wake excitation, measured data for inlet distortion, and a quasi-3D Euler code for pressure disturbances. Using these aerodynamic stimuli, and the blade's natural frequencies and mode shapes from a finite element model, the unsteady aerodynamic modal forces and the aerodynamic damping were calculated. A modal response solution was then performed. This system was applied to current engine designs. A recent investigation involved fan blade response due to inlet distortion. An aeromechanical test was run with two different distortion screens. The resulting distortion entering the fan was measured. With this input data, the predicted response agreed almost exactly with the measured response. In another application, the response of the LPT (low pressure turbine) blades of a counter-rotating supersonic turbine was determined. The blades were excited by both a wake and a shock wave. The shock response was predicted to be three times larger than that of the wake. Thus, the system identified a new forcing function mechanism for supersonic turbines. The results of the two applications were presented.

Dedoussis, et al., 1994 [9]presented a method for establishing signatures of faults in the rotating blades of a gas turbine compressor. The method employed a panel technique for the calculation of the flow field around blade cascades, with disrupted periodicity, a situation which was encountered when a blade fault has occurred. From this calculation, time signals of the pressure at a location on the casing wall, facing the rotating blades, were constituted. Processing these signals, in combination with "healthy" pressure signals allows the constitution of fault signatures. The proposed method employed geometrical data, as well as data about the operating point of the engine. It gave the possibility of establishing the fault signatures without the need of performing experiments with implanted faults. The successful application of the method was demonstrated by comparison of signatures obtained by simulation to signatures derived from experiments.

Menechini and Bearman, 1995[10] simulated the flow about an oscillating circular cylinder by using the discrete vortex method incorporating viscous diffusion. This flow was simulated considering a frame of reference fixed to the cylinder and with an oscillating cross flow. Force time histories were shown for a Reynolds number of 200 and for different values of amplitude (A) and frequency of oscillation (f). The lock-in boundary for vortex shedding was obtained. For values of amplitude above about 0.6D, an asymmetric mode of shedding was observed. Vortex formation length for different values of A and f were showed depending on distributions of $u_{r.m.s}/U$ across the wake, for various downstream stations.

Anagnostopoulos, 2000 [11] presented a numerical study of the flow past a circular cylinder forced to oscillate transversely to the incident stream at a fixed Reynolds number equal to 10^6. FEM was used for the solution of the Navier-Stokes equations, in the formulation where the stream function and the vorticity were the field variables. The cylinder oscillation frequency ranged between 0.8 and 1.20 of the natural vortex-shedding frequency, and the oscillation amplitude extended up to 50% of the cylinder diameter. The resolution of the characteristics of synchronized wakes was the focus of the study, the first task was the determination of the boundary of the lock-in region. The computation revealed that, when the cylinder oscillation frequency exceeds the frequency of the natural shedding of vortices, the flow was not absolutely periodic at subsequent cycles but a quasiperiodic flow pattern occurs, that created difficulty in the determination of the lock-in boundary. The time histories of the drag and lift forces for various oscillation parameters were presented, while the vorticity contours were used for the numerical flow visualization. The hydrodynamic forces, the phase angle between the lift force and the cylinder displacement, and the parameters of the wake geometry when steady state was reached, were presented in cumulative diagrams. The oscillation parameters affect the hydrodynamic forces and the geometry of the wake were selected and showed by these diagrams.

Williamson and Govardhan, 2004 [12],This review summarizes fundamental results and discoveries concerning vortex-induced vibration (VIV), that have been made over the last two decades, many of which were related to the push to explore very low mass and damping, and to new computational and experimental techniques that were hitherto not available. We bring together new concepts and phenomena generic to VIV systems, and pay special attention to the vortex dynamics and energy transfer that give rise to modes of vibration, the importance of mass and damping, the concept of a critical mass, the relationship between force and vorticity, and the concept of "effective elasticity," among other points. We present new vortex wake modes, generally in the framework of a map of vortex modes compiled from forced vibration studies, some of which cause free vibration. Some discussion focuses on topics of current debate, such as the decomposition of force, the relevance of the paradigm flow of an elastically mounted cylinder to more complex systems, and the relationship between forced and free vibration.

Moffatt et al., 2005[13] presented a decoupled aeromechanical system based on an advanced frequency-domain CFD solver with filly non-linear capability allowing resonant vibration predictions to be routinely performed during the design process. A new energy method was presented that solves the blade response without the knowledge of original mode shape scales. A robust FE-CFD mesh interface was developed for industrial use that can accurately deal with differences in mesh geometry, low mesh density and high mode shape gradients. The capability of the baseline CFD solver for blade row interaction flow prediction was further validated against the VKI transonic turbine stage. A forced response analysis was carried out on the NASA Rotor 67 transonic fan for demonstration purposes. The system was evaluated for a challenging industrial study of the ALSTOM 3-stage transonic test compressor. Where the forced response predictions of three crossing points on the Campbell diagram compare well with strain gauge test data. An investigation into aerodynamic damping of the first ten modes shows a high dependency on mode shape.

McBean et al., 2007[14], used a parallel multiblock Navier-Stokes solver with the k-ω turbulence model to solve the unsteady flow through an annular turbine cascade, the transonic Standard Test Case 4, Test 628. Computations were performed on a two- and three-dimensional model of the blade row with either the Euler or the Navier-Stokes flow models. Results were compared to the experimental measurements. Comparisons of the unsteady surface pressure and the aerodynamic damping were made between the three-dimensional, two-dimensional, inviscid, viscous simulations, and experimental data. Differences were found between the stability predictions by the two- and three-dimensional computations, and the Euler and Navier-Stokes computations due to threedimensionality of the cascade model and the presence of a boundary layer separation, respectively.

Young and Lai, 2007[15] simulated numerically the flow over a NACA0012 airfoil, oscillated sinusoidally in plunge. Two dimensional Navier–Stokes solvers at a Reynolds number of 20,000 were used for the numerical simulation. The wake of the airfoil was visualized using a numerical particle tracing method for high reduced frequencies ($1.0 < k < 10.0$) and small non-dimensional amplitudes ($h < 0.1$). Anomalous vortex shedding modes (involving multiple vortices shed per half-cycle of airfoil motion) that observed experimentally in the literature were reproduced numerically and were shown to be the result of interaction between the plunging frequency and a natural bluff-body shedding frequency. This resulted in a vortex lock-in phenomenon analogous to that seen for oscillating cylinders. However, the lock-in boundary was not symmetric about the natural shedding frequency, due to the sharp trailing edge forcing the flow to separate at the trailing edge on the windward side of the airfoil for the majority of the plunge cycle at higher frequencies and amplitudes.

Brøns, 2007[16]considered structures such as vortices and separation in the streamline patterns of fluid flow using dynamical systems theory. Bifurcation of patterns under variation of external parameters was studied using simplifying normal form transformations. Flows away from boundaries, flows close to fixed walls, and axisymmetric flows were analyzed in detail. In this research, the authors showed how to apply the ideas from the theory to analyze numerical simulations of closed cylindrical container vortex breakdown.

Forbes and Randall, 2007[17] presented an analytical model of the casing and simulated pressure signal associated with the rotor blades in order to understand the complex relationship between blade vibrations and casing response. A mathematical formulation was undertaken of the internal pressure signal due to both the rotating bladed disk as well as individual blade vibrations and the solution of the casing response was formulated. Excitation by the stator blades and their contribution to the casing response was also investigated. Some verification of the presented analytical model was provided by comparison with Finite Element Analysis results for various rotor rotational speeds.

Forbes and Randall, 2008[18] introduced an analytical model of a gas turbine casing and simulated pressure signal associated with the rotating blades, individual blade vibrations and transfer of stator blade vibrations in order to understand the complex relationship between casing response and the most important excitation forces. Due to the force interaction being through a fluid medium, a certain degree of randomness was introduced into the excitations, and the viability of this inherent randomness as a useful aid for separation of the contributing excitation forces from the system response was explored analytical solution for a circular ring, under the simulated operating conditions for a gas turbine with both periodic and turbulent force components included, has been presented. Importantly, the random contribution to the excitation of the casing and the rotor blades has been shown to contain information of the blade vibration characteristics. The separation of the different force signal types was also shown, with periodic contributions removed and the potential ability to separate the contribution to the casing vibration for different stages by taking advantage of the signal’s inherent cyclo-stationary properties.

Forbes and Randall, 2008[19], presented an analytical model for the response of a gas turbine casing to what was believed to be the dominant forces acting on it,: (i) the moving pressure waveform around each blade throughout its motion and (ii) the forces (and moments) applied through the stationary stator blades, to understand the form of the casing response. A simulated blade fault was added to the model to represent a damaged blade, of arbitrary form, by reducing the stiffness of one blade. The change in the contribution to the casing response measurements due to this simulated fault was explored as well.

Gourdain et al., 2009[20] showed how new challenges can be addressed by using parallel computing platforms for distinct elements of a more complex systems as encountered in aeronautical applications. Based on numerical simulations performed with modern aerodynamic and reactive flow solvers, this work underlined the interest of high-performance computing for solving flow in complex industrial configurations such as aircrafts, combustion chambers and turbo-machines. Performance indicators related to parallel computing efficiency were presented, showing that establishing fair criterions was a difficult task for complex industrial applications. Examples of numerical simulations performed in industrial systems were also described with a particular interest for the computational time and the potential design improvements obtained with high-fidelity and multi-physics computing methods. These simulations used either unsteady RANS methods or LES and dealt with turbulent unsteady flows, such as coupled flow phenomena (thermo-acoustic instabilities, buffet, etc.). Some examples of the difficulties with grid generation for some complex industrial applications were also presented.

Lampart, 2009[21] described the process of formation of endwall flows and evolution of vorticity from the endwall boundary layers. The losses due to the endwall were discussed in details. The entropy increases in the boundary layer were integrated at the endwall boundary layer in order to evaluate the losses theoretically. In the theoretical analysis, a certain load blade profile was considered. CDF was used for the theoretical analyses for the Durham 3D straight turbine cascade and the results were compared with the other available date from experiment. The comparison with the results of available experimental data of ERCOFTAC the calculations based on turbulent viscosity models are capable of capturing basic 3D flow effects in cascade flows. However, they over predict the level of losses in the wake and in the secondary flow region. The quantitative predictions are improved with the Reynolds stress model, but they are connected with a significant increase of computational costs.

Liu et al., 2012[22] studied numerically the complex flows around stationary and sinusoidal pitching airfoil by the finite element method combined with Arbitrary-Lagrangian –Eulerian (ALE) frame and explicit Characteristic Based Split Scheme (CBS). In particular, the static and dynamic stalls were analyzed in detail, and the natures of the static stall of NACA0012 airfoil were given from viewpoint of bifurcations. Following the bifurcation in Map, the static stall was proved to be the result from saddle-node bifurcation which involves both the hysteresis and jumping phenomena, by introducing a Map and its Floquet multiplier, which constructed in the numerical simulation of flow field and related to the lift of the airfoil. Further, because the saddle-node bifurcation was sensitive to imperfection or perturbation, the airfoil was then subjected to a perturbation which was a kind of sinusoidal pitching oscillation, and the flow structure and aerodynamic performance were studied numerically. The results show that the large-scale flow separation at the static stall on the airfoil surface can be removed or delayed feasibly, and the ensuing lift could be enhanced significantly and also the stalling incidence could be delayed effectively. As a conclusion, it can be drawn that the proper external excitation can be considered as a powerful control strategy for the stall. As an unsteady aerodynamic behavior of high angle of attack, the dynamic stall can be investigated from viewpoint of nonlinear dynamics. Lift enhancement and drag reduction were the main reasons to produce a rich variety of nonlinear phenomena.

Moshfeghi, et al., 2012[23] investigated the effects of near-wall grid spacing for the SST-K-ω model and study of the aerodynamic behavior of a horizontal axis wind turbine. The NREL Phase VI was used as the aerodynamic model. Eight different cases were investigated for the near wall grid spacing study. Furthermore, one case was studied in both the SST-K-ω and the Langtry-Menter transitional models. For all cases the total numbers of nodes were fewer than 5000,000. Thrust forces, flow patterns and pressure coefficients were compared at different wind speeds. The thrust values of the SST-K-ω were not in a good agreement with the test results. The streamlines show that the inboard section of the blade has a severe complex 3D flow which separates at low velocities; the mid-span section stays attached for higher velocities and the outboard part has 2D-like behavior and separates as the last part. Also, for were as with complex separation, reattachment and sever span wise flow (e.g., at the inboard section), the SST-K-ω miss predicts the pressure values. Generally, the SST-K-ω over predicts the separation by miss predicting the separation point. Besides, it was observed that Gamma–Theta transitional model behaves differently from the SST-K-ω, especially at the inner part and the results were closer to the test results.

Wang et al., 2013[24] proposed an in-house code and strategy, called TurboAVBP for turbo-machinery LES thanks to the coupling of multi-copies of the unstructured compressible reacting LES solver AVBP, designed to run efficiently on high performance massively parallel architectures. Aside from the specificity of such wall bounded flows, rotor/stator LES type simulations required specific attention and the interface should not interfere with the numeric scheme to preserve proper representation of the unsteady physics crossing this interface. A tentative LES compliant solution based on moving overset grids method was proposed and evaluated for high-fidelity simulation of the rotor/stator interactions. Simple test cases of increasing difficulty with reference numerical were detailed and prove the solution in handling acoustics, vortices and turbulence.

Lei et al., 2014[25] studied numerically the unsteady flow separation of airfoil with a local flexible structure (LFS) in Lagrangian frames in detail, in order to investigate the nature of its high aerodynamic performance. For such aeroelastic system, the characteristic based split (CBS) scheme combined with arbitrary Lagrangian-Eulerian (ALE) framework was developed firstly for the numerical analysis was of unsteady flow, and Galerkin method was used to approach the flexible structure. The local flexible skin of airfoil, which can lead to self-induced oscillations, was considered as unsteady perturbation to the flow. Then, the ensuing high aerodynamic performances and complex unsteady flow separation at low Reynolds number were studied by Lagrangian coherent structures (LCSs). The results show that the LFS has a significant influence on the unsteady flow separation, which was the key point for the lift enhancement. Specifically, the oscillations of the LFS can induce the generations of moving separation and vortex, which can enhance the kinetic energy transport from main flow to the boundary layer. The results gave a deep understand of the flow control for the flow over airfoil and the dynamics in unsteady flow separation.

Esfahani, et al., 2015[26] evaluated the effect of elliptical motion trajectory on the aerodynamic characteristics and propulsive performance of a flapping airfoil. A periodic horizontal motion (forward/backward) was combined with vertical motion (upward/downward) of the airfoil to introduce a new kinematic parameter, and an elliptical motion trajectory for flapping airfoil. The Navier–Stokes equations were used to simulate the unsteady flow field over a two dimensional NACA0012 airfoil. The Navier–Stokes equations were discretized based on the finite volume method and were solved with a pressure-based algorithm. The flow was assumed to be laminar and incompressible and transient terms were conducted using a second order Euler implicit scheme. It was shown that the combination of horizontal and vertical motions for the flapping airfoil changed the kinematics, motion trajectory and hence the effective angle of attack profile during the flapping cycle. The elliptical motion trajectory influenced the fluid structures and changed the vortex shedding pattern and wake zone behind the airfoil. In addition, the introduced kinematics have influenced the aerodynamics performance and propulsive performance of either pure plunging or pitching/plunging airfoil.

Šidlof, 2016[27] presented a CFD simulation of an elastically supported NACA0015 airfoil with two degrees of freedom (pitch and plunge) coupled with 2D incompressible airflow. The geometry of the airfoil, mass, moment of inertia, location of the centroid, linear and torsional stiffness was matched to properties of a physical airfoil model used for wind-tunnel measurements. The simulations were run within the Open FOAM computational package. The results of the CFD simulations were compared with the experimental data.

Khan and Wei, 2016[28] carried out a CFD analysis was to study the influence of local flexible structure on the lift performance of airfoil. Single mode vibrations of local flexible structure on the upper surface of the airfoil were investigated with various frequencies and amplitudes. Finite Volume Method was used to discretize the incompressible Navier-Stokes equations. Partial fluid structure interaction was examined under the dynamic mesh technique. The flow configurations was assumed to consist of flow over NACA0012 at Re=1000 and at a low angle of attack. Numerical simulations were conducted for different vibration frequencies and the corresponding flow field characteristics were investigated as well. Vibrations with a range of amplitudes were carried out under the same flow conditions and their results were compared with the conventional rigid airfoil. Vibration frequency close to the natural vortex shedding frequency resulted in the frequency lock-in or synchronization phenomenon. At the frequency lock-in condition and at some moderate vibration amplitude, the amplitude of lift coefficient oscillations was increased. These vibrations on the upper surface of the airfoil resulted in increasing the average lift coefficient, which was further increased with increasing the vibration amplitude. In addition, the displacement of local flexible structure was completely in phase with the vortex shedding. The length of local flexible structure was also varied between 0.1c and 0.2c and results showed that the length of 0.1c had better performance at higher vibration amplitudes. Pressure distributions and vortices around the local flexible airfoil were evaluated. Moreover; the power spectra that based on the lift coefficient were tested to imprisonment the flow field energy.

Khan et al., 2017[29]studied partial fluid structure interaction of an airfoil. The 2D incompressible Navier-Stokes equations were solved based on the finite volume method and dynamic mesh technique. The local flexible structure was assumed to vibrate in single mode located on the upper surface of the airfoil. The vibration frequency and amplitude influence were examined and the corresponding fluid flow characteristics were investigated which add an additional complexity to the inherent problem in unsteady flow. The study was conducted for flow over NACA0012 airfoil at $600 \leq Re \leq 3000$ at a low angle of attack. Vibration of flexible structure induced a secondary vortex which modifies the pressure distribution and lift performance of the airfoil. It was noted that, in the case of $Re \leq 1000$, the deformation of flexible structure was occurred in-phase with the vortex shedding. In other words, increasing maximum lift was linked with the positive deformation of flexible structure. At Re=1500 a phase shift of about $1/\pi$ was existed while they were out-of-phase at Re>1500. In addition, the oscillation amplitude of lift coefficient increased with increasing vibration amplitude for Re≤1500 while it decreased with increasing vibration amplitude for Re>1500. As a result of frequency lock-in, the average lift coefficient was increased with increasing vibration amplitude for all investigated Reynolds numbers (Re).

Chen, 2017[30] conducted a computational fluid dynamics (CFD) investigation over a two-dimensional axial-flow turbine rotor blade row to study the phenomena of turbine rotor discharge-flow overexpansion at subcritical, critical, and supercritical conditions. The following quantitative data, averaged or integrated across the two-dimensional computational domain encompassing two blade passages, were obtained over a series of 14 inlet-total to exit-static pressure ratios, ranging from 1.5 (unchoked, subcritical condition) to 10.0 (excessively high-pressure ratio, supercritical condition) , mean-flow Mach numbers, mean-flow angles, axial component of mean-flow Mach number, tangential-blade surface-pressure forces, mean-flow mass flux. Flow-path total-pressure-loss coefficients detailed flow features over the full domain of computation, such as the streamline patterns, Mach contours, pressure contours, blade surface pressure distributions, and so forth, were collected and presented. A formal, quantitative definition of the limit-loading condition based on the channel flow theory was proposed and explained. Contrary to the comments made in the historical documentation on this subject about the deficiency of the theoretical methods applied in analyzing these phenomena, using the modern CFD method for the study of this subject appears to be successful.

Moller et al., 2017[31] presented a numerical study on blade vibration for the transonic compressor rig at the Technische Universitat Darmstadt (TUD), Darmstadt, Germany. The vibration was experimentally observed for the second eigenmode of the rotor blades at nonsynchronous frequencies and was simulated for two rotational speeds using a time-linearized approach. The numerical simulation results were in close agreement with the experiment in both cases. The vibration phenomenon shows similarities to flutter. Numerical simulations and comparison with the experimental observations showed that vibrations occur near the compressor stability limit due to interaction of the blade movement with a pressure fluctuation pattern originating from the tip clearance flow. The tip clearance flow pattern travels in the backward direction, seen from the rotating frame of reference, and causes a forward traveling structural vibration pattern with the same phase difference between blades. When decreasing the rotor tip gap size, the mechanism causing the vibration was eased.

Luan, et al., 2018[32] focused on rotor-rotor interactions effects on unsteady characteristic and blade aerodynamic force. The investigation method was based on three-dimensional URANS simulations, in conjunction with SST turbulence model. At first, the experimental measurements were compared to evaluate ability of the numerical method in estimation of unsteady flows. The results showed that rotor-rotor interaction in the contra-rotating fan played an important role in aerodynamic efficiency. Unsteady effect increased flow losses of rotor 1, but effectively inhibited flow losses of rotor 2. The inhibition effect was mainly caused by wake recovery effect of upstream wakes in the flow passage of rotor 2. Meanwhile, negative jet flow enhanced boundary layer energy of the blade of rotor 2, so that flow separation was postponed. Different configurations consider five sets of axial spacing dimensions. Specific survey of flows under the same operation conditions indicates that axial spacing was responsible for the unsteady interaction effect. The blade aerodynamics analysis showed that the influence of the downstream potential flow disturbance on rotor 1 was greater than the effect of the upstream wake on rotor 2.

Rajanna et al., 2018[33]presented a parametric study to optimize gas-turbine performance under off-design conditions by articulating the rotor blades in both clockwise and counterclockwise directions. Articulating the pitch angle of turbine blades in coordination with adjustable nozzle vanes can improve performance by maintaining flow incidence angles within the optimum range at certain off-design conditions. To observe the effect of rotor pitching on the performance of the gas turbine, a computational fluid dynamics (CFD) study was performed using the finite element formulation for compressible flows with moving domain. Results obtained from the CFD simulation for different rotor pitch angles were presented in this paper. The results show that after pitching the rotor blade in clockwise direction, the flow was able to recover a more optimal flow field associated to the gas turbine inlet condition and makes the flow fully attached. The results also show that clockwise pitching of the rotor increases the relative velocity magnitude which reduces the losses in converting the momentum to rotor torque. Whereas, pitching in the counterclockwise direction increases the absolute velocity magnitude at the exit of the rotor. The computational results show that pitching the rotor blade in clockwise direction can help in achieving the better performance at the turbine stage.

Jain et al., 2019[34] conducted massively parallel wall-modeled Large Eddy Simulations (LES) to simulate flow through a single stage power turbine sector of a gas-turbine engine under realistic operating conditions. The numerical framework in the current work uses finite volume based compressible CharLES solver that utilizes a moving Voronoi diagram based grid generation. To test grid sensitivity and evaluate the capability of the solver in predicting turbo-machinery flows, three grids of varying resolution were used to simulate flow through the baseline gas-turbine under design operating conditions. After assessing the flow solution quality and establishing simulation parameters, LES simulations were conducted to investigate the performance of gas-turbine at off-design conditions. The conditions include the rotor design point at 100% speed, and off-design points at 75%, and 50% speeds subject to high temperatures from the combustor exit flow. The results showed that the internal flow became highly unsteady as the rotational speed of rotor deviates from the design point leading to reduced aerodynamic performance. This study demonstrated that the current framework was able to robustly simulate the unsteady flow in a three-dimensional moving rotor environment for US Army Future Vertical Lift program towards design variable speed gas-turbine engines.

Zheng et al., 2019[35] studied the influence of tip gap size on aeroelastic stability in a 1.5 stage compressor with an in-house fluid-structure interaction code. A three-dimensional unstructured finite-volume compressible flow solver was applied in the fluid domain and a structure dynamic solver with the modal superimposition method for blade motion was used in the structure domain. Rotor tip clearances of 1%, 2% and 3% of tip axial chord at maximum rotor loading conditions at off-design speeds were analyzed for aeroelastic stability. The tip leakage flow and vortex structure was seen near the blade tip region at a larger tip gap size. The aeroelastic stability of rotor blade at different tip gap sizes was mainly influenced by the 1st torsion mode, and the variation of aerodynamic damping was not monotonous. The key factors affecting the aeroelastic stability of rotor, when tip gap size increased, were the intensity of the tip vortex and shock wave.

2.2 Experimental Work

Lifshits, 1986[36]used the experience accumulated by SwRI with various types of rotating equipment to present more comprehensive combined vibration severity limits. These limits were divided into several severity regions, and cover filtered and unfiltered vibration. The appropriate correction factors were also introduced to equitably accommodate different machine designs, installations, and vibration problems. Vibration severity limits were provided for relative shaft displacement, for shaft displacement with respect to bearing clearance, and for vibration measurements taken on machine casing or bearing housing. The use of these limits was clarified by reviewing the results obtained from five field studies of actual operating equipment. Advantages, disadvantages, and use of various transducer types (proximity probes, velocity pickups, accelerometers, dual probes), as well as sources of machinery vibration (sub synchronous instabilities, resonance, imbalance, misalignment, etc.) were analyzed to assure proper application of the vibration limits.

Ongoren and Rockwell, 1988[37]studied vibration effect of a cylinders of various cross-section subjected to controlled oscillations in a direction transverse to the incident flow. Excitation was at frequency f_e relative to the formation frequency of f_0^* large-scale vortices from the corresponding stationary cylinder, and at Reynolds numbers in the range $584 < Re < 1300$. Modifications of the near wake were characterized by visualization of the instantaneous flow structure in conjunction with body displacement-flow velocity correlations. At $f_e / f_0^*=0.5$, that correspond to subharmonic excitation, as well as at $f_e / f_0^*=1$, the near wake structure was phase-locked (synchronized) to the cylinder motion. However, the synchronization mechanism was distinctly different in these two regimes. Near or at $f_e / f_0^*=1$, the phase of the shed vortex with respect to the cylinder displacement switches by approximately π. Over a wide range of f_e / f_0^*, the perturbed near wake rapidly recovered to a large-scale anti-symmetrical mode similar in form to the well-known Karman vortex street. The frequency f_0 of the recovered vortex street downstream of the body showed substantial departure from the shedding frequency f_0, from the corresponding stationary body. It locks-on to resonant modes corresponding to $f_e / f_0^*=1/n$. This wake response involved strictly hydrodynamic phenomena. It showed, however, a resonant behavior was convectively unstable and was similar to that of coupled flow-acoustic systems.

Lifson, et al., 1989[38] presented a basis for selecting and justifying vibration monitoring equipment for power-generating gas turbines. Users of industrial gas turbines from utility and petrochemical companies were surveyed; a utility forced outage data base was analyzed; typical vibration limits were presented; and the current capabilities of commercial monitoring systems and vibration transducers were summarized. The industry survey by site visits and questionnaire develops common trends; it itemizes malfunctions that can be successfully identified with appropriate vibration monitoring; it summarized current practices, benefits, limitations, and operating experience with various transducer types, as applied to harsh gas turbine environments. Vibration limits, trending, and sources of vibration were addressed. Operational factors were considered in planning and cost justifying vibration monitoring systems for a basic trip protection, periodic measurements, and on-line computerized continuous protection. Seventeen case histories and examples illustrated and supported these findings. Analysis of the utility-generated data base complements the industry survey; it isolates the contribution of different vibration-related outages for base loaded and peaking units; graphic results break down these outages into duration, man-hours to repair, and frequency of occurrence.

Mathioudakis, et al., 1990[39] presented the results from an experimental investigation of the compressor casing vibration of an industrial gas turbine. It was demonstrated that statistical properties of acceleration signals can be linked with engine operating conditions. The power content of such signals was dominated by contributions originating from the stages of the compressor, while the contribution of the shaft excitation was secondary. Using nonparametric identification methods, accelerometer outputs were correlated to unsteady pressure measurements taken by fast response transducers at the inner surface of the compressor casing. The transfer functions allow reconstruction of unsteady pressure signal features from the accelerometer readings. A possibility was thus provided for "seeing" the unsteady pressure field of the rotor blades without actually penetrating through the casing, but by simply observing its external surface vibrations.

Greenblatt and Wygnanski, 2000[40] presented a review of the control of flow separation from solid surfaces by periodic excitation. The emphasis was placed on experimentation relating to hydrodynamic excitation, although acoustic methods as well as traditional boundary layer control, such as steady blowing and suction, were discussed in order to provide an appropriate historical context for recent developments. The review examines some aspects of the excited plane mixing-layer and shows how its development lays the foundation for a basic understanding of the problem. Flow attachment to, and separation from, a deflected flap was then shown to be a paradigm for isolating controlling parameters as well as understanding the basic mechanisms involved. Particular attention was paid to separation control on airfoils by considering controlling parameters such as optimum reduced frequencies and excitation levels, performance enhancement, efficiency, reduction of post-stall unsteadiness, compressibility and other important features. Additional topics covered include excitation of separation bubbles, control and exploitation of diffuser flows, three-dimensional effects, the influence of longitudinal curvature and possible applications to unmanned air vehicles. The review closed with some recent developments in the control and understanding of incompressible dynamic stall, specifically illustrating the control of dynamic stall on oscillating airfoils. The crucial time-scale disparity between dynamic stall and periodic excitation was identifying as well.

Govardhan and Williamson, 2002[41]studied the transverse vortex-induced vibrations of a cylinder with no structural restoring force ($k = 0$). In terms of the conventionally used normalized flow velocity, U^*, the present experiments correspond to an infinite value (where $U^* = U/f_N D$, f_N = natural frequency, D = diameter). A reduction of mass ratios m^* (mass/displaced mass) from the classically studied values of order $m^* = 100$, down to $m^* = 1$, yields negligible oscillations. However, a further reduction in mass exhibits a surprising result: large-amplitude vigorous vibrations suddenly appeared for values of mass less than a critical mass ratio, $m^*_{crit} = 0.54$. The classical assumption, since the work of den Hartog (1934), has been that resonant large-amplitude oscillations exist only over a narrow range of velocities, around $U^* \sim 5$, where the vortex shedding frequency was comparable with the natural frequency. However, in the present study, authors demonstrated that, so long as the body's mass was below the critical value, the regime of normalized velocities (U^*) for resonant oscillations was infinitely wide, beginning at around $U^* \sim 5$ and extending to $U^* \to \infty$. The result was in precise accordance with the predictions put forward by Govardhan and Williamson (2000), based on elastically mounted vibration studies (where $k > 0$). The author deduced a condition under which the unusual concept of an infinitely wide regime of resonance occurred in any generic vortex-induced vibration system.

Seifert, et al., 2004[42]studied experimentally the separation control, by nominally two-dimensional periodic excitation at Reynolds numbers ranging from 3×10^4 to 4×10^7, including compressibility effects. The tests demonstrated that active control using oscillatory flow excitation can effectively delay flow separation from, and reattach separated flow to, aerodynamic surfaces at various flight conditions. At Reynolds number below 10^5, where transition does not occur naturally and cannot be passively forced, active separation control may be the only effective method for delaying separation and generating useful lift. The essence of active separation control relies on exploiting instabilities that were inherent in the flow, generally requiring relatively small amplitude excitation. Effective excitation frequencies generate one to four vortices over the controlled region at all times, irrespective of Reynolds number, and perturbations should preferably be amplified over the region that was susceptible to separation. Periodic excitation was vastly superior to steady blowing in terms of performance benefits and eliminates abrupt flow responses, which were undesirable from a control point of view. The effects of compressibility in the absence of shocks were weak and undesirable effects accompanying separation, such as vortex-shedding and buffet, can be significantly reduced or completely eliminated. The shock-wave/boundary-layer interaction produced a separation which can be enhanced when the excitation was introduced to the separation upstream.

Lam and Leung, 2005[43] reported an experimental investigation of the vortex shedding wake behind a long flat plate inclined at a small angle of attack to a main flow stream. Detailed velocity fields were obtained with particle-image velocimetry (PIV) at successive phases in a vortex shedding cycle at three angles of attack, $\alpha = 20^\circ$, 25° and 30°, at a Reynolds number $Re \approx 5300$. Coherent patterns and dynamics of the vortices in the wake were revealed by the phase-averaged PIV vectors and derived turbulent properties. A vortex street pattern comprising a train of leading edge vortices alternating with a train of trailing edge vortices was found in the wake. The trailing edge vortex was shed directly from the sharp trailing edge while there were evidences that the formation and shedding of the leading edge vortex involve a more complicated mechanism. The leading edge vortex seems to be shed into the wake from an axial location near the trailing edge. After shedding, the vortices were convicted downstream in the wake with a convection speed roughly equals to 0.8 the free-stream velocity. On reaching the same axial location, the trailing edge vortex, as compared to the leading edge vortex, was found to possess a higher peak vorticity level at its center and induce more intense fluid circulation and Reynolds stresses production around it. It was noted that the results at the three angles of attack collapsed into similar trends by using the characteristic length of the flow (the projected plate width).

Gostelow, et al., 2005[44] demonstrated similarities between the vortex shedding from blunt trailing-edged transonic turbine nozzle blades and from oscillating bluff bodies. Under subsonic conditions the turbine nozzle cascade shed wake vortices in a conventional von Kármán vortex-street. This was linked with a depressed base pressure and associated energy separation in the wake. Under transonic conditions a variety of different shedding configurations was observed with vortices shedding and pairing in several different ways. Similarities were addressed between the observed structures and those from vortex shedding in some other physical situations. The authors investigated the similarity between the vortex wakes shed from cylinders and airfoils in sinusoidal heaving motion in low speed flow and the wakes shed from the turbine nozzle cascade in transonic flow. The established field of vortex-induced vibration provided a developed classification scheme for the phenomena observed. The paper brought together three previously unrelated fields of investigation and, by showing that the three were essentially related, provided the basis was for a new synthesis.

Cleaver et al., 2010[45] measured the force and supporting particle image velocimetry for a plunging NACA 0012 airfoil at a Reynolds number of 10,000, at pre-stall, stall, and post-stall angles of attack. The lift coefficient for pre-stall and stall angles of attack at larger amplitudes showed abrupt bifurcations with the branch determined by initial conditions. With the frequency gradually increasing, very high positive lift coefficients were observed, this was termed mode A. At the same frequency with the airfoil impulsively started, negative lift coefficients were observed, this was termed mode B. The mode A flow field was associated with trailing-edge vortex pairing near the bottom of the plunging motion causing an upwards deflected jet, and a resultant strong upper surface leading-edge vortex. The mode B flow field was associated with trailing-edge vortex pairing near the top of the plunging motion causing a downwards deflected jet, and a resultant weak upper surface leading-edge vortex. Because of the insufficient strength of the trailing-edge vortex, the bifurcation was not observed for small amplitudes nor at larger angles of attack due to greater asymmetry in the strength of the trailing-edge vortices. The deflected mode B wake was downward because of the natural preference created by the train edge vortices.

Tereshchenko et al., 2015[46] presented the results of an analysis of the gas-dynamic control of flow around the guide blades of axial compressor stage for the vibration intensity of rotor blades. It was shown that gas-dynamic action on flow around blades equalized the flow velocity field before the rotor and reduced the level of resonant stresses in blades in the case of their resonant excitation.

Hsieh, Low and Chiew, 2017[47] investigated the flow characteristics of the wake in the initial branch for a vibrating cylinder using a new PIV technique capable of a high sampling rate of 200 Hz. The experiments were carried out over a wide range of reduced velocities to better understand the important trends. The mean velocities and turbulence characteristics were obtained by ensemble averaging repeated velocity measurements. Their study revealed new insights on the flow characteristics of the wake in the initial branch. In particular, the cylinder vibration was found to lead to the formation of oblique jets, which have a profound influence on the mean flow velocity, turbulence intensity, formation and convection of the vortices, and variations to the stagnation and separation points of the cylinder during vibration.

Qu et al., 2019[48] presented a comprehensive measurement for a flow losses and flow field data downstream of an ultra-high-lift aft-loaded low pressure turbine cascade for different incoming wake passing frequencies, and the mechanisms through which incoming wakes influence secondary flow were examined via numerical calculations. Reynolds numbers ranging from 25000–100000 (based on the axial chord and inlet velocity) were considered in both the presence and absence of the wakes. At low Reynolds numbers of 25000 and 50000, increasing wake passing frequency gradually suppressed the suction surface separation bubble and increased the cross-passage pressure gradient, and the unsteady wakes clearly improved the through flow characteristics of the cascade passage. Furthermore, the larger separation bubble on the suction surface hindered the migration of the secondary vortices from the endwall to span. Consequently, incoming wakes were not beneficial for suppressing secondary flow at low Reynolds numbers. At the high Reynolds numbers of 80000 and 100000, increasing wake passing frequency afforded stronger inhibition of the secondary flow owing to the reduction in blade loading originating from the “negative jet” influence of the wakes. In addition, another advantage was presented for decreasing secondary flow losses by transport of incoming wakes in the cascade passage.

2.3 Theoretical and Experimental Work

Doorly and Oldfield, 1985[49]found that flow unsteadiness caused a considerable influence on the aerodynamic and heat-transfer performance of turbomachinery blades. The most significant contribution to this unsteadiness was caused by "wake passing," the term used here to describe the flow produced on a downstream blade row as it periodically chops through the wakes shed by the upstream blade row. The effect occurs both in the compressor and turbine blade passages.

Henderson, et al., 2005[50]studied the influence of free-stream turbulence on wake dispersion and boundary layer transition processes in a 1.5-stage axial compressor. An inlet grid was used to produce turbulence characteristics typical of an embedded stage in a multistage machine. The grid turbulence strongly enhanced the dispersion of inlet guide vane (IGV) wakes. This modified the interaction of IGV and rotor wakes, leading to a significant decrease in periodic unsteadiness experienced by the downstream stator. These observations have important implications for the prediction of clocking effects in multistage machines. Boundary layer transition characteristics on the outlet stator were studied with a surface hot-film array. Observations with grid turbulence were compared with those for the natural low turbulence inflow to the machine. The transition behavior under low turbulence inflow conditions with the stator blade element immersed in the dispersed IGV wakes closely resembled the behavior with elevated grid turbulence. It was concluded that with appropriate alignment, blade element behavior of an embedded row in a multistage machine can be indicated by the blade element behavior in a 1.5-stage axial machine.

Persico et al., 2012 [51] studied the three-dimensional unsteady aerodynamics of a low aspect ratio, high pressure turbine stage. In particular, the results of fully unsteady three - dimensional numerical simulations, performed with ANSYS-CFX, were critically evaluated against experimental data. Measurements were carried out with a novel three dimensional fast-response pressure probe in the closed-loop test rig Machine Fluid Dynamics Laboratory of the Politecnico di Milano. An analysis was first reported about the strategy to limit the CPU and memory requirements while performing three dimensional simulations of blade row interaction when the rotor and stator blade numbers were prime to each other. What emerges as the best choice was to simulate the unsteady behavior of the rotor alone by applying the stator outlet flow field as a rotating inlet boundary condition (scaled on the rotor blade pitch). Thanks to the reliability of the numerical model, a detailed analysis of the physical mechanisms acting inside the rotor channel was performed. Two operating conditions at different vane incidence were considered, in a configuration where the effects of the vortex-blade interaction were highlighted. Different vane incidence angles led to different size, position, and strength of secondary vortices coming out from the stator, thus promoting different interaction processes in the subsequent rotor channel. However some general trends were recognized in the vortex blade interaction: the sense of rotation and the span wise position of the incoming vortices play a crucial role on the dynamics of the rotor vortices, determining both the time mean and the time-resolved characteristics of the secondary field at the exit of the stage.

Jungst et al., 2015[52] added to the understanding of non-synchronous blade vibration caused by unsteady flow close to the stability limit of transonic compressor rotors. Blade vibrations were measured in the rotating frame of reference by strain gauges applied to the blades and additionally in the stationary frame of reference by capacitive tip clearance/tip timing sensors. Furthermore unsteady pressure transducers in the casing wall were used to analyze the flow phenomena during high blade vibration amplitudes. During the transient experiments, the compressor was back-pressured into its stability limit. Two transient measurements of a compressor setup with an enlarged tip clearance of 2.5% blade chord were analyzed at -part speed and design speed. This means that subsonic and transonic operation conditions were analyzed. In both cases, nonsynchronous vibration occurred and limited the compressor operation. The mechanism leading to these vibrations was based on an unsteady flow pattern that rotates relative to the rotor, reported as rotating instability.

2.4 Summary

In general, as far as the author know, there have been few studies and investigations on the aerodynamic flow in gas turbines. In particular, the vibration effects on this flow between the turbine blades have not been covered appropriately. Therefore, the more relevant studies are listed as:

The following conditions will be taken into account in this study. The effects of the vibration at different frequency levels of the airfoil on the aerodynamic flow and the observed vortices formed as a result of the vibrations. In addition, the finite element method will be used to model the Navier-Stokes equations. It will be used the aerodynamic flow into the passage between two blades of turbine and utilized the computational fluid dynamics (CFD) to investigate pressure distribution between the blades with/without vibration by using shaker based on the SST k-ϵ model.

Table 2.1 Summarize results of literature studies.

N0. Ref	Researcher name	Year	Type of study	Case study	The main conclusions
29	**Khan et al.,**	2017	Numerical	Investigated effects of the vibration at different frequency levels of the airfoil on the aerodynamic flow and the observed vortices formed due to the vibrations.	They found that the lift performance was directly proportional to the vibration at low Reynolds numbers, but it was inversely at higher values of the Reynolds numbers that resulted from the lock-in phenomena. That reveals that vibration may affect the fluid flow charactersitics.
30	**Chen, 2017**	2017	Numerically	Studied the aerodynamic flow into the passage between two blades of the turbine.	Utilized computational fluid dynamics (CFD) to investigate pressure distribution, streamlines, and Mach numbers between the blades. That means CFD can be safely used for vibration simulation.
33	**Zheng et al.,**	2019	Numerically	Studied the influence of tip gap size on aeroelastic stability in a 1.5 stage compressor with an in-house fluid-structure interaction code.	The key factors affecting the aeroelastic stability of the rotor when tip gap size increased were the intensity of the tip vortex and shock wave. RNg K-ϵ model can be used for the fluid simulation.

52	***Qu et al.,***	2019	Numerically and Experientially	Presented a comprehensive measurement for flow loss and flow field data downstream of an ultra-high-lift aft-loaded low-pressure turbine cascade for different incoming wake passing frequencies. The mechanisms through which incoming wakes secondary influence flow were examined via numerical calculations	Increasing wake passing frequency afforded stronger inhibition of the secondary flow owing to the reduction in blade loading originating from the "negative jet" influence of the wakes. In addition, another advantage was presented for decreasing secondary flow losses by transport of incoming wakes in the cascade passage. RNg K-ϵ model can be used for the fluid simulation.
47	***Hsieh, Low, and Chiew,***	2017	Experientially	Investigated the flow characteristics of the wake in the initial branch for a vibrating cylinder using a new PIV technique capable of a high sampling rate of 200 Hz.	Oblique jets have a profound influence on the mean flow velocity, turbulence intensity, formation and convection of the vortices, and variations in the stagnation and separation points of the cylinder during vibration.
----	**Present work**	2022	Experimental and Numerical	The aerodynamic flow between turbine cascade blades with and without the vibration effect	When vibration increases, the mean velocity increases, and the pressure coefficient increases.

CHAPTER THREE

EXPERIMENTAL STUDY

3. Introduction

This chapter involves the experimental aspect. The experimental is done in post graduate laboratories of Mechanical Engineering department at University of Babylon. All experiments have been implemented with ambient conditions of 1 bar pressure and (25 ºC -30ºC) temperature. Effect of vibration on the aerodynamic characteristic of flow on the cascade blade for the rotatory turbine (model frame 5) supplied by a General Electric company (G.E) is investigated in detail. The blade root is exposed to a transverse forced vibration in sinusoidal form. In addition, this chapter involves designing and manufacturing a prototype exactly similar to that brought from the Hilla gas turbine engine. Mechanisms used for the installation of the used devices and equipment along with measurement systems are also presented. The procedure of operating the devices and implementing the experiments is summarized at the end of this chapter. Fig. 3-1-a, and b show the whole system and necessary devices for the experimental work.

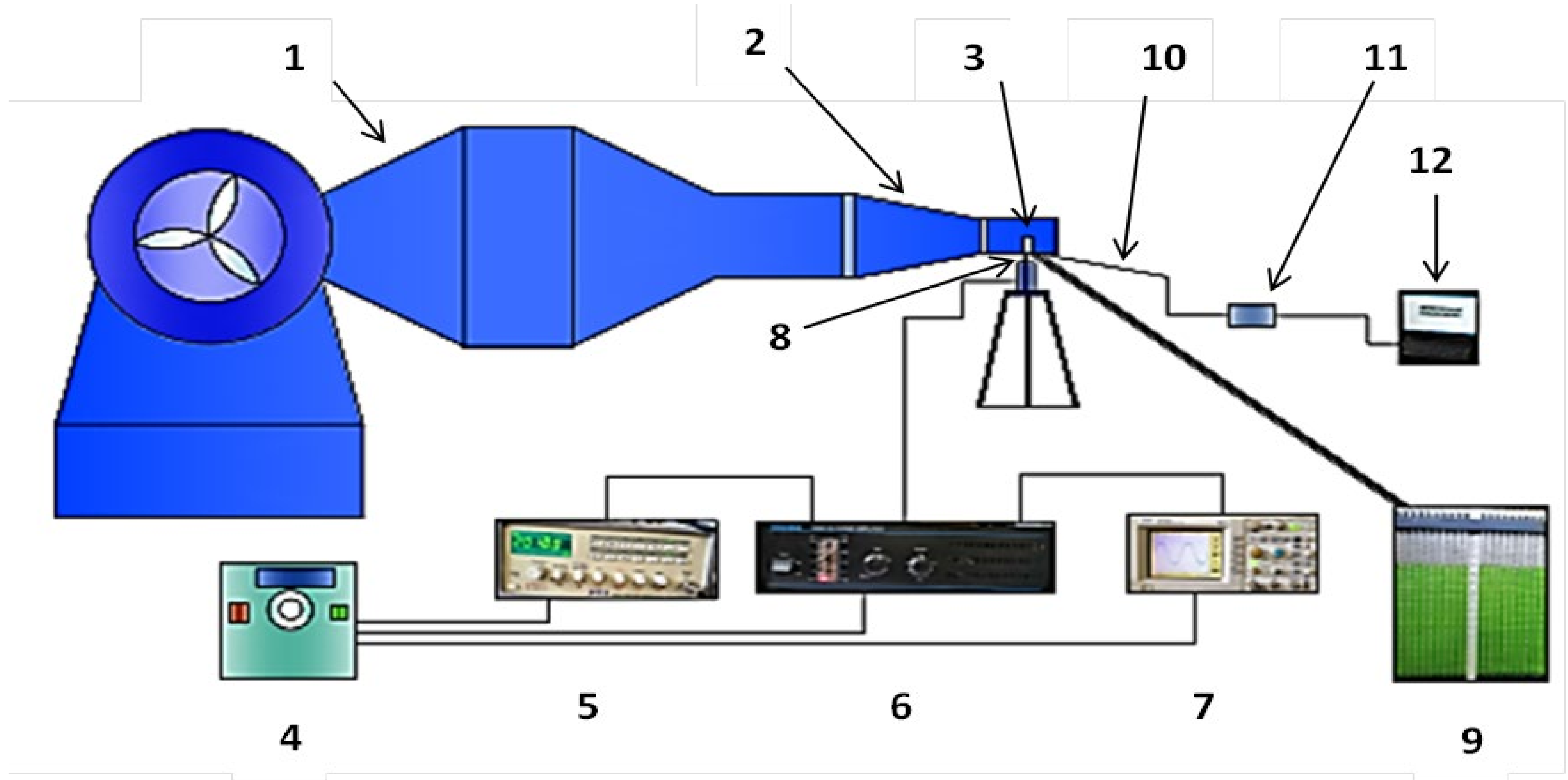

number	name	number	name	number	name	number	name
1	Wind tunnel	4	power supply	7	oscilloscope	10	accelerometer
2	Converter part	5	function generator	8	shaker	11	Vibrometer
3	Model	6	amplifier	9	multitube manometer	12	laptop

Fig. 3-1-a: Schematic Diagram of expermint Rig

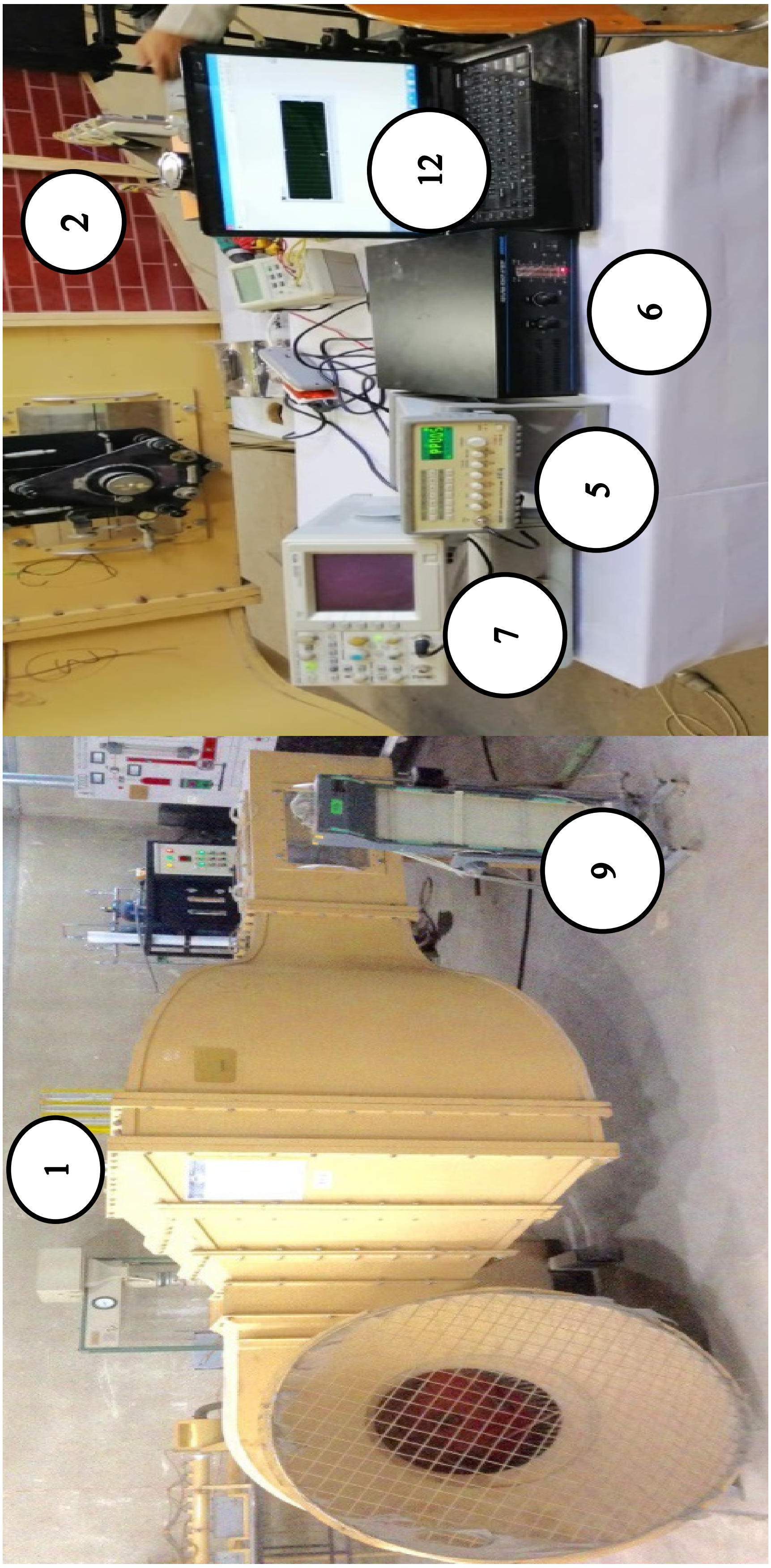

Fig. 3-1-b: Experimental Setup

3.1. Experiment Rig

Based on Fig. 3-1, the rig consists of two parts, working devices from (1) to (8), and measurement tools from (9) to (12).

(1) Wind Tunnel

(2) Extended-Part Tunnel Design

(3) Blade Model Preparation

(4) Power Supply

(5) Function Generator

(6) Power Amplifier

(7) Oscilloscope

(8) Vibration Shaker

(9) Manometer

(10) Accelerometer

(11) Data Collector

(12) Laptop (LabVIEW Program)

3.1.1. Wind Tunnel

The tunnel used is the open type with a closed test section. Air enters the test section (49 ×49×122) cm. Air reaches the test section after it passes through a fine screen. The screen is made of a sheet of cloth with small holes to permit the streamlining. There are two layers of screen sheets where the distance between them is 23cm. The model is placed on the test-section. The pressure probes transmit the signal to the multi-tube manometer through a rubber tube attached to it. Air speed through the section can be varied, by changing the speed ratio of the electrical motor that drives the blower fan. The maximum air speed reaches 22m/s.

3.1.2. Test Part and Extended-Part

Two extended parts were added along to the subsonic wind tunnel of the fluid laboratory at University of Babylon for accomplishing the experimental work. The first part is the process of manufacturing the part responsible for reducing the section of the wind tunnel from 49cm× 49cm to 22cm × 13cm. This part was manufactured from wooden boards. This part of the wind tunnel is connected after a grid of regular wiring for the purpose of regulating airflow at the attachment points of this part of the tunnel and the part containing the practical model as shown in figure 3-3a.

The second part was a rectangular duct with dimensions of 22cm × 13cm containing five movable plates attached to the mainframe in a way that provides different plate angles to redirect air on the blade assembly. Four blades were fixed identical to the real angle in the gas-turbine system. The four blades were interconnected with each other to one root (made of iron) using a traditional high-quality glue (the iron base was attached to a shaker (vibrator) by means of a screw mediating in the blade set as shown in figure 3-3b.

Two parts were added in the wind tunnel used and located in the fluid laboratory for the purpose of modifying it in proportion to the practical part to simulate the real situation as much as possible.

The model used in the practical part consists of a set of blades that were manufactured as previously separated, as it consists of four blades arranged as shown in assuming that the arc formed by these blades is very small [53], so it is possible to consider that this group located on a straight line instead of an arc line as the researchers mentioned in the practical part of chapter two.

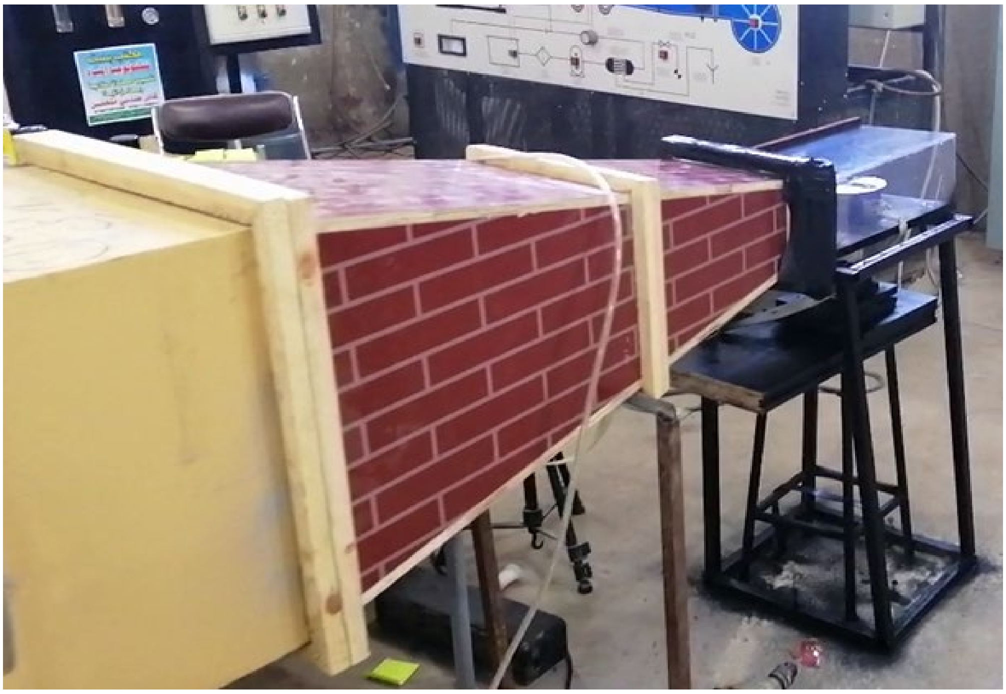

Fig. 3-3-a: Extended part added to the wind tunnel

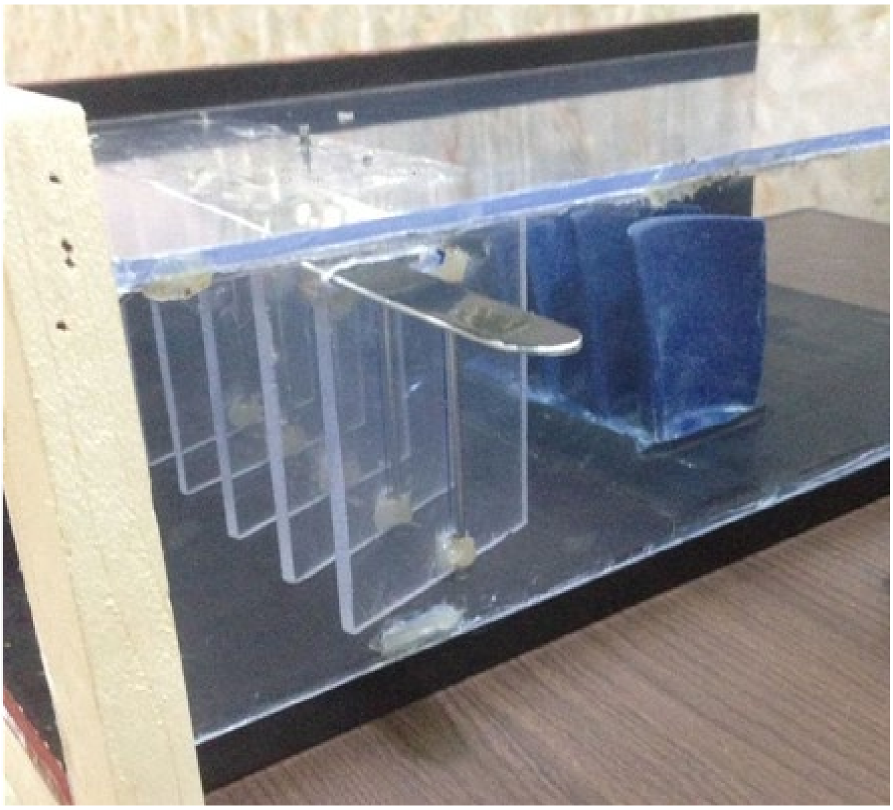

Fig. 3-3-b: Test-Section part added to the wind tunnel

Air is applied on the cascade blades at atmosphere pressure at 22 m/s and temperature (25 C^o-30 C^o). The blade is divided with several lines that represent the study area for the flow between the set of blades that the readings are confined between the endwall and the midspan. Three instruments are distributed in one line on the basis of dividing this line into four equal sections, i.e. one of these instruments is in the middle of the line and at the first and last quarter of the line of instruments.

3.1.3. Blade Model Preparation

The tested model identical to the real blade's shape was of GE turbine used in Hilla power station manufactured with high accuracy according to the dimensions of the real blade used in the gas turbine engine. A model identical to the real shape was manufactured with high accuracy by preparing a specific mold. First of all, the original sample is brought and coated with a very thin layer of anti-adhesion material. Next, a mixture of composite materials is poured onto the prepared mold. The fine details of the original sample of the blade were copied accurately. In the second stage, another mold was produced from two parts, and their accuracy and consistency are adjusted through four screws at the corners of the mold. The whole test rig used in this experimental work consists of four successive blades, well-connected at the bottom by a base that is connected in turn with the vibrator (shaker), which is responsible for generating vibration for the model. A specific shaker is designed to generate the required value of frequency similar to that located at the Hilla gas turbine station. The forced vibration was applied by a vibration shaker with different levels of frequency (9, 16, 23, and 33 Hz) and a constant amplitude value (3mm).

3.1.4. Power Supply

This device supplies and controls the electric power with AC current to the function generation device. Voltage regulator single phase variance 0-250V voltage converter power converter voltage transformer 220V (Input voltage:110/220V, Output voltage:0-250V,Frequency:50/60Hz, accuracy of voltge stabilization :220V±2%, 110V±6%). The power supply regulates the value of output voltage to achieve the required power for each case of the study. The power supply is shown in Fig. 3-4

Fig. 3-4: Power supply

3.1.5. Function Generator

Function generator type **μ**_TEK FG-703CM was used to generate frequencies within the range from (5Hz to 50Hz±1%) in the form of a sine wave. The function generator was calibrated by the oscilloscope device to ensure the form and the frequency of the generated wave while the generated signal is passed to the power amplifier then to the exciter. This function generator has a frequency range from 0.3Hz to 3MHz and the waveform of sinusoidal, triangle, square, ramp, and TTL output, as shown in Fig. 3-5.

Fig. 3-5: Function generator

3.1.6. Power Amplifier

Power amplifier type SINOCERA YE5871A within three-stage amplification: a differential pre-amplification, a driving amplification, and an asymmetric compensating power amplifier. The amplification of frequency range from 5Hz to 10 kHz±2% is the limitation of this device. It is used to amplify the signal of the sine wave which is generated by a function generator and passed to the exciter to make it vibrate accordingly. The power amplifier is shown in Fig. 3-6.

Fig. 3-6: Power Amplifier

3.1.7. Oscilloscope

Oscilloscope type ATTEN ADS-7202CA was used to monitor and calibrate the output signal of the function generator. A digital storage oscilloscope (DSO) is an oscilloscope that stores and analyses the input signal digitally rather than using analog techniques. The error of the oscilloscope is ±1%.

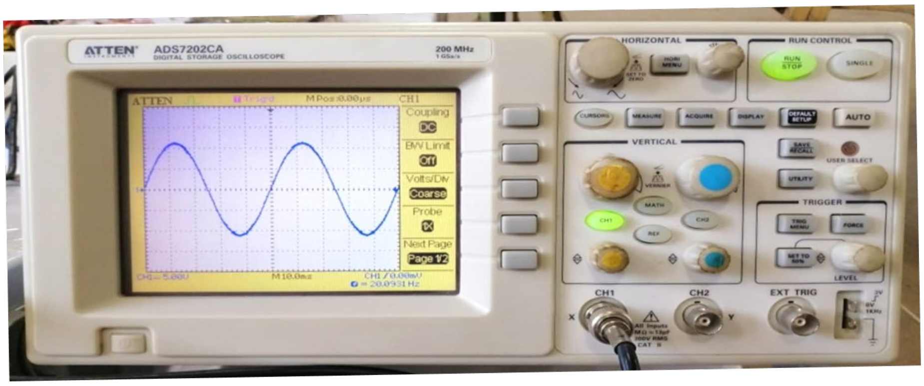

Fig. 3-7: Oscilloscope

3.1.8. Vibration Shaker

Shaker JZK-2 was used in the experimental work. It mainly consists of two parts; the first part is a moving coil and the second part is a fixed magnetic cylinder. A magnetic force is generated by electromagnetic action when an AC is applied from a power amplifier to the moving coil. With the highest vibration amplitude (±3 mm), this exciter responds with the frequency range 3Hz to 5 kHz±2%. The dynamic resulted force can be given by [54];

Fig. 3-8: The vibration genereator

$$F = 0.102B * L * I * 10 \tag{3.1}$$

3.1.9. Manometer

An 18-tube manometer is used to measure pressure on models in subsonic wind tunnels and blades test sets. A backboard with a graded scale holds each manometer tube. For safety and convenience, the manometer uses water as the manometer fluid as shown in Fig. 3-7. The whole manometer tube assembly is mounted on a swivel to be tilted in preset increments in order to increase the sensitivity of the measurement. The manometer has a human error with ±3% and it was provided with the operating instruction and the filling repression.

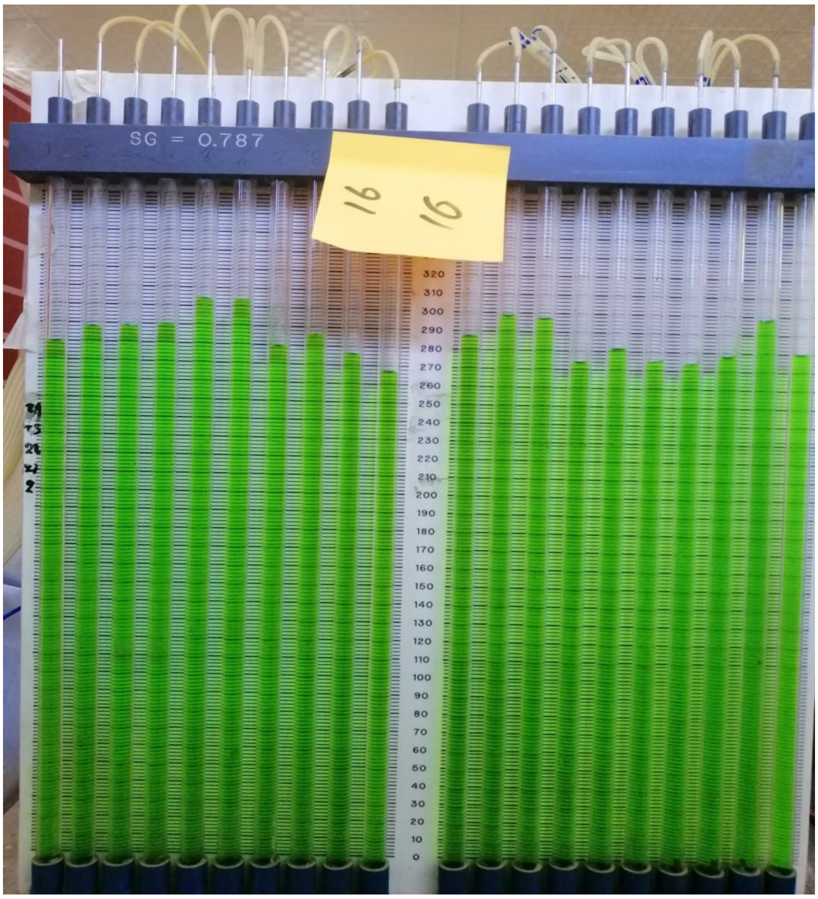

Fig. 3-9: Multi-Tube Manometer

3.1.10. Accelerometer

An accelerometer is a transducer, used to measure the frequency of pipe by exerting a force on it. The accelerometer type 4368 Bruel & Kjaer is an instrument used to measure the frequency of the tested model with an error of ±0.3%, as shown in figure 3.10. The vibrational motion is often converted into an electrical signal. The voltage output of the device is due to the cyclic deformation of the piezoelectric crystals. The frequency, rise time, the maximum and minimum voltage can be obtained from the electrical output of the accelerometer.

Fig. 3-10: Accelerometer

3.1.11. Data Collector

The process of measuring electrical or physical phenomena, such as voltage, current, temperature, pressure, or sound, is referred to as data acquisition (DAQ). Sensors, DAQ measuring gear, and a computer with programmable software make up a DAQ system with an error of ±0.3%. The DAQ from National Instruments is a cutting-edge field balancing instrument for balancing spinning machinery in one or two planes under real-world conditions.

Fig. 3-11: Data Collector

3.1.12. LabVIEW Program

LabVIEW is a system software for engineering applications that demand rapid access to hardware and data insights as well as test, measurement, and control. The LabVIEW programming environment makes hardware integration for engineering applications easier, so you can get data from NI (National Instrument device) and third-party hardware in a uniform manner. LabVIEW can interoperate with and reuse libraries from other software and open-source languages to ensure interoperability with other engineering tools. The frequency and amplitude of the acceleration sensor are measured using this software, as illustrated in Fig. 3-12.

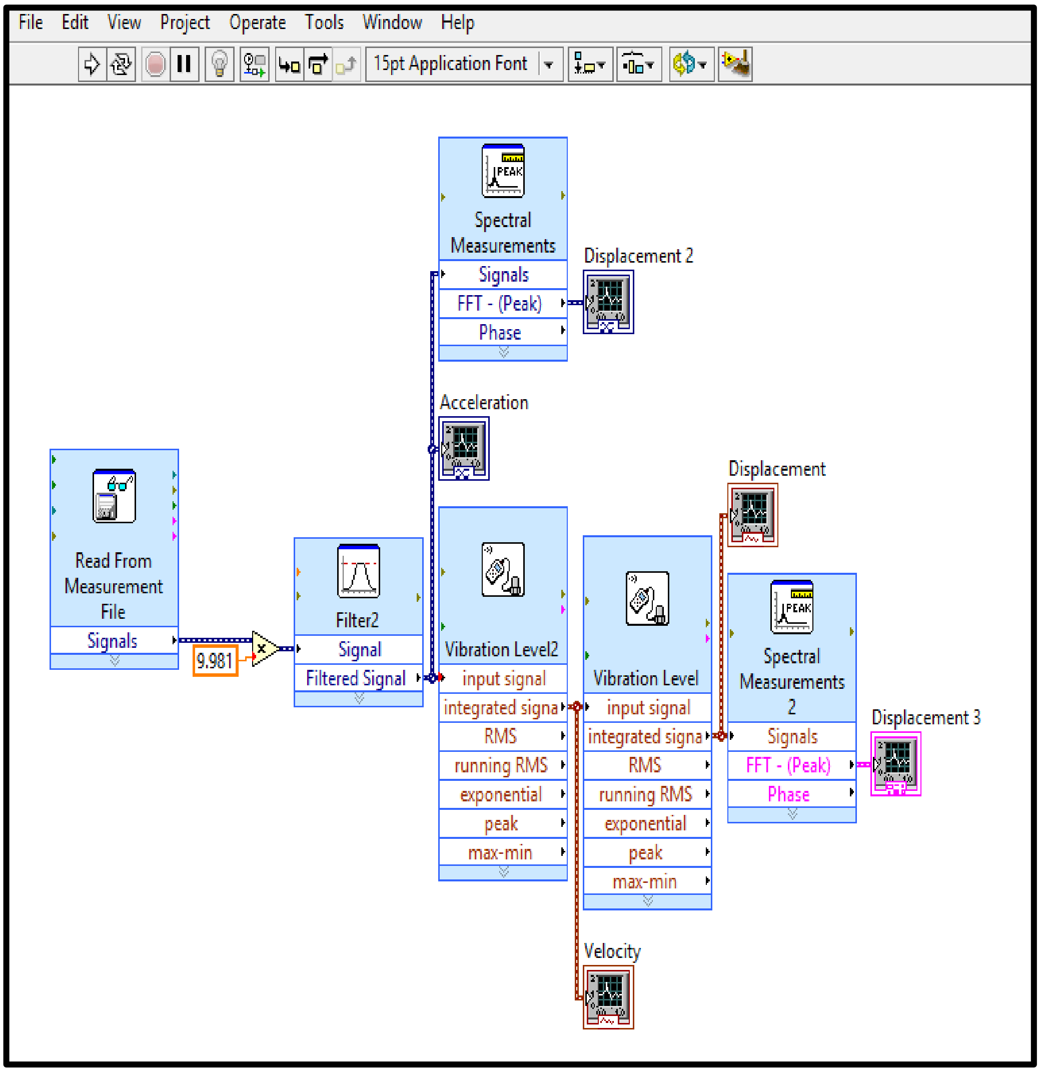

Fig. 3-12: Block Diagram of LabVIEW

3.1.13. Pressure Measurement Taper Preparation

Eighteen pressure tube instruments are used to record the pressure distribution on the blades. Nine of them are placed on each end of the blade, as shown in Fig. 3-13. One of these ends was responsible for recording pressure (the region of the pressure side of the blade, P.S.). The other is next to the suction side (S.S.) and these pressure tube instruments are distributed in the form of three horizontal lines, a line containing three pressure tube instruments. The first, second, third lines of the instruments were placed at 6, 21, and 36 mm from the base of the blade, respectively. These lines represent the study area for the flow between the set of blades that the readings are confined between the end wall and the midspan. Fig. 3-13 shows the distribution of the instruments on the surfaces of the blade. These pressure tube instruments are set with a multi-tube manometer to measure pressure at different positions and then calculate velocity by using the Bernoulli equation as equation 3.2. Air is right on the cascade blades at atmosphere pressure at 22 m/s and temperature 300K.

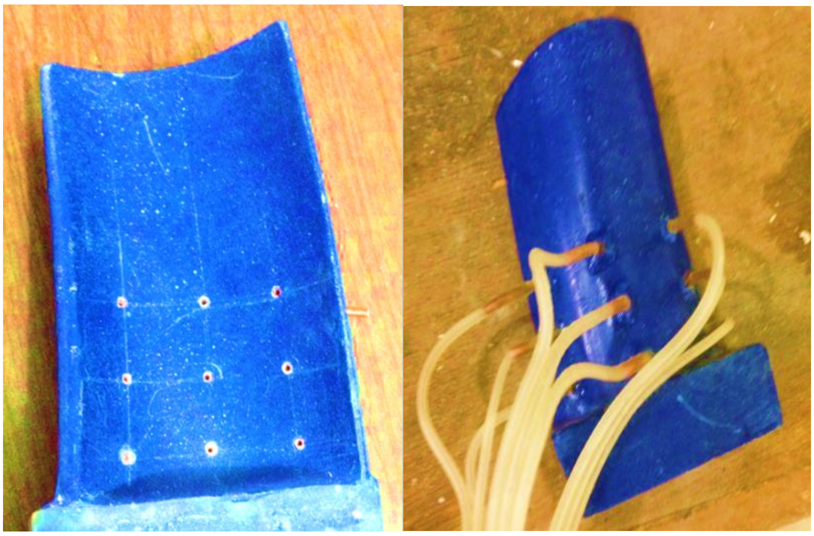

Fig. 3-13: Distribution of manometer tubes on the blade.

Eighteen instruments on the blade are set with a multi-tube manometer to measure pressure at different positions and then calculate velocity by using the Bernoulli equation as equation 3.2.

$$U = \sqrt{\frac{2(p_{total} - p_{static})}{\rho}} \tag{3.2}$$

3.1.14. Velocity Measurement

Flow velocity measuring devices allow the flow velocity of fluid media such as gases and air to be measured. Flow velocity measuring device is used to measure airflow in the wind tunnel before cascade blades rig with an error of ±1%.

Fig. 3-14: Velocity measurement

3.2. Materials and Manufacturing of Blade

3.2.1. Materials for the Pattern and Mold

The materials used in preparing the mold and the model are made of three different materials that are combined with each other in a special engineering and chemical way to produce the desired shape of the blade mold.

The main material is casting polyester (ES 1060), which is a liquid polyester material that has a high potential to interact with other additives and produce a mixture that has the ability to form and take the true shape with high accuracy, being liquefied in its first state and then begins to solidify after that to give a material high hardness and toughness.

As for the second material, it is the reinforcing material of the polyester after its hardening and it consists of gypsum powder, and the last material is the hardener that is responsible for the interaction between these two materials and merging with each other to form the final material for the model used in the practical side.

3.2.2. Preparation of Blade Mold

A mold is manufactured that has the ability to produce more than one blade with high specifications and accuracy identical to the original shape and is easy to use and install in order to obtain an equal set of precision and measurement of samples that are used in the practical side as shown in the figures 3-15 and 3-16.

Fig. 3-15: The first stage of mold production

Fig. 3-16: Final mold production

3.2.3. Blade Manufacturing Steps

Mix the required quantity of liquid polyester and powder gypsum in a ratio of 3:1 of polyester: powder gypsum and mix them together mechanically well for a period ranging from 5-10 minutes to ensure homogeneity and then add the hardener gradually and in an amount commensurate with the amount of the two basic materials polyester and powder gypsum and the ratio is from 5 to 6% of the weight of the two basic materials. A mixture of composite materials in the same proportions is prepared and mixed for five minutes by mechanical mixing to ensure good homogeneity in the mixture as shown in figure 3-17 and 3-18.

(a) (b) (c)

Fig. 3-17: blade pattren molding

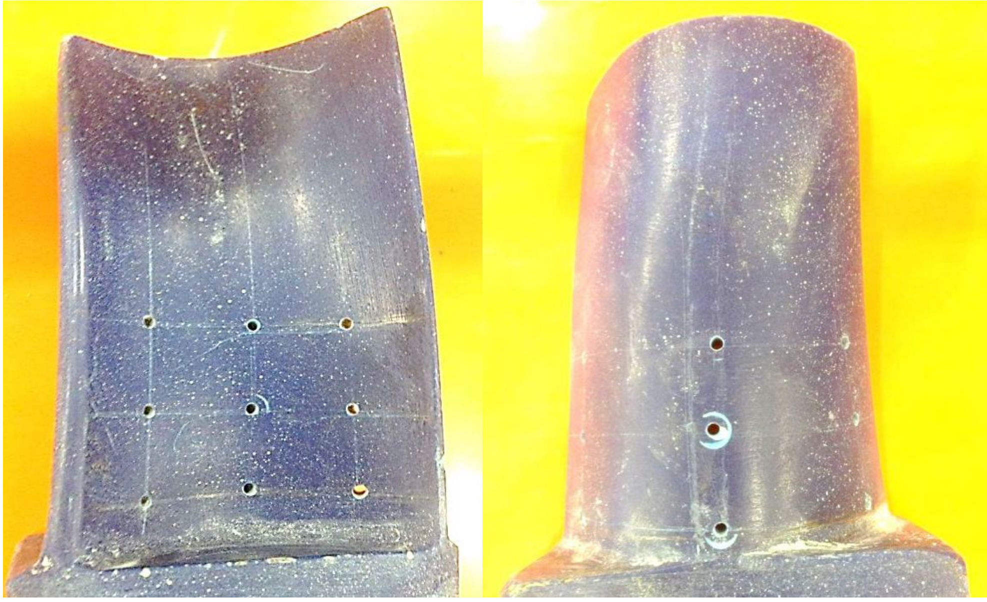

Fig. 3-18: final blade pattern

3.3. Experimental Procedure

3.3.1. The Used Procedure for This Experiment

Connect all operating devices and measuring equipment for the experiment in their appropriate places and accordance with the operating conditions.

Table 3-1: Blade details and boundary conditions of the experimental work

property	**value**
Span	96 mm
chord length at the root	58 mm
maximum camber at the root	17.96 mm
chord length at the tip	54.7 mm
maximum camber at the tip	11.6 mm
inlet velocity	22 m/s
blade vibration	harmonic (sinusoidal) 3-33Hz

1) The air pressure readings around the blade are recorded for 18 locations by means of pressure instruments on a multi-tube manometer, as previously explained. Readings are taken first without shaking for comparison purposes.

2) Generate vibration through the shaker and its associated devices, which are responsible for the amount of frequency and amplitude of the vibration. After this procedure, readings are taken from a multi-tube manometer.
3) Step (2) is repeated, but for different frequencies values, while the amplitude stays unchanged.

3.3.2. Flow Velocity Calculation

Bernoulli's equation is used to find the velocity of air in different regions near the blade walls as shown in equation 3.2.

3.3.3. Pressure Coefficient (C_P) Calculation

The pressure coefficient is defined as the difference in average static pressure between the first and last stations. The pressure coefficient is a dimensionless number which describes the relative pressures throughout a flow field in fluid dynamics [55].

$$C_P = \frac{P - P_\infty}{\frac{1}{2}\rho_\infty U^2} \tag{3.3}$$

The working conditions are 25 ^{0}C- 30^{0}C and 1 bar, so the air properties are taken at that point, as shown in Table 3-2

Table 3-2 Air Properties [56]

Parameters	**Values**	**Units**
Density (ρ)	1.225	Kg/m^3
Specific Heat (C_p)	1005	J/(kg.K)
Thermal Conductivity (k)	0.0258	W/(m.K)
Viscosity (μ)	1.789 x 10^{-5}	Kg/m s

Table 3-3: Boundary Condition

Boundary Condition	**Value**	
Velocity inlet	22 m/s	
Outlet	Flow outlet	
Temperature inlet	25 °C -30 °C	
Gas turbine Blade Sections (from the root)	Height level section of the blade from the root	Value of Vibration Excitation
	First level (6mm)	Frequency(9, 16, 23, and 33) Hz
	Second level (21mm)	
	Third level (36mm)	

3.3.4. Uncertainty

The accurate measurement of the experimental work depends on accuracy, quality of instruments, and reading the values through devices. To investigate the reliability of the results and conclusions that drawn from the data. The experiment is repeated five times for each test in the same conditions.

The error in devices and equipment can affect the uncertainty of measurement that produces uncertainty propagation (σ_x). Thus, the error of experimental results for all the experimental rig is ≈ ± 5% calculated by assuming the square of an uncertainty. It was considered a measurement of x that is subject to some error of device, each of uncertainty σ_i, see more details in Appendix [A]

$$\sigma = \sqrt{\frac{\sum_1^n (x_i - \bar{x})^2}{n-1}} \tag{3.4}$$

where i = 1,2, ...,I. [57]

3.4. Simulation Model Based on the Practical Model

The manufactured samples are used to produce models of the blades used in the practical side in order to prepare the shape of the mathematical model used in the simulations in chapter three because the specifications of the shape of the blade are not clearly defined and the companies producing gas turbine stations do not reveal the specifications of the material from which the blade alloy is made and the drawing equations of the blade shape, as it is one of the secrets of manufacturing that international companies do not reveal, and this is well-known by researchers in this field. Therefore, researchers resort to preparing approximate shapes of the shape of the real blade. Some of them worked on drawing the root and top of the blade by printing it on paper and then fed it into computer programs in the form of coordinates and making some changes in terms of rotating the center of the blade shape at the root from its shape at the top until it gives a shape close to reality. Nevertheless, that work is not very accurate because the real shape of the blade is diffuse at the lowest point, as well as the rotation angle of the center of the airfoil. Therefore, this method was developed but with high accuracy, using the practical side of this research.

The two parts of the mold are prepared by lubricating them with molding insulation to avoid the form sticking to it. A new material called silicone rubber is used, consisting of two materials, silicone and a hardener. This material is characterized by being an easy-to-form liquid material that takes the shape of the mold to be molded and hardens after a period of time to produce a shape identical to the model with high accuracy. This material is characterized as having good flexibility and ease of cutting and dividing the sample in the form of sections that are used later in the formation of the studied mathematical model.

The silicone material is mixed with the hardener by 95% of the silicone to 5% of the hardener, and the hardener is gradually added in the form of drops with good mechanical stirring to ensure the mixture is well homogeneous. Mix in all the mold to help out the air bubbles that form during the mixing process. Leaving the mixture to solidify for 12 hours, after which the mold is opened and the sample is extracted and cleaned well with a soft cloth to remove the polish to prevent the sample used from sticking to the mold.

The sample is placed again inside the first part of the mold for the purpose of placing the blade dividing lines into ten sections and the first reference line that is used to match the sections later. Then the sample is placed inside the second part of the mold and the second reference line is drawn, which is used with the second reference line to match the position of the sections in their correct position and accurately match the true shape of the model as shown in the Fig. 3-20 and Fig. 3-19.

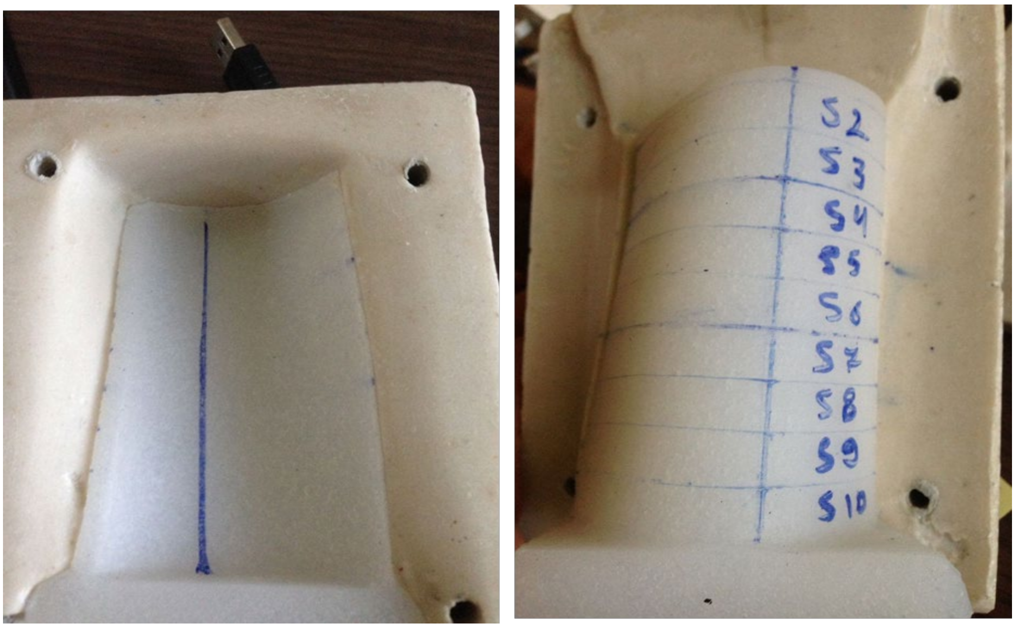

Fig. 3-20: silicone blade pattern

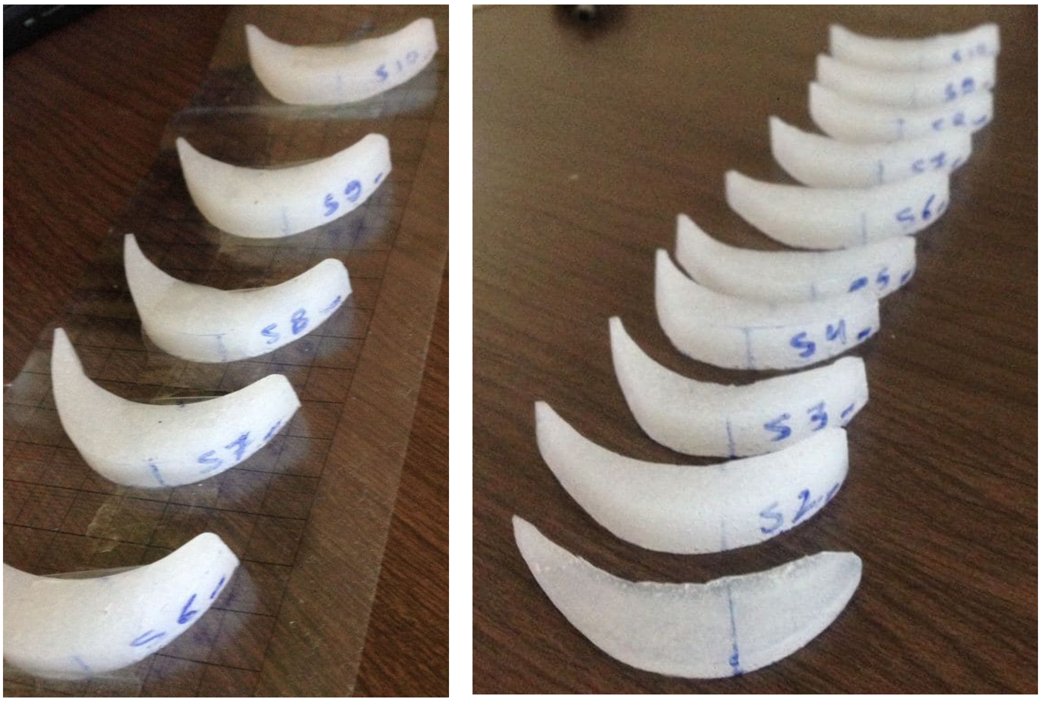

Fig. 3-19: sections of silicone airfoil pattern

The blade model is cut using a sharp tool into ten sections of equal thickness for the first nine sections, which were 1 cm thick, and the tenth section was half a centimeter thick to show us the change of profile of each of the model' s sections as shown in the figure 3-20.

These sections are placed sequentially on transparent graphic paper that contains an adhesive that helps the sections stick to it and not move while working on it. The sections are scanned using a scanner and the actual measurements are processed by taking a scale drawing between the lines of the image graph and the actual scale of the graph paper lines. After obtaining a computer image as shown in Fig. 3-21.

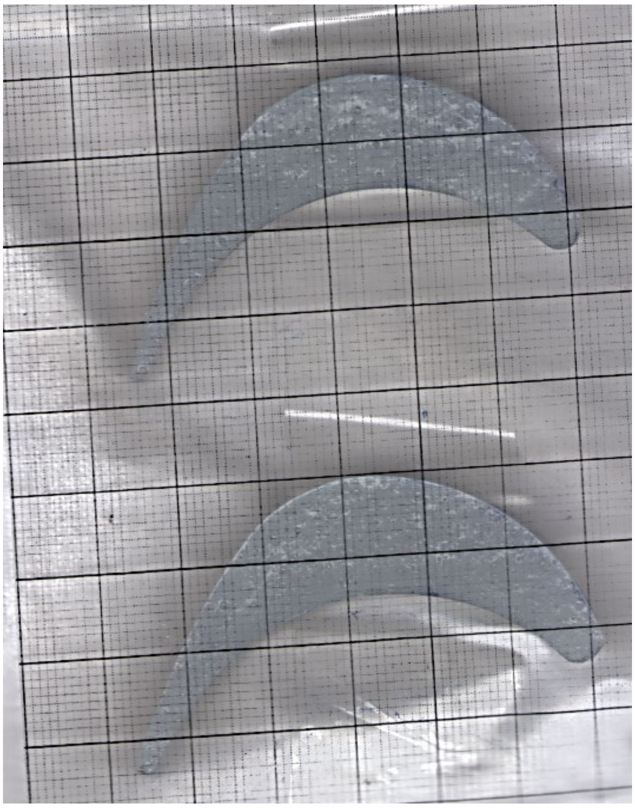

Fig. 3-21: scanned image of airfoil pattern sections

This image is transferred to the AutoCAD software[58] for the purpose of processing the scale of the image and drawing the borders for each section, using Spline instructing as it takes the shape corresponding to the image and has the feature of adjustment (fitting) to give a smooth and accurate curve of curvature as shown in figure 3-22.

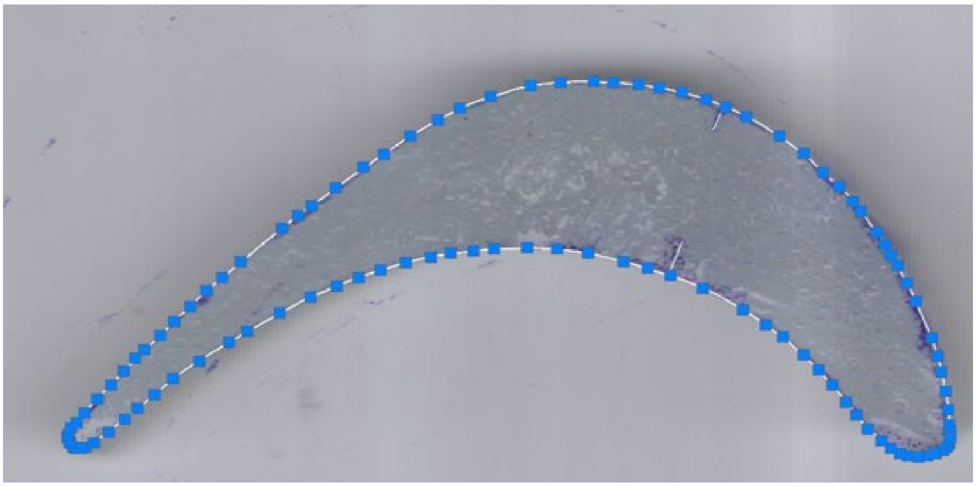

Fig. 3-22: curve of airfoil produced by Autocad

The coordinates that make up the curve are exported through AutoCAD software and converted into x and y values, and thus the process of drawing the shape involved in the simulation process becomes easier because the program deals with these readings. Through the above, the model is built for each of its levels according to the thickness of each section, which will be entered into ten levels in the Solidworks software[59], and an airfoil shape for the blade section is drawn at each level, starting from the root, and also the height represents the thickness of the section right down to the airfoil shape at the top as shown on figure 3-24.

Fig. 3-23: actual blades showing the required curves

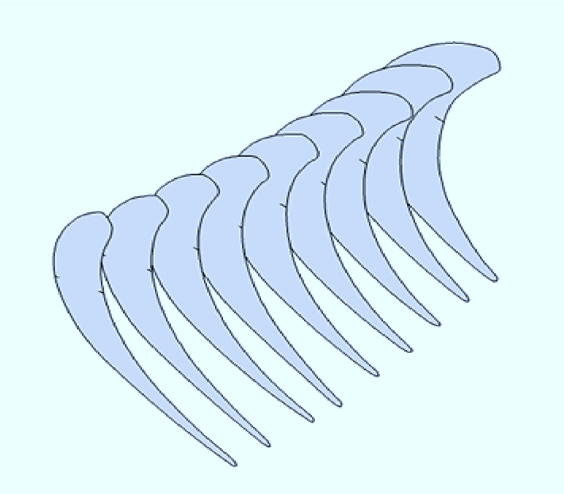

Fig. 3-25: sections modelled by SoldWorks software

A set of perpendicular images are taken on the real model and entered into the computer for the purpose of performing the same previous steps in order to extract the shape of the tangential curves of the sections curves at each level and enter them into the SolidWorks software to draw the final shape of the model as shown in figure 3-25.

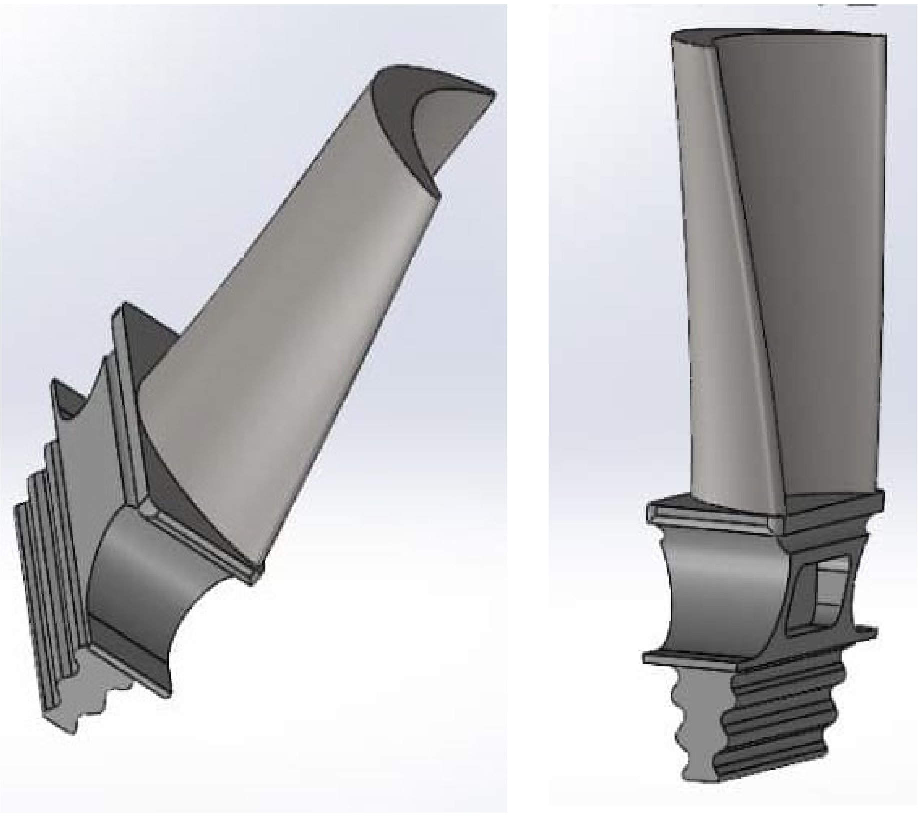

Fig. 3-24: simulated model by SoldWorks software

CHAPTER FOUR

CFD MODELING STUDY

4. Introduction

In the present study, a numerical approach using the finite element method has been carried out by commercial code COMSOL Multiphysics 5.6 to investigate fully developed turbulent flow over the cascade blade of a gas turbine with vibration effect. The main characteristics of the theoretical modeling along with the related governing equations will be presented in detail. In addition, efficient assumptions and boundary conditions will be stated clearly. Finally, a numerical solution for the problem under the boundary and working conditions are going to be presented as well.

4.1. Mathematical modeling

In this section, the governing differential equations of the fluid flow are presented. The three basic equations that govern any physical aspect of a fluid flow are mass conservation, momentum conservation, and energy conservation. All of these equations will be given in terms of partial differential equations. The fluid flow over a flat plate is governed by Reynolds-averaged Navier– Stokes and energy equations [56].

Continuity equation:

$$\rho\nabla.(U) = 0 \tag{4.1}$$

Momentum equation:

$$\rho(U.\nabla)U = \nabla.[-PI + (\mu + \mu_r)(\nabla U + (\nabla U)^T)] \tag{4.2}$$

Energy equation:

$$\rho C_P U.\nabla T = \nabla.[(k + k_T)\nabla T] \tag{4.3}$$

The three-dimensional unsteady-state governing equations are as follows:

Continuity and momentum equations can be given in term of used generalized coordinates as follows:

The momentum equation of x-axis component can be obtained via putting the fluid particle’s momentum change rate equal to the overall forces caused by the surface stresses: *Component of the momentum equation in the x-axis*

$$\frac{\partial u}{\partial t}+u\frac{\partial u}{\partial x}+v\frac{\partial u}{\partial y}+w\frac{\partial u}{\partial z} = -\frac{1}{\rho}\frac{\partial p}{\partial x}+\frac{\mu}{\rho}\frac{\partial u^2}{\partial x^2}+\frac{\mu}{\rho}\frac{\partial u^2}{\partial y^2}+\frac{\mu}{\rho}\frac{\partial u^2}{\partial z^2} \tag{4.4}$$

Component of the momentum equation in the y-axis

$$\frac{\partial v}{\partial t}+u\frac{\partial v}{\partial x}+v\frac{\partial v}{\partial y}+w\frac{\partial v}{\partial z} = -\frac{1}{\rho}\frac{\partial p}{\partial y}+\frac{\mu}{\rho}\frac{\partial v^2}{\partial x^2}+\frac{\mu}{\rho}\frac{\partial v^2}{\partial y^2}+\frac{\mu}{\rho}\frac{\partial v^2}{\partial z^2} \tag{4.5}$$

And Component of the momentum equation in the z-axis

$$\frac{\partial w}{\partial t}+u\frac{\partial w}{\partial x}+v\frac{\partial w}{\partial y}+w\frac{\partial w}{\partial z} = -\frac{1}{\rho}\frac{\partial p}{\partial z}+\frac{\mu}{\rho}\frac{\partial w^2}{\partial x^2}+\frac{\mu}{\rho}\frac{\partial w^2}{\partial y^2}+\frac{\mu}{\rho}\frac{\partial w^2}{\partial z^2} \tag{4.6}$$

4.1.1. Case Study Assumptions

Many assumptions have been made to simplify the problem under considerations. They are:

1. Unsteady state conditions.
2. Incompressible flow.
3. Constant physical properties for all fluid flow.
4. No phase change for all the flowing fluids.
5. Newtonian fluid.
6. Three-dimensional analysis
7. Turbulent flow.

4.2. Selection of a Suitable Turbulent Model

The main target of this research beside geometry modeling, numerical setup, and convergence problem, is to define the flow parameters distribution in a 3D turbine stage with twisted rotor blade. For the purposes of the turbulence modeling, the standard k – ε turbulence model, RNG k – ε is used. The Reynolds stress model (RSM) is applicable for modeling effects of additional vortices, found in flow and shear stress effects over fluid particles [60]. The standard k – ε model showed quite good values, especially for the turbulent kinetic energy, in the core flow [60]–[65]. The RNG model showed the highest prediction of lift and maximal lift angle [66], [67]. The k – ε turbulence models are appropriate for flows characterized by high adverse pressure and aerodynamic properties. This model allowed for a more accurate near wall treatment with an automatic switch from wall function to low-Reynolds number formulation, based on grid spacing [67]–[70].

Finally, Table 4-1 presents some advantages and disadvantages of the four models of turbulent that were used in the present study.

Table 4-1: Advantages and disadvantages of the four models of turbulent, [71]

Model	Strengths	Weaknesses
Standard k-ε	Robust, economical, reasonably accurate; long accumulated performance data.	Mediocre results for complex flows with severe pressure gradients, strong streamline curvature, swirl and rotation.
RNG k-ε	Good for moderately complex behavior like jet impingement, separating flows, swirling flows, and secondary flows.	Subjected to limitation due to isotropic eddy viscosity assumption. Same problem with round jets as standard k-ε.
Realizable k-ε	Offers largely the same benefits as Sk-ε but also resolves the round-jet anomaly.	Subjected to limitations due to isotropic eddy viscosity assumption.
SST k-ε	Physically most complete model (transport, and an isotropy of turbulent stresses are all accounted for).	Requires more (CUP); tightly coupled momentum and turbulence equations.

For the above reasons, RNG $k-\varepsilon$ turbulence model is the appropriate one to formulate our problem. The model, which consists of two equations, specifies a general characterization of turbulence via two transport and partial differential equations. The energy within the turbulence is set via first transport, which is known as turbulent kinetic energy (k). The second transport is termed dissipation of turbulent (ε), which determines the dissipation rate for turbulent kinetic energy (k). From transport equations, the turbulent mechanical energy (k) and its rate of dissipation (ε) are determined from transport equations. These equations are given by [61]:

$$\rho\frac{\partial k}{\partial t}+\rho U.\nabla k=\nabla.\left(\left(\mu+\frac{\mu_T}{\sigma_k}\right)\nabla k\right)+G-\rho\varepsilon \tag{4.7}$$

$$\rho\frac{\partial \varepsilon}{\partial t}+\rho U.\nabla \varepsilon=\nabla.\left(\left(\mu+\frac{\mu_T}{\sigma_\varepsilon}\right)\nabla \varepsilon\right)+C_{\varepsilon 1}\frac{\varepsilon}{k}P_k-C_{\varepsilon 2}\rho\frac{\varepsilon^2}{k} \tag{4.8}$$

The model constants are given as

$$C_\mu=0.09;\ C_{\varepsilon 1}=1.44;\ C_{\varepsilon 2}=1.92; \sigma_k=1.0; \sigma_\varepsilon=1.3 \tag{4.9}$$

For more convenient, the above equations are given in simplified forms as shown:

$$u\frac{\partial(\rho k)}{\partial x}+v\frac{\partial(\rho k)}{\partial y}+w\frac{\partial(\rho k)}{\partial z}$$
$$=\frac{\partial}{\partial x}\left(\frac{\mu_t}{\sigma_k}\frac{\partial k}{\partial x}\right)+\frac{\partial}{\partial y}\left(\frac{\mu_t}{\sigma_k}\frac{\partial k}{\partial y}\right)+\frac{\partial}{\partial z}\left(\frac{\mu_t}{\sigma_k}\frac{\partial k}{\partial z}\right)+G$$
$$-\rho\varepsilon \tag{4.10}$$

$$u\frac{\partial(\rho \varepsilon)}{\partial x}+v\frac{\partial(\rho \varepsilon)}{\partial y}+w\frac{\partial(\rho \varepsilon)}{\partial z}$$
$$=\frac{\partial}{\partial x}\left(\frac{\mu_t}{\sigma_\varepsilon}\frac{\partial \varepsilon}{\partial x}\right)+\frac{\partial}{\partial y}\left(\frac{\mu_t}{\sigma_\varepsilon}\frac{\partial \varepsilon}{\partial y}\right)+\frac{\partial}{\partial z}\left(\frac{\mu_t}{\sigma_\varepsilon}\frac{\partial \varepsilon}{\partial z}\right)+C_{\varepsilon 1}\frac{\varepsilon}{k}G$$
$$-C_{\varepsilon 2}\rho\frac{\varepsilon^2}{k} \tag{4.11}$$

In these equations (G) is the generation term, (μ_t) is the turbulent (or eddy) viscosity, (σ_k andσ_ε) are the turbulent Prantl numbers for (k) and (ε) respectively and

($C_{\varepsilon 1}$ and$C_{\varepsilon 2}$) are constants. The turbulent viscosity (μ_t) is computed by combining (k) and (ε) as follows [61]:

$$\mu_t = \rho C_\mu \frac{k^2}{\varepsilon} \tag{4.12}$$

4.3. Numerical CFD Formulation

CFD simulation is the most important part of industrial projects. Almost all industrial cases that exist in our world have, somehow, a connection with fluid dynamics. For the analysis of moving objects (or flow around objects) in CFD codes, some hypothetical models exist for turbulent simulation. The geometry of the cascade blades, mesh generation, boundary conditions along with assumptions, and analysis options are presented in this section.

4.3.1. Geometrical considerations

The turbine blade is firstly designed and modeled with SOLIDWORKS software. Clear explanations about the whole process of model generation are presented in the previous chapter (Sec. 3.4) and the flow analysis is carried out using CFD under unsteady state condition.

The reference blade under consideration, can be graphically represented by Fig. 4-1 in which the blade configurations with leading and trailing edge are showed. The blade length and chord are 96mm and 58mm, respectively. It is worthy to mention that the manufactured blade in this work is designed close to the real dimensions of blades from gas turbine station found in Hilla gas-turbine station.

4.4. Selection of the Computational Domain

One of the most important steps need to be done before the numerical analysis, is the preparing the blade geometry and blade domain to attain more accurate results. The three-dimensional domain involves one blade inside the passage flow path, with cyclic boundary conditions utilized to simulate the blade model. The domain extended 96mm from the hub to the tip of the blade, it is along of the length of blade. The computational domain of model-1 (General Electric (GE) blade) is presented in Fig. 4-1, and same computational domain is used for the suggested model. A section of single blade was taken and represented by the COSMOL milieu to simulate the actual flow domain of all blades as possible, for the first stage of gas turbine. The simulated section repeats around the rotor shaft by 360°.

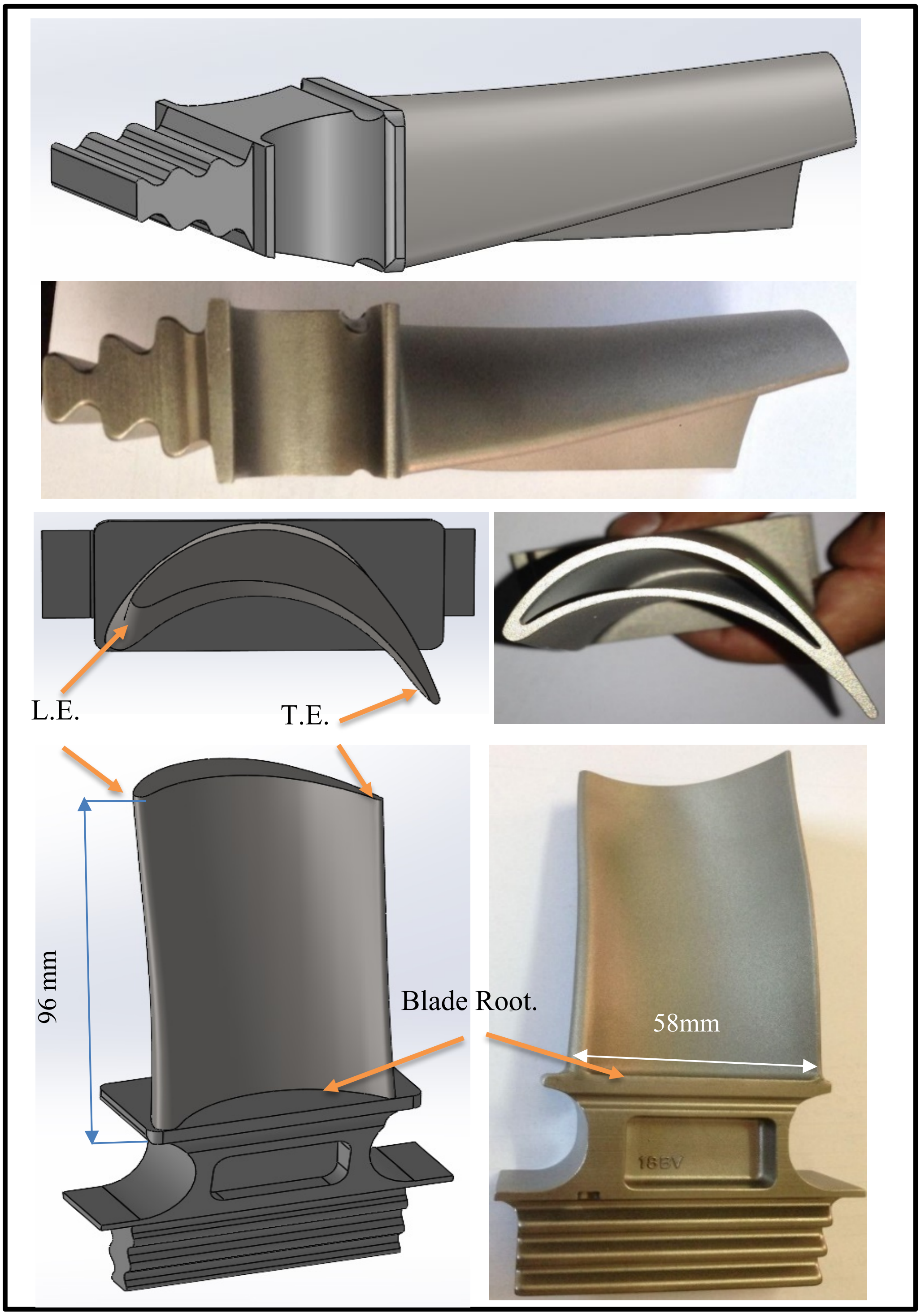

Fig. 4-1: simulated and real blades

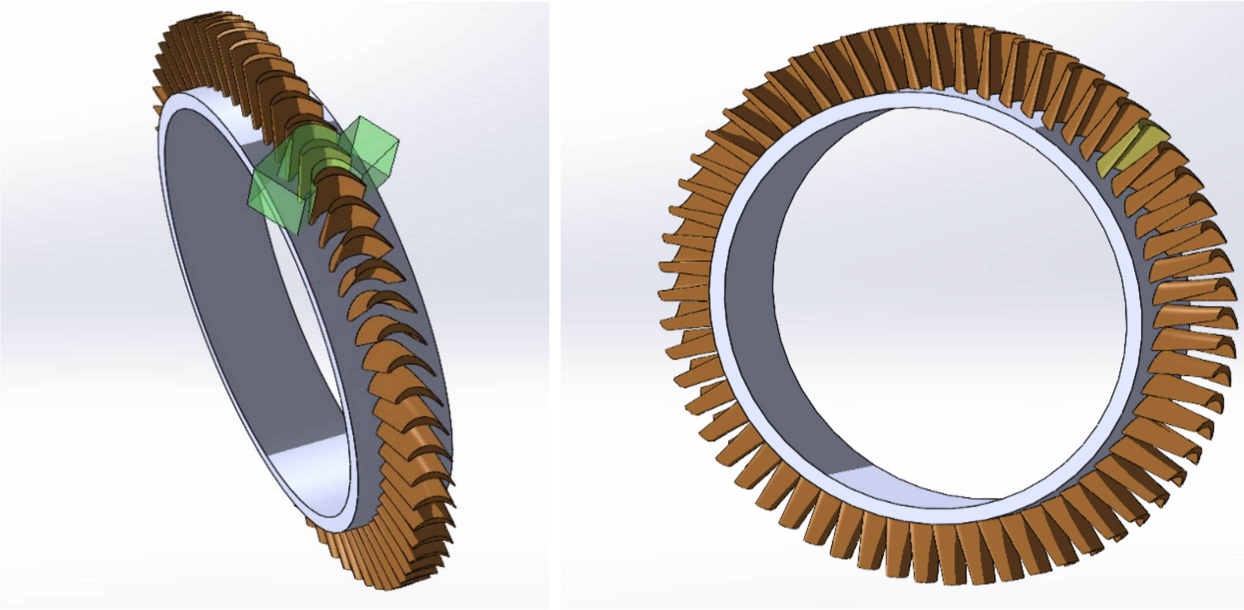

Figure 4-2: turbine cascade blade

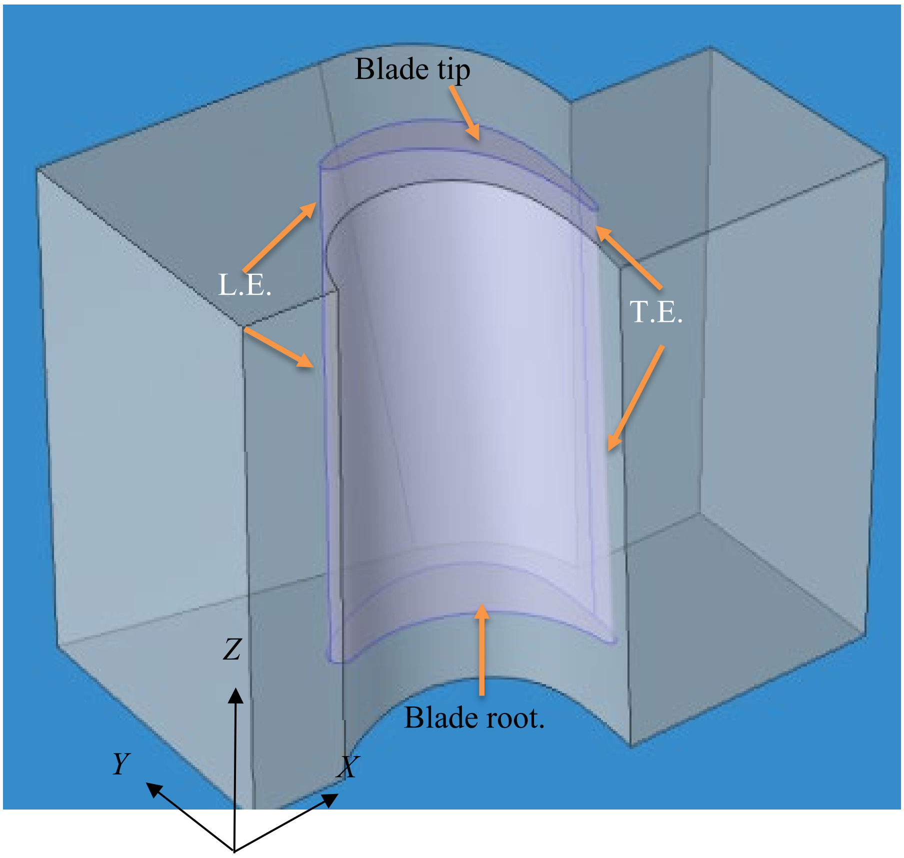

Fig. 4-2: Shows the section of blade domain

4.5. Mesh Generation

The model geometry is generated by using COMSOL 5.6 design modeler. Unstructured tetrahedral mesh used in the current work which leads to minimize the time spent for generating meshes and better accuracy. The model is more complicated to be treated with classical unstructured mesh, and to allow mesh to be more convenient to analyze the flow - scope features. In the present model, the conforming mesh with tetrahedral type has been used to generate mesh for the flow domain and solid blade.

Numerical error and accuracy of the results are sensitive to the elements number. The overall elements number are (1288503) and nodes (59271138) with the other mesh data (face size, body size, conforming method 'tetrahedrons' and layer Y+) is explain by Table 4-2 to ensure that the mesh count does not go high while maintaining the accuracy and features of the model. The flow domain has been inflated to pick up the boundary layers effective. Five layers with (Y+) have been prepared for boundary layer zone with a first aspect ratio of 5 and growth rate of 20%. The volume size of tetrahedral is about 5mm^3 as shown in Fig. 4-3.

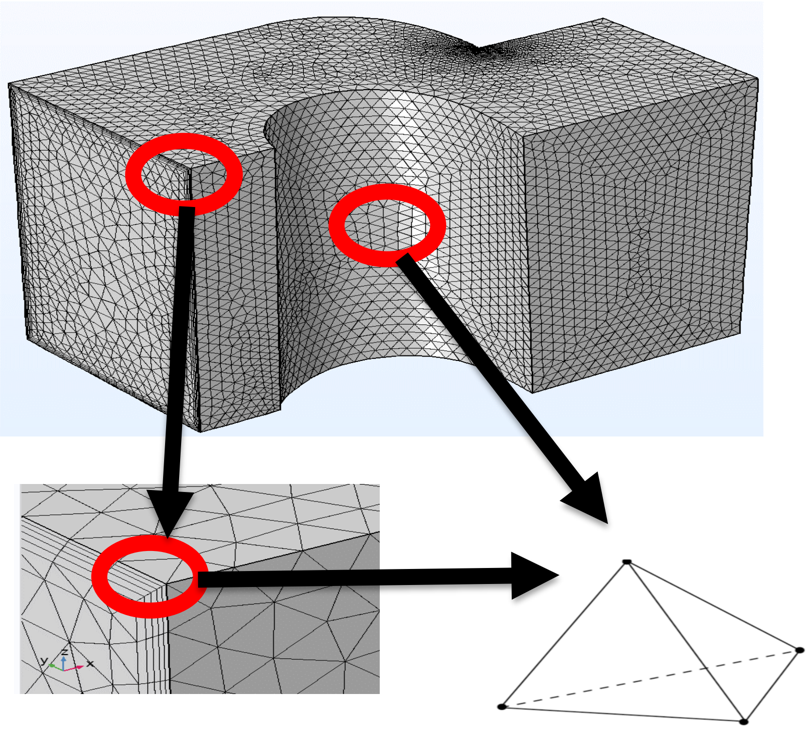

Fig. 4-3: The tetrahedral mesh type of extremely fine

Table 4-2: Mesh data of models

Object Name	**Mesh**
Physics Preference	CFD
Element Order	Program Controlled
Sizing	
Size Function	Curvature
Mesh size	Fine
Min Size	0.10 mm
Max Face Size	1.0 mm
Max Tet Size (volume)	5.0 mm^3
Growth Rate	Default (1.20)
Quality	
Check Mesh Quality	Yes, Errors
Smoothing	High
First Aspect Ratio	5
Maximum Layers	5
Growth Rate	1.2
View Advanced Options	No
Advanced	
Number of CPUs for Parallel Part Meshing	Program Controlled
Pinch Tolerance	Default (0.180 mm)
Statistics	
Number of vertex elements:	20
Number of edge elements:	1372
Number of boundary elements:	47528
Number of elements:	1288503
Minimum element quality:	0.1838
Number of nodes	5927113

4.5.1. Grid Independence Test

To obtain a grid independent solution a grid refinement test was performed. The Table 4-3 and describe the result as satisfactory for the grid refinements. In this problem 1288503 elements are used for the whole domain. Using more elements are time consuming and do not improve the result significantly.

Table 4-3: Grid Independence Test at inlet velocity of 120 m/s.

Number of Elements	433065	1069612	1187551	1288503	1683513	2091204
Time (hrs.)	0.19	0.31	0.47	01.28	03.13	04.32
Average Velocity downstream blade m/s	125.587	126.249	126.756	127.80	127.905	127.915
Average Velocity upstream blade m/s	290.587	292.466	293.641	296.06	296.303	296.3558

U at (x, y, z) = (0.045992, 0.0502, 0.0945) and (0.092447, 0.00678, 0.0945) before and after blade respectively.

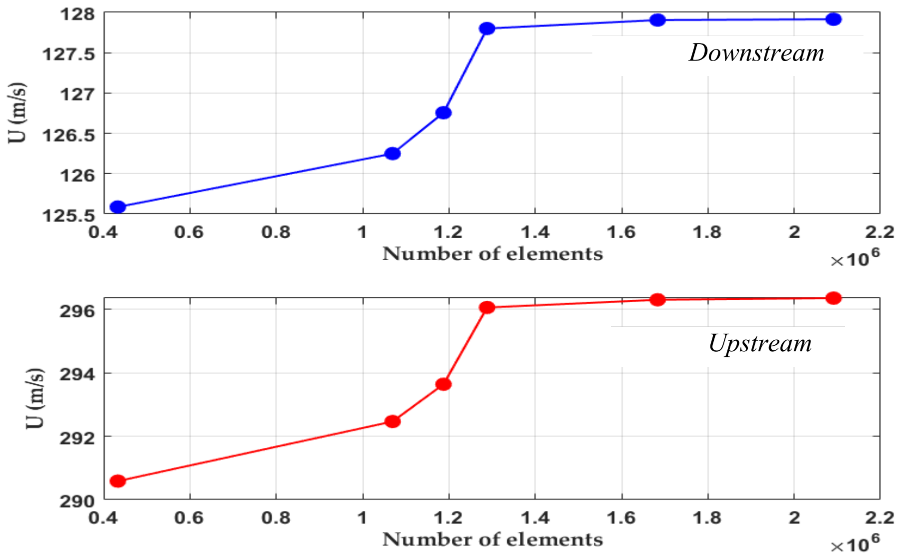

Fig. 4-4: grid independence for velocity upstream and downstream the blade.

4.5.2. The Boundary Conditions and Air Properties

The boundary conditions of the current work.are shown in Table 4-4:

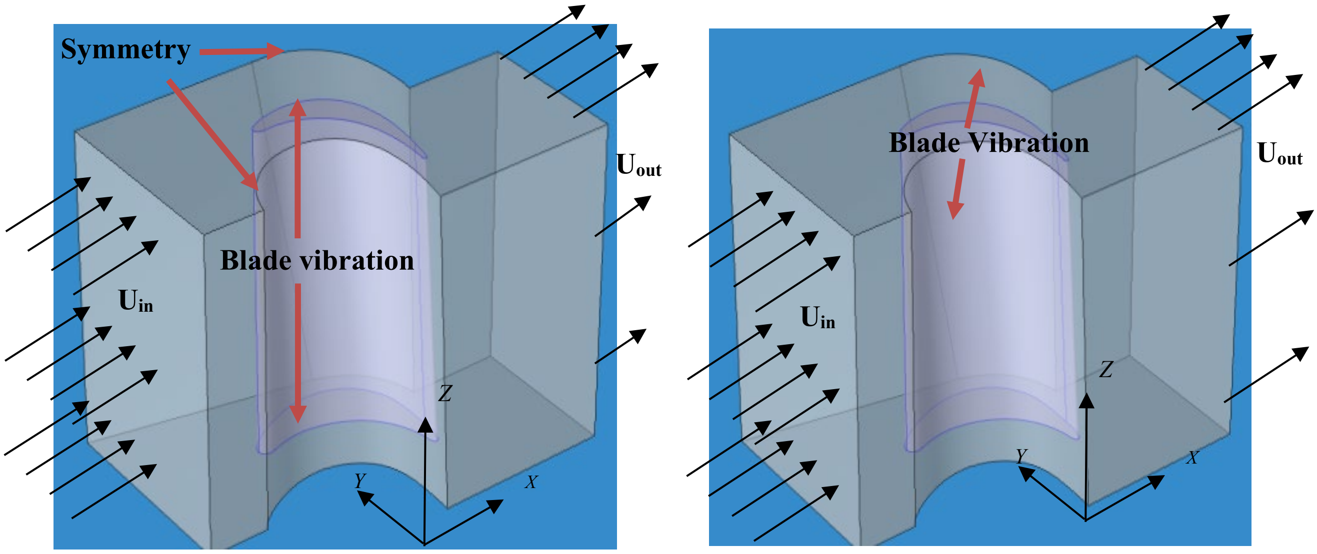

Case 1 excitation of Vibration perpendicular direction to the root

Case 2 excitation of Vibration parallel direction to the root

Fig. 4-5: Shows the boundary conditions for two case study for excitation of Vibration.

Table 4-4: Boundary Conditions

Boundary condition	value
working fluid	Air
Velocity inlet	22 and 120 (m/s)
Outlet	Flow outlet
Turbulent intensity	5%
Share condition	No slip
Temperature	300 k
Blade vertical motion	Harmonic (sinusoidal)
Mesh status	Moving mesh for fluid domain

Simple harmonic motion is expressed as sine-wave vibrational movement on blade. The sinusoidal vibrational velocity profile is represented as [54], [64]:

$$V = 2\pi f a \sin(2\pi f t) \tag{4.13}$$

4.6. Non-dimensional Numbers

4.6.1. Reynolds Number

The Reynolds number is the ratio between the inertia force to the viscous force of the boundary layer of velocity[45], [65]:

$$Rev = \frac{2\pi f a_v c}{\mu} \tag{4.14}$$

Where air flow density is ρ calculated from air properties table 4-1 at 25^0C, the U has been velocity of annulus air flow with different frequency effect , **C** is chord length for the blade and μ is dynamic viscosity of fluid flow also calculated from air properties table [72].

4.6.2. Pressure coefficient C_p

The pressure coefficient is a dimensionless quantity that describes the relative pressure during the fluid flow [55]:

$$C_p = \frac{P - P_\infty}{\frac{1}{2}\rho_\infty U^2} \tag{4.15}$$

4.6.3. Turbulence Intensity

The turbulence intensity, *I*, defined as the ratio of the root-mean-square of the velocity fluctuations, to the mean flow velocity [71].

$$I = \frac{\acute{u}}{u_{avg}} = \frac{\left(\frac{2k}{3}\right)^{\frac{1}{2}}}{u_{avg}} \tag{4.16}$$

Where (k) is the turbulent kinetic energy, and u_{avg} is the mean flow velocity.

4.6.4. Error Calculation for the Validation

The simulation results were compared with the experimental results by calculating absolute overall error with the use of the following equation[54]

$$E = \sum_{i=1}^{n} \frac{\left|U^{i}{}_{CFD} - U^{i}{}_{EXP}\right|}{U^{i}{}_{EXP}} * 100 \qquad (4.17)$$

Where U is air velocity with different frequency. $|U^{i}{}_{CFD} - U^{i}{}_{exp}|$ isthe difference absolute between actual and simulated values**.**

4.7. Code Validation

The reliability of the 3D models needs to be confirmed with results of other research works. The verification of current study proved the physics modeling which carried out by [47] and his model as shown in figure 4-7. The comparison was made on a contour basis between the maximum and minimum velocity profiles for nine cases of air velocities and frequencies. In general, the percentage of code validation is 96%, which shows a highly agreement between the current simulation results and Hsieh, Low and [47]. All models are performed at same data setup of numerical analysis (methodology, scheme and running). The results of the validation are illustrated by figure. 4.8 and 4.9. The vibration frequency was 33.3 Hz.

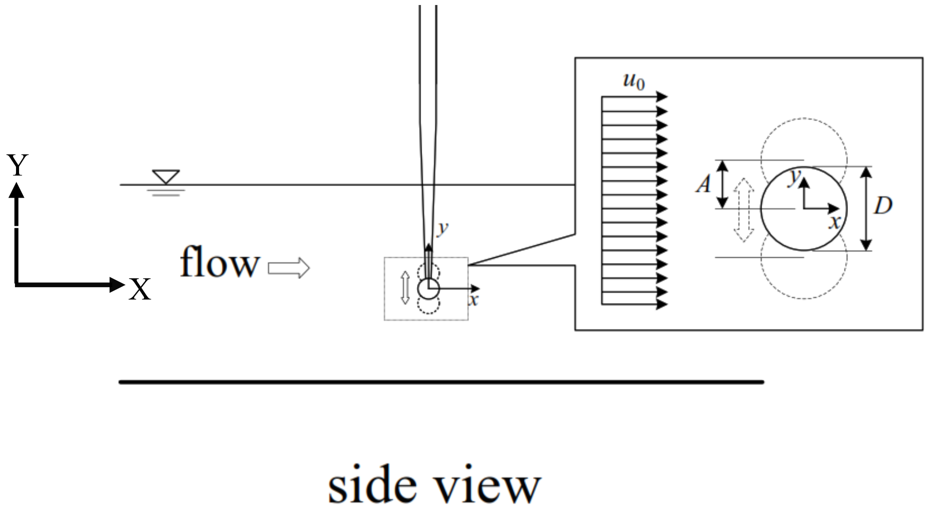

Fig. 4-7: Experimental setup for ref. [47]

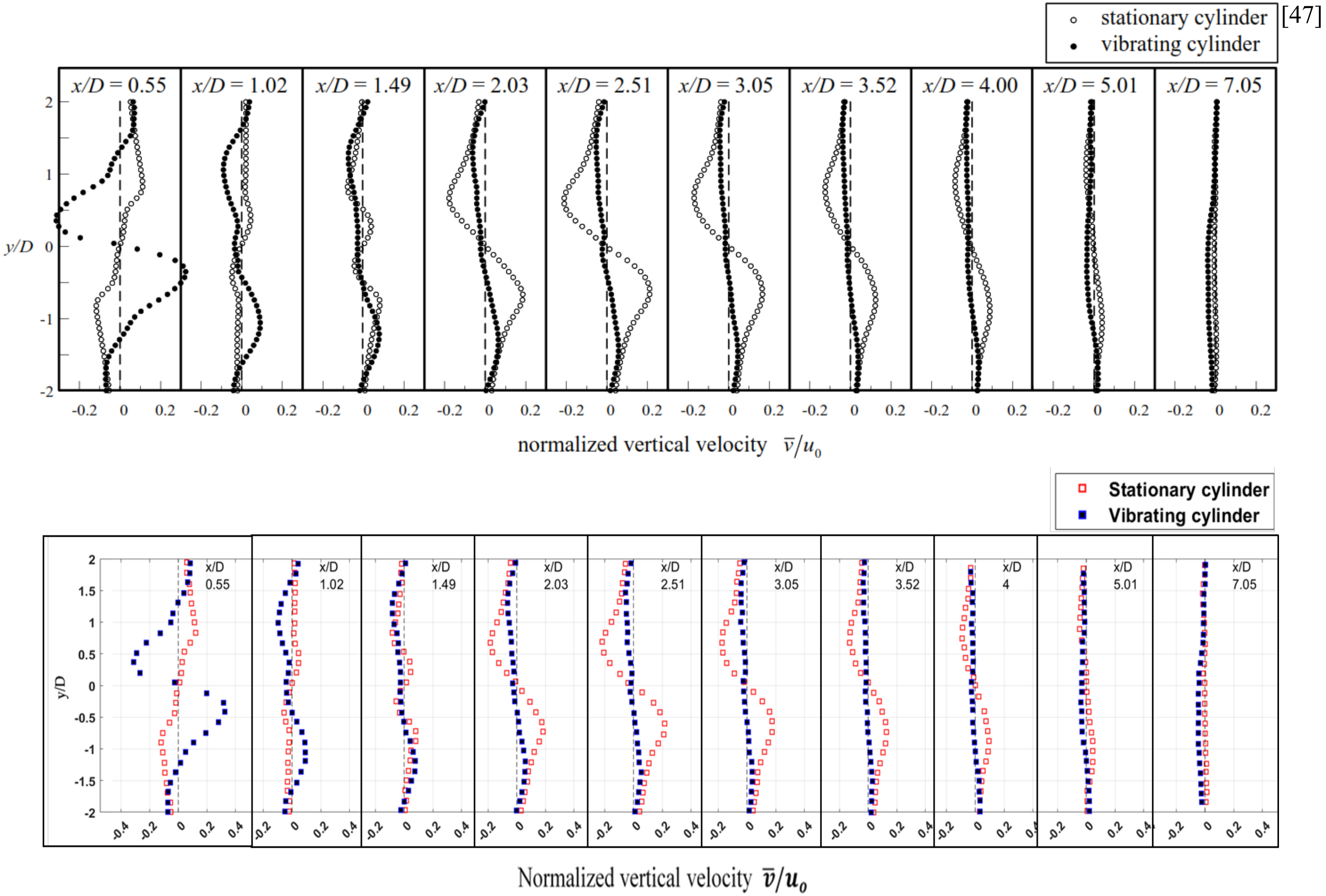

Fig. 4-8: work validation for normalized horizontal velocity

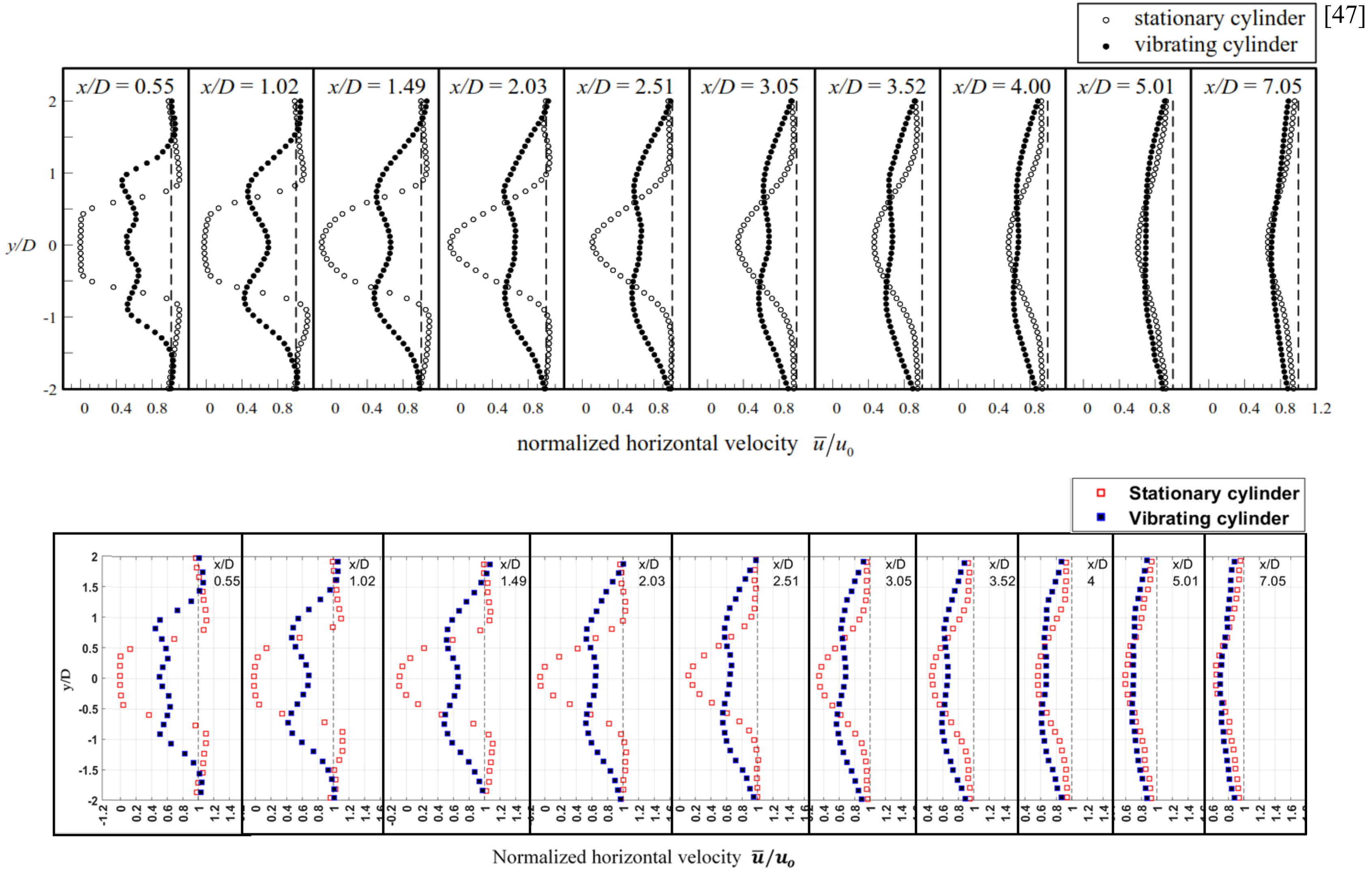

Fig. 4-9: work validation for normalized vertical velocity

CHAPTER FIVE

RESULTS AND DISCUSSION

5. Introduction

The numerical and the experimental results of this work are going to be presented in this chapter. The complexity of the experimental work limits the concluded results. The numerical simulation was not an easy step for modeling effect of vibration of flow aerodynamic characteristics of blade. However, post processing of the available results provided by COMSOL achieve wide range of numerical results. To ensure accuracy of the numerical results, code validation is presented in the last section.

5.1. Results Visualization by COMSOL Multiphysics

5.1.1. Velocity Profile around the Blade

Fig. 5-1 and Fig. 5-2 are used to show the ability of the COMSOL Multiphysics in presenting the results clearly, but they will be discussed in the next paragraphs. Fig. 5-1 shows the distribution of fluid velocity inside the mathematical model that was studied in this work. The figure presents three sections representing three different levels of height from the root (hub side) of the blade. It was noticed that each form of the body contour is different at each level, because each level has a special shape, as the blade shape changes at each level of the blade from its base. The goal of this change is to obtain the highest extracted energy from the fluid passing over the blade surface and a change in the velocity amount above and below the airfoil section of the blade results in a pressures difference that leads to the lift the blade or its rotation around rotating shaft, where the turbine blade works on the principle of airplane wing. Fig. 5-1 gives the progression of the aerodynamic flow around the blade for successive times and it is semi-stable with time. Fig. 5-1 (a)-(c) shows this for the flow without the effect of vibration on the blade.

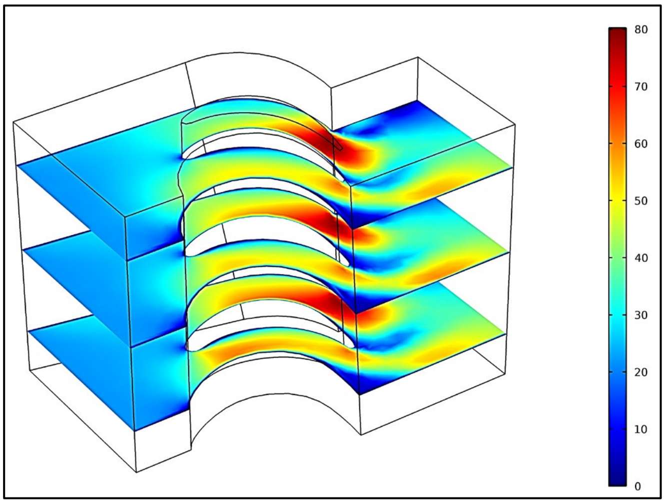

(a)

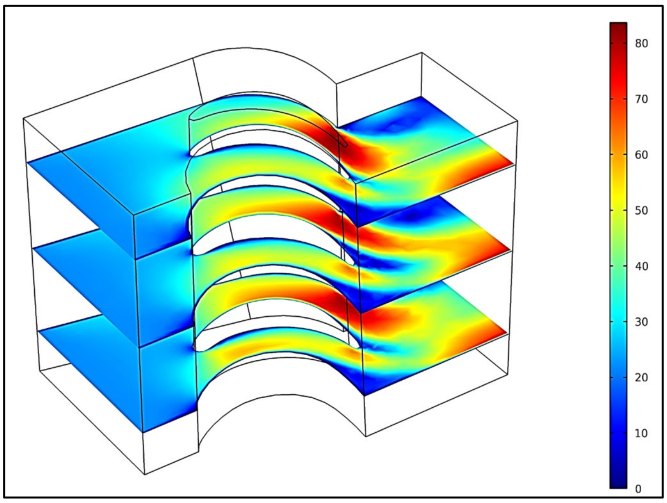

(b)

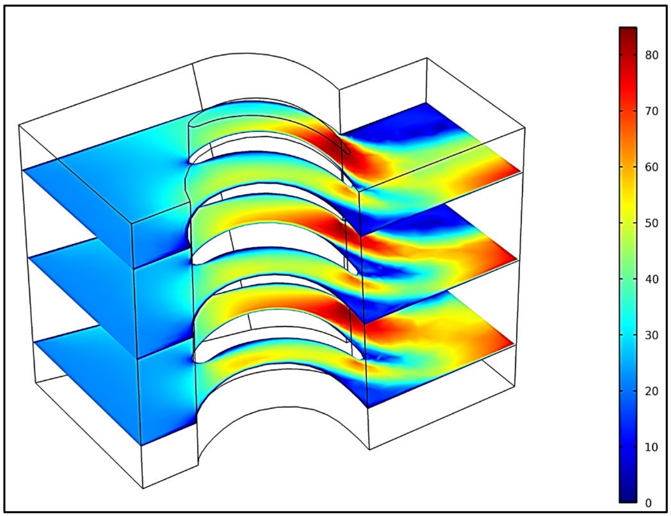

(c)

Fig. 5-1: body contour of velocity distribution in horizontal sections

Fig. 5-2 shows the velocity distribution of the fluid as two-dimensional slices or segments perpendicular to the blade base, through which the fluid velocity in the passage between two successive blades can be noticed. COMSOL Multiphysics enables to draw several vertical or horizontal levels on the root of the blade. This is for the purpose of finding the required results at any point in the mathematical model and giving a clear picture about the behavior of the flow around the blade.

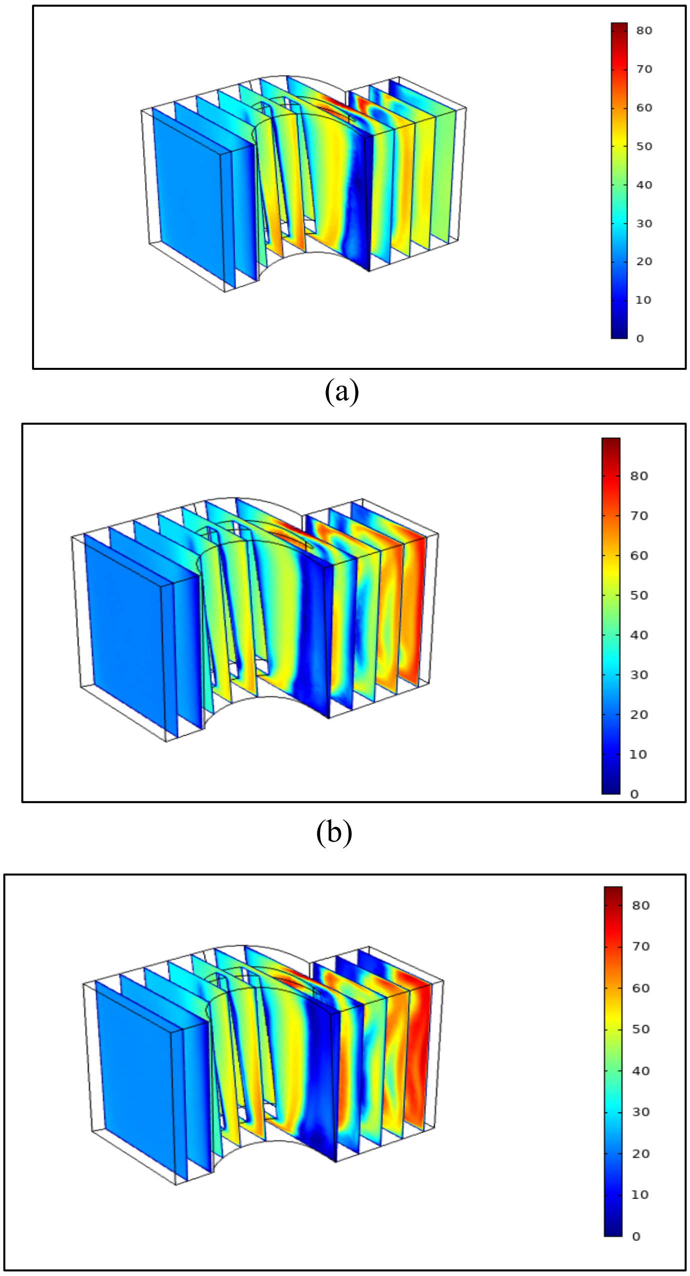

(a)

(b)

(c)

Fig. 5-2: body contour of velocity distribution (m/sec) in vertical sections

5.1.2.Pressure Profile around and on the Blade

Fig. 5-3 shows the distribution of fluid pressure around the blade for different horizontal levels, where the fluid enters at high pressure and velocity, so that it has high kinetic energy. Most of which is extracted and converted into a rotational movement of the cascade blades to move the turbine rotary around the turbine center. By this figure, it is possible to note that the pressures is developed applied by the fluid on the blade surface in order to make a difference in the pressures in pressure side (P.S.) and suction side (S.S.) behind the blade as clarified in Fig. 5-4 for full blade. The pressures is high in Fig. 5-4-(a) in front (P.S.) of the blade and low on the back surface (S.S.) of the blade as shown in Fig. 5-4-(b).

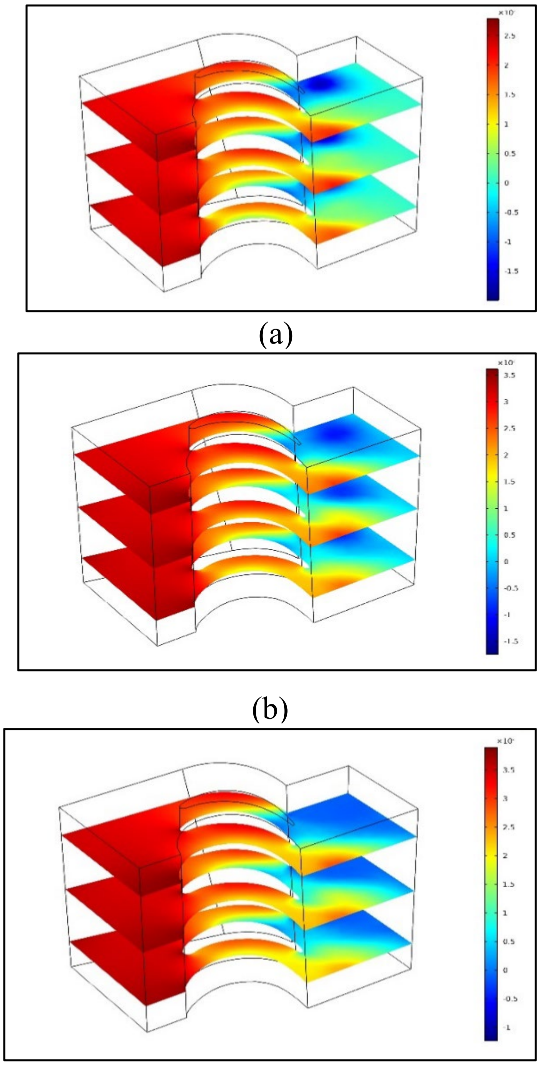

(a)

(b)

(c)

Fig. 5-3: body contour of pressure (bar) distribution in horizontal sections

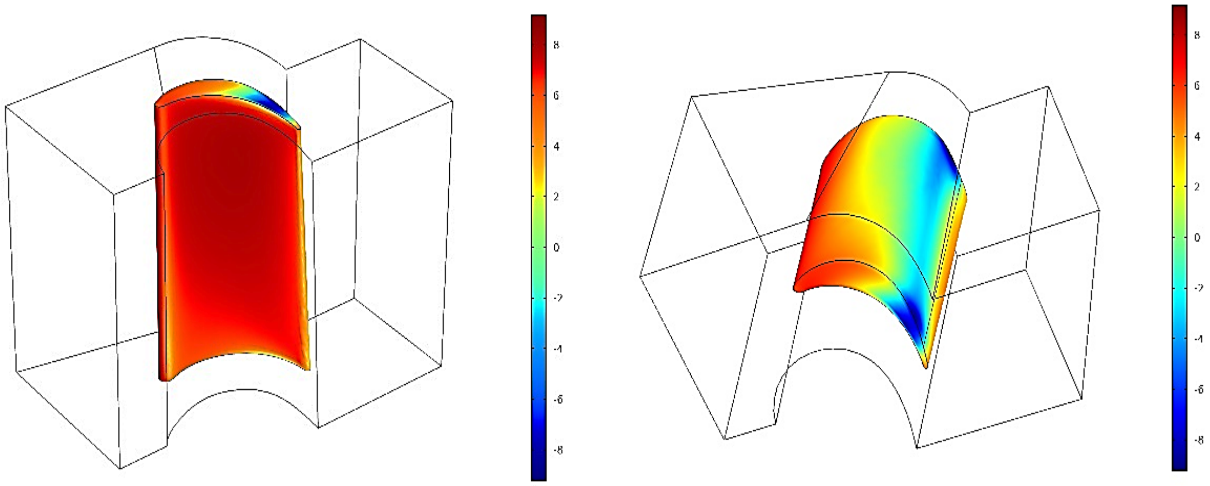

(a)

(b)

Fig. 5-4: body contour of pressure distribution (bar) on blade surface.

5.2. Validation of Experimental Data

Studying the pressures distribution exerted on the gas turbine blade is important because it gives a clear explanation of the aerodynamic flow behavior and the resulting kinetic energy. Therefore, the results focused on presenting the pressure distribution by the pressure coefficient formula, as well as the results of the flow velocity of the fluid around the blade for the gas turbine by fluid velocity at any point to reference velocity. Fig. 5-5 to Fig. 5-7 represent the pressure coefficient and velocity profile in six positions at the upper blade (suction side) and lower blade (pressure side), with and without vibration. The zero-vibration state comparison of a part of a real blade simulation was made to form the behavior of the fluid around the blade and show the flow behavior in experimental results.

The principle of generating movement in the blade of gas turbine depends on the differences in pressures generated as a result of the fluid flow around the blade, as the shape of the blade works to accelerate the flow in the suction region and decrease the pressure in this region so that the value of the pressure near the body is less than the around pressure of the body. This leads blade movement upward. On one hand, the shape in the pressure side region causes a slowdown in the velocity of the fluid and leads to an increase in the amount of pressure at this region, so the resultant force on the blade is in the direction of the upward movement. The shape of the sectioning blade plays a fundamental role in the generation the driving force. It is evident in Fig. 5-5 to Fig. 5-7, a clear increase in the pressure coefficient is observed in the pressure side, which starts from the region of air collision with the body and increases as the fluid advances to the midpoint chord to reach the highest value of the pressure scheme and then begins to decrease at the tail region in the blade. As for the pressure coefficient in the suction side region, it starts from its highest value in the leading edge of the blade and begins to decrease to the middle of the chord, where it begins to rise, and then decreases again and increases at the end of the blade. The main reason for pressure increasing in the middle region is the disturbance in the flow and the separation of the fluid in the passage flow.

It is noticed from the velocity figures, that the fluid velocity increases in the suction side region of the flow before reaching the blade to its highest value at the middle of the chord, due to the shape of the blade where the pressure is low. This achieve the purpose of generating the kinetic force from the fluid to the blade. As for the pressure side, it is noticed a significant decrease in the amount of velocity to achieve a higher value of the pressure applied to the blade, to participate with the pressure drop in the suction side region to generate the blade movement.

It is possible to classify the effect of each factor in the current work through these figures as follows:

a. Effect of vibration of blade on the pressure coefficient.

b. Effect of vibration of blade on the velocity profile.

c. The effect of the blade section shape at different position on the distribution of pressure coefficient and velocity profile.

5.2.1. Vibration Effect on the Pressure Coefficient

Fig. 5-5 to Fig. 5-7 show pressure coefficient at the pressure side and suction side for each of the three-blade levels adopted in the experimental work first level (6mm from root of blade), second level (21mm from root of blade), and third level (36mm from root of blade). The subfigures (a) show the value of the pressure coefficient at the frequencies applied on the blade (0, 9, and 16 Hz). The subfigure b shows the results at frequencies of (0, 23, and 33 Hz) to show the effect of vibration on pressure distribution. In the middle of the chord, Fig. 5-5 shows that numerical results are (-0.85, 1.37) for the suction and pressure sides of the blade, respectively, at level 6mm from the base. The experimental results are (-0.91, 1.43) reveals an increase of 5% approximately.

Secondly, Fig. 5-6 shows that numerical results are (-0.63, 1.22) for the suction and pressure sides of the blade, respectively, at level 21mm from the base, However, the experimental results are (-0.60, 1.14) that reveals a decrease of 6% approximately. Finally, Fig. 5-7 shows that numerical results are (-0.60, 0.39) for the suction and pressure sides of the blade, respectively, at level 36mm from the base.

The experimental results are (-0.41, 0.41) reveals an increase of 6% approximately. It is noticed through the figures that the general flow behavior is similar, but with small changes in the value of the pressure coefficient at each of the three-blade sections (three levels), where the effect of vibration increases the amount of pressure coefficient in the pressure side before the middle chord region and almost is very close value with zero frequency curve in the middle chord and then starts to increase after this region. As for the suction side region, the matter is exactly the opposite, where the effect of vibration is slightly increased by the amount of pressure coefficient at the ends of the blade and that value increases clearly at the middle chord of the blade. Because wall vortices induced by passage vortex begin to form from the L.E. and increase in strength after the middle of the blade and reach the T.E., therefore, the effect of vibration is cascading with its appearance.

5.2.2. Vibration Effect on the Velocity Profile

The subfigures c and d from Fig. 5-5 to Fig. 5-7, show the value of the velocity profile at the pressure side and suction side for each of the three-blade levels adopted in the experimental research, where figure c shows the value of the pressure coefficient when the value of frequencies applied on the blade is (0, 9, and 16 Hz) while the sub figure d shows the results when the frequencies are (0, 23, and 33 Hz) to show the effect of vibration on pressure distribution. The behavior of the general flow velocity at nearly all levels is identical with little differences in velocity due to the magnitude of the exerted vibration. The vibration reduces the velocity in the suction side region and increases the pressure side region.

5.2.3. Effect of the Section Shape of the Blade on the Pressure and Velocity

Fig. 5-5 to Fig. 5-7 give a clear picture of the effect of the section shape of the blade on the pressure coefficient and velocity profile at each test case. The pressure coefficient increased in the case of vibration at the first level (at 6 mm from the root of the blade) and decreases in the suction side region. While the fluid velocity increased in the pressure side region and decreased in the suction side when there is no vibration. The reason for this is that the vibration of the root of the blade leads to deflect the path of fluid particles towards the top of the flow passage and this, in turn, increases the turbulence of the flow, which in turn leads to the generation of vortices that directly affect the amount of pressure and velocity at the level. As for the second level, an increase in the rate of the pressure difference at the pressure side and the suction side is noticed, as well as the more regular form of the first level for two reasons; the first is the change in the shape of the blade segment to a more uniform shape and the second is that it moves away from the root of the blade.

While the third level is more regular, as is evident from Fig. 5-5, for both pressure and velocity diagrams, and the area representing the pressure difference is greater than its predecessors, and this gives the perception that the possibility of obtaining all the changes wider range of the blade. This is the desired purpose of changing the shape of the blade at each level to obtain the largest possible amount of kinetic energy from the fluid to the blade. From the fluid to the feather is more due to the continuation of pressure differences over a as for the velocity chart, it is less on the suction side in the case of vibration. At the pressure side region, it decreases with the increase in vibration, but the velocity profile chart is more regular than the previous levels due to its moving away from the effect of the blade base.

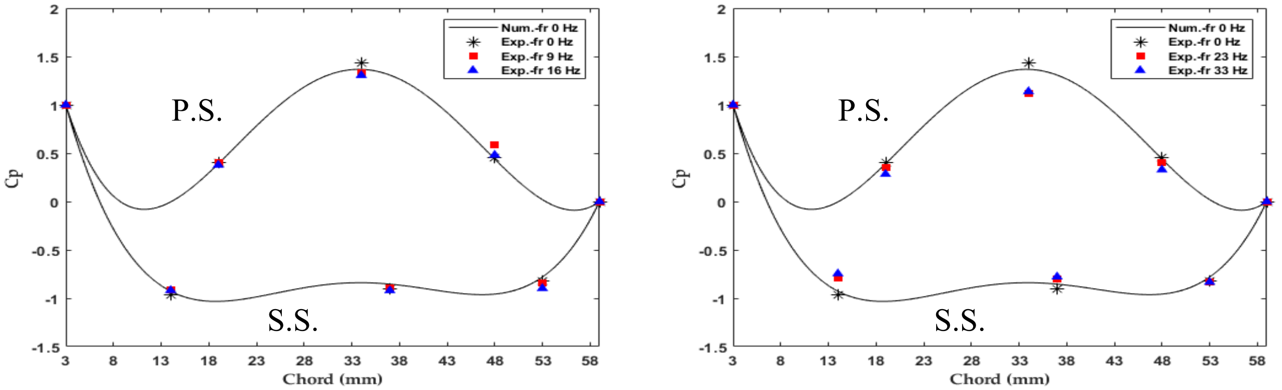

(a). Pressure coefficient distribution with frequency (0, 9, 16) Hz.

(b). Pressure coefficient distribution with frequency (0, 23, 33) Hz.

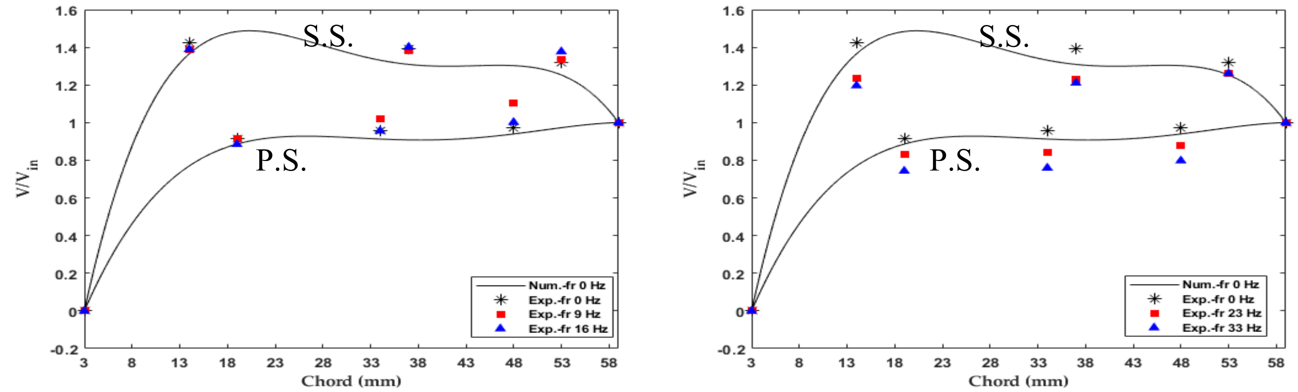

(c). Velocity distribution with frequency (0, 9, 16) Hz.

(d). Velocity distribution with frequency (0, 23, 33) Hz.

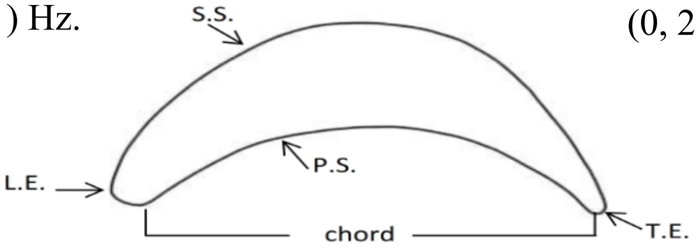

(e) Shape the section blade at level 6mm from the base.

Fig. 5-5: Show pressure coefficient and velocity distribution for first level.

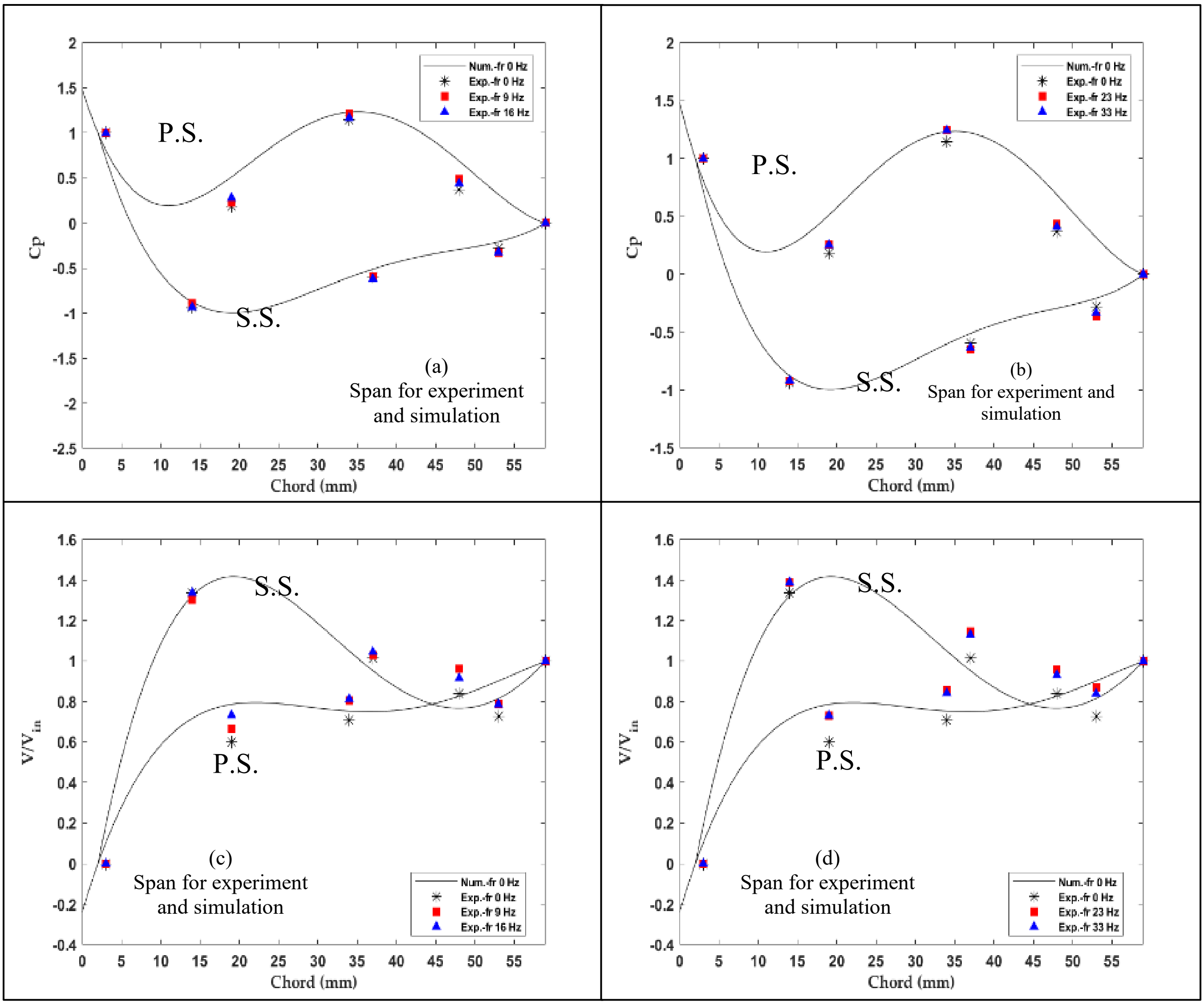

Fig. 5-6: Show pressure coefficient and velocity distribution for second level.

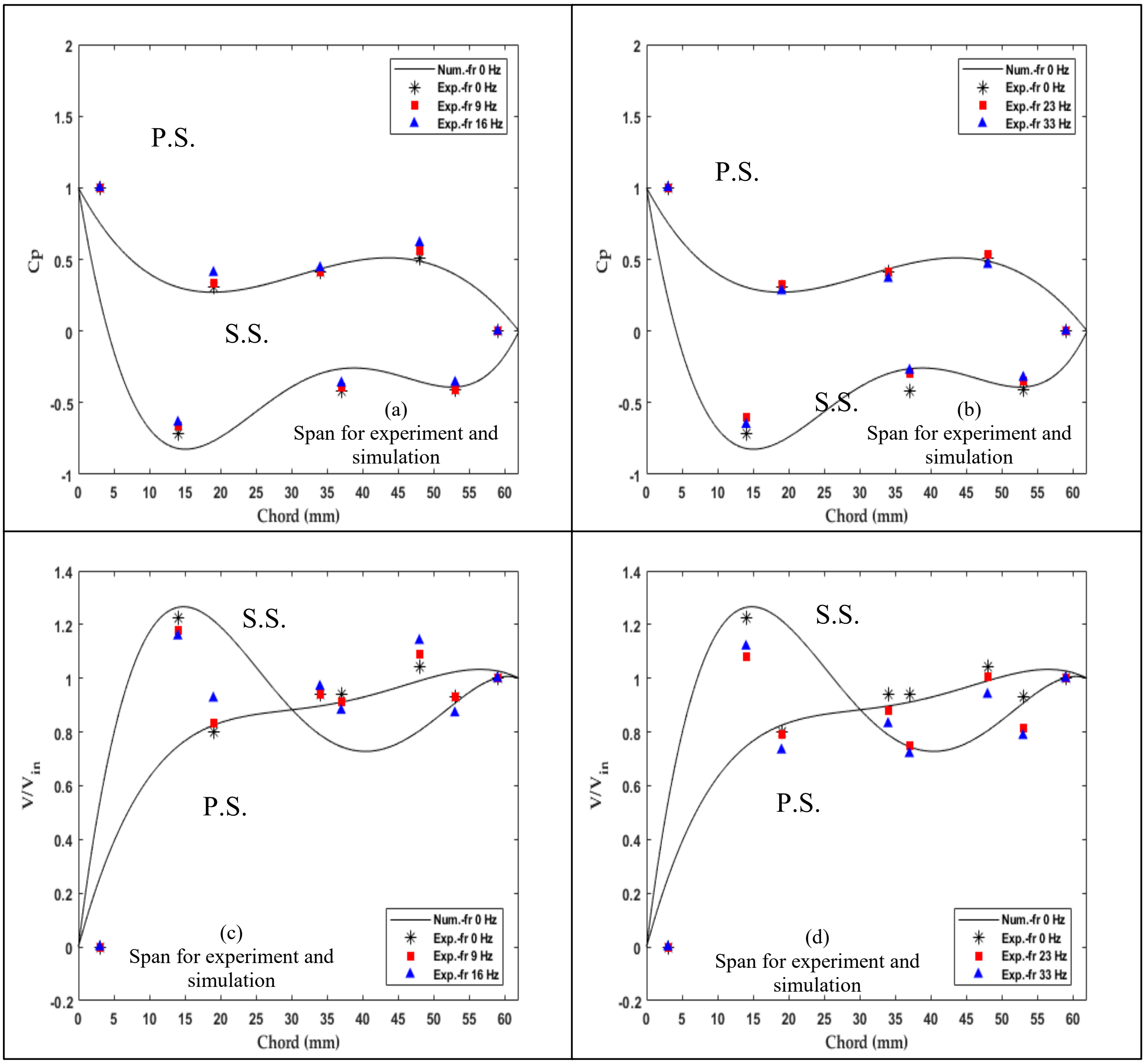

Fig. 5-7: Show pressure coefficient and velocity distribution for third level.

5.3. CFD Results for the Experimental Work

In this part, the results of the simulation of the mathematical model will be reviewed, which simulates the conditions that were applied on the practical side in terms of the velocity of the inlet fluid and the vibration applied to the blade. The velocity of the inlet fluid was 22 m/sec and the vibration on the blade with (0, 9, 16, 23, and 33) HZ.

5.3.1. Velocity Distribution around the Blade

The experimental work was simulated to investigate extra result data to use for comparison. Fig. 5-8 to Fig. 5-12 show the distribution of fluid velocity around the blade and the vibration applied to the blade with different values (0, 9, 16, 23, and 33) HZ and an entry velocity of 22 m/s similar to the experimental case that was conducted in the laboratory.

As for the subfigures (a-d), they represent different levels in height from the blade base, where Fig. 5-8-(a) represents the first level (height of the level by 6 mm) and the second level is illustrated by Fig. 5-8-(b) where it is located at a height of 21 mm from the root and the third level rises from the root 36 mm as in Fig. 5-8-(c) and finally last level shown in Fig. 5-8-(d) rises from the root by 90 mm.

The flow chronology is from the left to right for each figure. The first figure from the left shows the first stage of the development of the aerodynamic flow around the blade at a certain time (t=0.001sec) to complete the process of velocity distribution, as shown by the middle column figures, where the time is 0.002sec. The figures were arranged in a matrix format. The columns represent the change in the location of the levels (span level) in terms of its height from the root with the change in vibration values, and the rows represent the effect of time for each level and a study of the effect of vibration on the fluid velocity distribution.

The third column of the figures are located to the right. It shows the state of the effect of vibration on the fluid velocity distribution, where the time is 0.1sec. It was noted that the occurrence of deformation in the body contour depends on the value of the vibration applied to the blade. Nevertheless, these figures are identical to the figures preceded by the middle column figures in the absence of vibration (at zero frequency).

Through, these figures, it was noticed that a change in the velocity distribution, as it increased in regions and decreased in other, because the vertical vibration of the blade works on a change in the airfoil section of the blade, whether it is an increase in the cross-sectional area, which occurs when the blade rises to the top or a decrease in the cross-sectional area when descending, and by repeating this process periodically leads to an increase the amount of induced vortices touching the surface of the blade. The increasing in the change of section due to the movement of the airfoil causes the fluid in contact with it to be pushed.

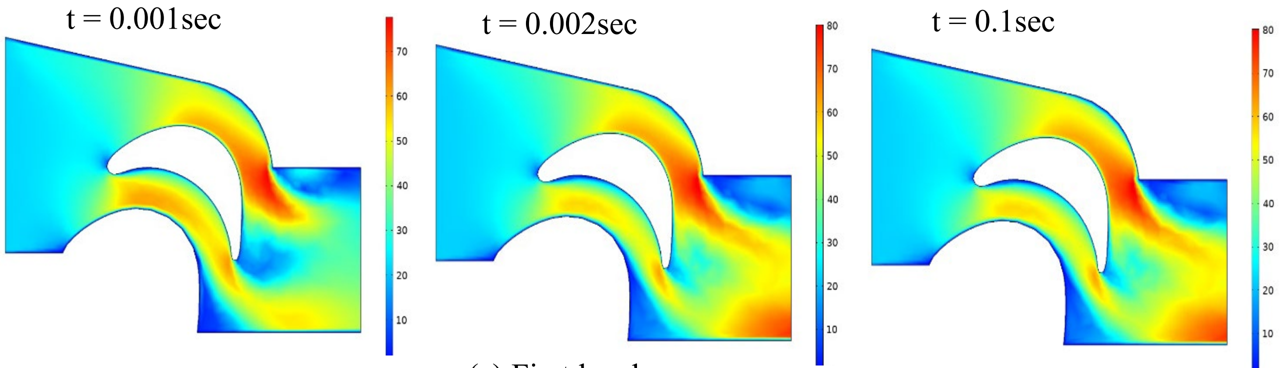

(a) First level

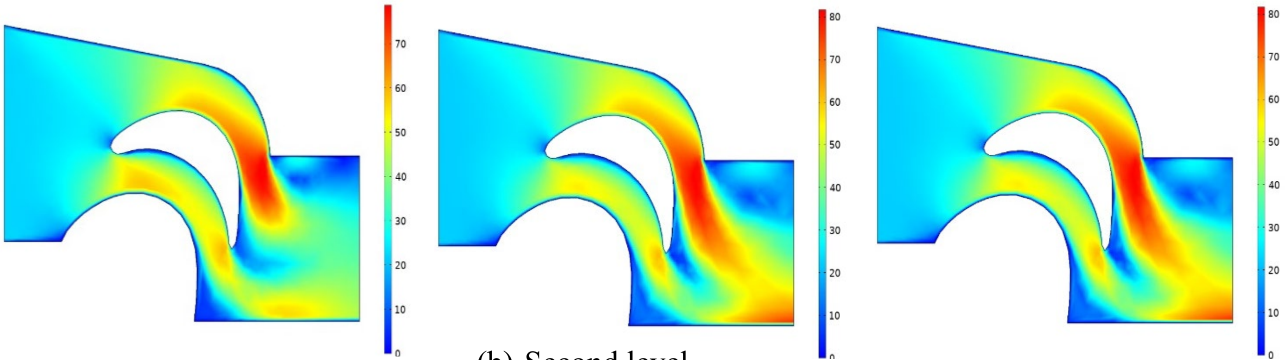

(b) Second level

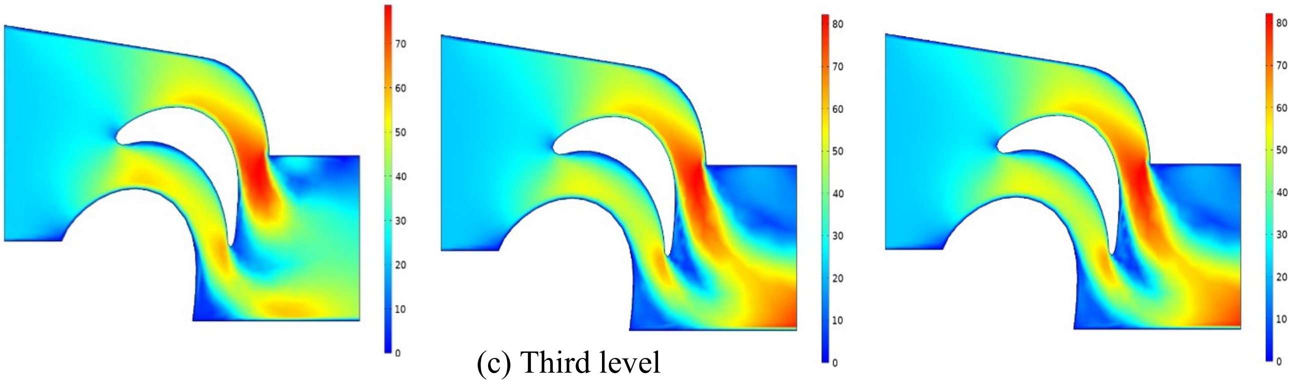

(c) Third level

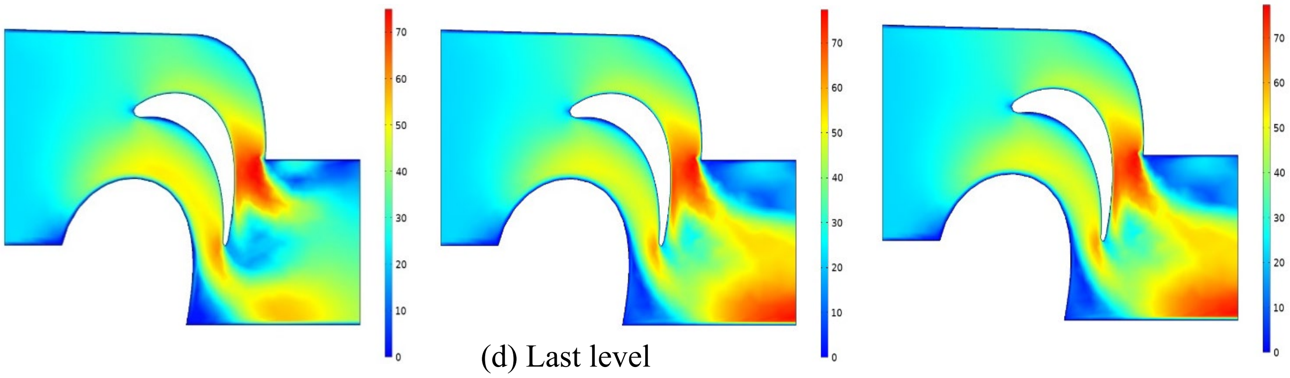

(d) Last level

Fig. 5-8: body contour of velocity distribution without vibration at inlet velocity 22m/s.

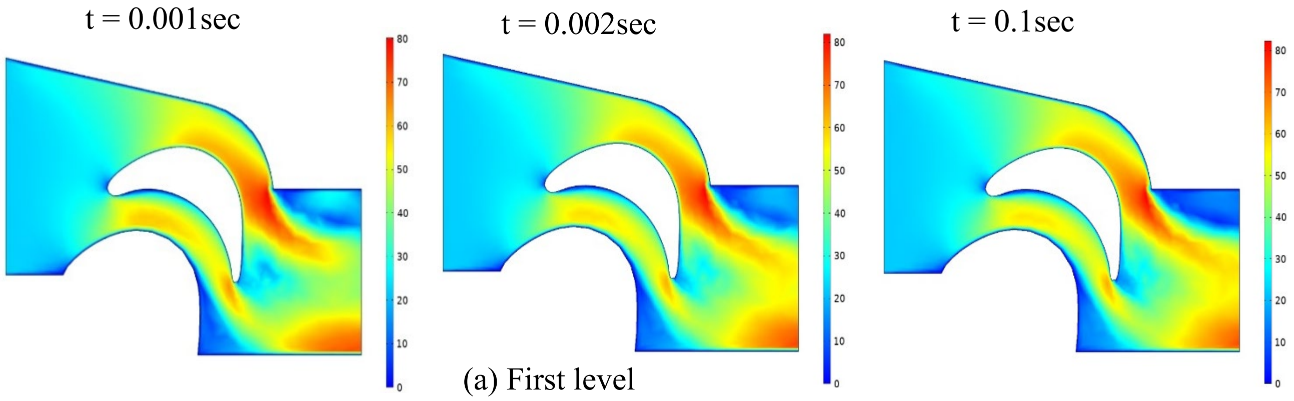
t = 0.001sec

t = 0.002sec

t = 0.1sec

(a) First level

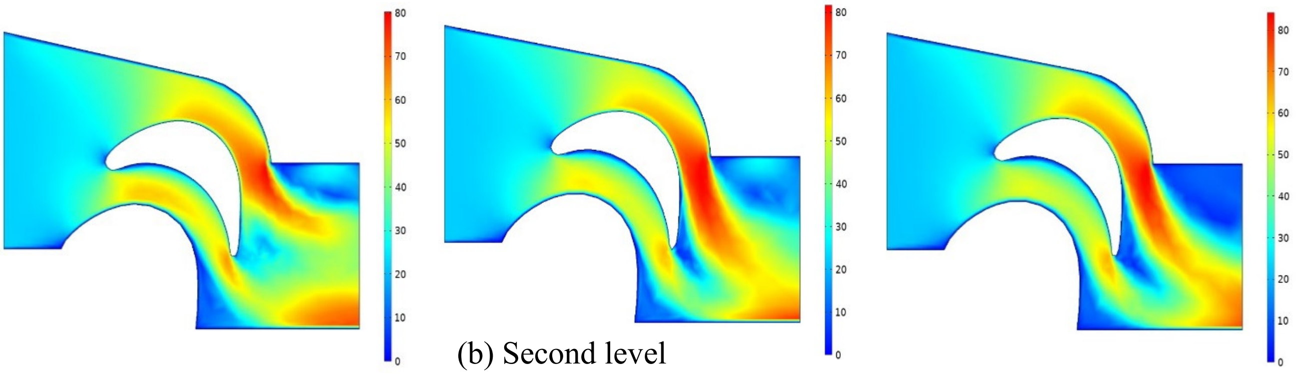

(b) Second level

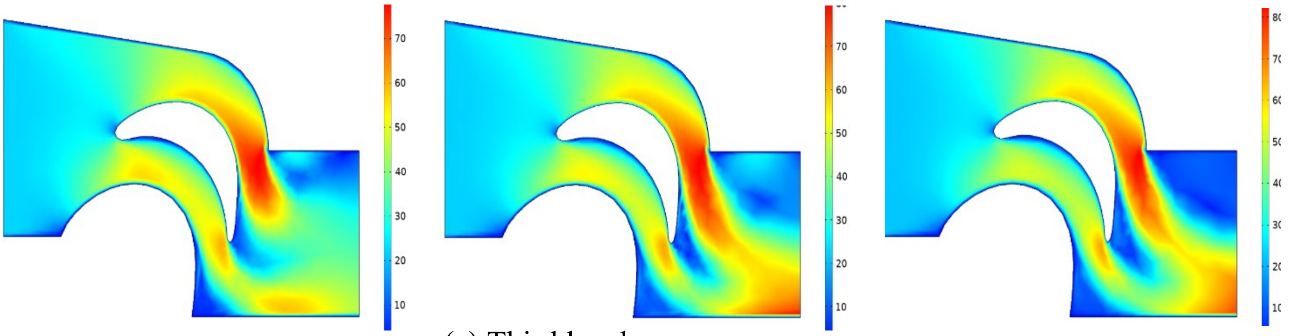

(c) Third level

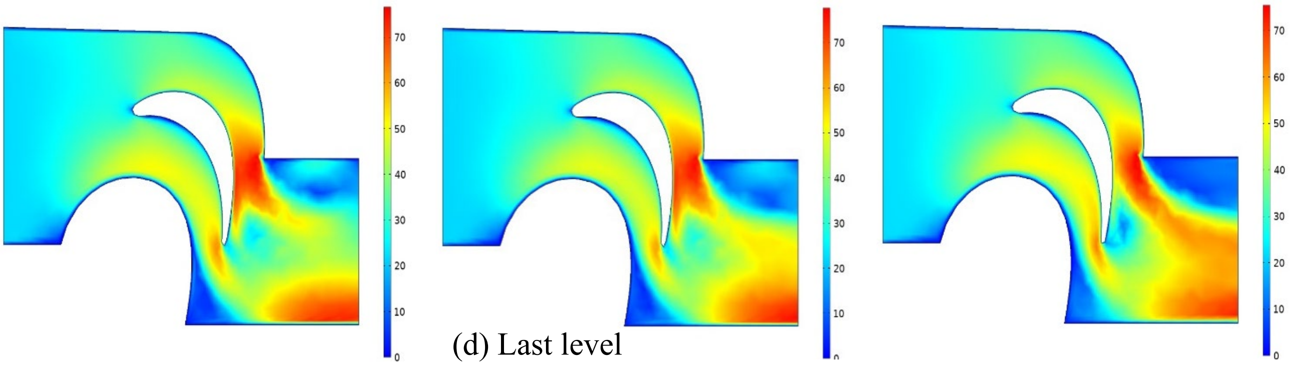

(d) Last level

Fig. 5-9: body contour of velocity distribution at 9Hz and inlet velocity 22m/s.

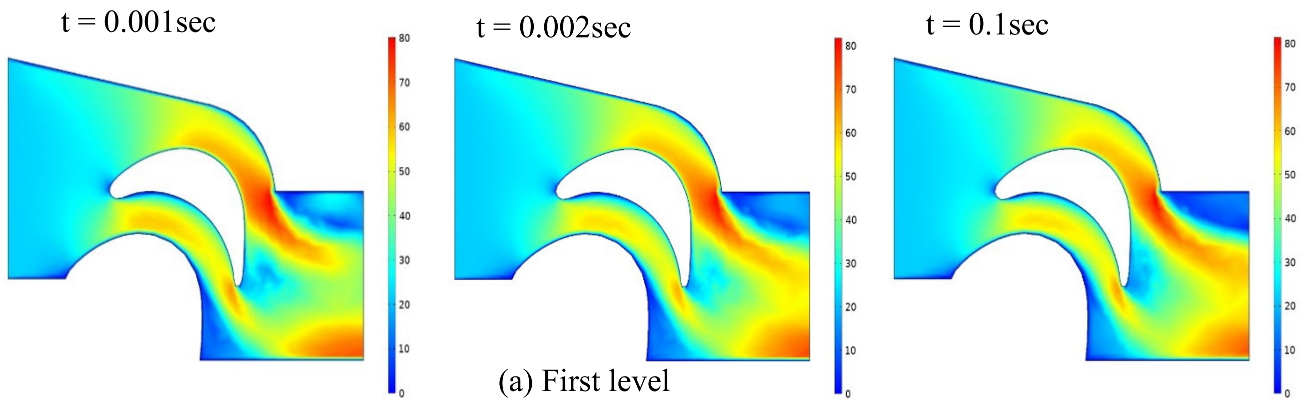

(a) First level

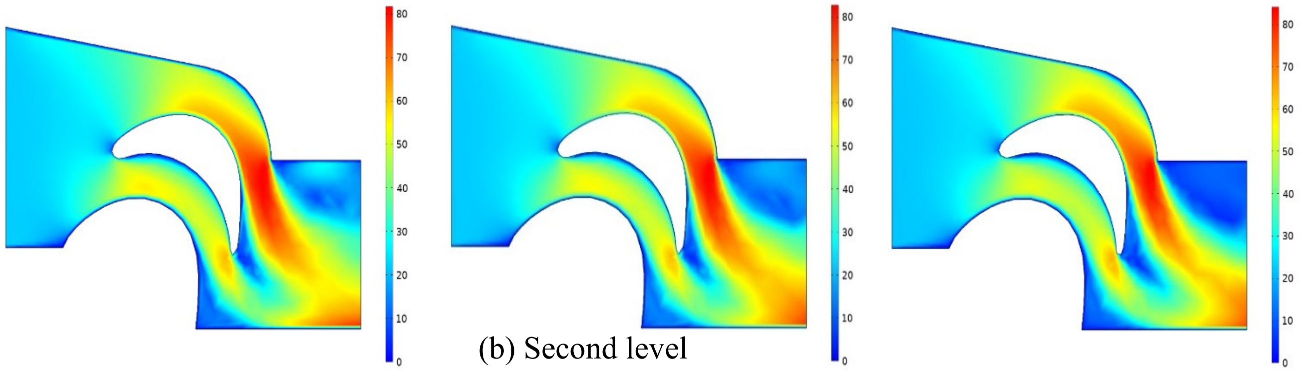

(b) Second level

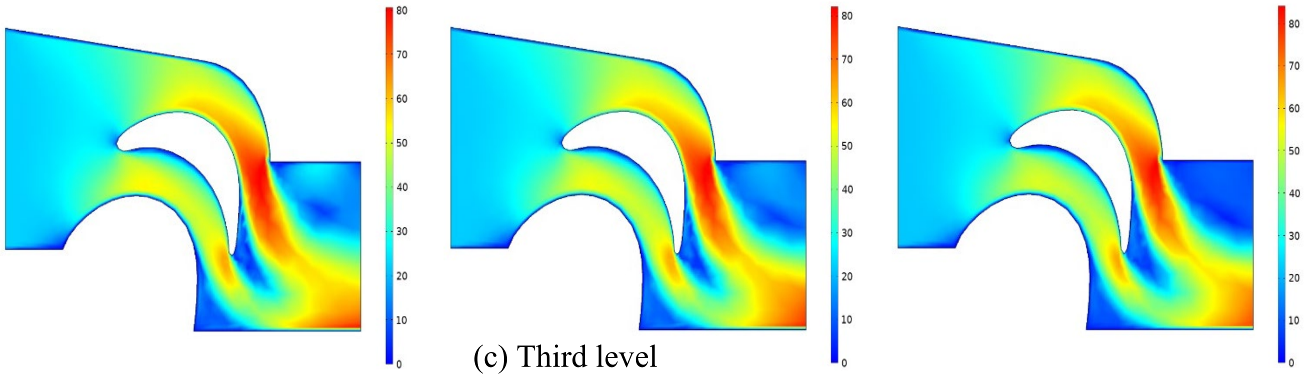

(c) Third level

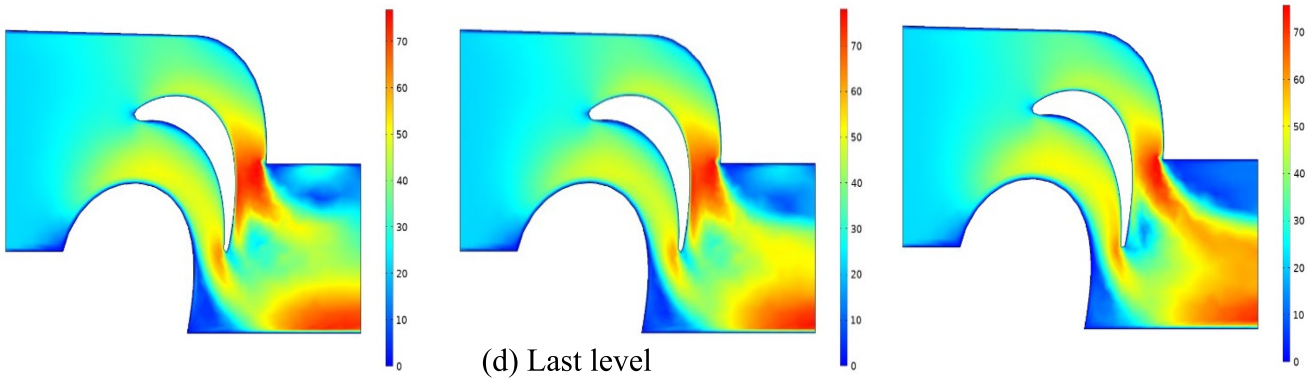

(d) Last level

Fig. 5-10: body contour of velocity distribution at 16Hz and inlet velocity 22m/s.

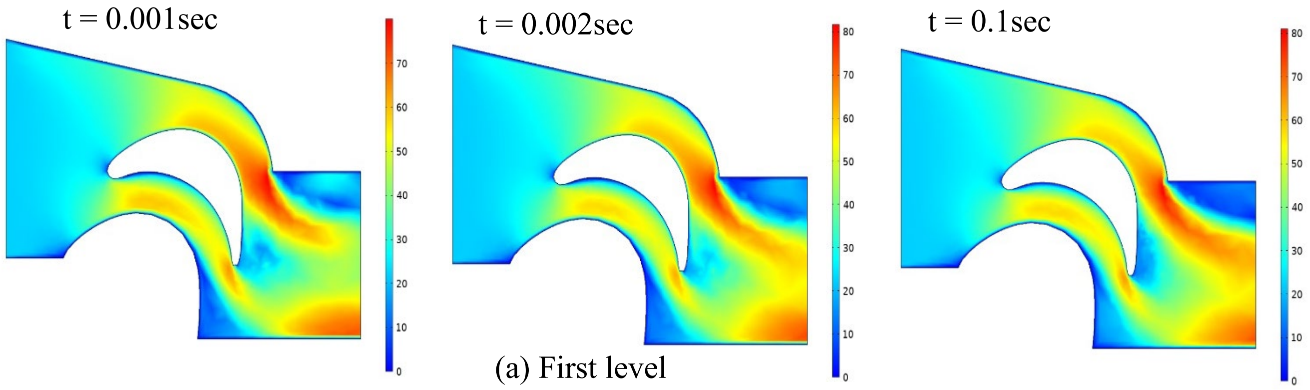

(a) First level

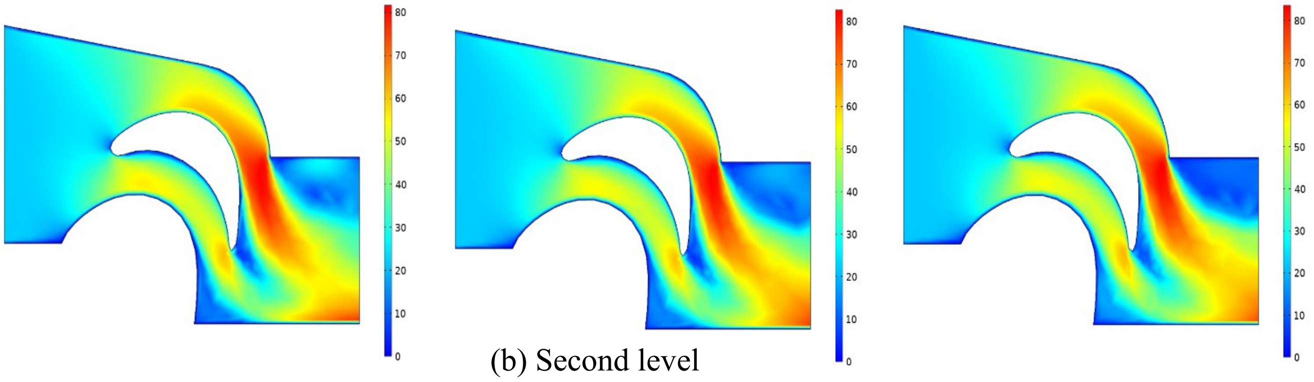

(b) Second level

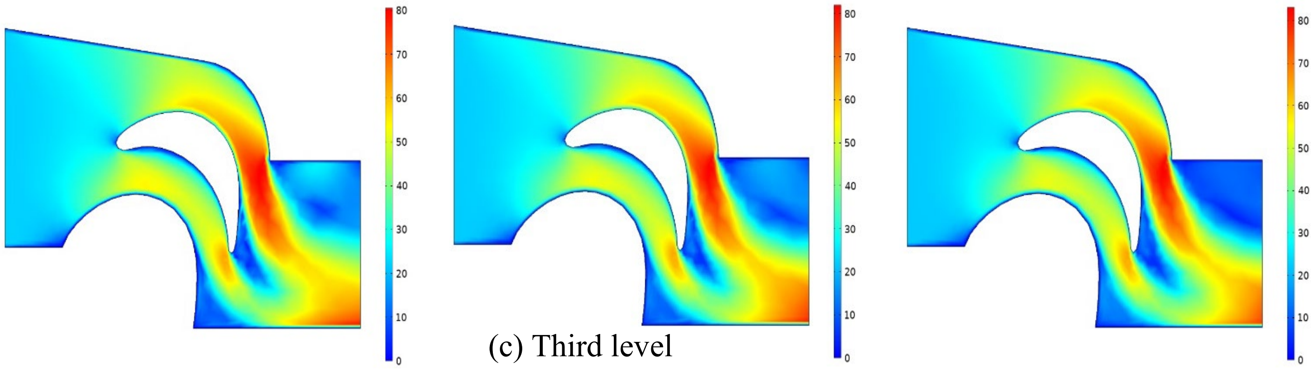

(c) Third level

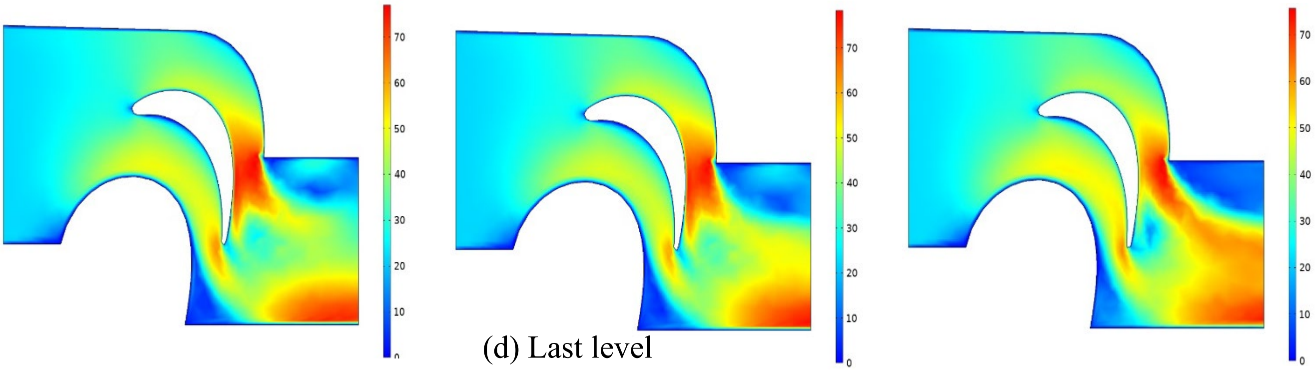

(d) Last level

Fig. 5-11: body contour of velocity distribution at 23 Hz and inlet velocity 22m/s.

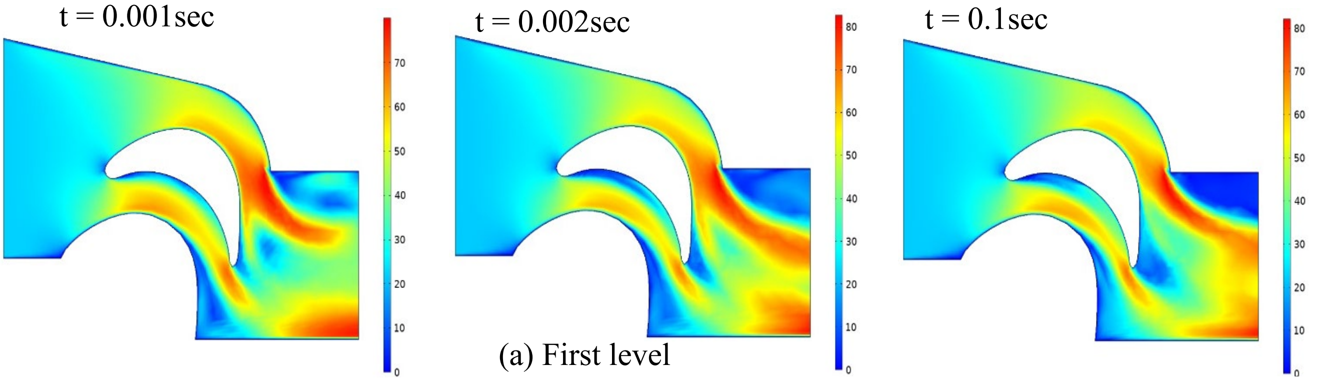

(a) First level

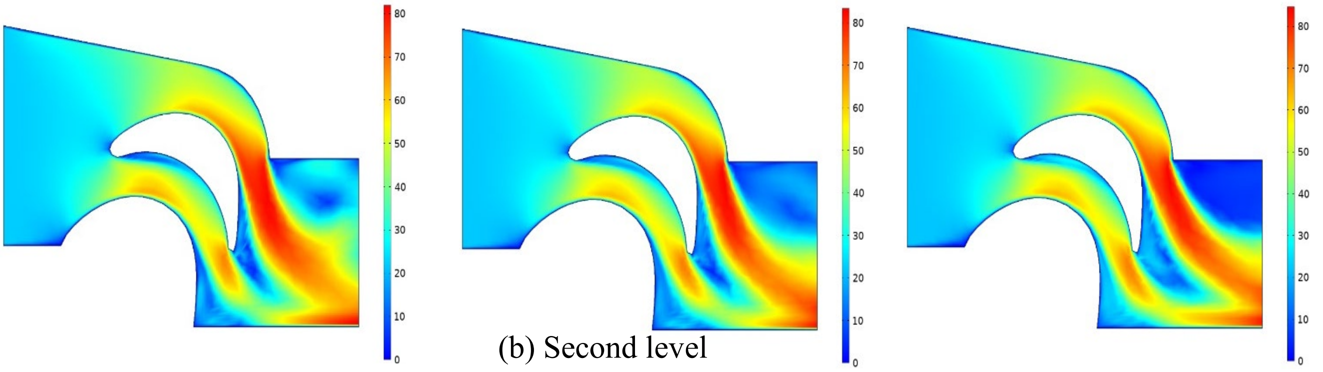

(b) Second level

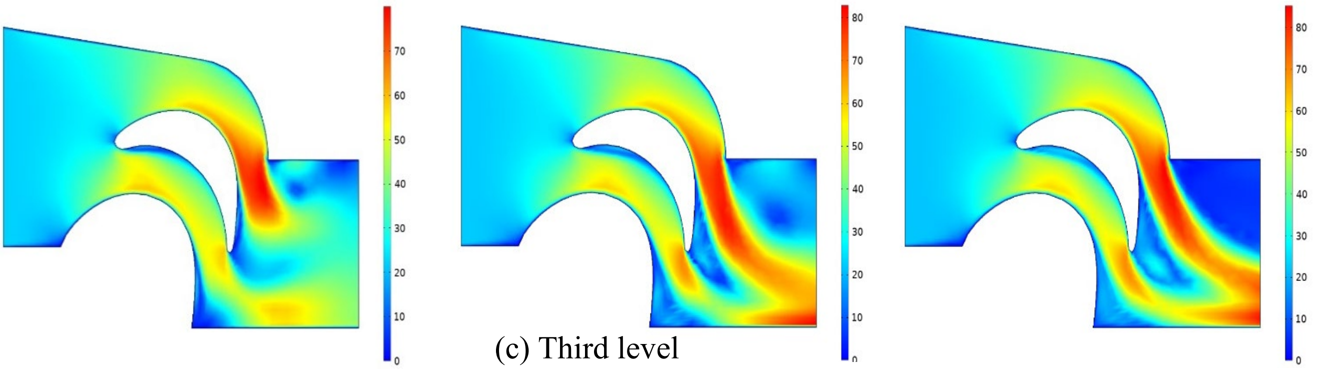

(c) Third level

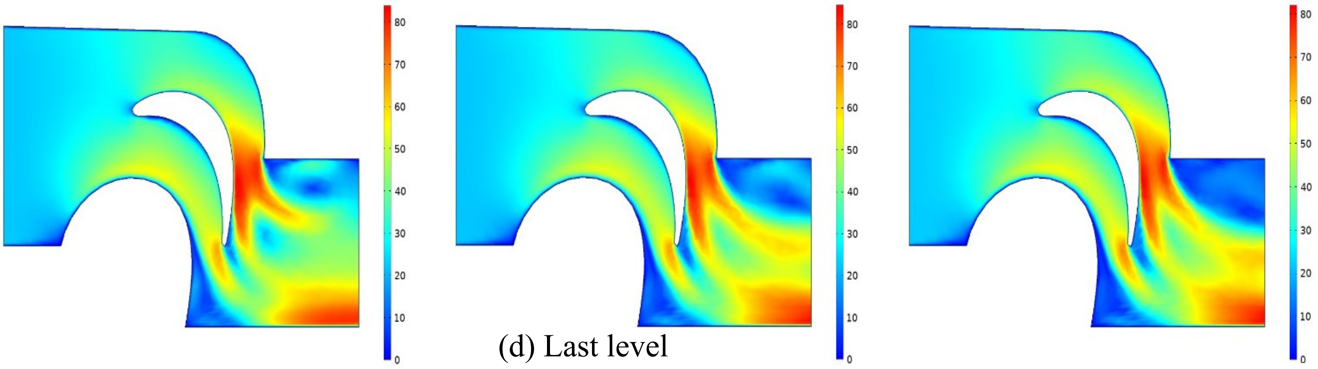

(d) Last level

Fig. 5-12: body contour of velocity distribution at 33 Hz and inlet velocity 22m/s.

5.3.2. Pressure Profile around the Blade

Fig. 5-13 toFig. 5-17 represent the pressure distribution around the blade and the vibration applied to the blade with different values starting from (0-33) Hz and an entry speed of 22 m/s similar to the practical case that was conducted in the practical laboratory.

Fig. 5-13-(a) represents the height of the level by 6 mm, and the second level is illustrated by the figure b, where it is located at a height of 21 mm from the root and the third level is 35 mm higher than the root as in the Fig. 5-13-(c), and finally the Fig. 5-13-(d) rises from the root by 90 mm.

It was noticed that the fluid enters at high pressure and decreases during its progression through the presidency and then to the exit region. It was also noted that the deformation in the body contour of the pressure distribution of the fluid is a result of the vibration on the blade, which in turn increases the pressure regions near the pressure side and decreases it in the suction side. This is because the velocity of the fluid near the walls of the P.S., which leads to an increase in pressure in this region.

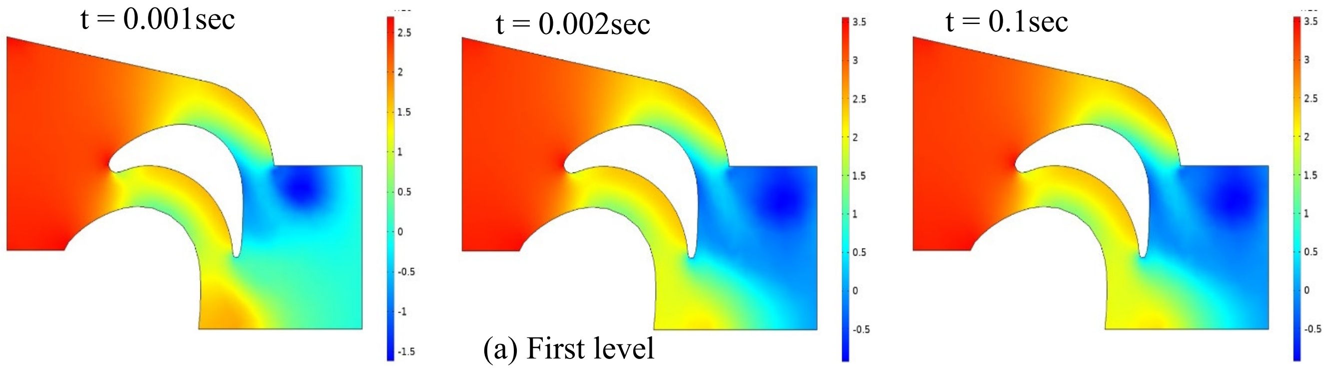

(a) First level

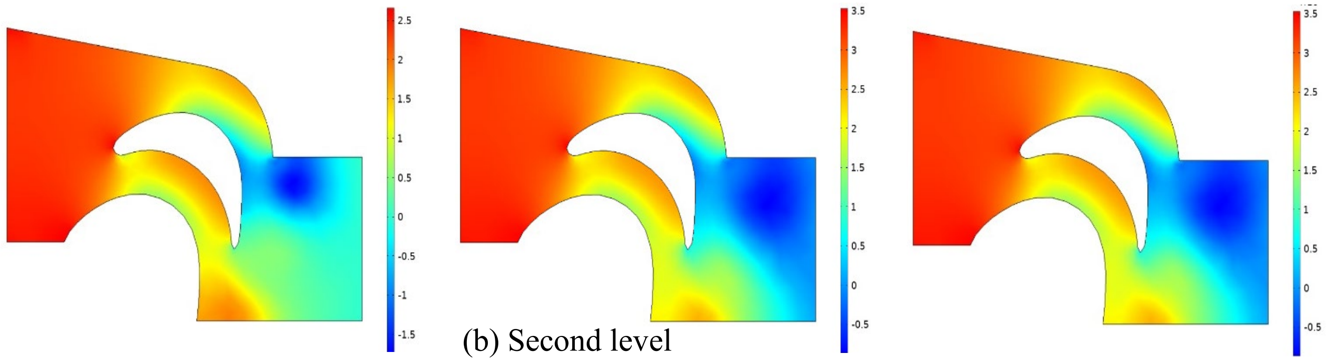

(b) Second level

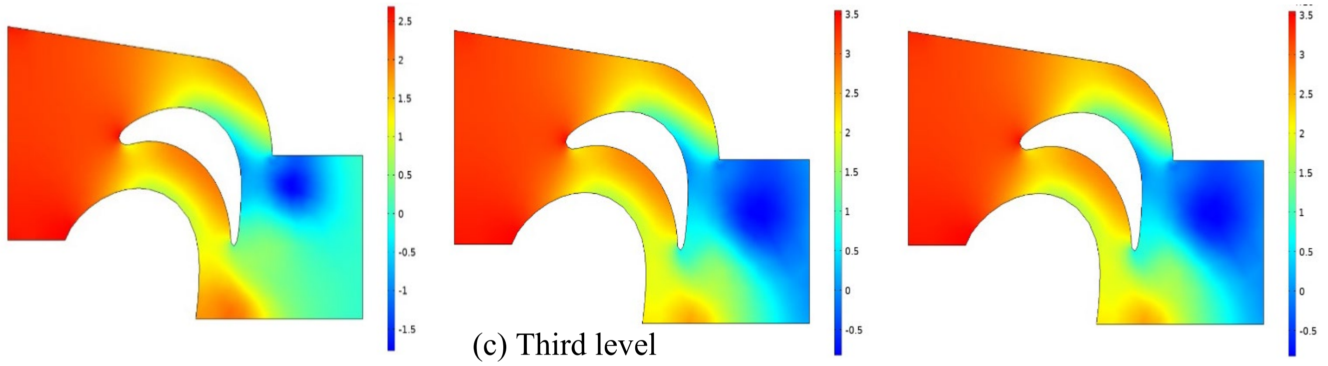

(c) Third level

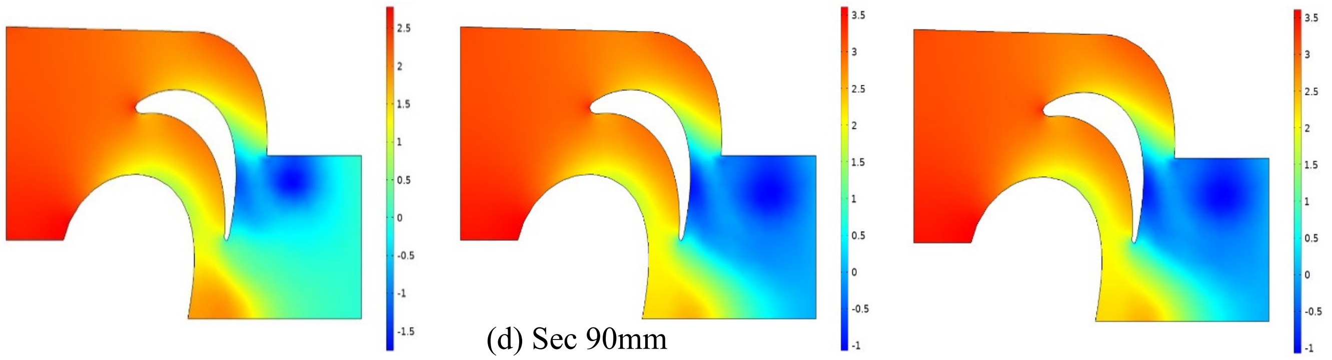

(d) Sec 90mm

Fig. 5-13: body contour of pressure distribution in (×10^3pa) without vibration and inlet velocity 22m/s.

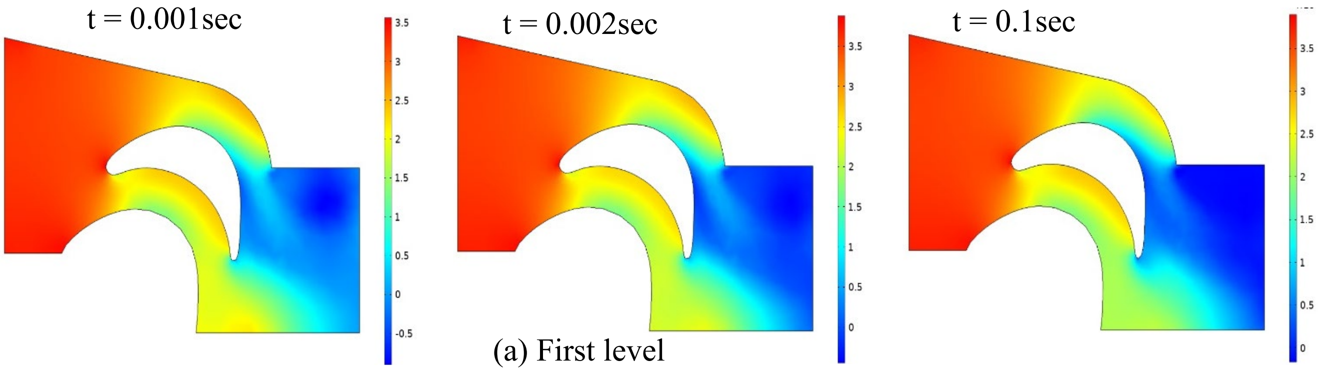

(a) First level

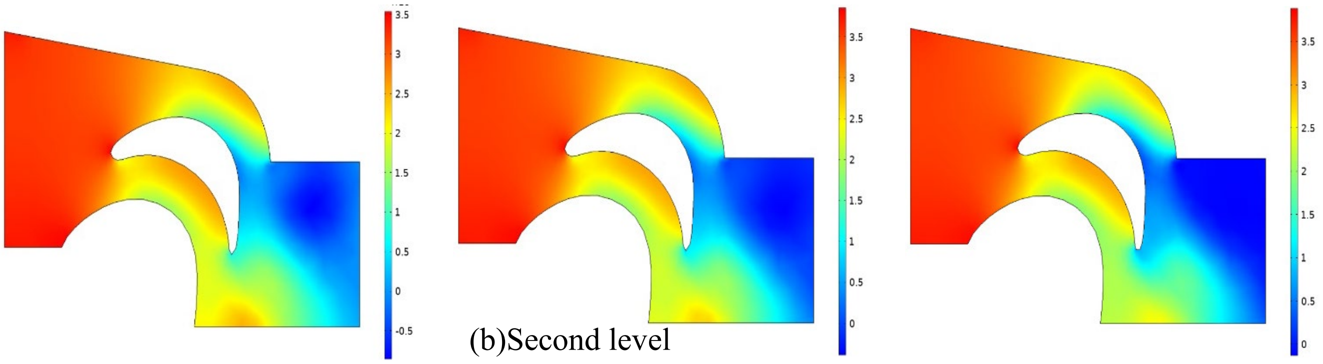

(b)Second level

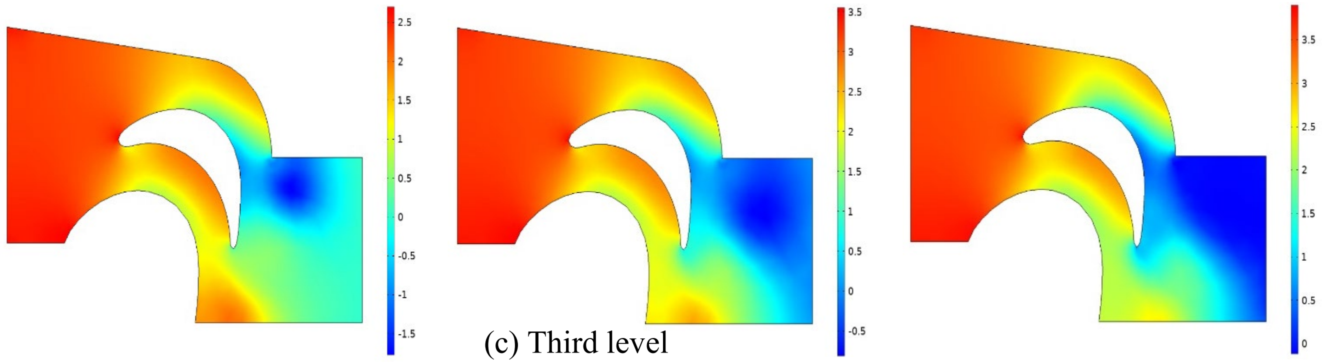

(c) Third level

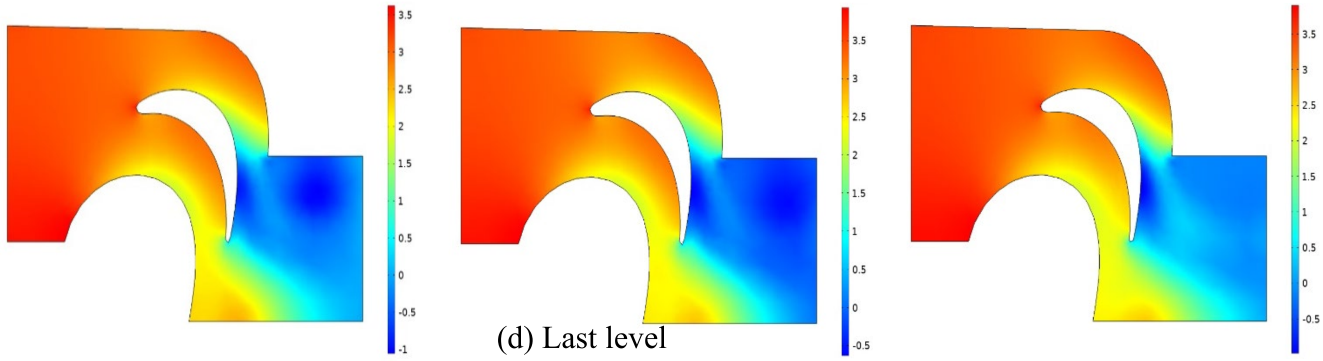

(d) Last level

Fig. 5-14: body contour of pressure distribution (×10^3pa) at 9Hz and inlet velocity 22m/s.

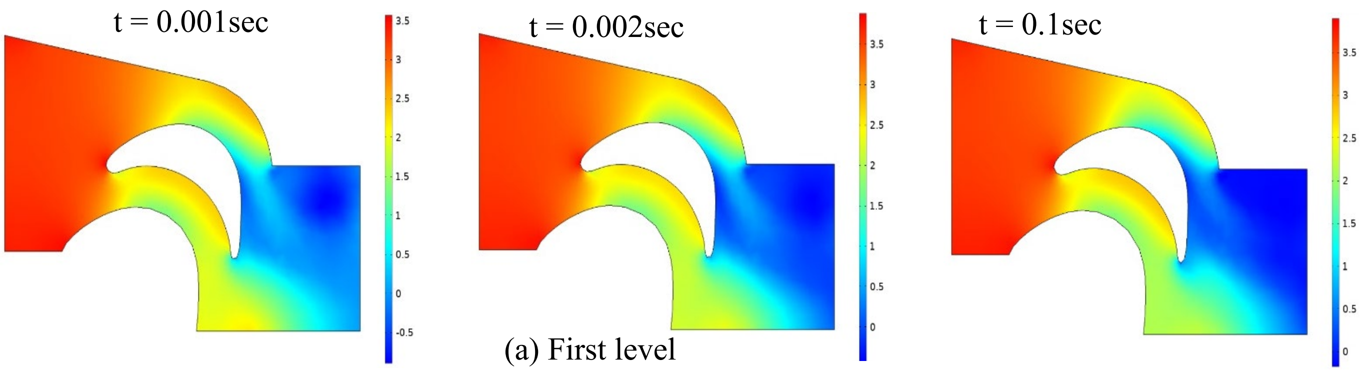

(a) First level

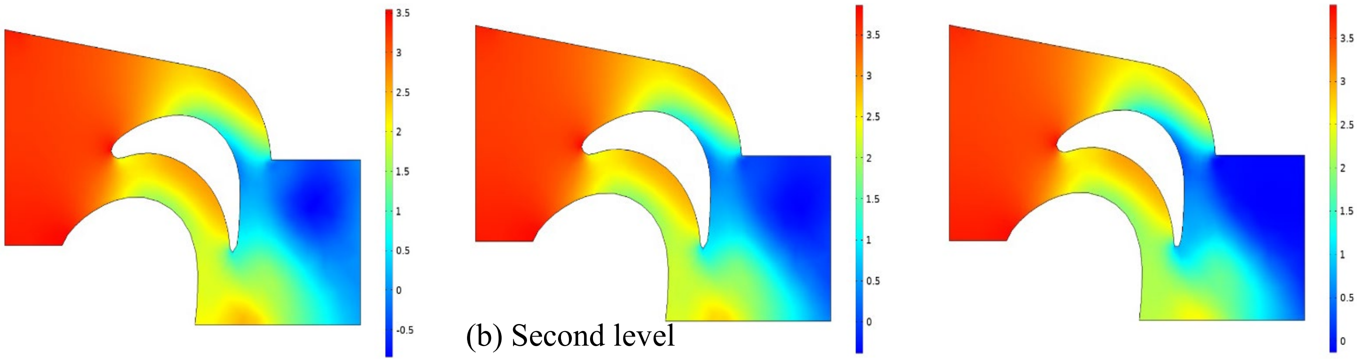

(b) Second level

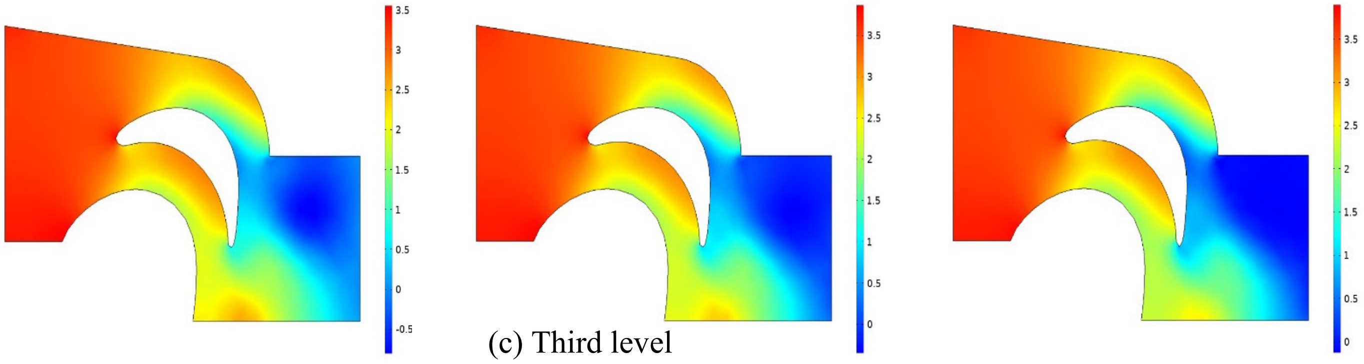

(c) Third level

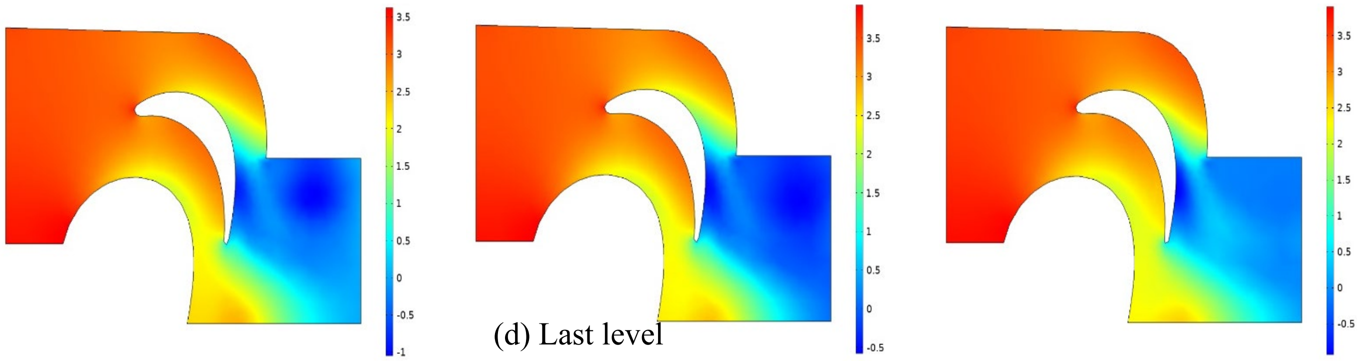

(d) Last level

Fig. 5-15: body contour of pressure distribution (×10^3pa) at 16 Hz and inlet velocity 22m/s.

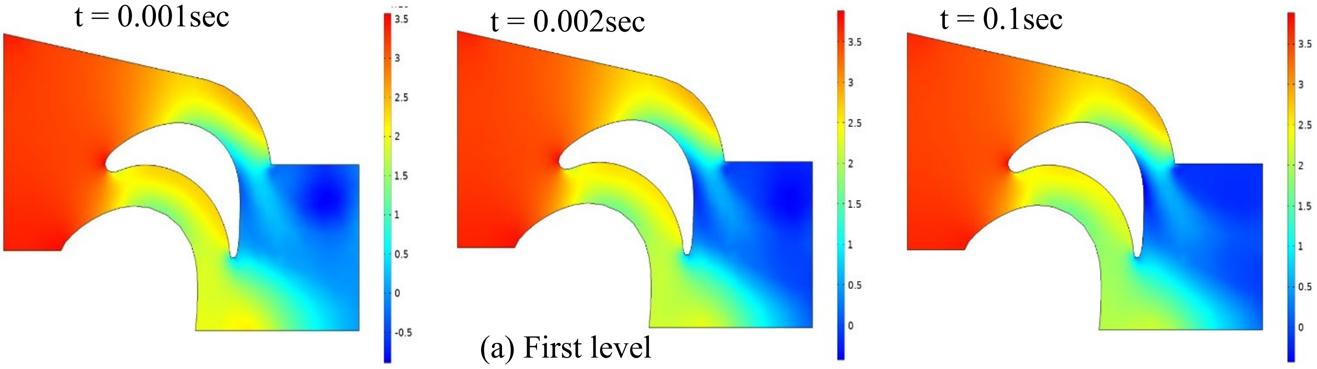

(a) First level

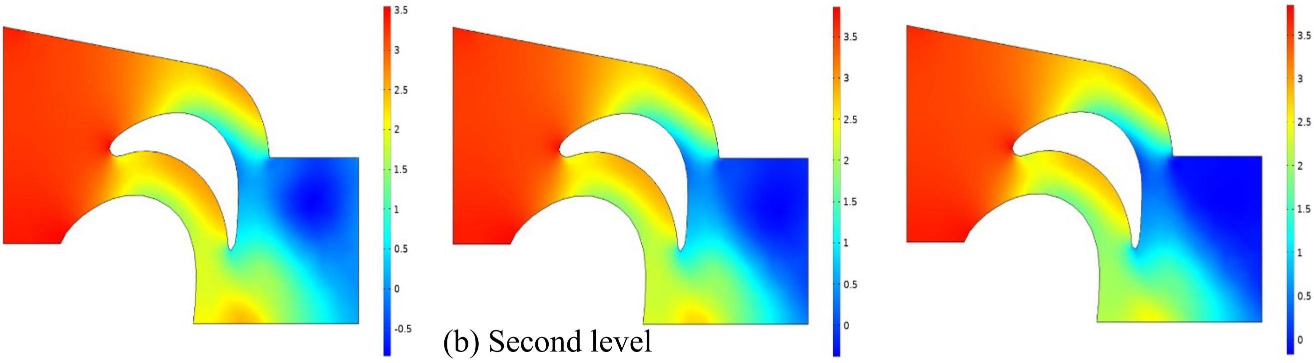

(b) Second level

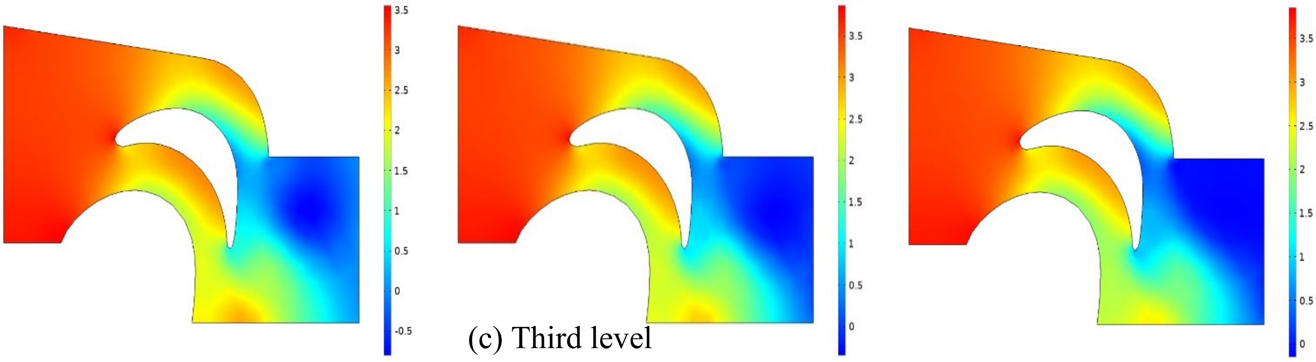

(c) Third level

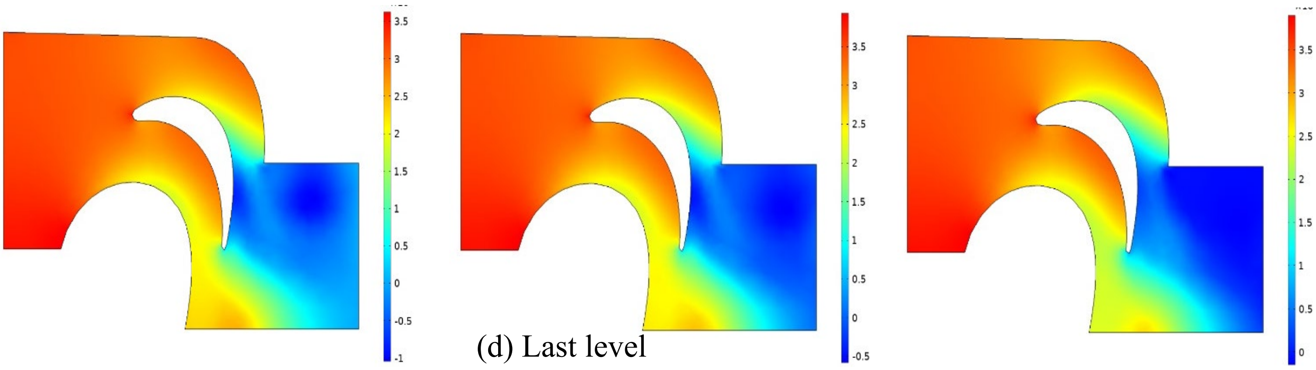

(d) Last level

Fig. 5-16: body contour of pressure distribution (×10^3pa) at 23 Hz and inlet velocity 22m/s.

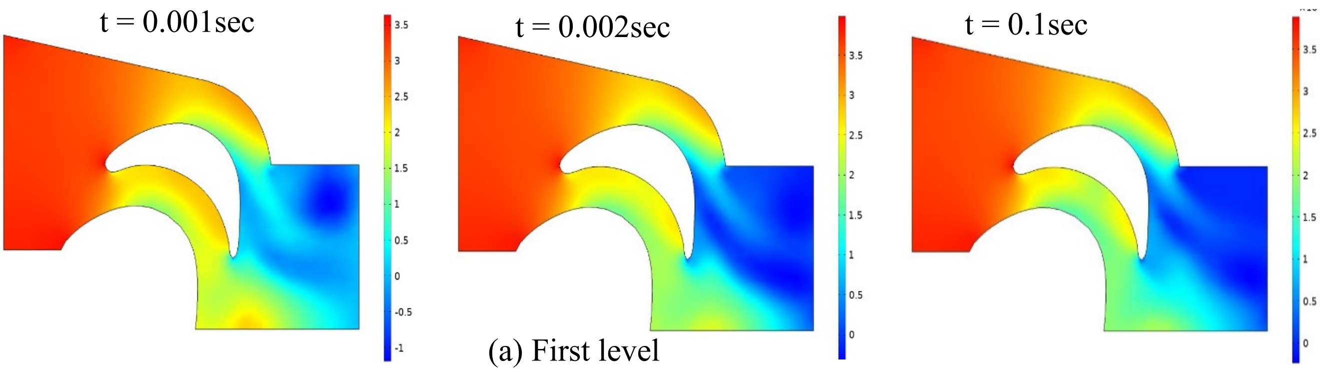

(a) First level

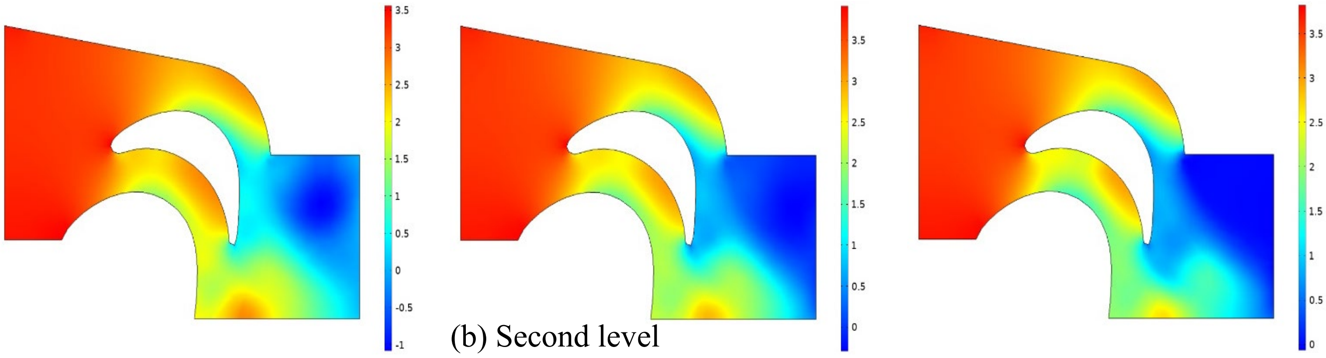

(b) Second level

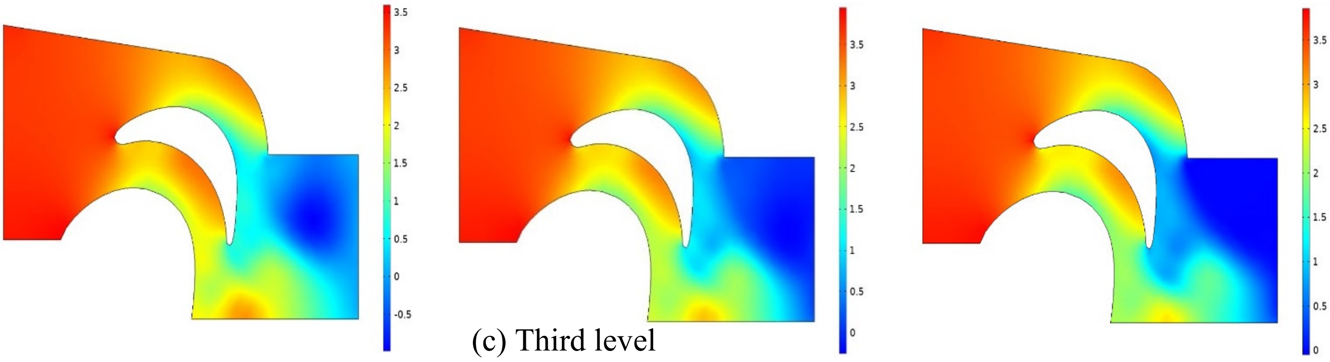

(c) Third level

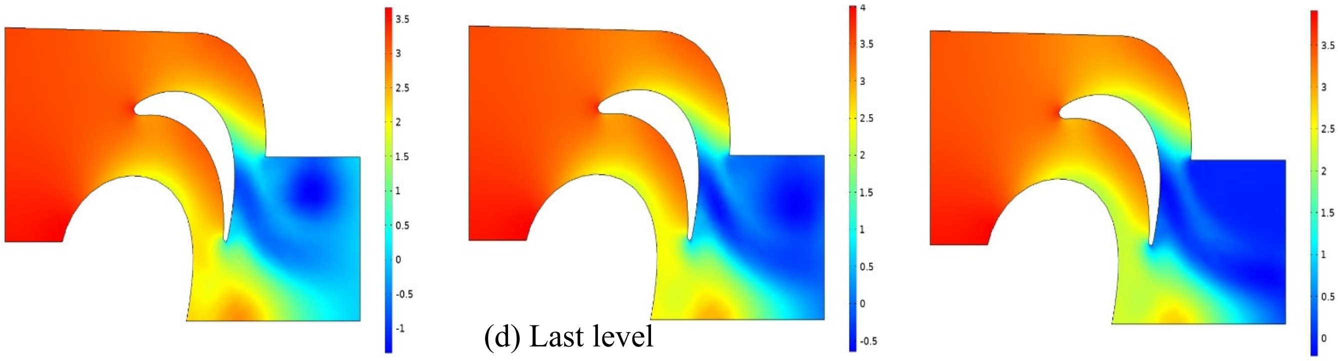

(d) Last level

Fig. 5-17: body contour of pressure distribution (×10^3pa) at 33 Hz and inlet velocity 22m/s.

5.3.3. Vertical Segments of Pressure and Velocity Distribution

Figure 5-18 shows four vertical segments on the blade root for clear image of the velocity and pressures distribution of the flowing fluid and the change in their values at each segment provided that the inputs and conditions are identical to the experimental work. The first segment is close to the leading edge (L.E.). The second segment is in the first quadrant of the chord, the third segment is in the middle of the chord, and the final segment is located in the third quadrant of the chord.

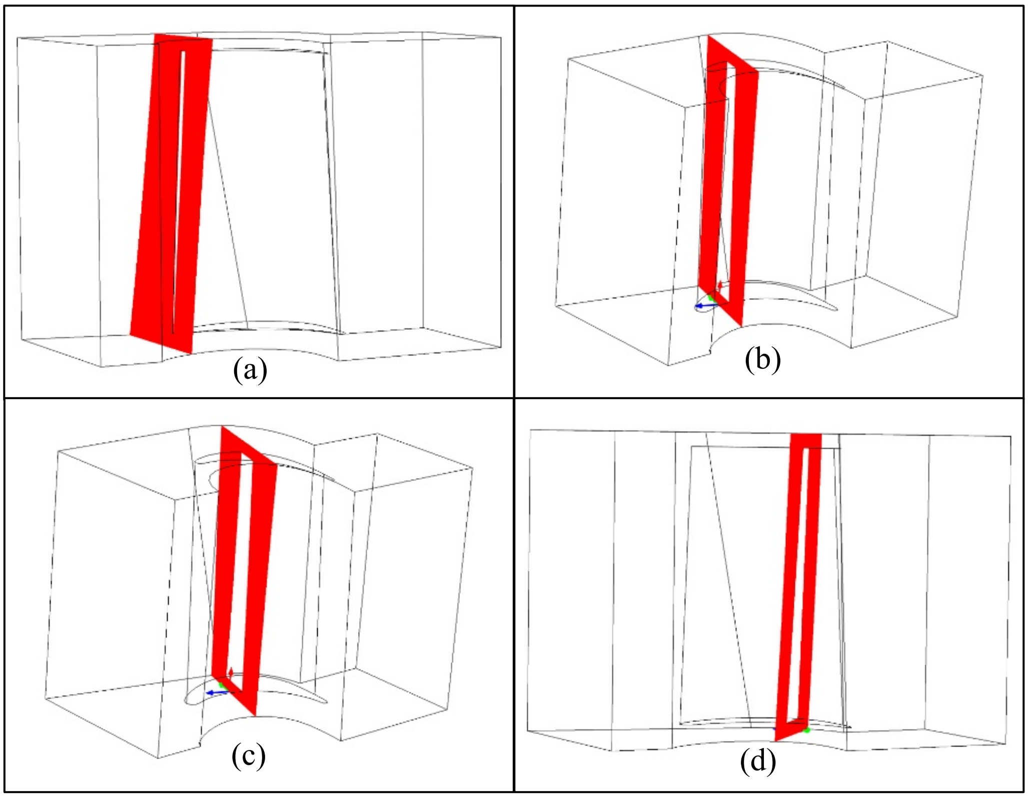
(a) (b) (c) (d)

Fig. 5-18: Vertical segments in the model.

Each column in the Fig. 5-19 and Fig. 5-20 reveals the state of the fluid velocity and pressure distribution, respectively, at specific frequency. The row in each column represents a specific section as the first row is the state of the first segment and the second row represents the second segment and so on. The subfigures (a) to (f) show that the segment (vertical section) consists of two sides (P.S. at the right and the S.S. at the left). Through these figures, it was noticed that the velocity of the fluid is higher in the S.S.

than its velocity at the P.S., and the gradient in velocity is increasing in P.S. and decreasing in the S.S. towards the flow passage region. That is, the velocity of the fluid increases from the surface of the blade in the S.S to the left end, and the velocity increases from the blade surface in the P.S. to the right end. The main reason of that is the nature of the blade section shape, which plays the role of generating a difference between the pressures caused by the difference in the velocity of the liquid in the S.S. and P.S.

It was also noted that the velocity distribution lines increased significantly due to a change in the blade section, which causes a change in the amount of velocity in the pressure and suction regions of the blade. This change continues along the passage flow of the fluid, which produces eddies due to the difference in fluid velocities and directions. Vibration generates disturbances in the fluid velocity distribution, and these disturbances increase with the increase of vibration and become more effective at the surface of the blade, which means the counter vortices is increasing.

Fig. 5-20 represents the distribution of the fluid pressure lines around the blade. It noticed that the fluid pressure is less in the suction region than at the pressure region, and the pressure gradient is increasing for both the suction and the pressure regions towards the fluid passage flow. That is, the fluid velocity decreases from the surface of the blade in the suction region to the left end, and the pressure decreases from the blade surface in the pressure region to the right end. It is also noted that the distribution of the pressure lines decreases significantly due to a change in the blade section, which causes a change in the amount of velocity in the pressure and suction regions.

This change continues along the passage flow of the fluid, which produces vortices due to the fluid pressure difference. Vibration generates disturbances in the fluid velocity distribution, and these disturbances increase with the increase of vibration and become more effective at the surface of the blade, which means the induction vortices increase gradually. However, the value of the pressure at one-point decreases with the increase in the amount of vibration.

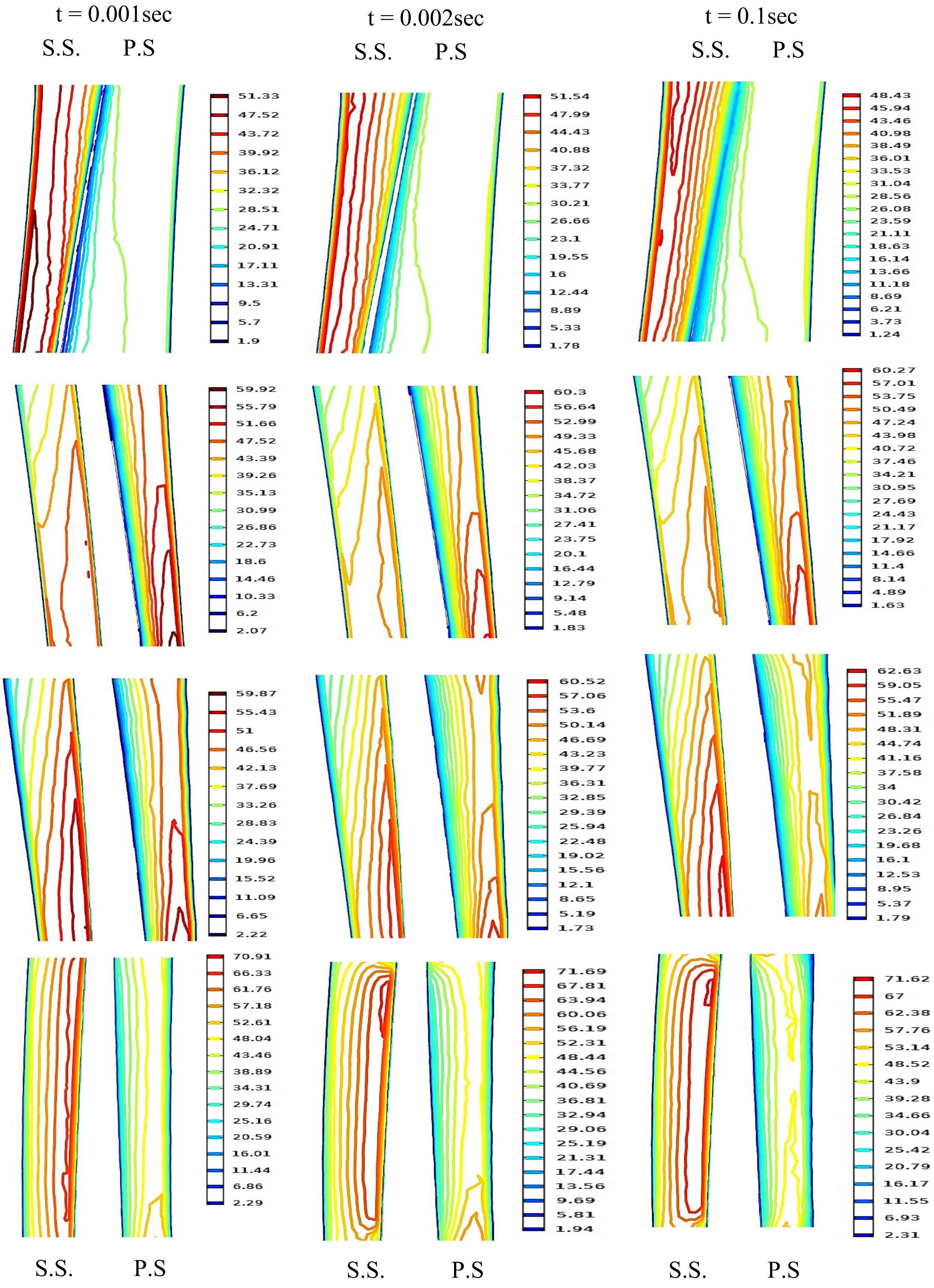

(a) 0 Hz (b) 9 Hz (c) 16 Hz

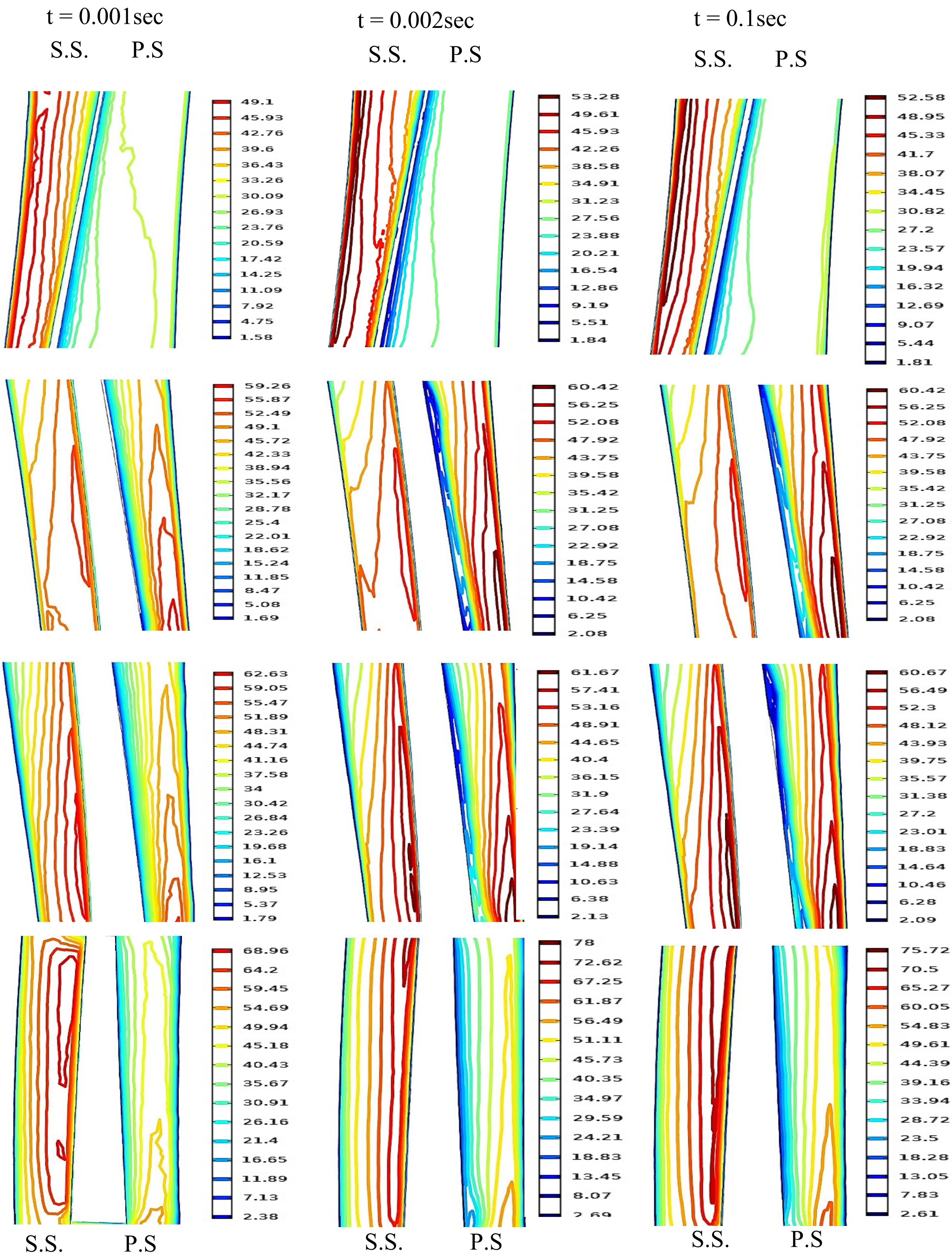

(d) 23 Hz (e) 33 Hz (f) 100 Hz

Fig. 5-19: velocity distribution for vertical segment under effect of vibration at 22m/s.

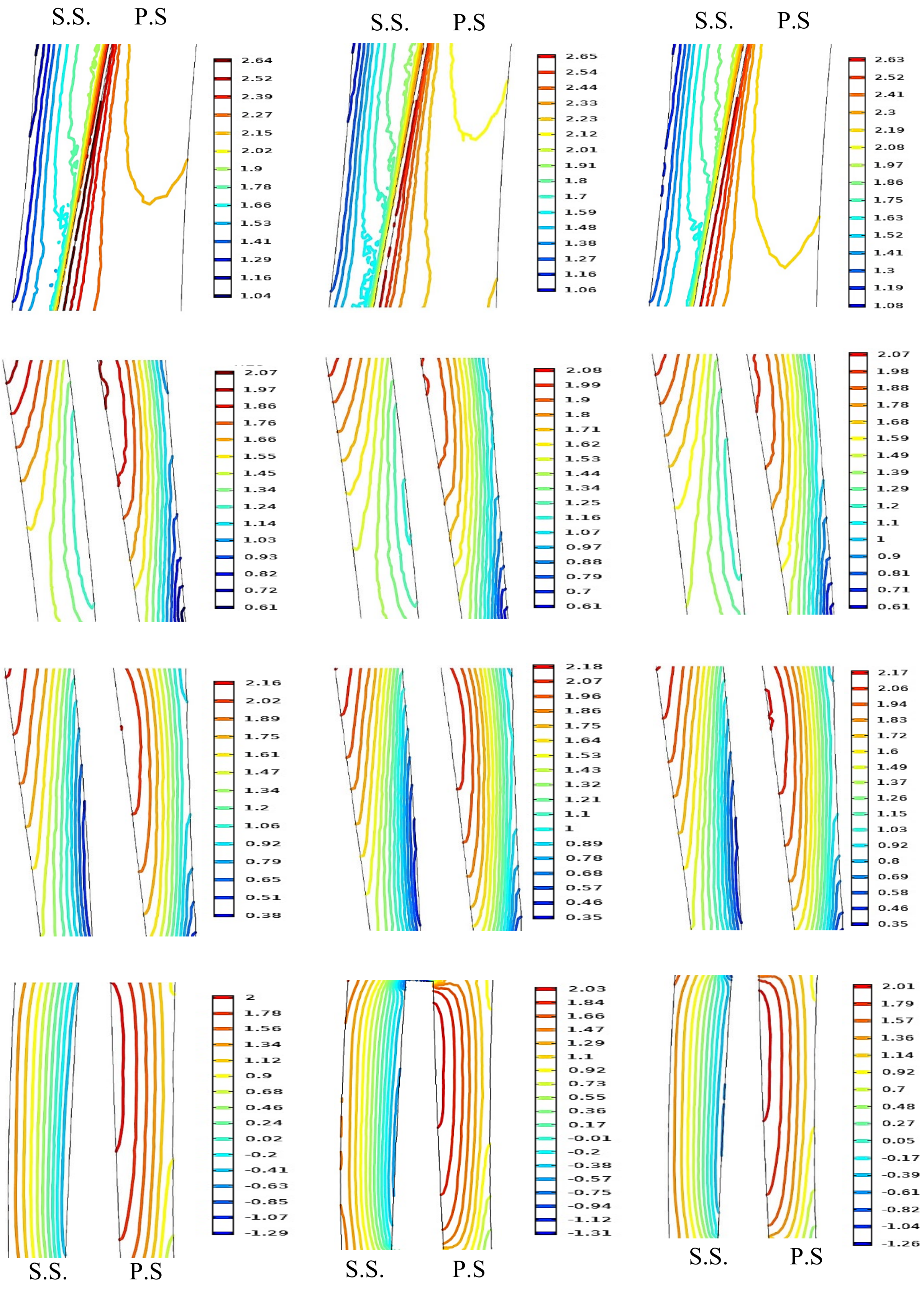

(a) 0 Hz (b) 9 Hz (c) 16 Hz

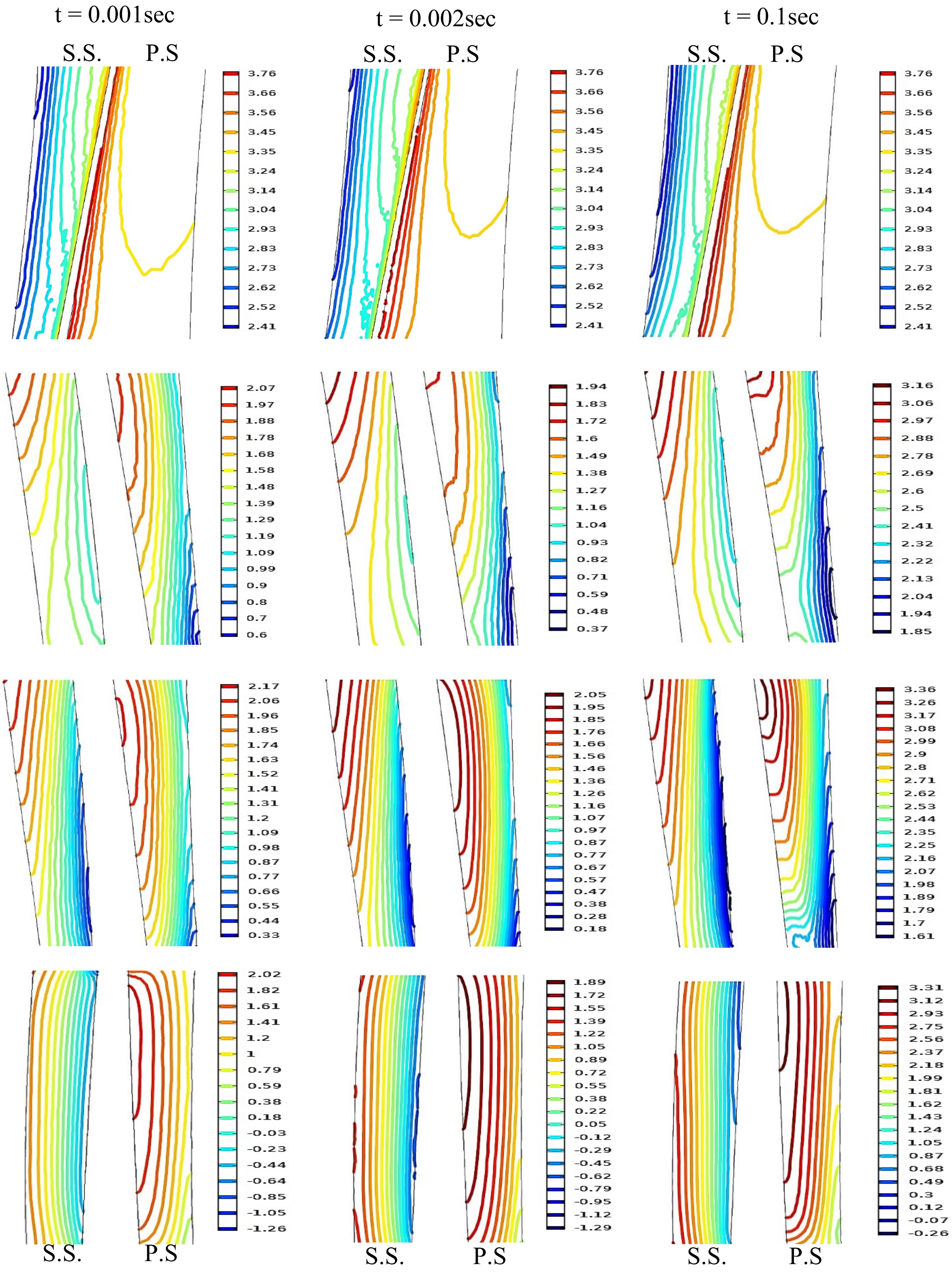

(d) 23 Hz (e) 33 Hz (f) 100 Hz

Fig. 5-20: Pressure distribution (×10^3pa) for vertical segment under effect of vibration at 22m/s.

5.4. Numerical Results

In this part, the theoretical case of the actual fluid velocity entering from the stator to the rotator turbine of 120 m/s is studied. The external vibration applied to the blade are taken for same values of the experimental work. The results of the analytical work will be reviewed according vibration direction, perpendicular and horizontal direction, respectively.

5.4.1.Radial Vibration Effect on the Blade

In this part, the effect of vibration is studied for the same previous values and amplitude of vibration, but in a perpendicular direction to the base.

5.4.1.1. Velocity Distribution around the Blade

Fig. 5-21 to Fig. 5-25 show the distribution of fluid velocity around the blade for the four horizontal sections. Fig. 5-21 shows the stages of fluid velocity distribution with time, where the subfigures in the left column present the stage of fluid velocity distribution in a specific time and the second column shows the stage of fluid velocity distribution in the next time than the previous case to be almost stable with the progress of time as shown by the subfigures in the third column of Fig. 5-21 which is identical to the column of the subfigures of the four horizontal sections in the same figure which of zero vibration. The remaining subfigures show the effect of vibration on the fluid velocity distribution in the numerical model. Vibration increases the fluid velocity and it is noticeable in the third column on the right, where it is noticed an increase in different regions and a decrease in others.

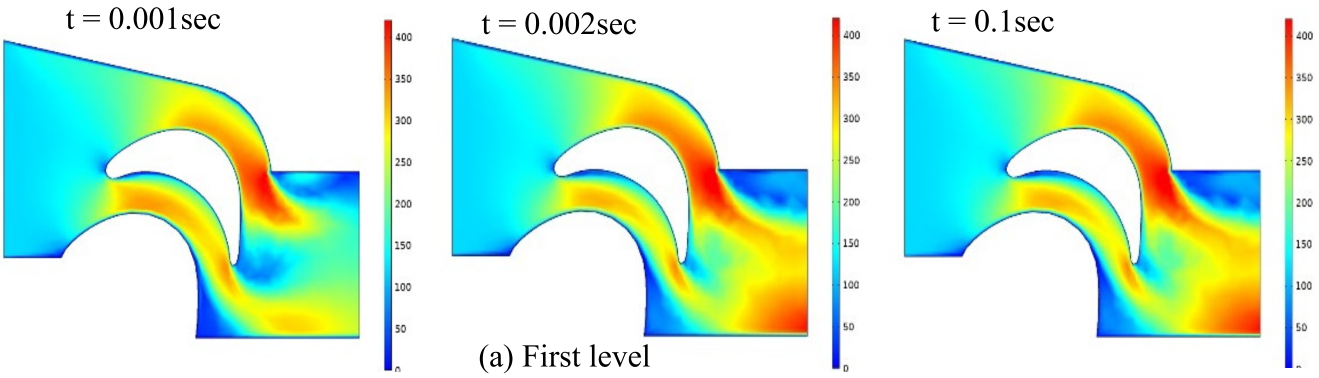

(a) First level

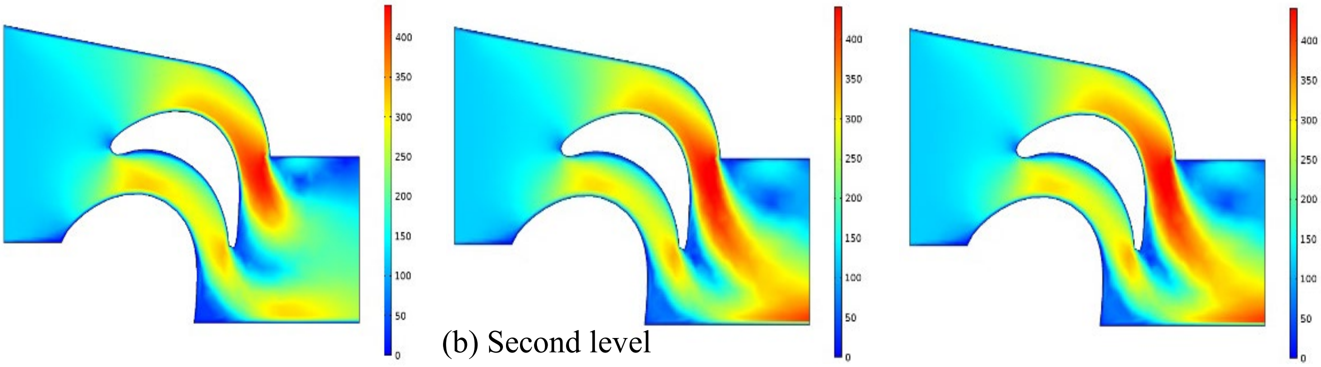

(b) Second level

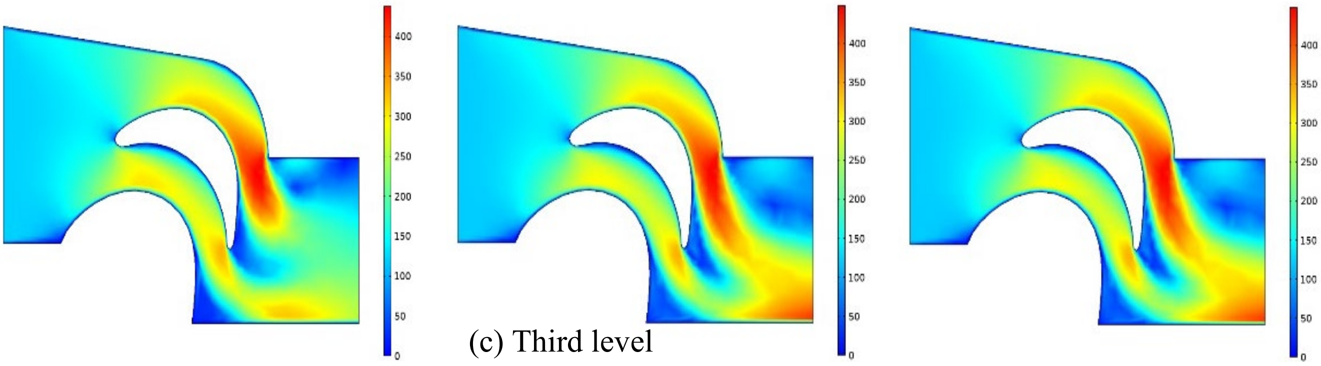

(c) Third level

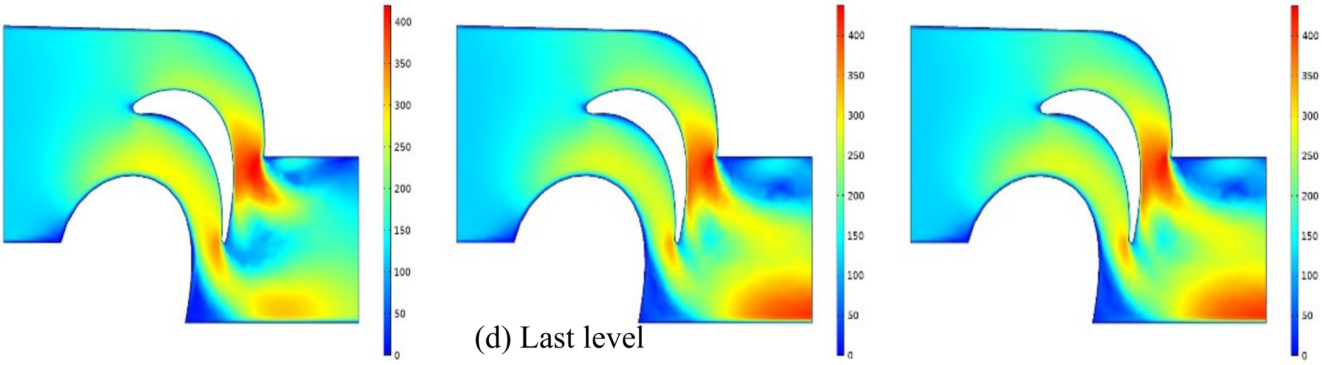

(d) Last level

Fig. 5-21: body contour of velocity distribution without vibration and inlet velocity 120m/s.

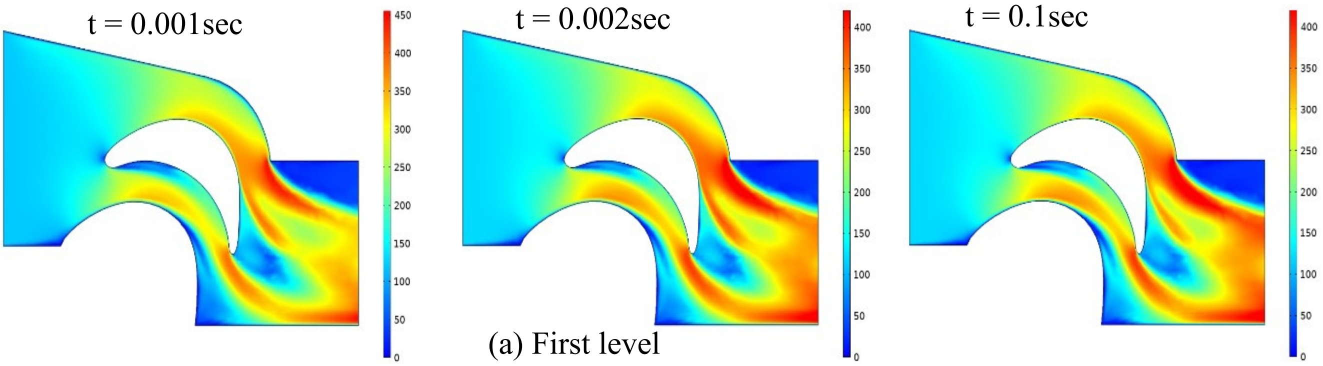

(a) First level

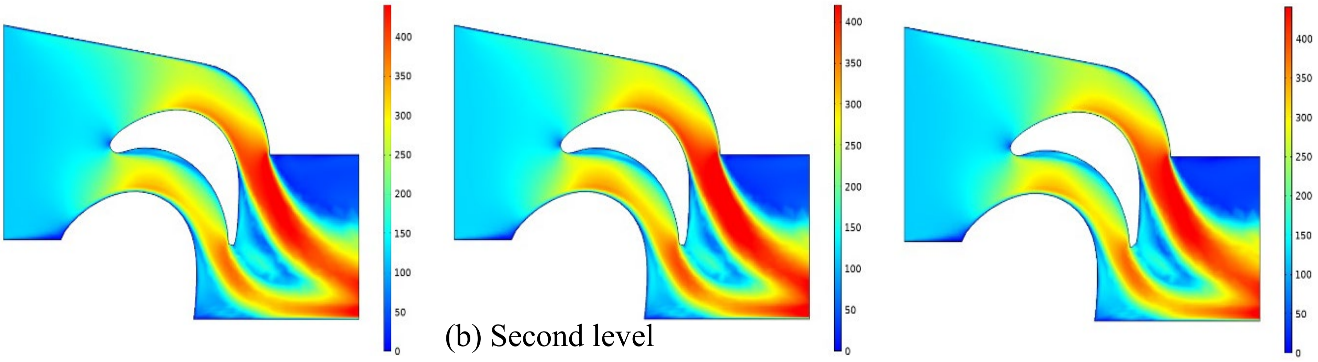

(b) Second level

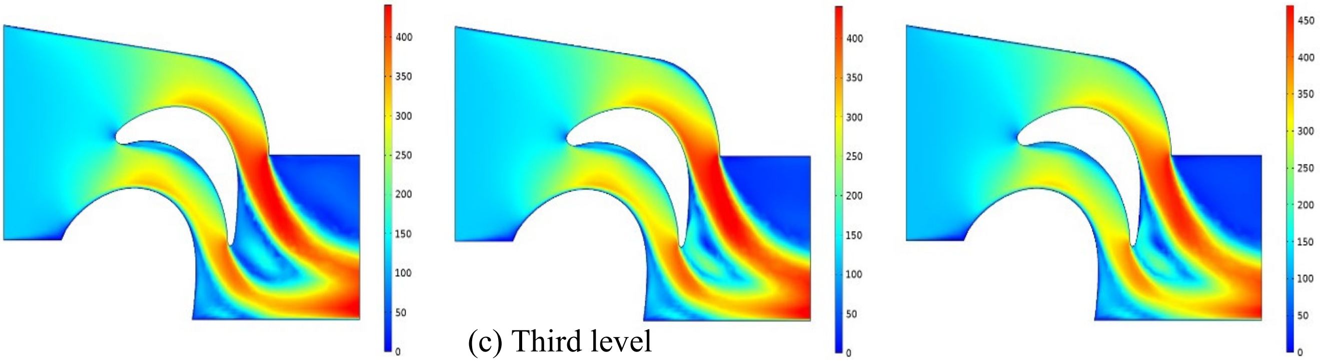

(c) Third level

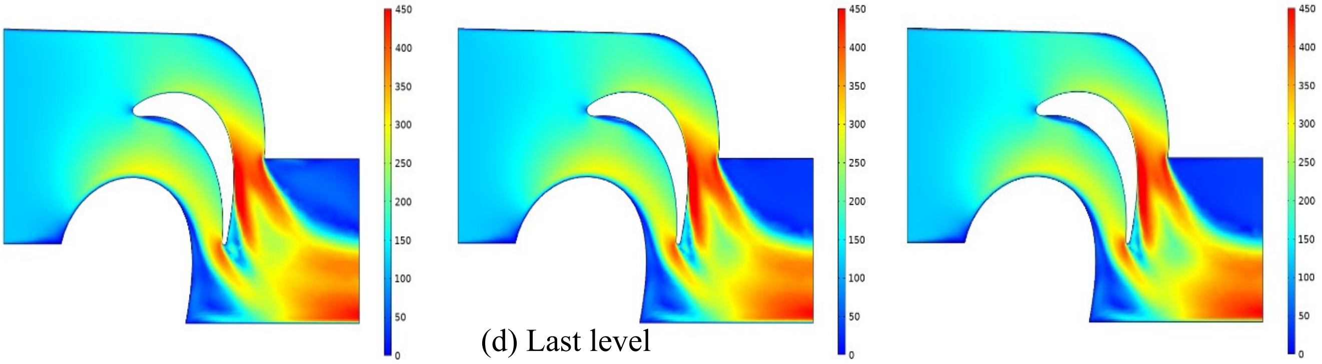

(d) Last level

Fig. 5-22: body contour of velocity distribution at 9Hz and inlet velocity 120m/s.

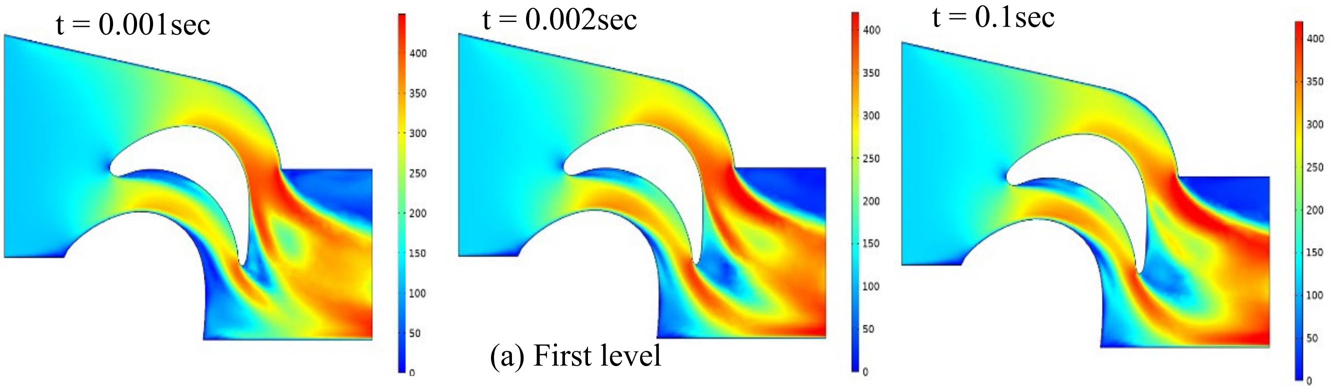

(a) First level

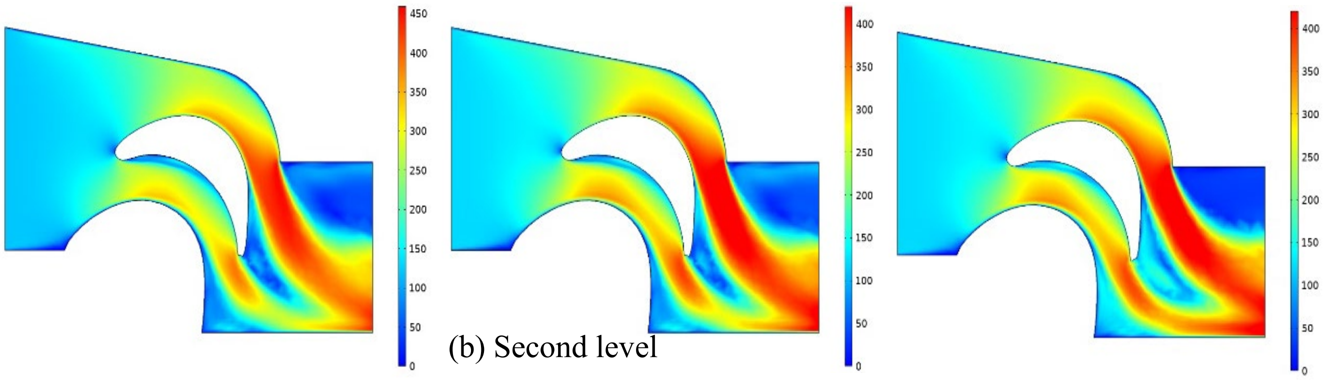

(b) Second level

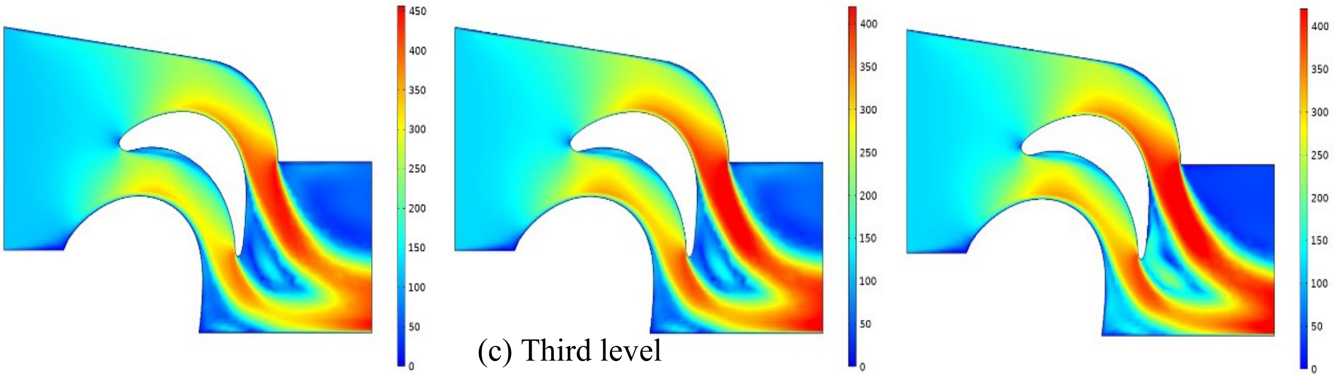

(c) Third level

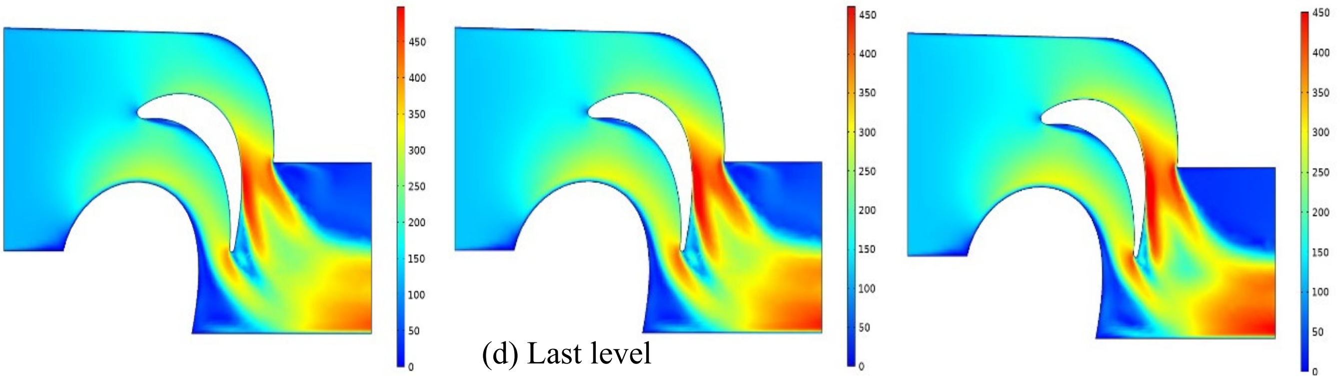

(d) Last level

Fig. 5-23 : body contour of velocity distribution at16Hz and inlet velocity 120m/s.

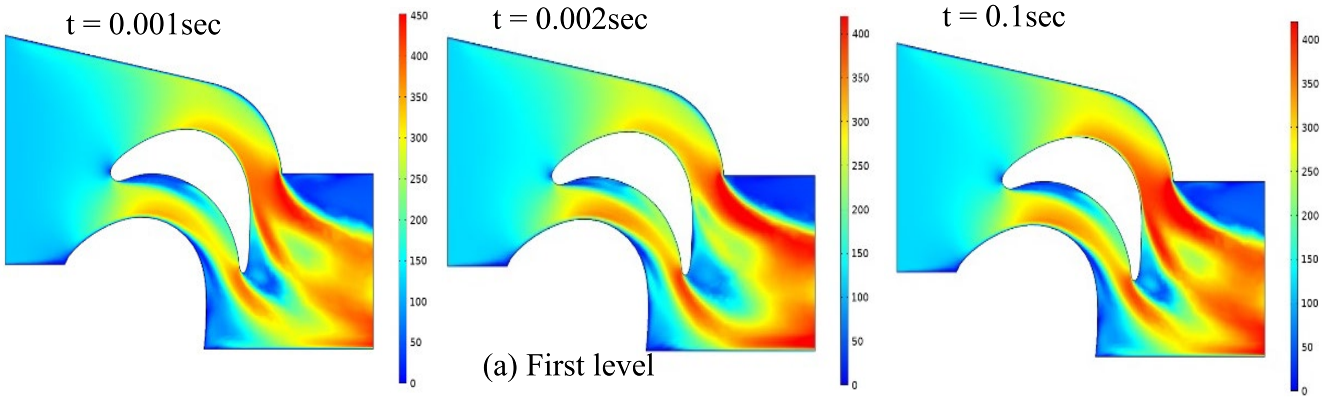
t = 0.001sec

t = 0.002sec

t = 0.1sec

(a) First level

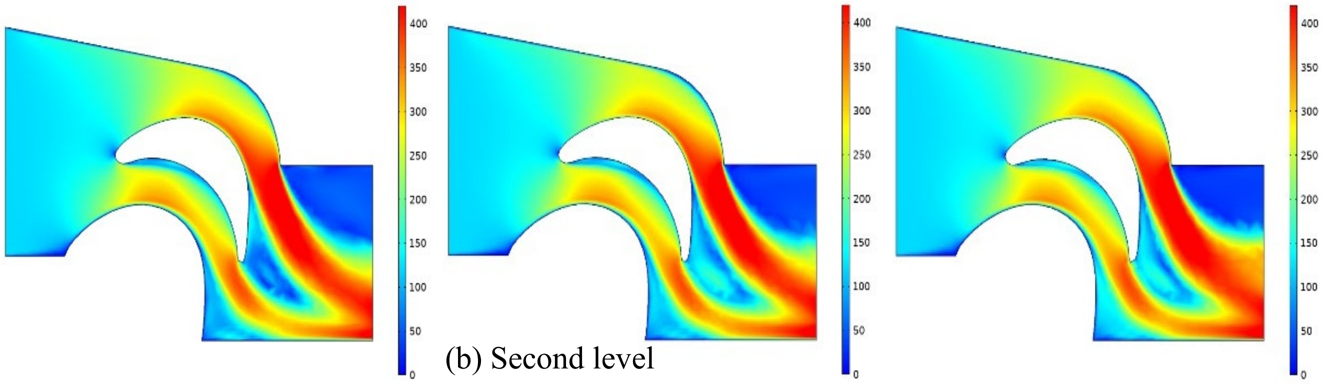

(b) Second level

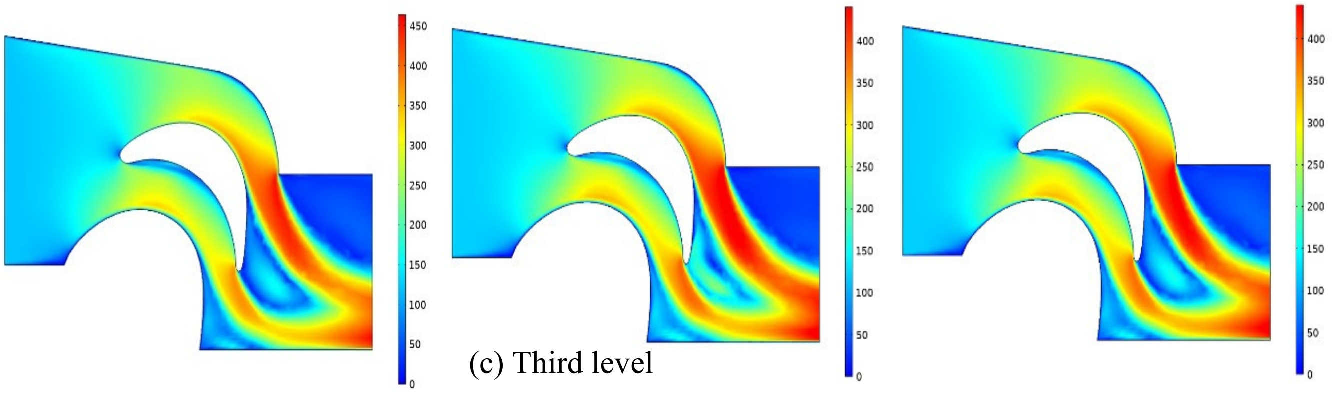

(c) Third level

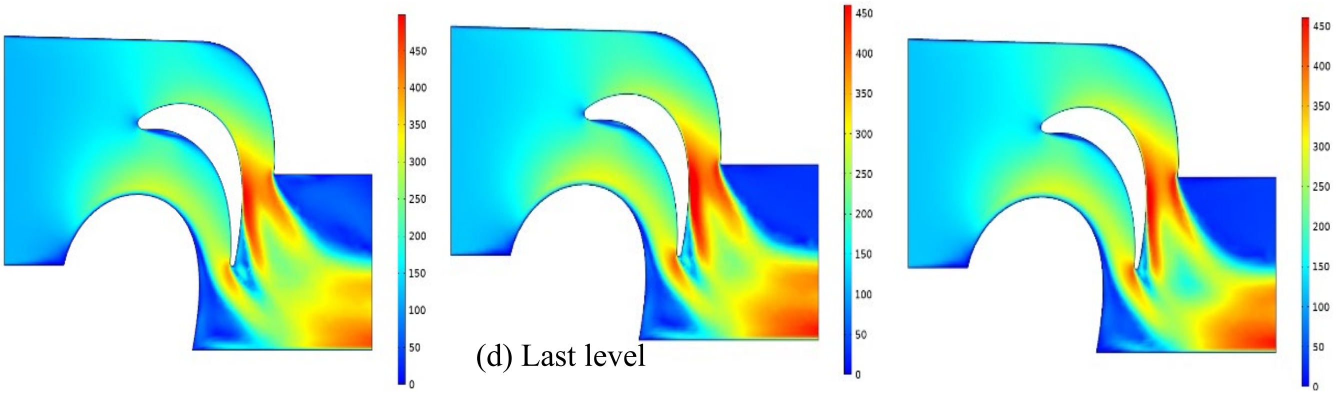

(d) Last level

Fig. 5-24: body contour of velocity distribution at 23Hz and inlet velocity 120m/s.

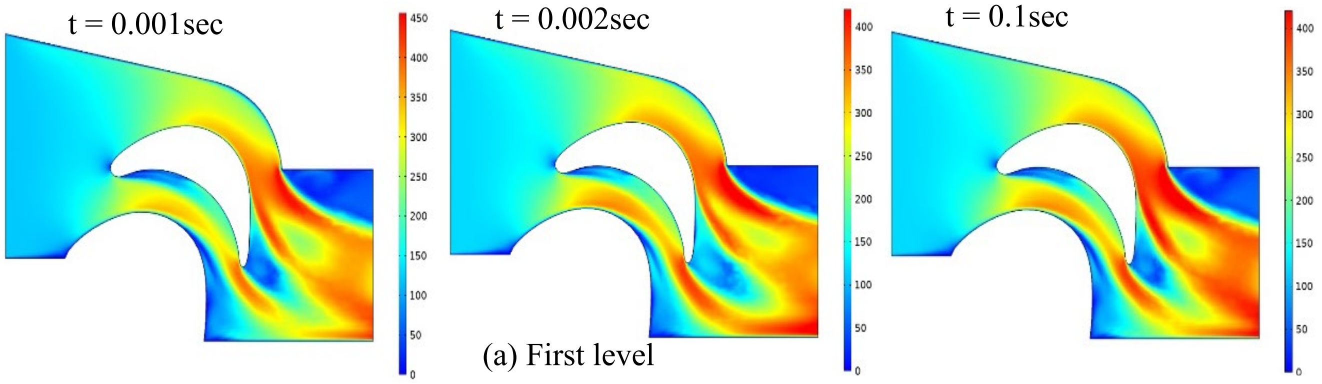

(a) First level

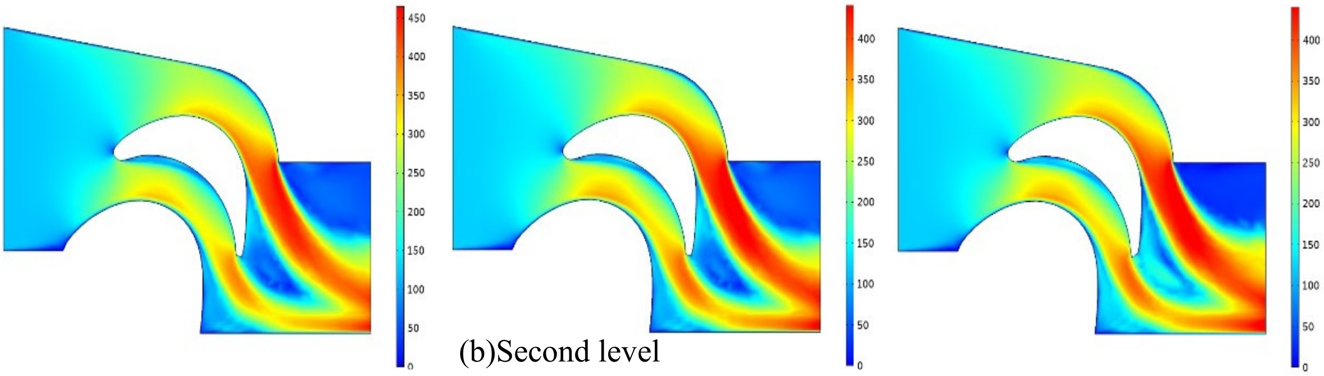

(b)Second level

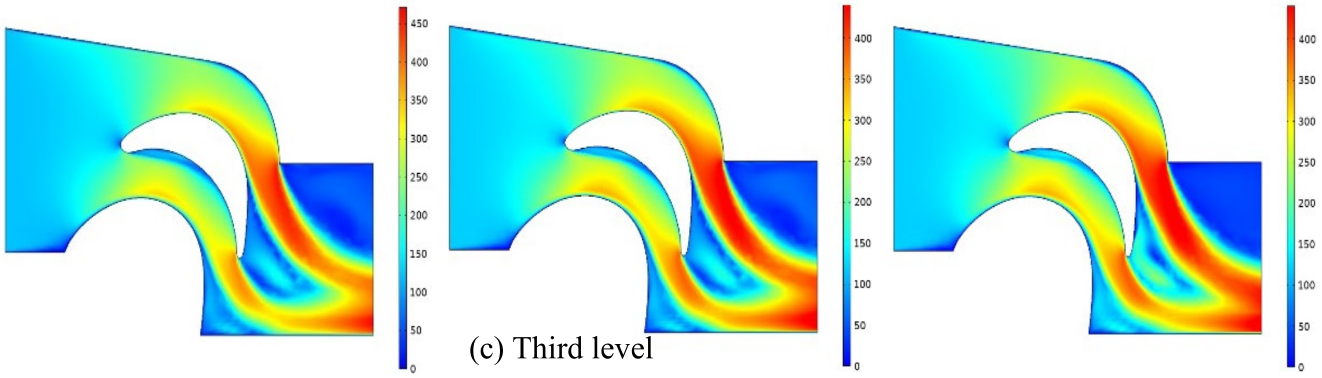

(c) Third level

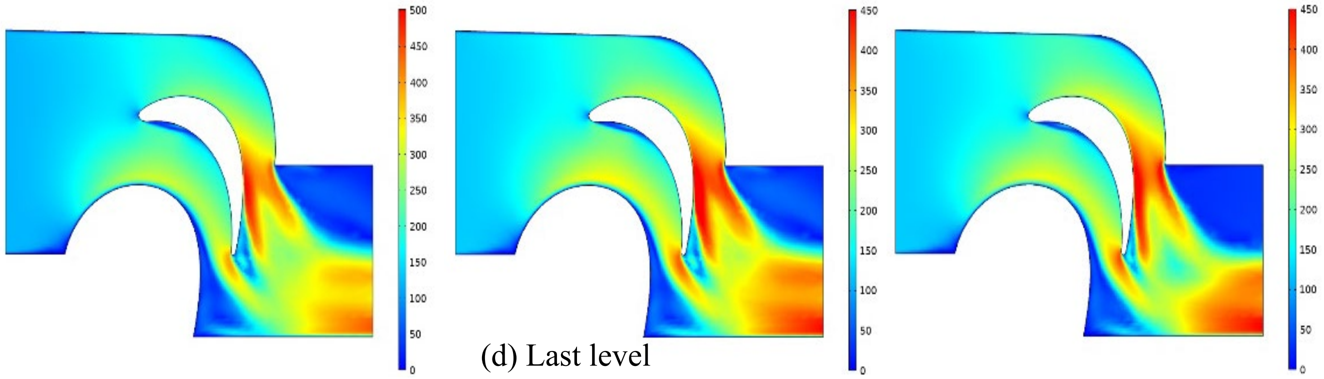

(d) Last level

Fig. 5-25: body contour of velocity distribution at 33 Hz and inlet velocity120m/s.

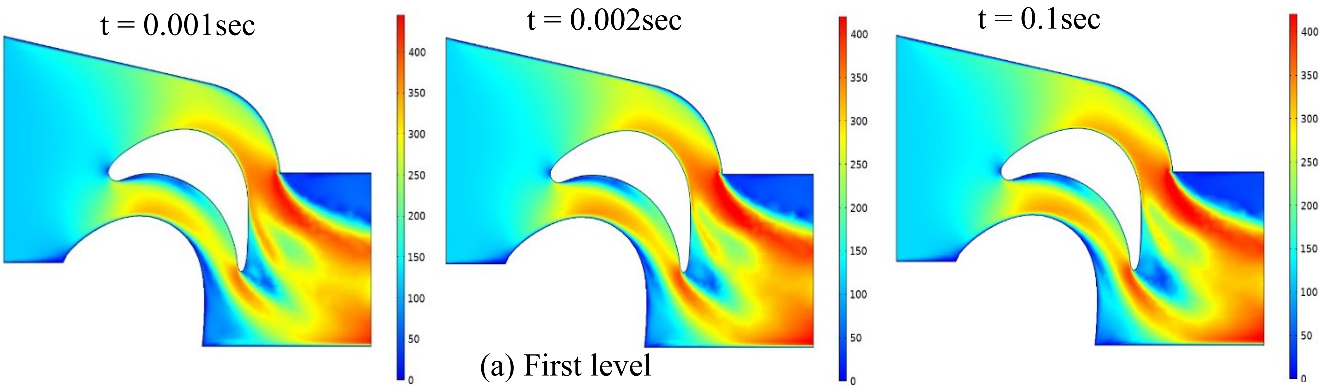

(a) First level

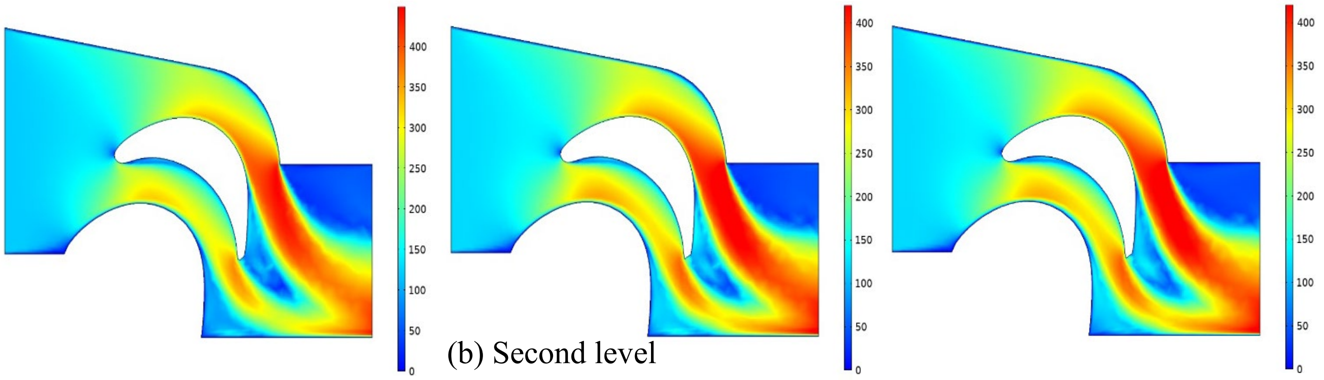

(b) Second level

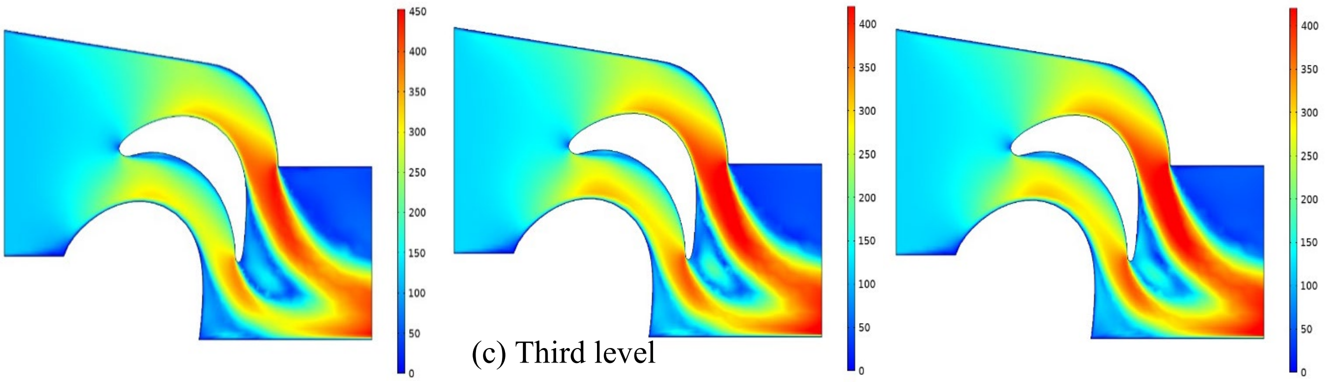

(c) Third level

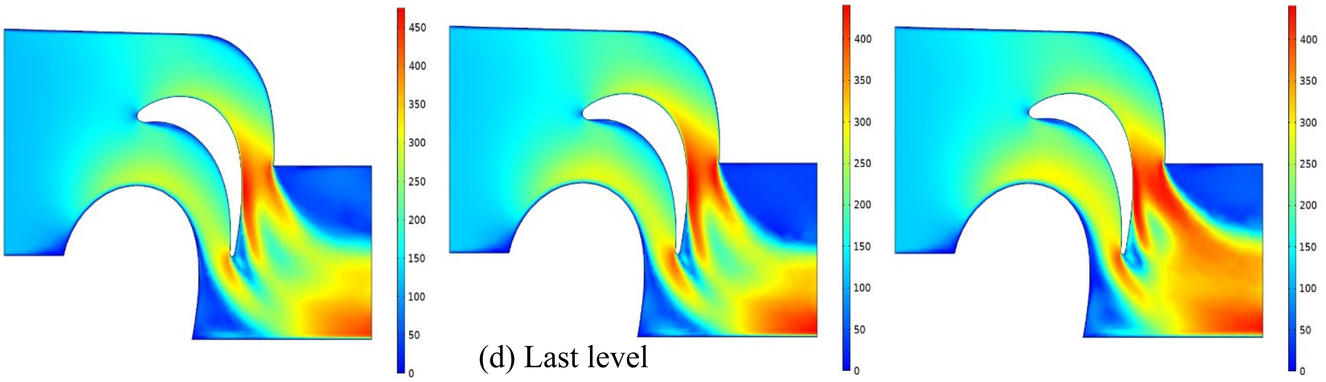

(d) Last level

Fig. 5-26: body contour of velocity distribution at 100 Hz and inlet velocity 120m/s.

5.4.1.2. Pressure Distribution around the Blade

Fig. 5-27 to Fig. 5-31 show the stages of fluid pressure distribution with time, where the subfigures in the left column show the stages of fluid pressure distribution for a specific time and the second column show the stages of fluid pressure distribution in the next time than the previous case to be almost stable with the progress of time as shown by the subfigures in the third column (right side) of the Fig. 5-27 which is identical to the column of the subfigures of the four horizontal sections in the same figure (zero vibration). The remaining figures show effect of vibration on the fluid pressure distribution in the numerical model. Vibration decreases the fluid pressure and it is noticeable in the third column on the right, where it is noticed a decrease in different regions and an increase in others.

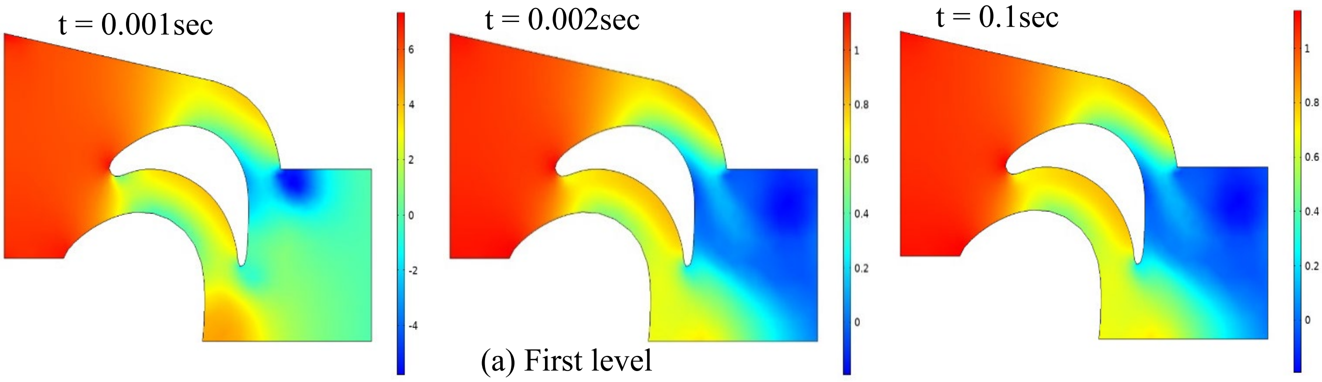

(a) First level

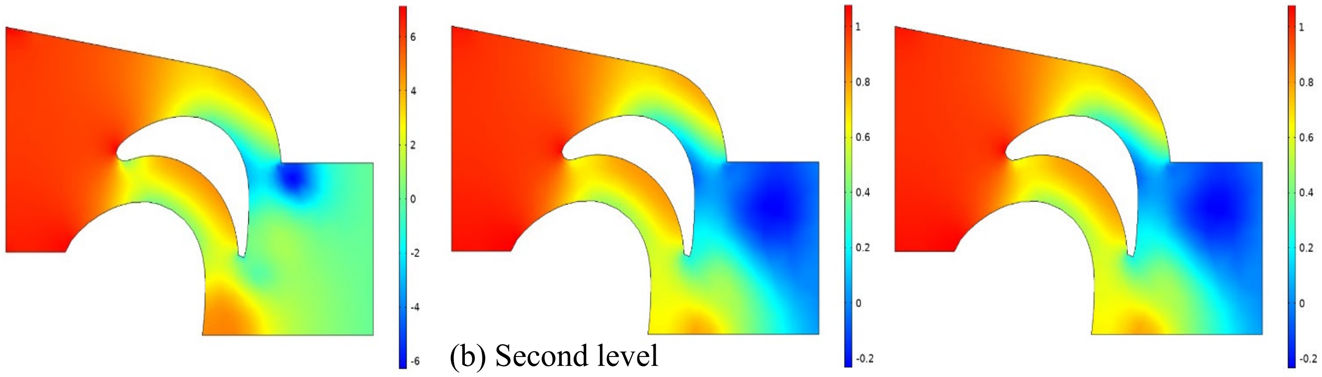

(b) Second level

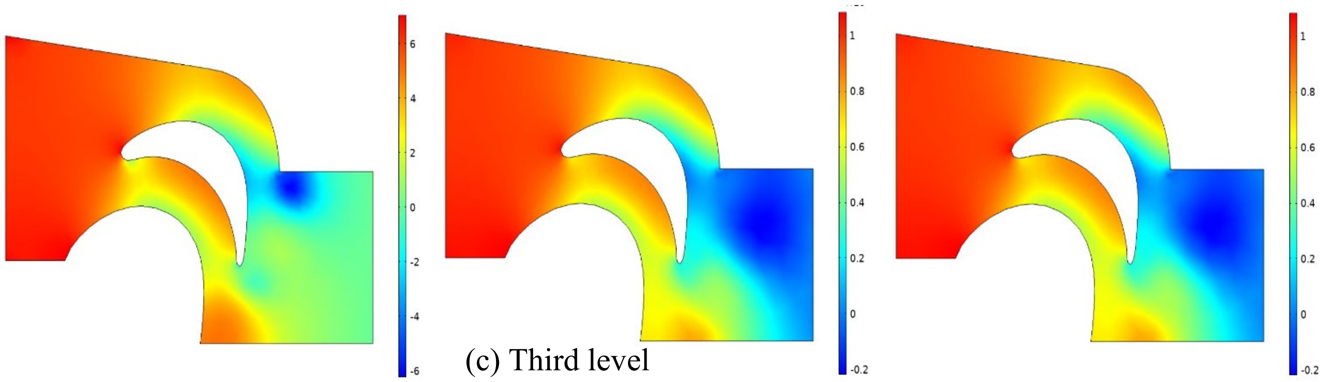

(c) Third level

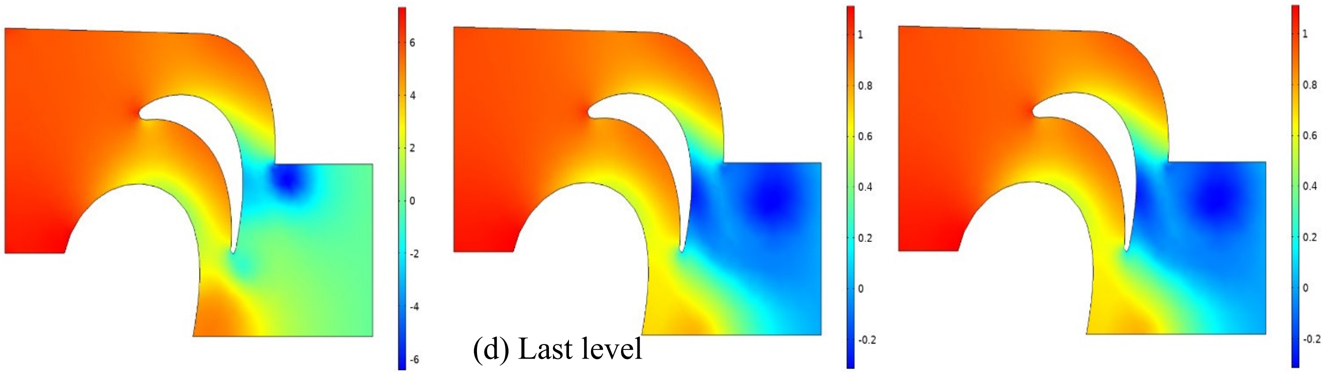

(d) Last level

Fig. 5-27: body contour of pressure distribution (×10^6pa) without vibration and inlet velocity 120m/s.

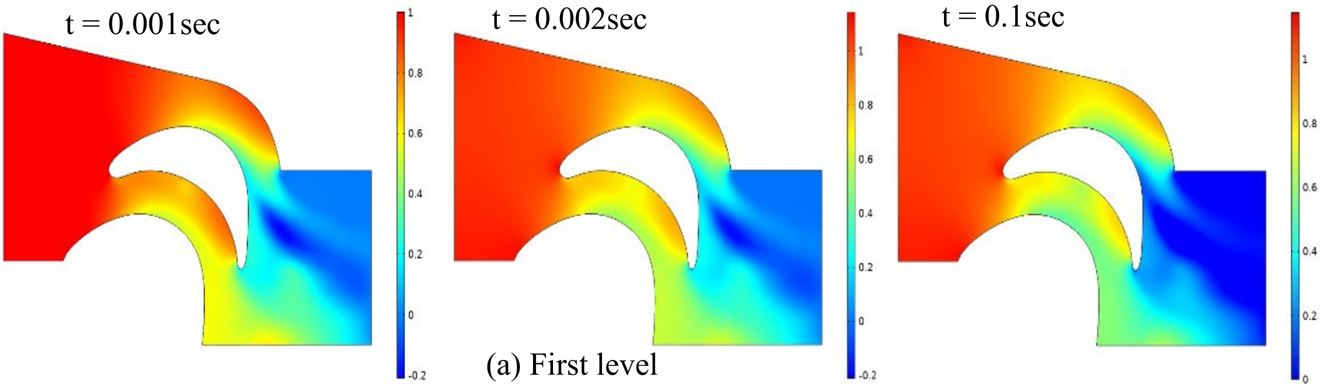

(a) First level

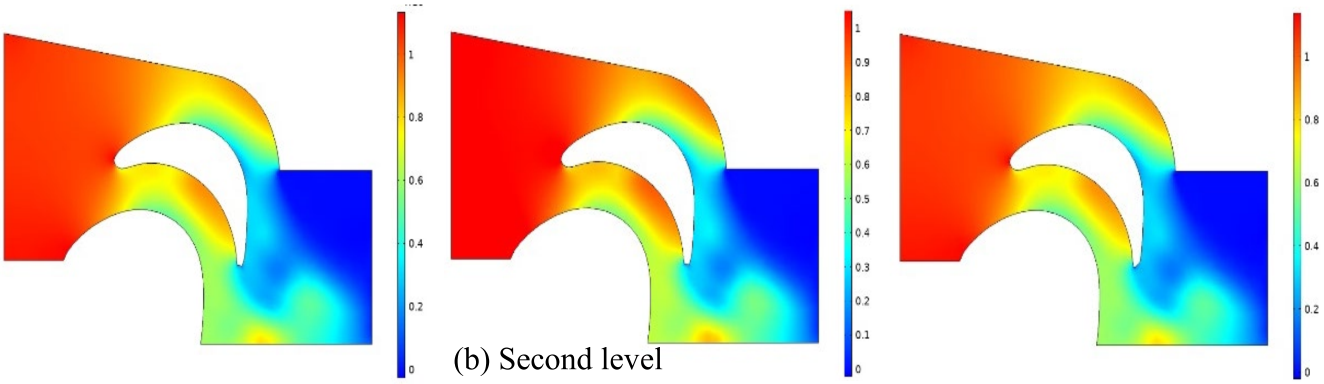

(b) Second level

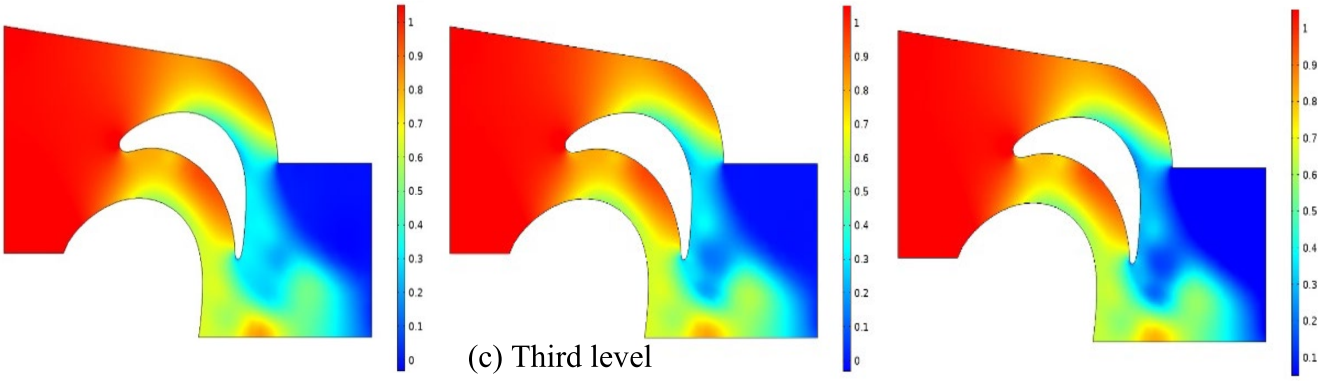

(c) Third level

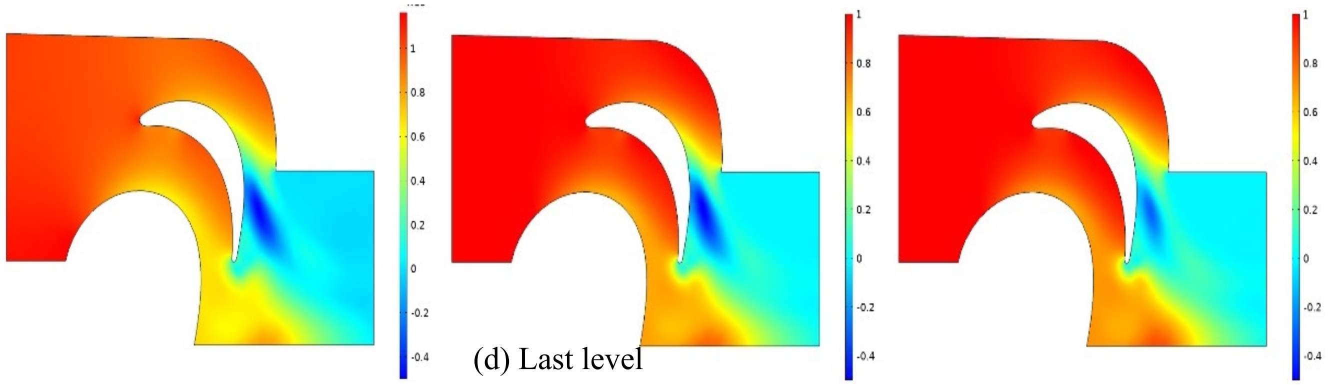

(d) Last level

Fig. 5-28: body contour of pressure distribution (×10^6pa) at 9Hz and inlet velocity120m/s.

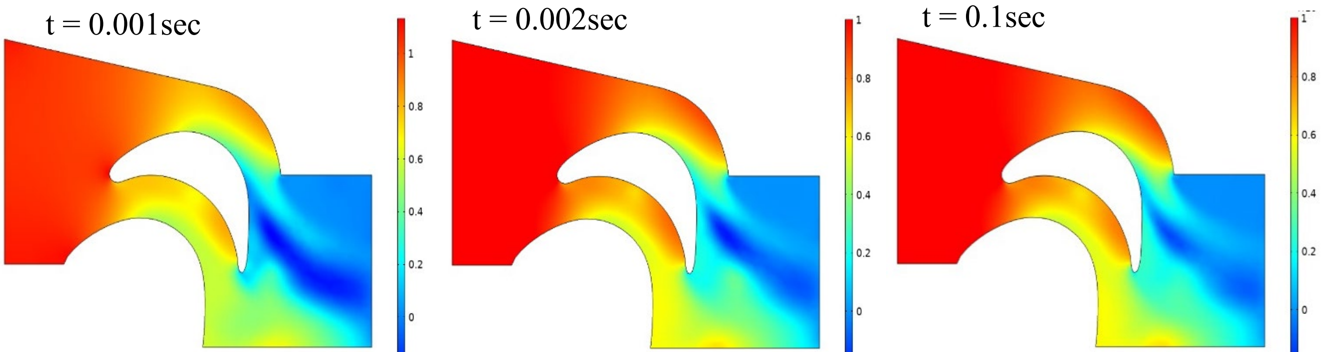

(a) First level

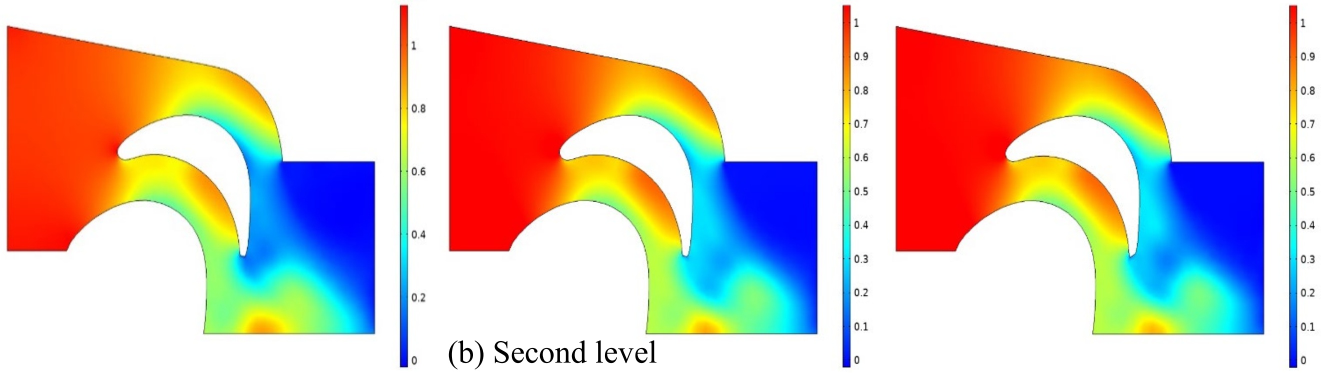

(b) Second level

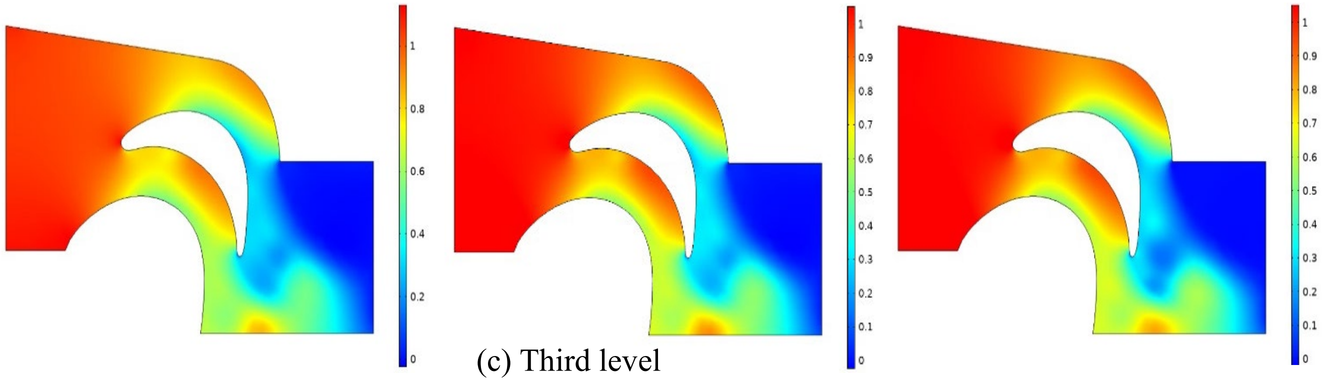

(c) Third level

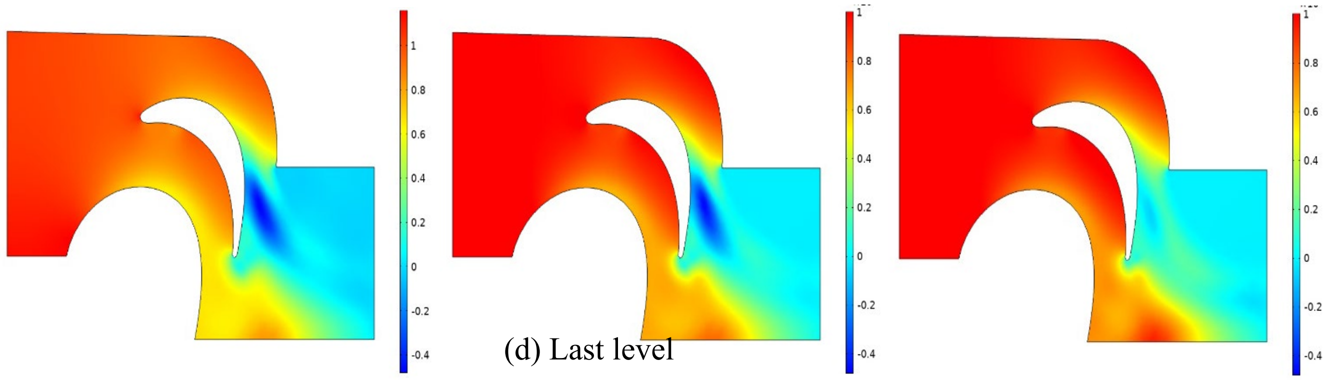

(d) Last level

Fig. 5-29: body contour of pressure distribution (×10^6pa) at 16Hz and inlet velocity120m/s

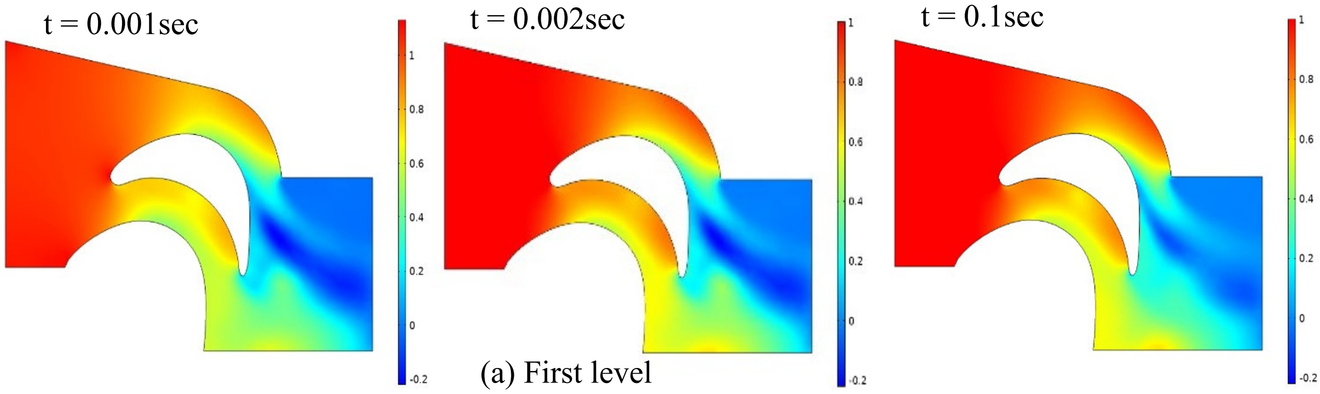

(a) First level

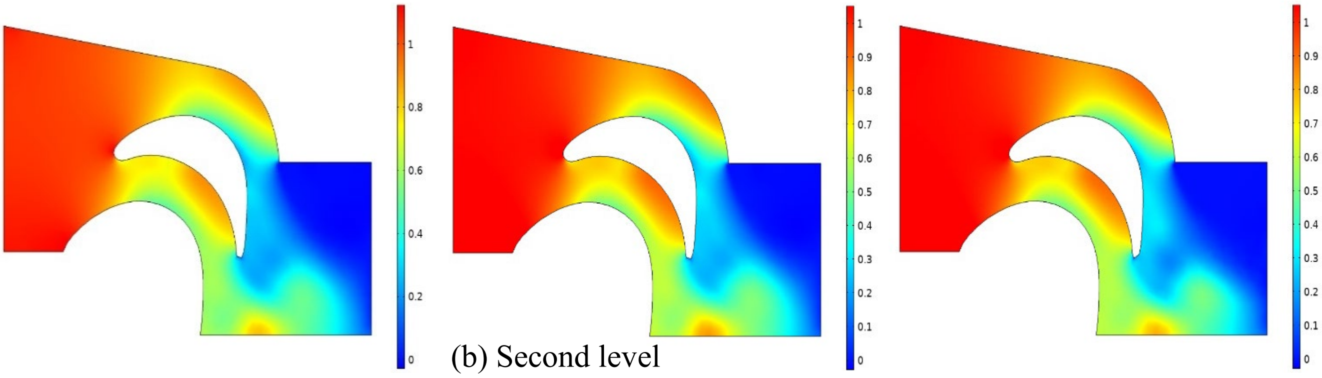

(b) Second level

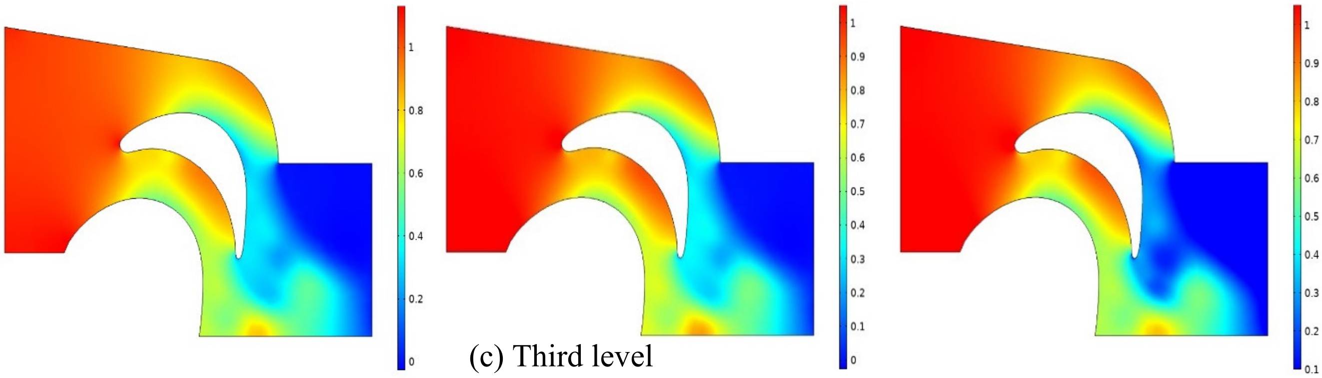

(c) Third level

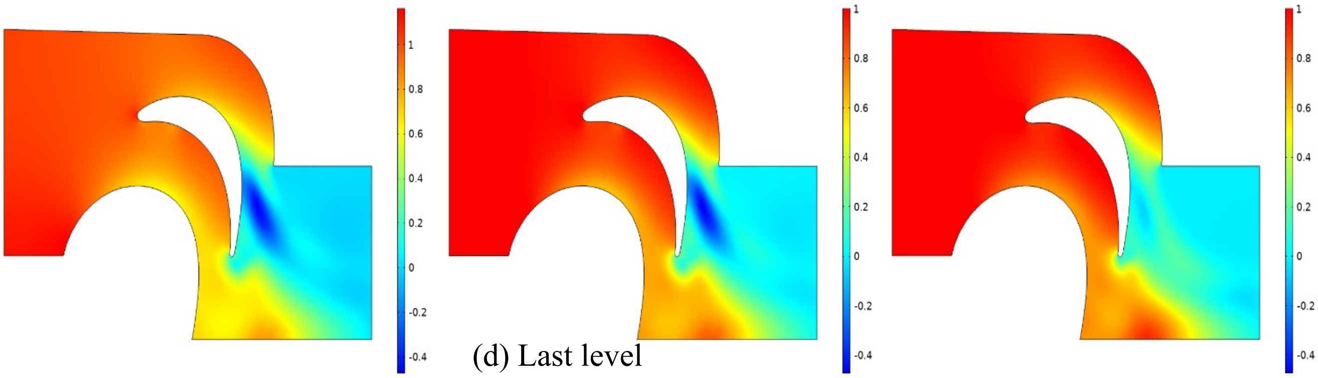

(d) Last level

Fig. 5-30: body contour of pressure distribution (×10^6pa) at 23Hz and inlet velocity120m/s.

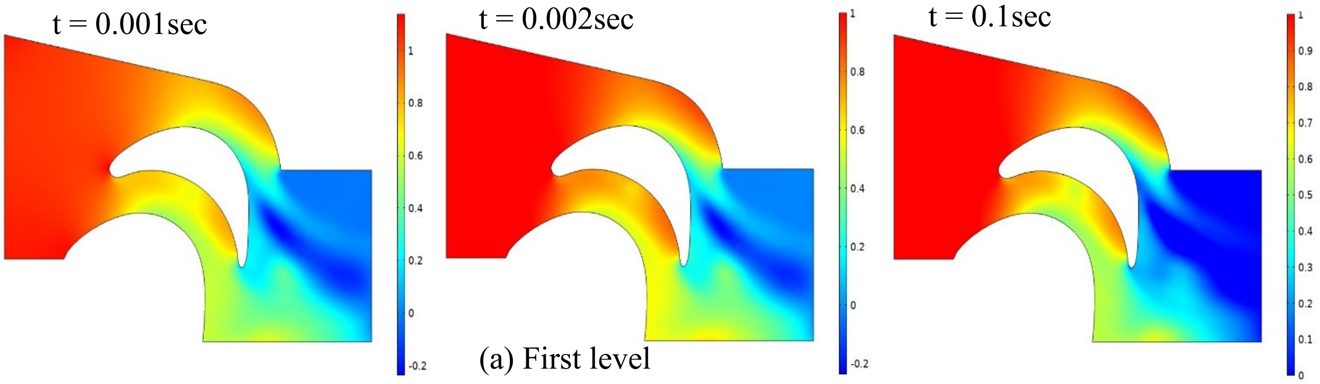

(a) First level

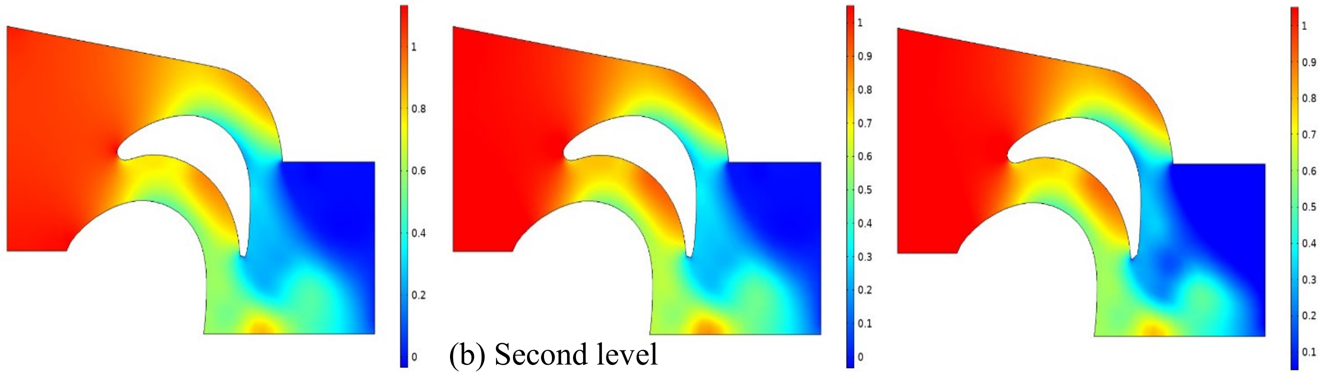

(b) Second level

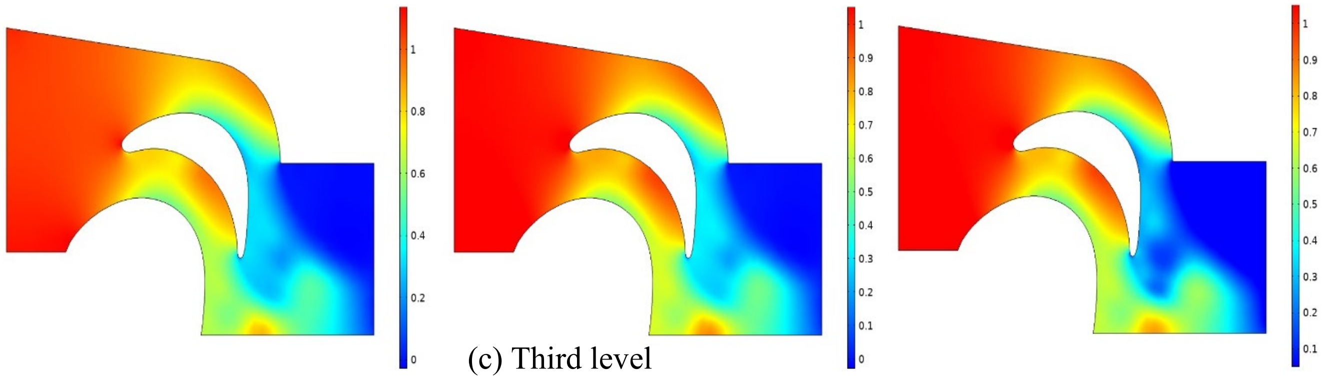

(c) Third level

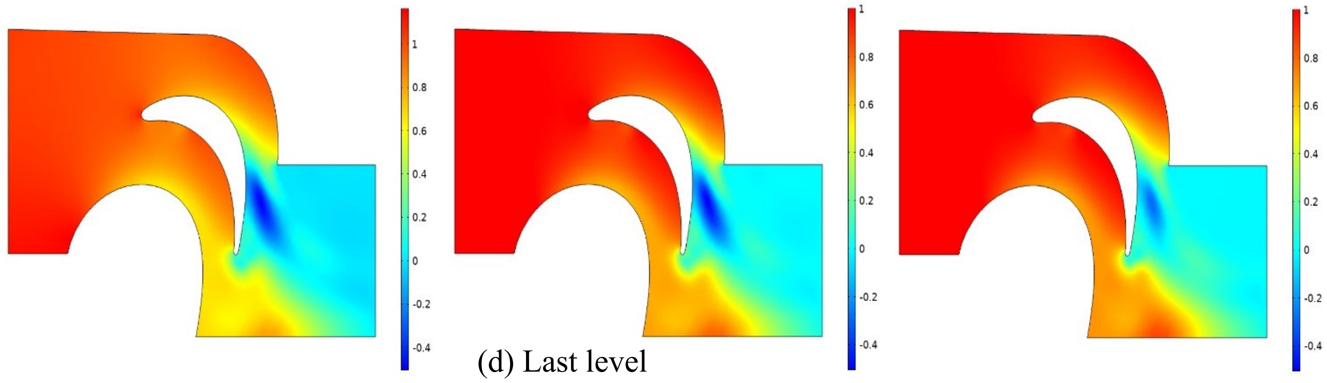

(d) Last level

Fig. 5-31: body contour of pressure distribution (×10^6pa) at 33Hz and inlet velocity 120m/s.

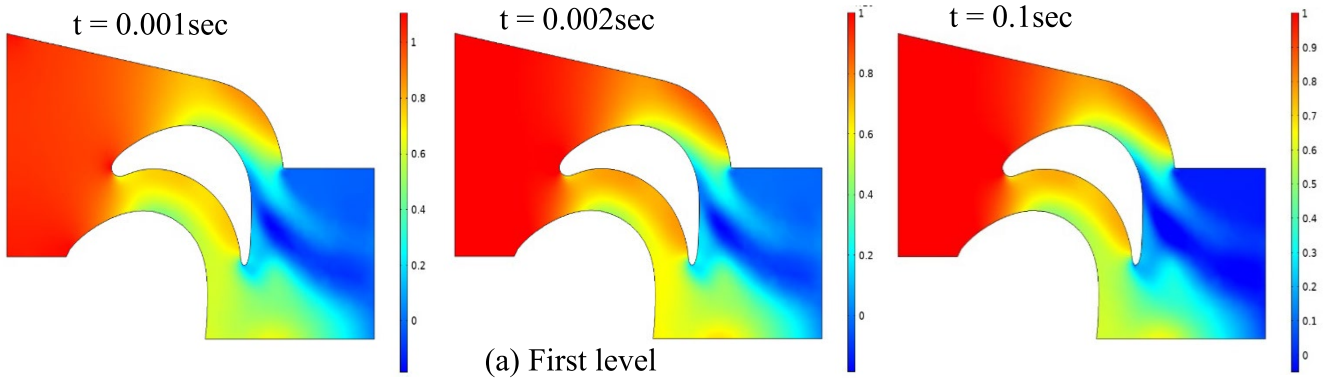

(a) First level

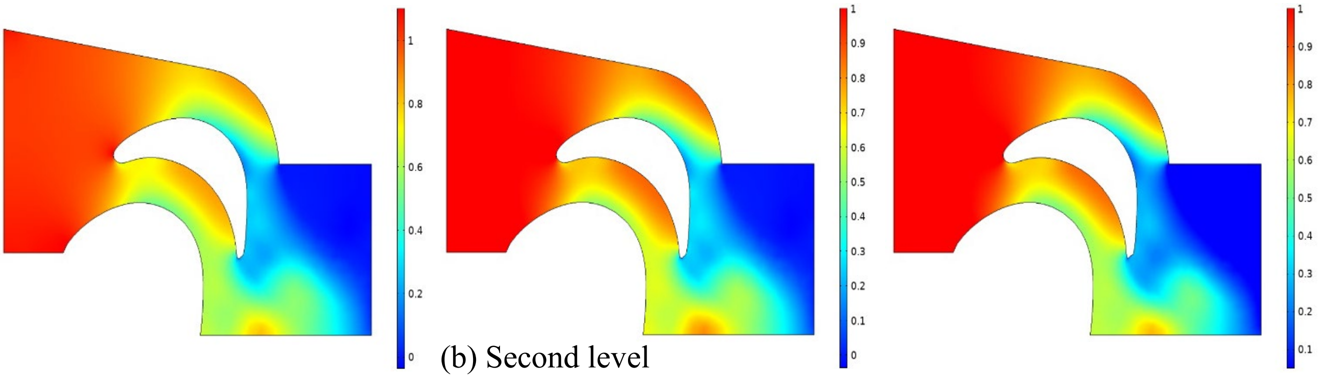

(b) Second level

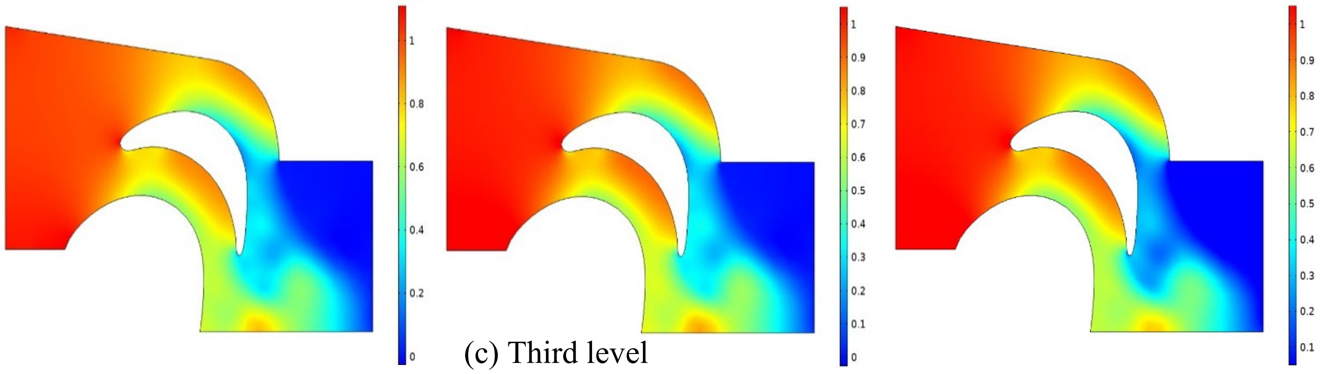

(c) Third level

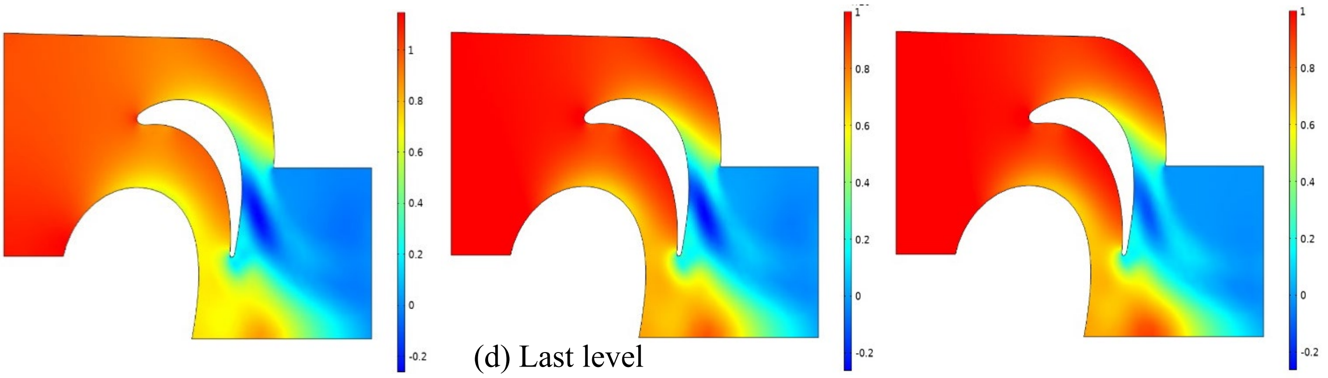

(d) Last level

Fig. 5-32: body contour of pressure distribution (×10^6pa) at 100Hz and inlet velocity 120m/s.

Fig. 5-33 shows the distribution of fluid velocity in the four vertical sections on the root of the blade, which shows the amount of that velocity in the form of contour lines at each of its values. The first column on the left of the figure represents the effect of segment (vertical section) position change from the chord at each level of vibration, and each row of the figure represents the effect of vibration variation on the section.

The fluid has a behavior similar to what was mentioned in the numerical simulation of the experimental work, but it is noticed an increase in the velocity of the fluid entering (120m/sec) the rotating turbine, and there is an increase in the disturbances of the velocity and pressure distribution lines as shown in figure 5-34. This means an increase in the generation of eddies in the flow field generated from near the blade surface. The effect of vibration is evident in the first and second row, and less in the third and fourth row.

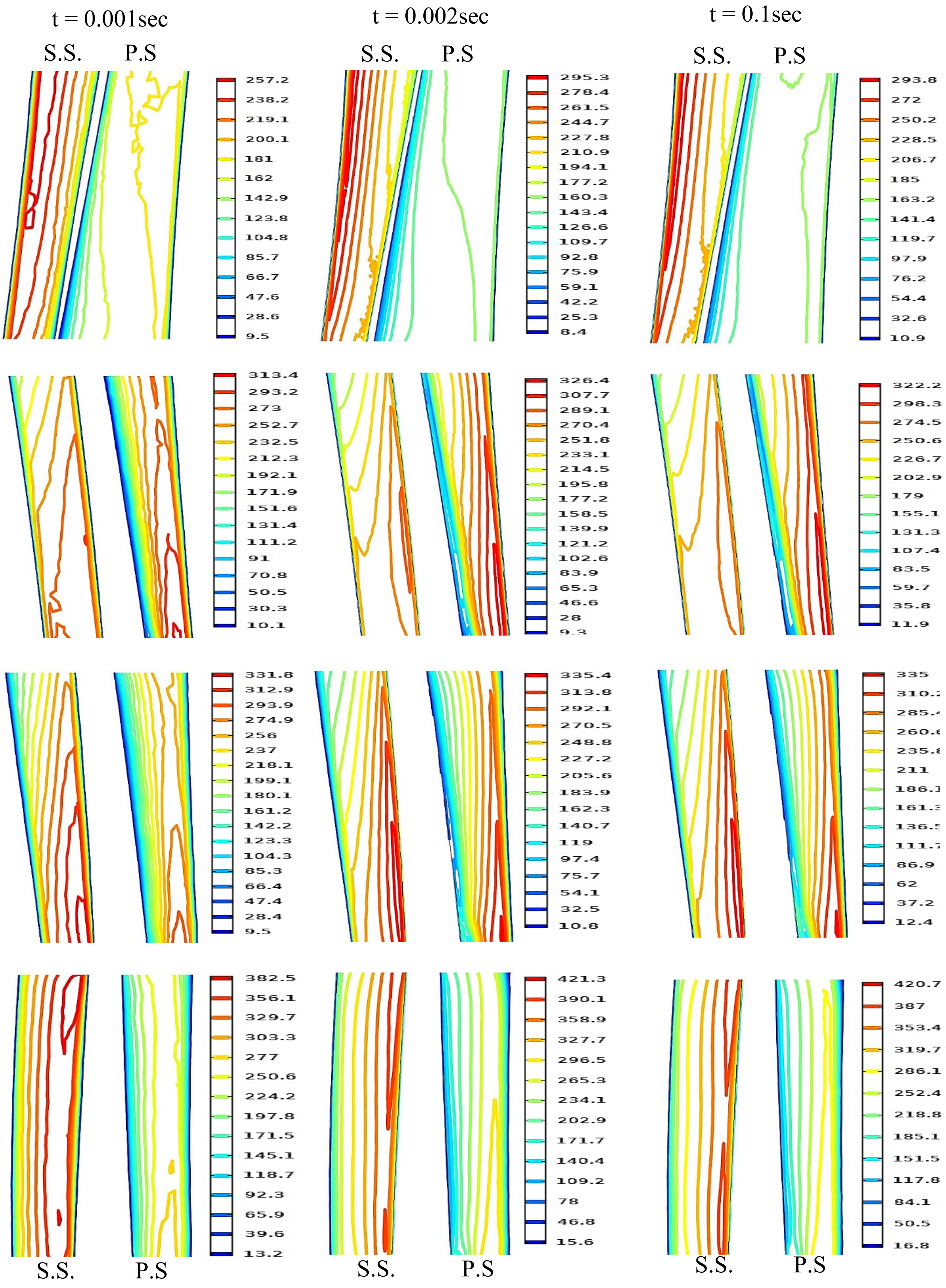

(a) 0 Hz (b) 9 Hz (c) 16 Hz

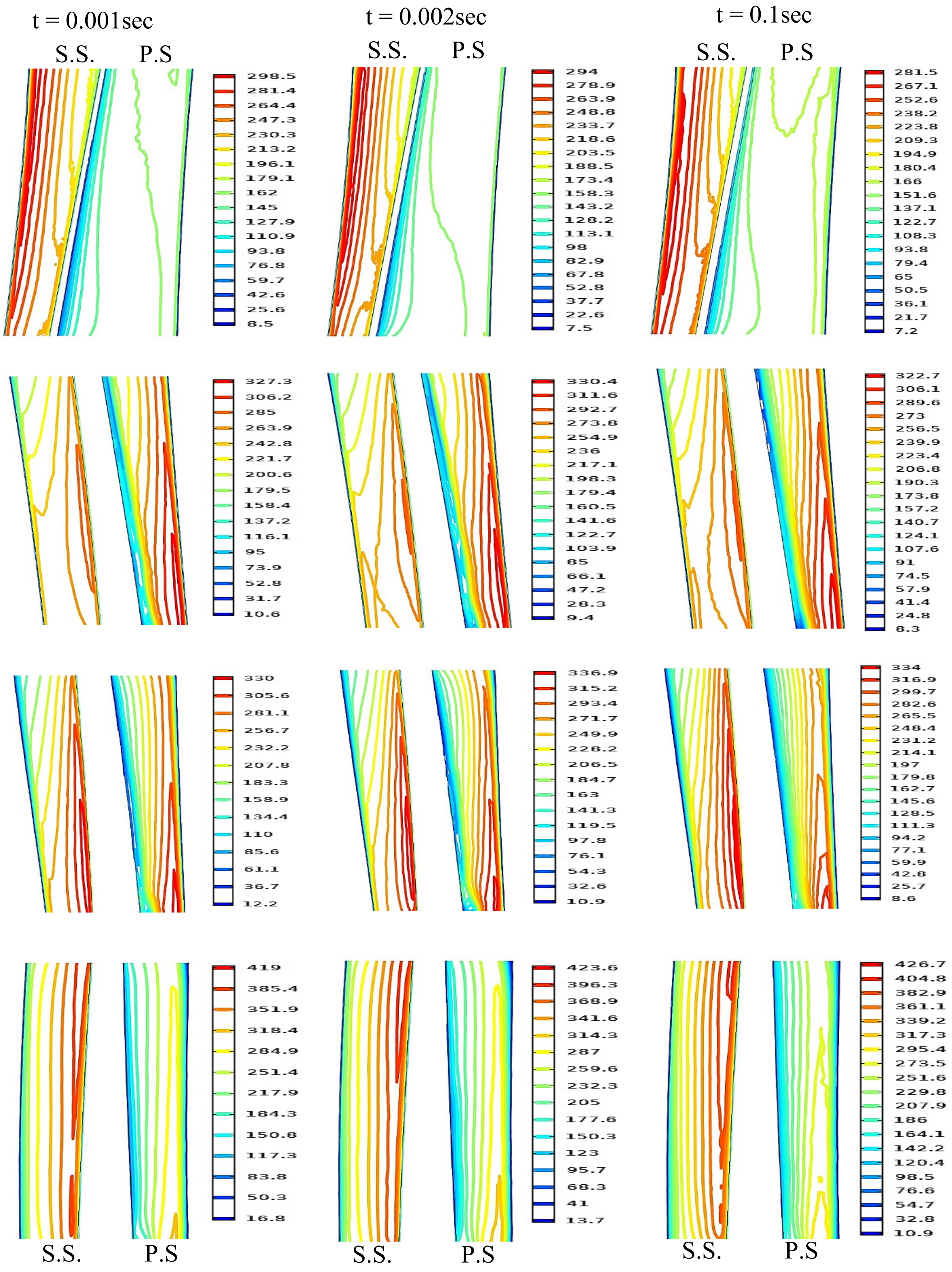

(d) 23 Hz (e) 33 Hz (f) 100 Hz

Fig. 5-33: velocity distribution for vertical segment under effect of vibration at 120m/s.

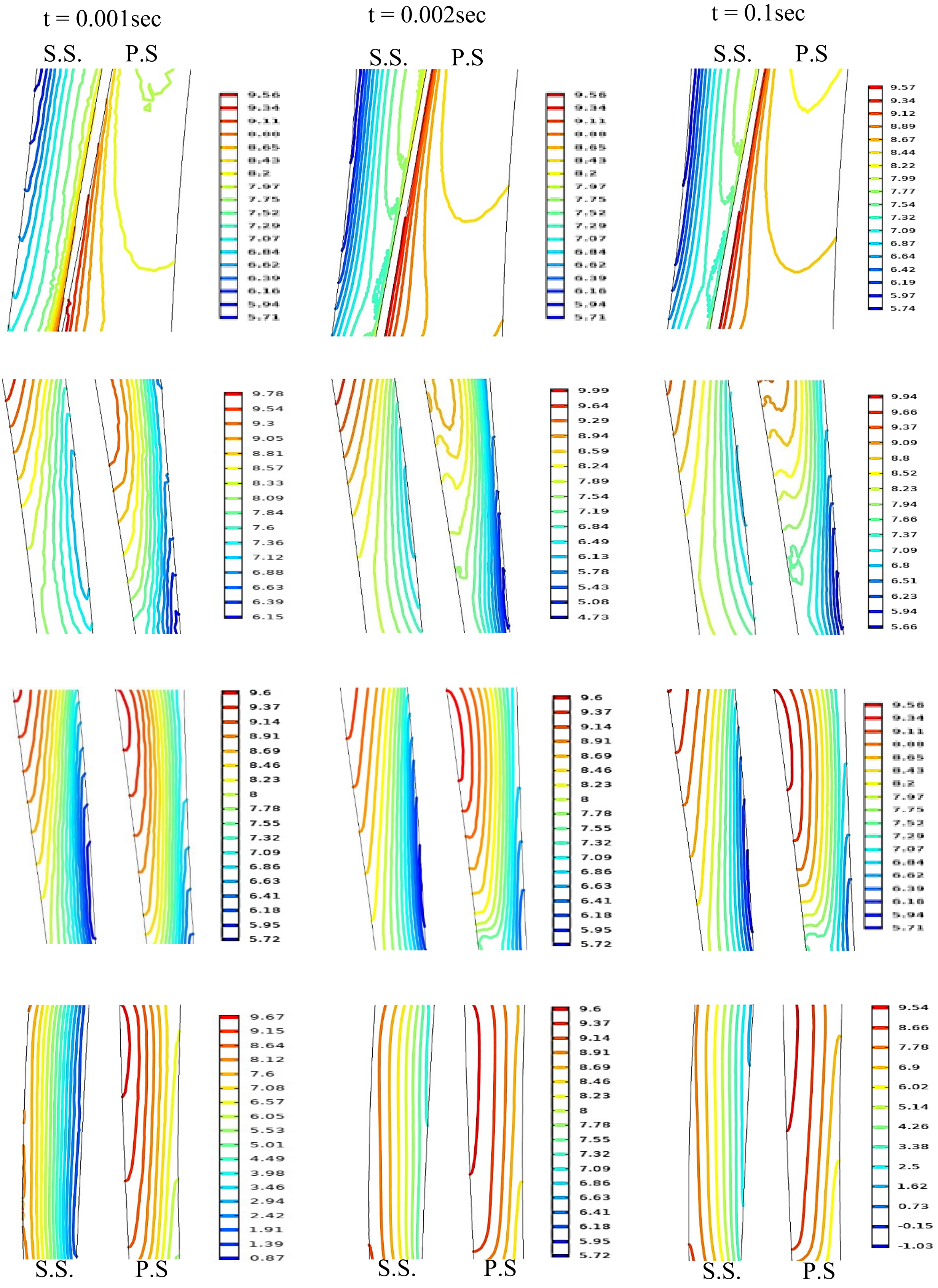

(a) 0 Hz (b) 9 Hz (c) 16 Hz

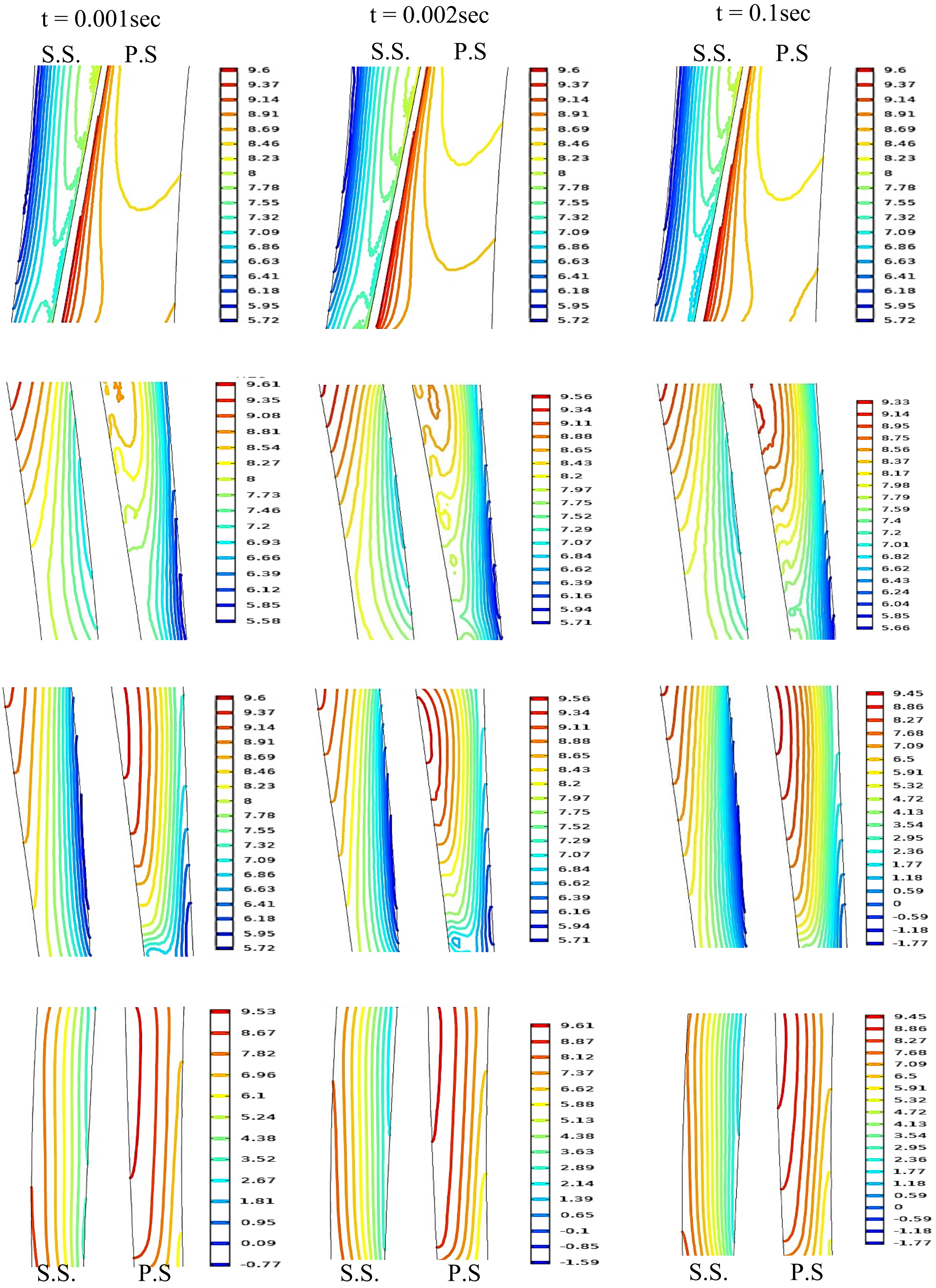

(d) 23 Hz (e) 33 Hz (f) 100 Hz

Fig. 5-34: pressure distribution ($\times10^5$pa) for vertical segment under effect of vibration at 120m/s.

5.4.2.Horizontal Vibration Effect on the Blade

In this part, the effect of vibration is studied for the same previous values and amplitude of vibration, but in a parallel direction to the base.

5.4.2.1. Effect of Vibration Direction on Velocity and Pressure Distribution

Fig. 5-35 and Fig. 5-36 represent the distribution of fluid velocity and pressure, respectively, in the horizontal section parallel to the root of the blade at a height of 6 mm from the base. Subfigure (a) to (f) represent the case of external vibration applied to the blade with vibration values starting from 0 to 100 Hz and an input velocity of 22 m/s. The column in the figure show the effect of time and the vibration from top to bottom on the same level. The first and second subfigure show the stages of progress of the fluid velocity and pressure distribution with time. The next three subfigures represent the effect of vibration on the fluid for three different locations of the blade. The third subfigure in one column when the blade is at its maximum vibration amplitude position. The fourth subfigure is the case when the blade returns to the starting point. The final subfigure is at the lowest point of the vibration amplitude that the blade reaches. The last three subfigures are identical due to the zero vibration.

One row of all subfigures gives the effect of vibration at one level during the same time period of the numerical study. The effect of vibration increases with an increase in its amplitude as seen from Fig. 5-35 to Fig. 5-35.

Effect of vibration is smaller after an increasing the vibration frequency 33 to 100 Hz. Effect of the movement of the blade on the distribution of fluid velocity by increasing the amount of that velocity at the suction region in case of the rise of the blade towards that region and decreasing the area of high velocity at the pressure region, which in turn leads to an increase in pressure at the pressure side and a decreasing at the suction side. Nevertheless, in the case of the descent of the blade towards the pressure region, the area of high velocity at the pressure region increases, and this leads to decreasing the pressures applied to the blade. The vortexes generated behind the blade are affected by the upper and lower motion due to vibration of the blade, which can be observed from the same row in the distribution forms of the velocity and pressure lines. In addition, the blade pushes the closed fluid upwards, which leads to an increase in the vertical velocity component of the fluid when the direction of the vibration is upward.

Fig. 5-37 and Fig. 5-38 show the distribution of fluid velocity and pressure around the blade for the second horizontal plane, 21 mm above the base. It shows the effect of changing the shape of the blade section on the fluid velocity and pressure distribution, as the high velocity values increase in similar regions in the first stage. As for the shape of the vortices generated behind the blade, it changes successively with the corresponding changes that occur in the fluid velocity distribution. It is also noted similar behaviors of the other levels. Where, the vortices formed in the area of the passage flow behind the blade are enlarged and their position is closer to the mid-span and the tip.

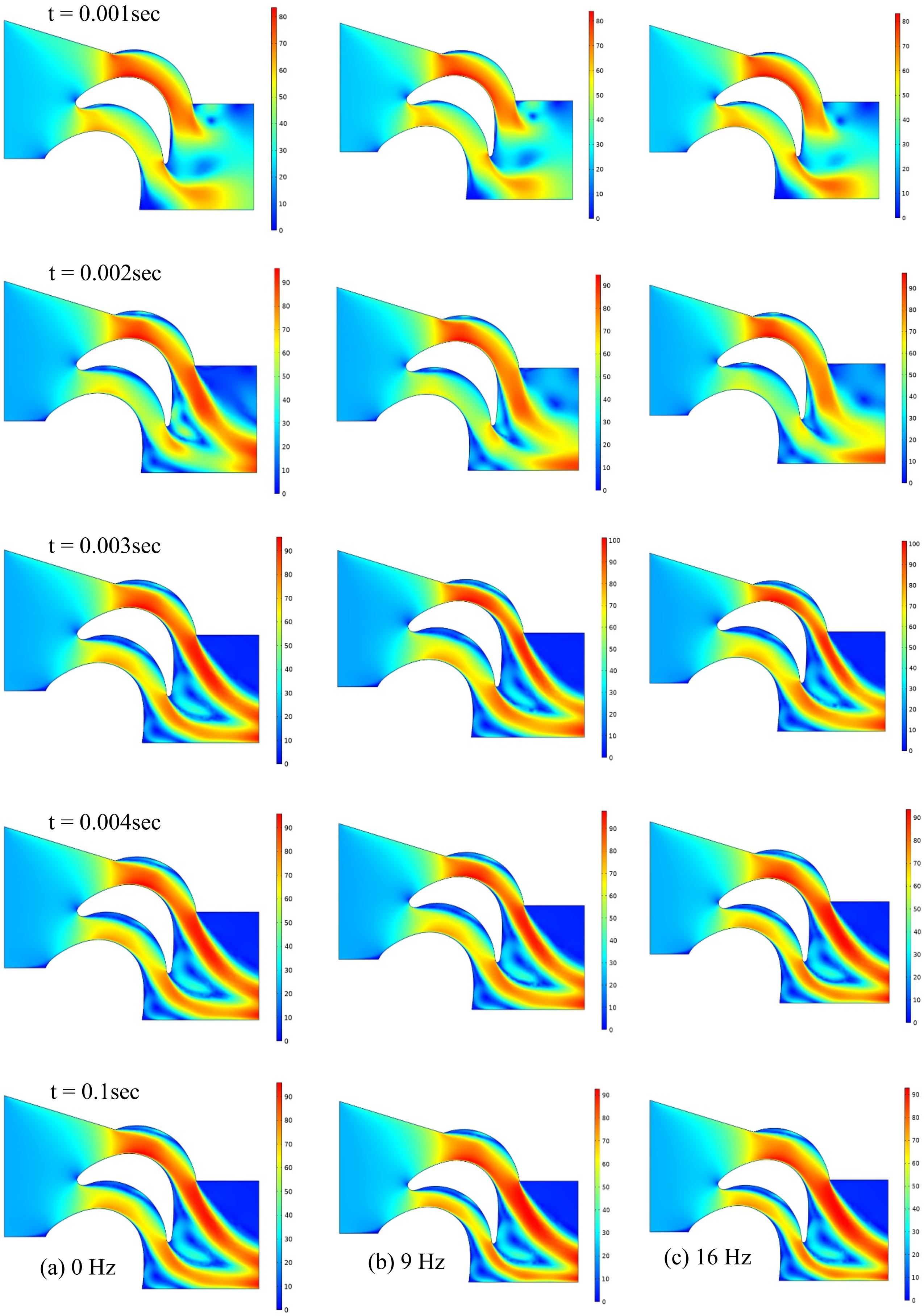
t = 0.001sec
t = 0.002sec
t = 0.003sec
t = 0.004sec
t = 0.1sec
(a) 0 Hz
(b) 9 Hz
(c) 16 Hz
0
10
20
30
40
50
60
70
80
90
100

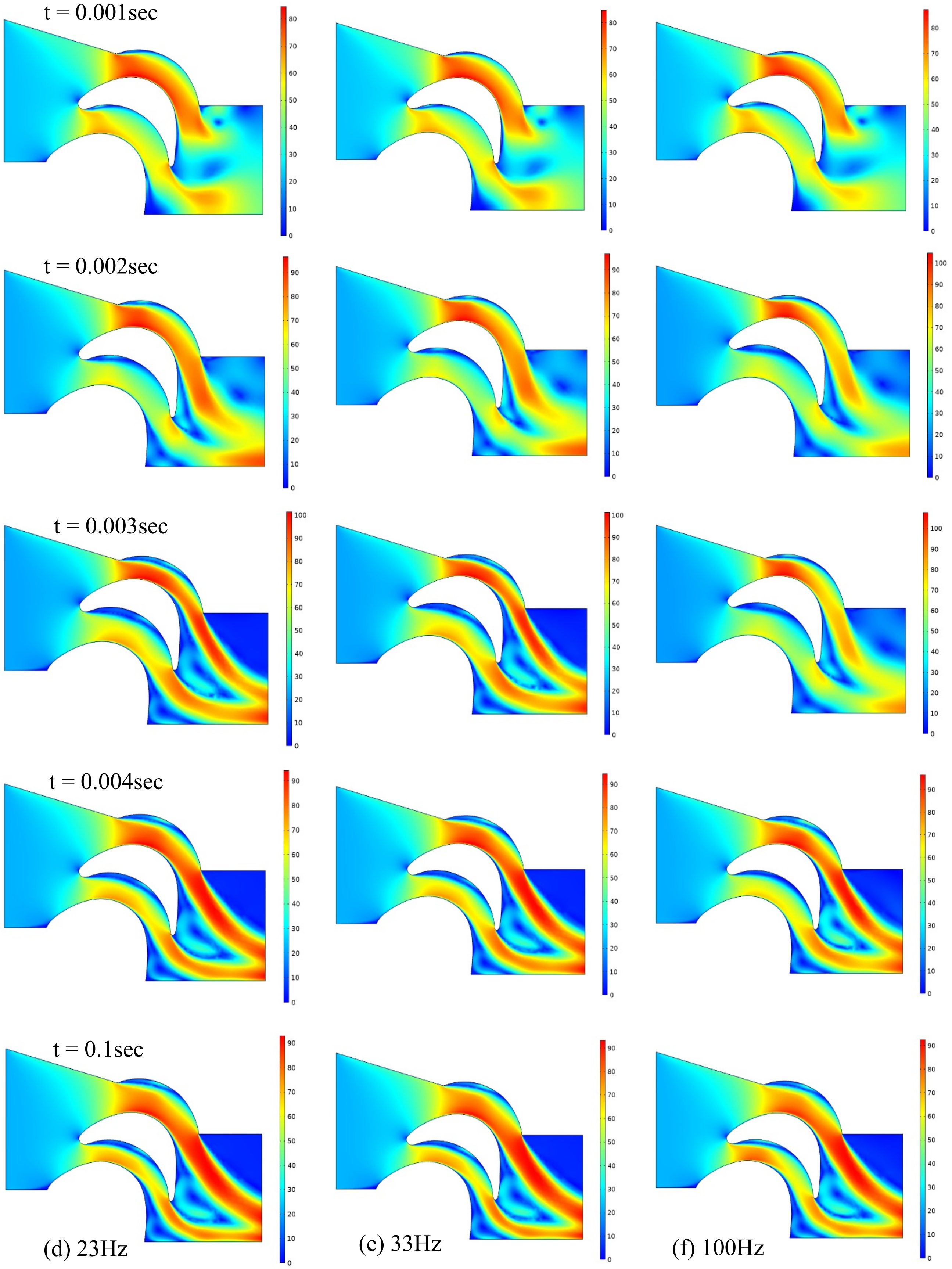

(d) 23Hz (e) 33Hz (f) 100Hz

Fig. 5-35: body contour of velocity distribution at first level with frequency (0 to 33) Hz and 22m/s.

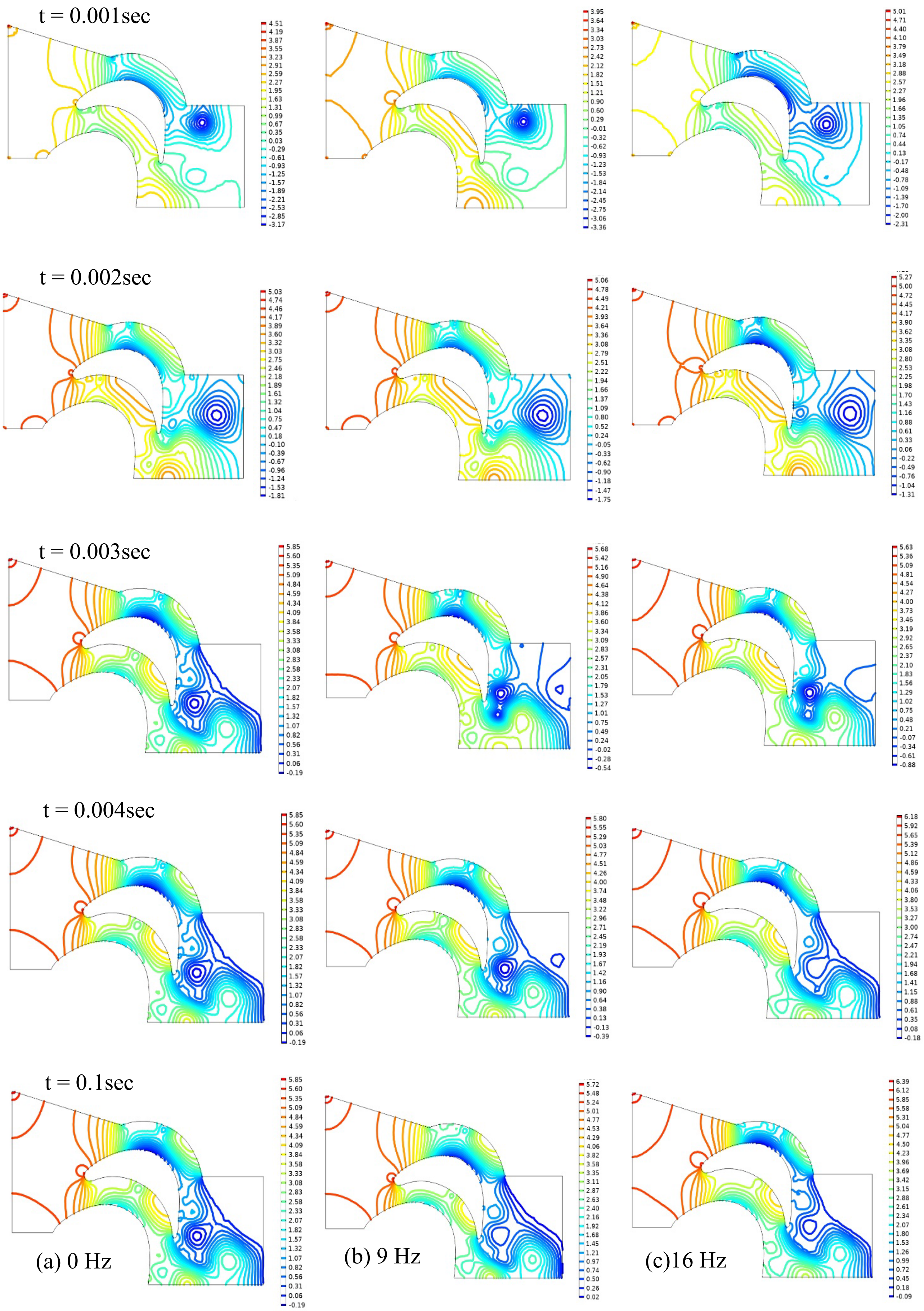

(a) 0 Hz (b) 9 Hz (c)16 Hz

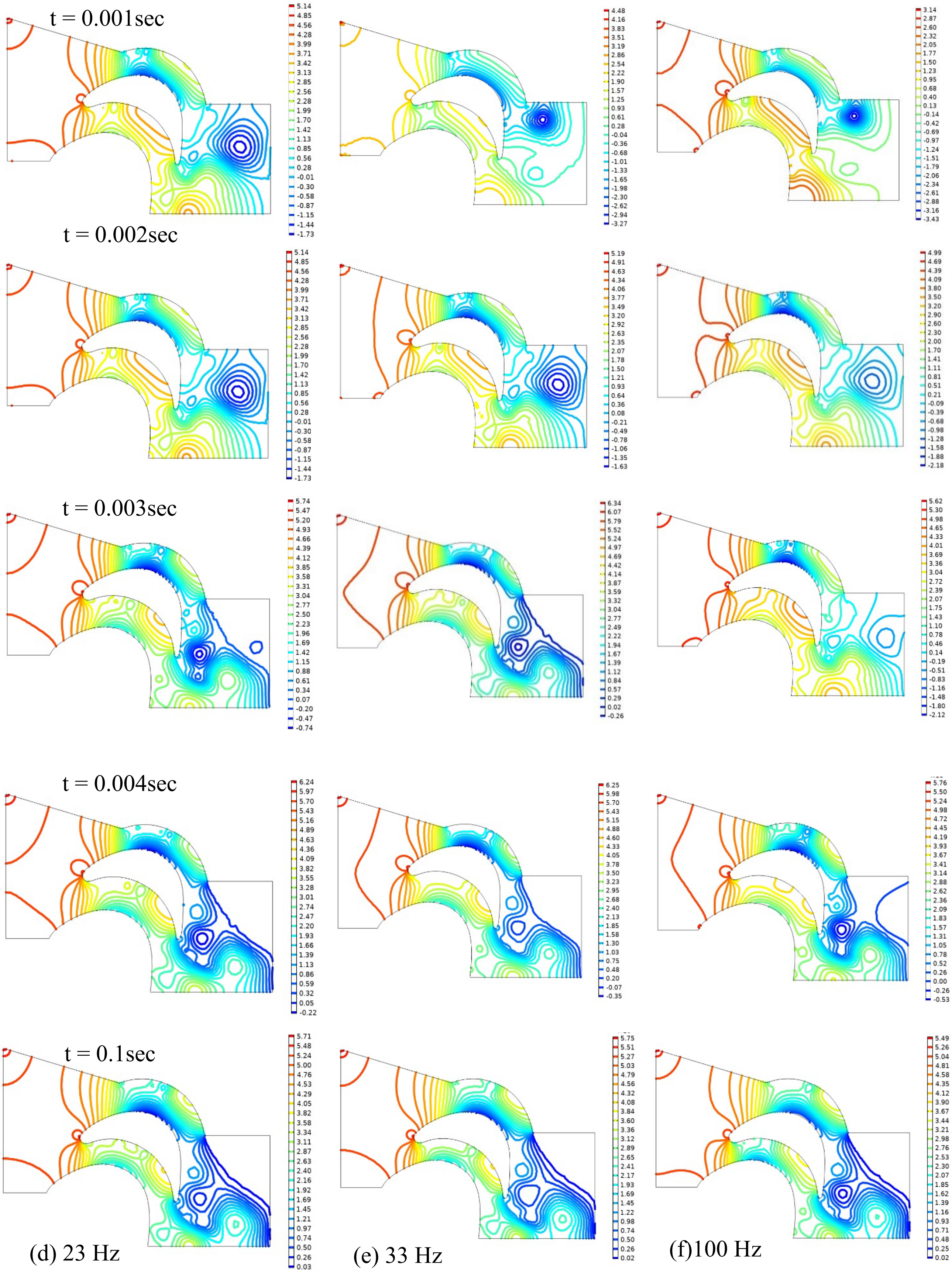

(d) 23 Hz (e) 33 Hz (f)100 Hz

Fig. 5-36: body contour of pressure distribution (×10^3pa) at first level with frequency (0 to 33) Hz and 22m/s.

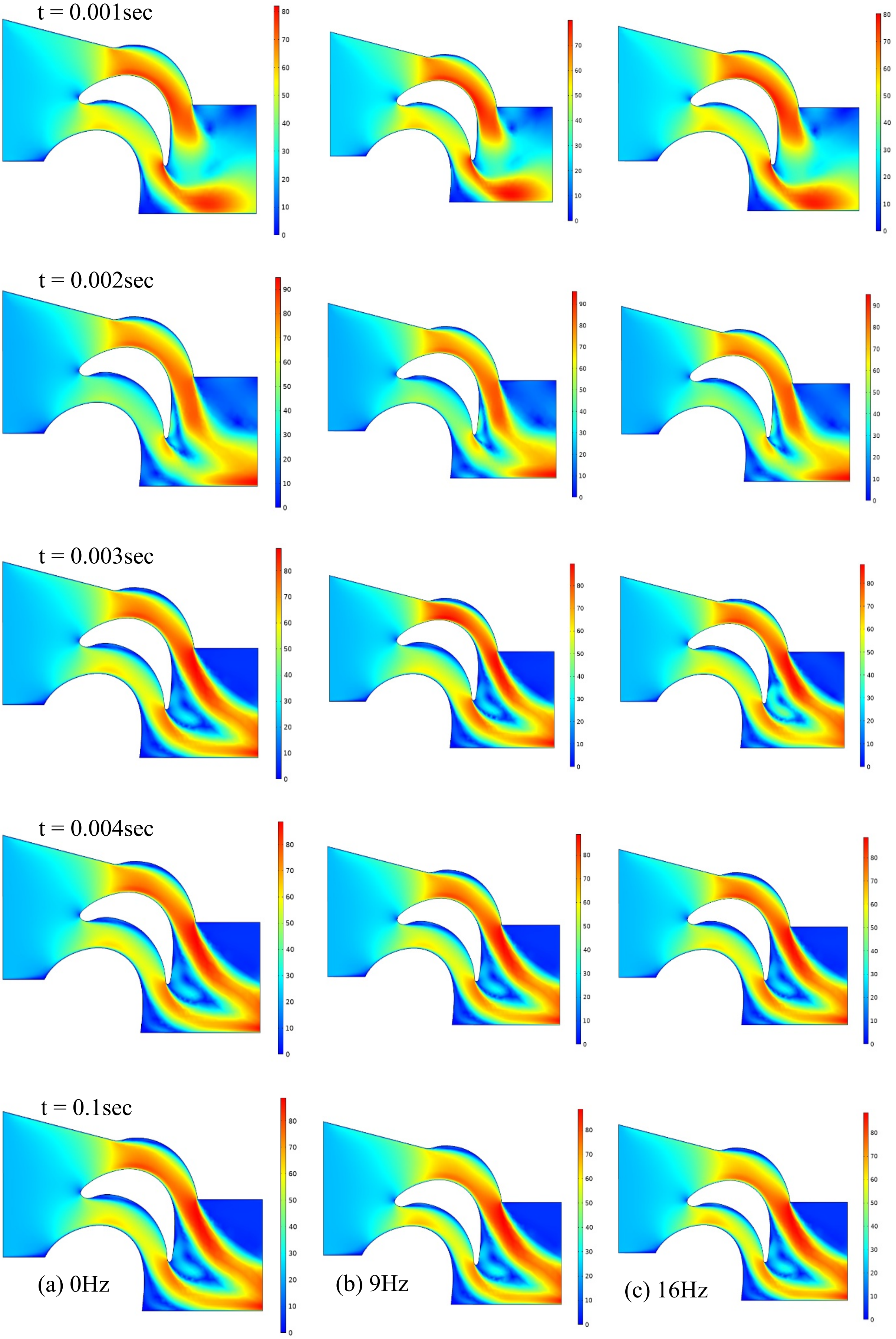

(a) 0Hz (b) 9Hz (c) 16Hz

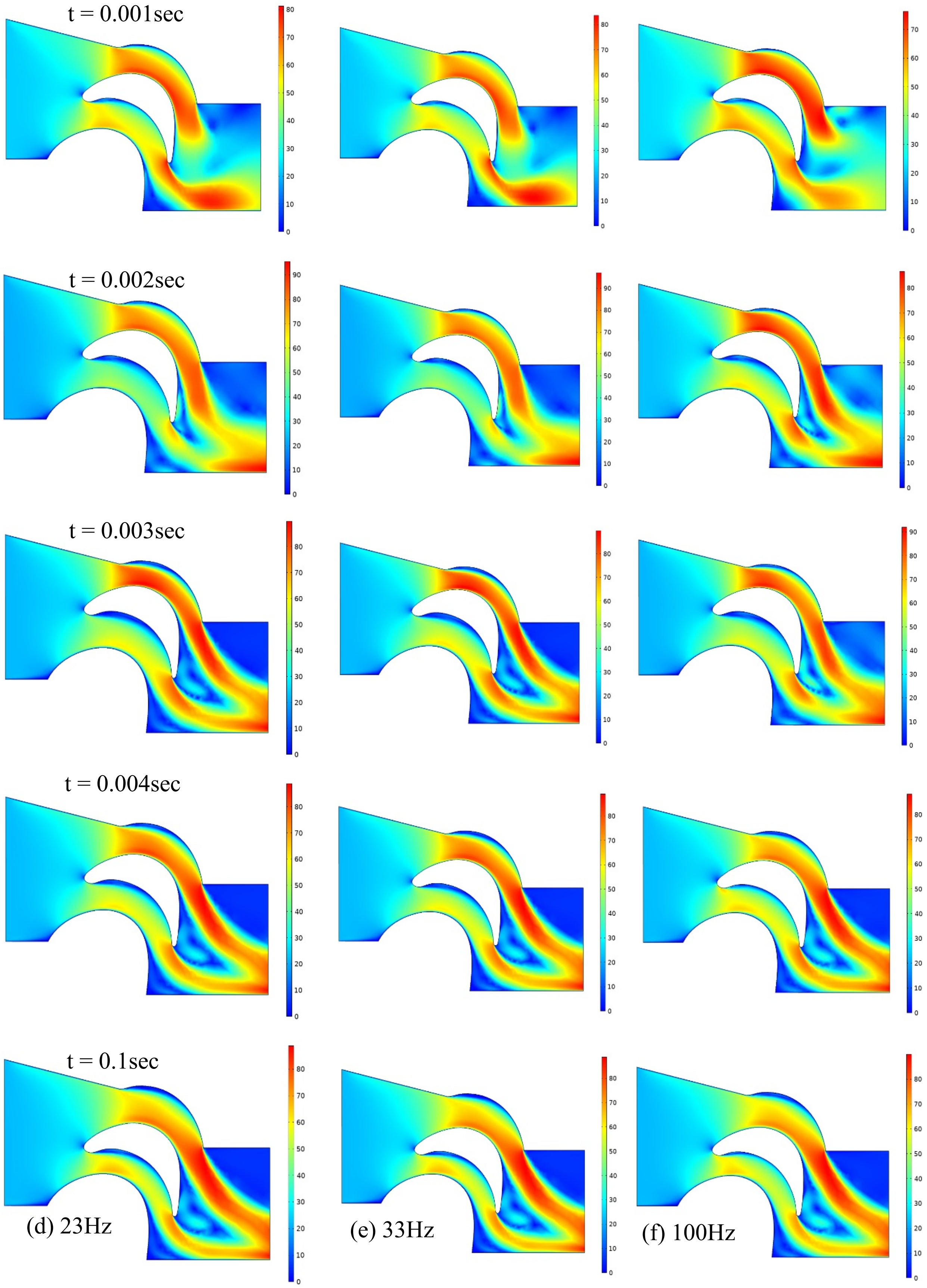

(d) 23Hz (e) 33Hz (f) 100Hz

Fig. 5-37: body contour of velocity distribution at second level with frequency (0 to 33) Hz and 22m/s.

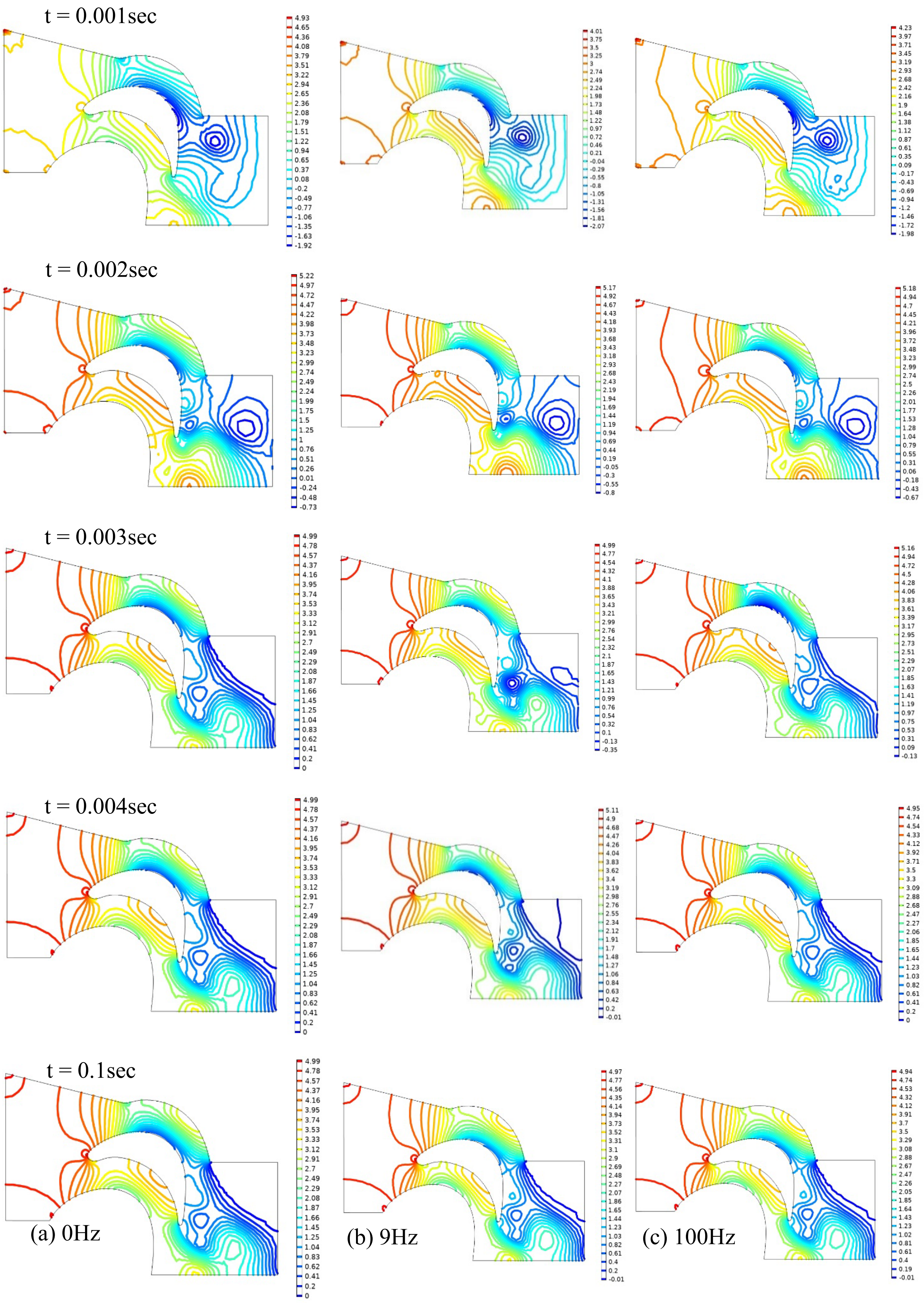

(a) 0Hz (b) 9Hz (c) 100Hz

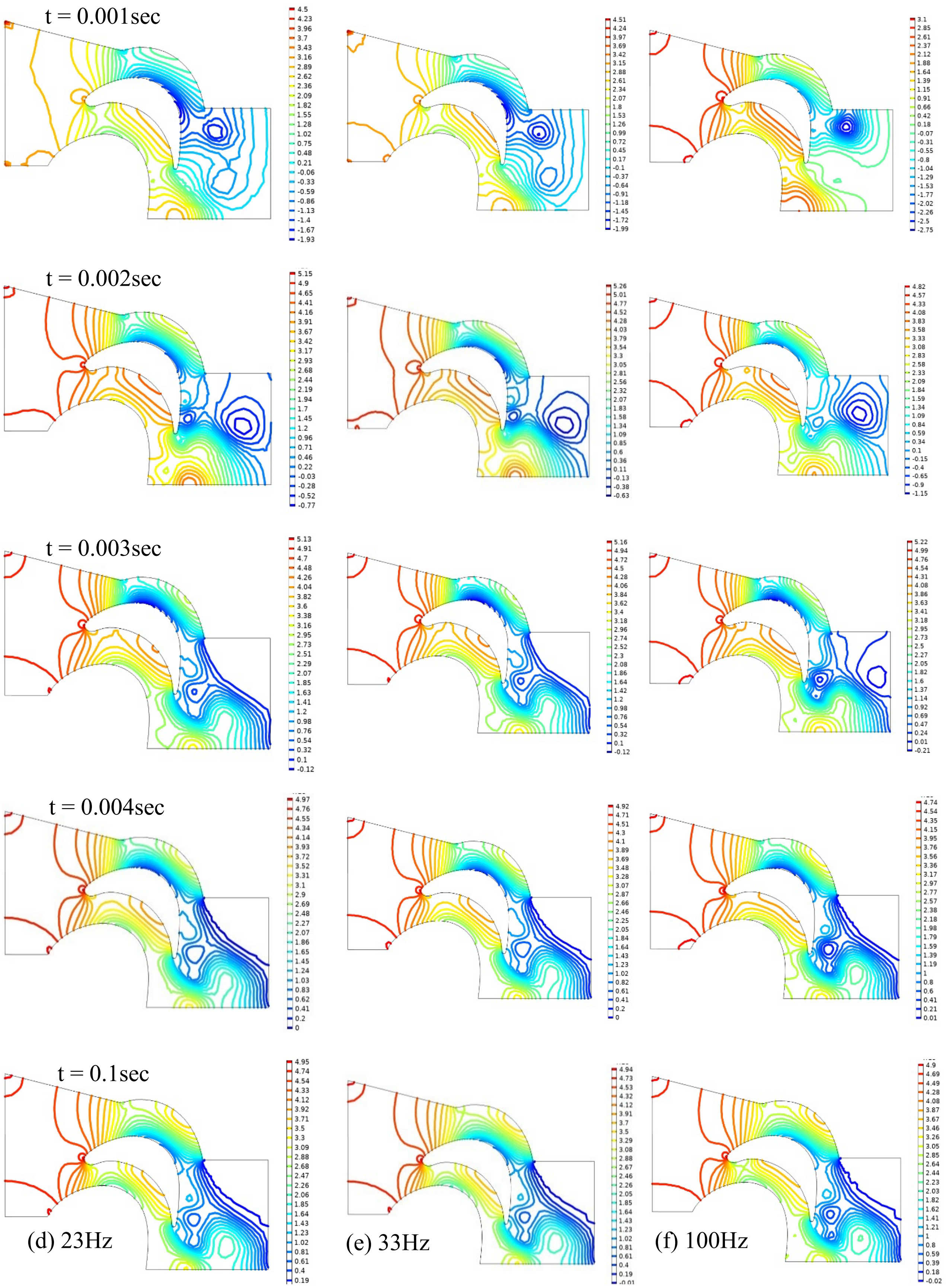

(d) 23Hz (e) 33Hz (f) 100Hz

Fig. 5-38: body contour of pressure distribution (×10^3pa) at second level with frequency (0 to 33) Hz and 22m/s.

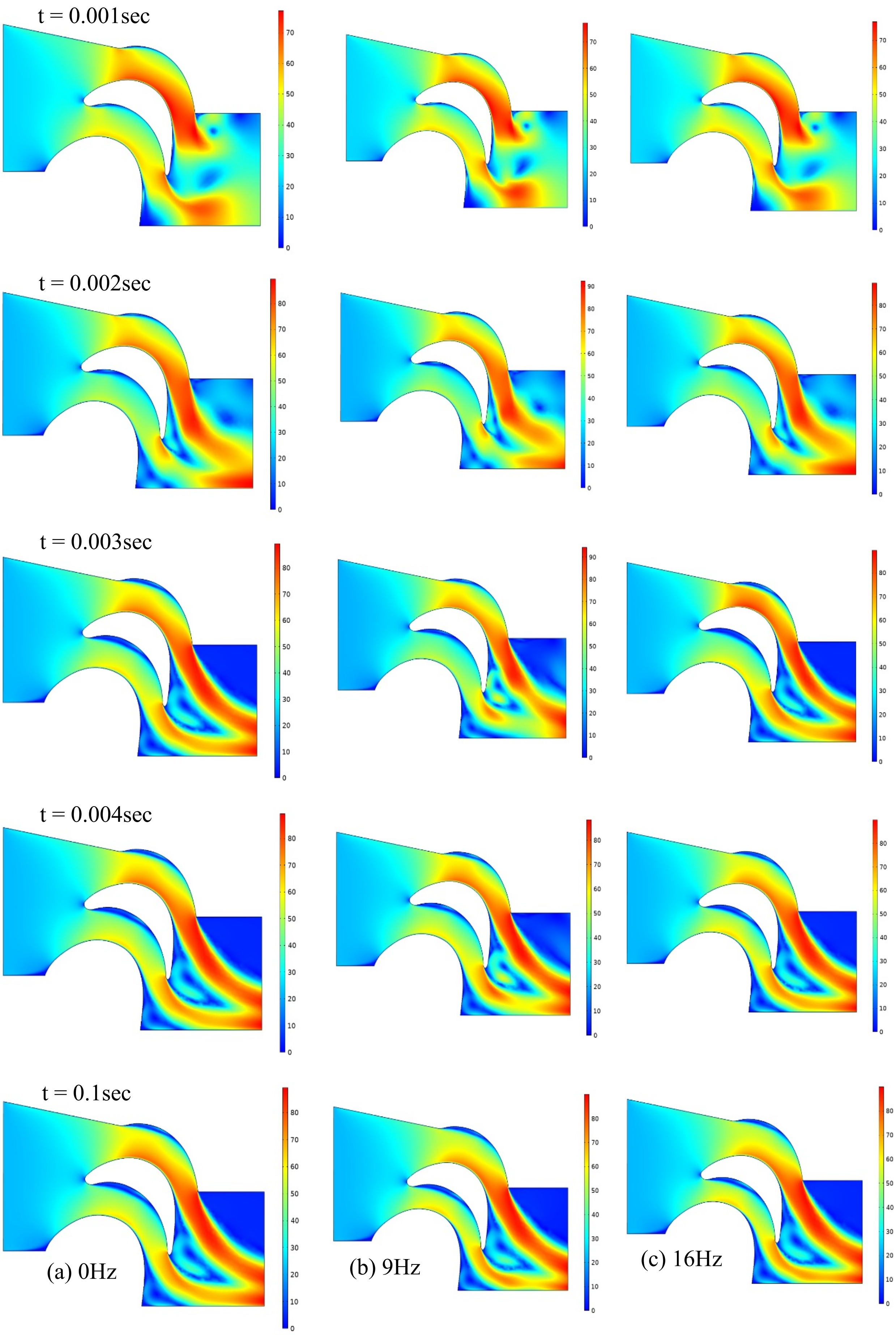
t = 0.001sec
70
60
50
40
30
20
10
0
t = 0.002sec
90
80
70
60
50
40
30
20
10
0
t = 0.003sec
t = 0.004sec
t = 0.1sec
(a) 0Hz
(b) 9Hz
(c) 16Hz

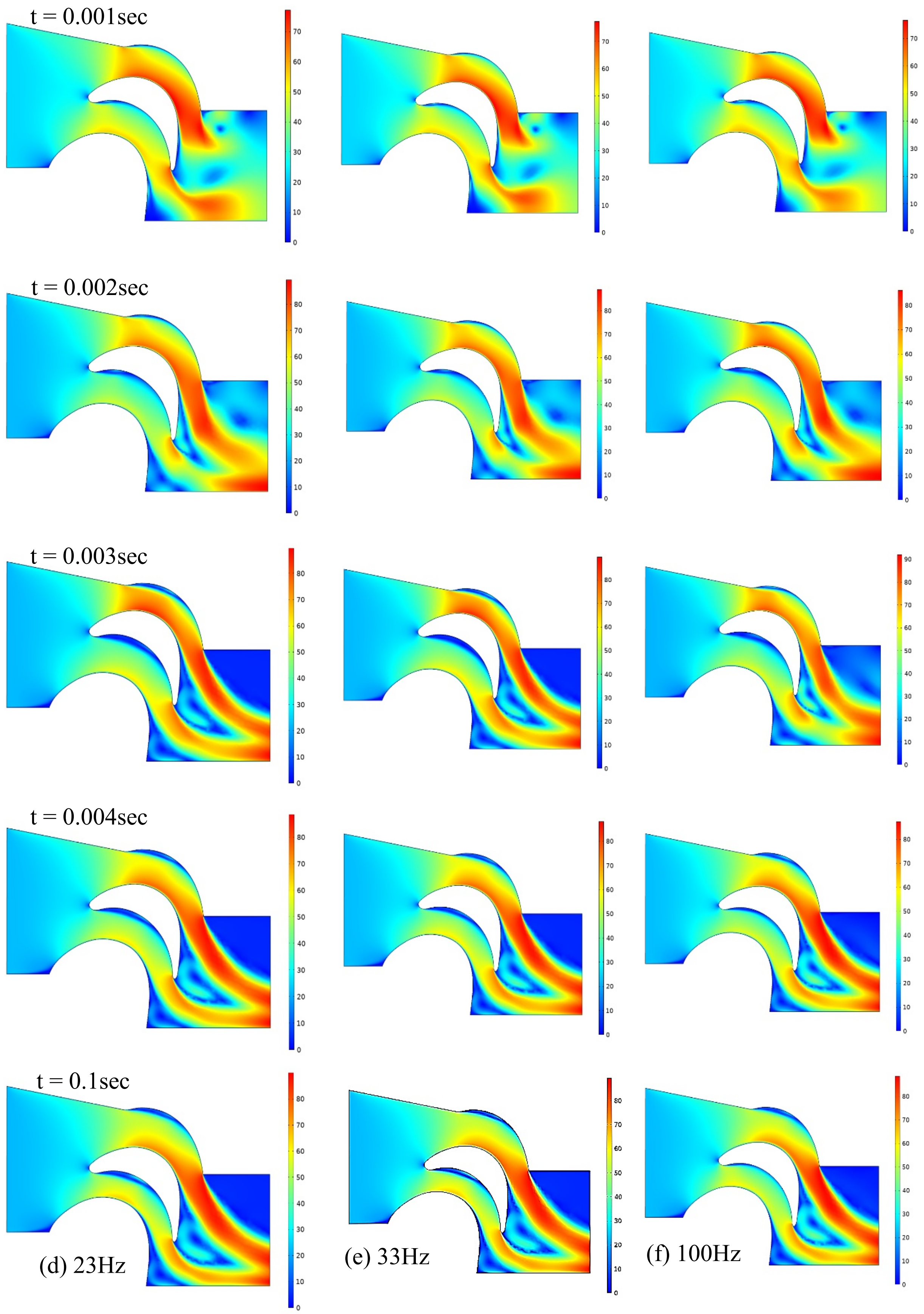

Fig. 5-39: body contour of velocity distribution third level with frequency (0 to 33) Hz and 22m/s.

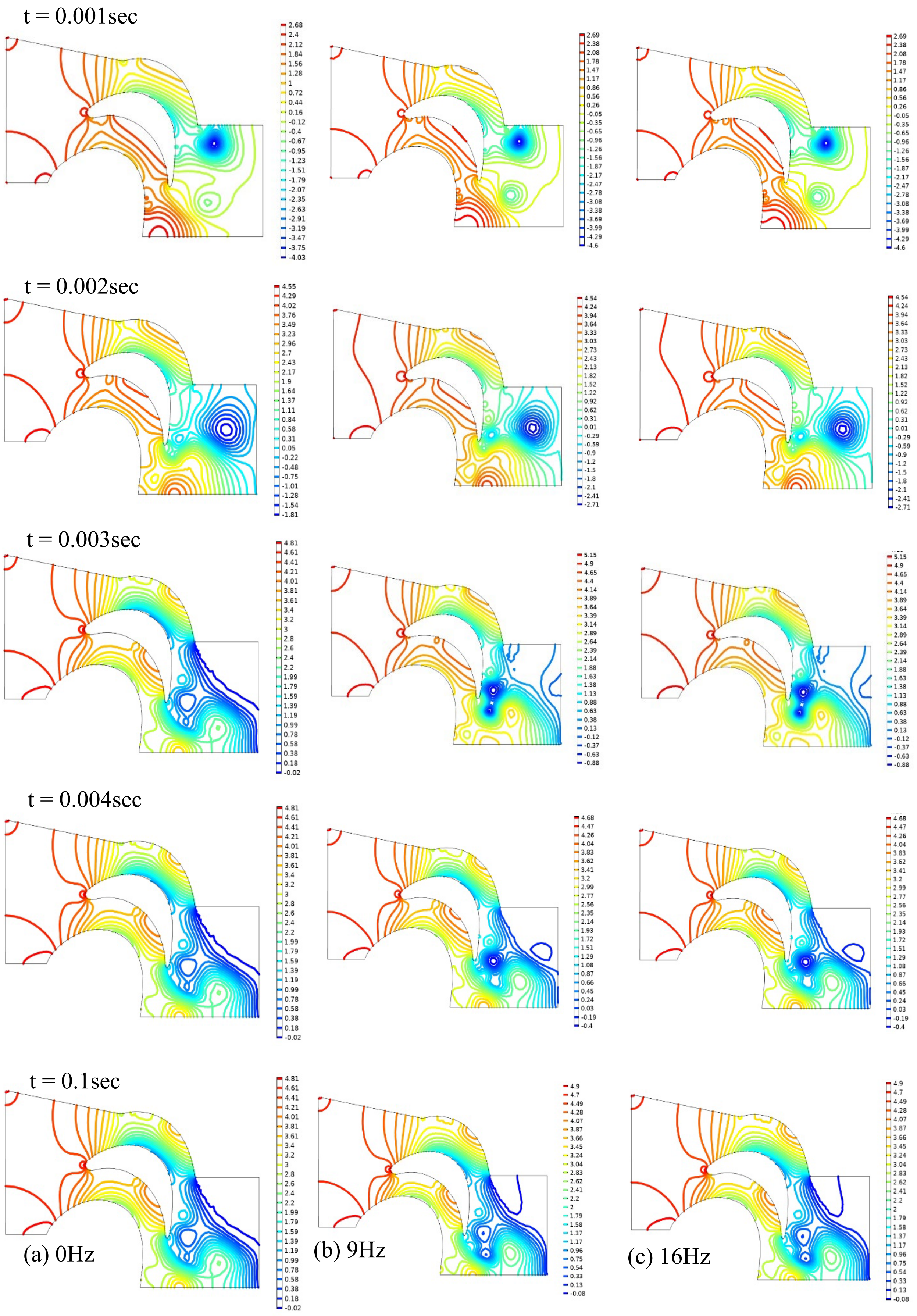
t = 0.001sec
2.68
2.4
2.12
1.84
1.56
1.28
1
0.72
0.44
0.16
-0.12
-0.4
-0.67
-0.95
-1.23
-1.51
-1.79
-2.07
-2.35
-2.63
-2.91
-3.19
-3.47
-3.75
-4.03
2.69
2.38
2.08
1.78
1.47
1.17
0.86
0.56
0.26
-0.05
-0.35
-0.65
-0.96
-1.26
-1.56
-1.87
-2.17
-2.47
-2.78
-3.08
-3.38
-3.69
-3.99
-4.29
-4.6
2.69
2.38
2.08
1.78
1.47
1.17
0.86
0.56
0.26
-0.05
-0.35
-0.65
-0.96
-1.26
-1.56
-1.87
-2.17
-2.47
-2.78
-3.08
-3.38
-3.69
-3.99
-4.29
-4.6
t = 0.002sec
4.55
4.29
4.02
3.76
3.49
3.23
2.96
2.7
2.43
2.17
1.9
1.64
1.37
1.11
0.84
0.58
0.31
0.05
-0.22
-0.48
-0.75
-1.01
-1.28
-1.54
-1.81
4.54
4.24
3.94
3.64
3.33
3.03
2.73
2.43
2.13
1.82
1.52
1.22
0.92
0.62
0.31
0.01
-0.29
-0.59
-0.9
-1.2
-1.5
-1.8
-2.1
-2.41
-2.71
4.54
4.24
3.94
3.64
3.33
3.03
2.73
2.43
2.13
1.82
1.52
1.22
0.92
0.62
0.31
0.01
-0.29
-0.59
-0.9
-1.2
-1.5
-1.8
-2.1
-2.41
-2.71
t = 0.003sec
4.81
4.61
4.41
4.21
4.01
3.81
3.61
3.4
3.2
3
2.8
2.6
2.4
2.2
1.99
1.79
1.59
1.39
1.19
0.99
0.78
0.58
0.38
0.18
-0.02
5.15
4.9
4.65
4.4
4.14
3.89
3.64
3.39
3.14
2.89
2.64
2.39
2.14
1.88
1.63
1.38
1.13
0.88
0.63
0.38
0.13
-0.12
-0.37
-0.63
-0.88
5.15
4.9
4.65
4.4
4.14
3.89
3.64
3.39
3.14
2.89
2.64
2.39
2.14
1.88
1.63
1.38
1.13
0.88
0.63
0.38
0.13
-0.12
-0.37
-0.63
-0.88
t = 0.004sec
4.81
4.61
4.41
4.21
4.01
3.81
3.61
3.4
3.2
3
2.8
2.6
2.4
2.2
1.99
1.79
1.59
1.39
1.19
0.99
0.78
0.58
0.38
0.18
-0.02
4.68
4.47
4.26
4.04
3.83
3.62
3.41
3.2
2.99
2.77
2.56
2.35
2.14
1.93
1.72
1.51
1.29
1.08
0.87
0.66
0.45
0.24
0.03
-0.19
-0.4
4.68
4.47
4.26
4.04
3.83
3.62
3.41
3.2
2.99
2.77
2.56
2.35
2.14
1.93
1.72
1.51
1.29
1.08
0.87
0.66
0.45
0.24
0.03
-0.19
-0.4
t = 0.1sec
4.81
4.61
4.41
4.21
4.01
3.81
3.61
3.4
3.2
3
2.8
2.6
2.4
2.2
1.99
1.79
1.59
1.39
1.19
0.99
0.78
0.58
0.38
0.18
-0.02
(a) 0Hz
4.9
4.7
4.49
4.28
4.07
3.87
3.66
3.45
3.24
3.04
2.83
2.62
2.41
2.2
2
1.79
1.58
1.37
1.17
0.96
0.75
0.54
0.33
0.13
-0.08
(b) 9Hz
4.9
4.7
4.49
4.28
4.07
3.87
3.66
3.45
3.24
3.04
2.83
2.62
2.41
2.2
2
1.79
1.58
1.37
1.17
0.96
0.75
0.54
0.33
0.13
-0.08
(c) 16Hz

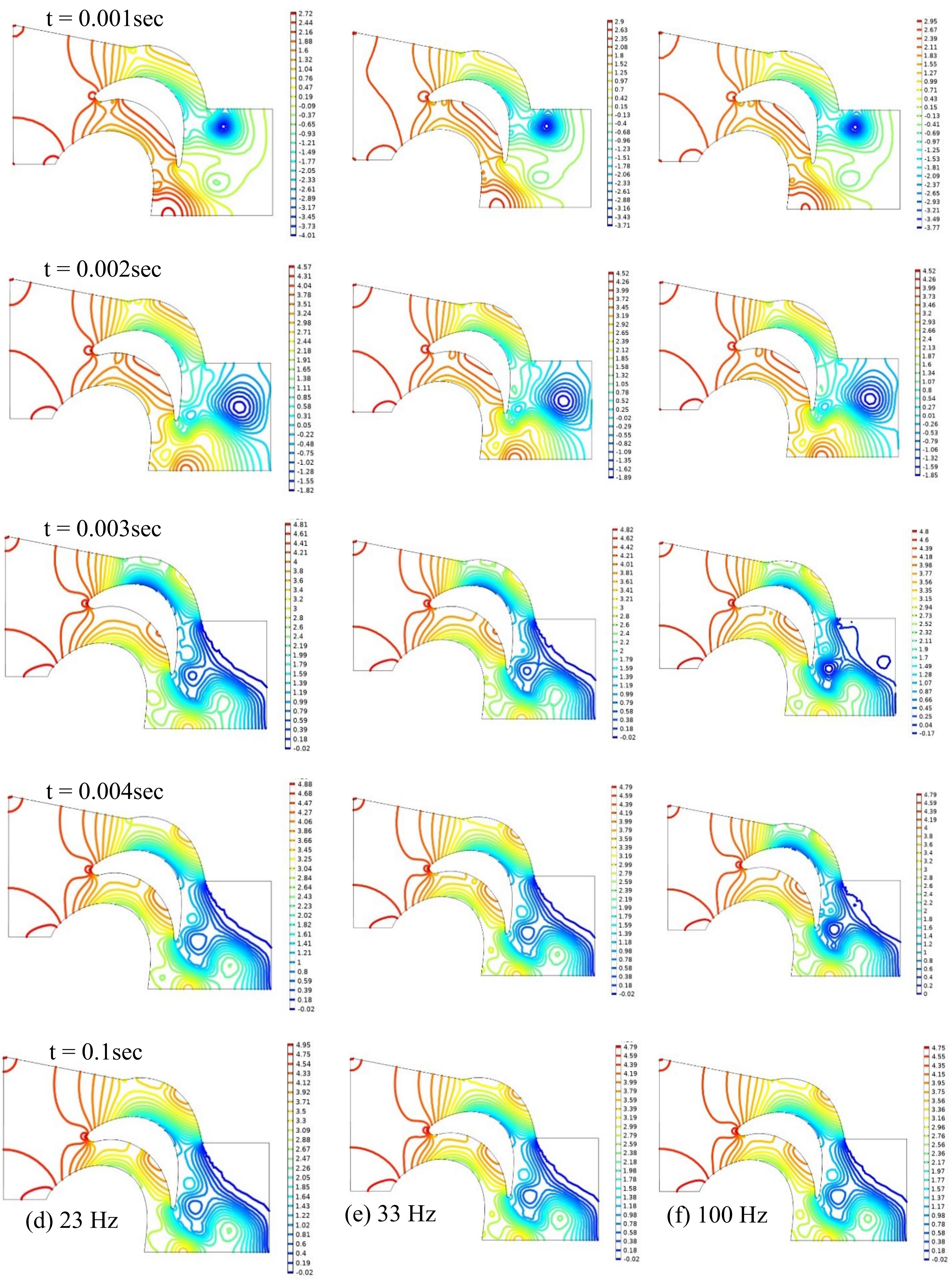

(d) 23 Hz (e) 33 Hz (f) 100 Hz

Fig. 5-40: body contour of pressure distribution (×10^3pa) at third level with frequency (0 to 33) Hz and 120m/s.

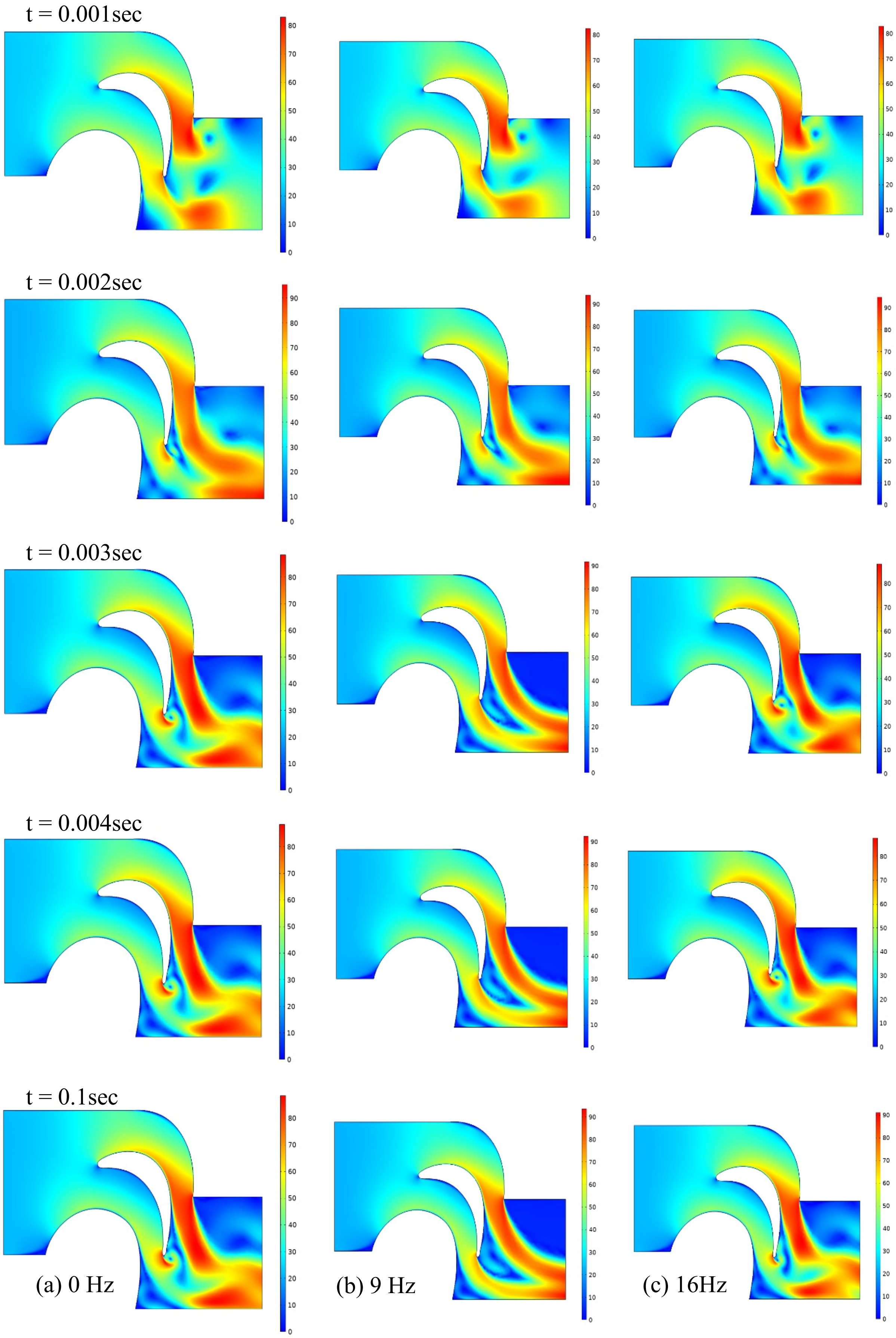
t = 0.001sec
t = 0.002sec
t = 0.003sec
t = 0.004sec
t = 0.1sec
(a) 0 Hz
(b) 9 Hz
(c) 16Hz

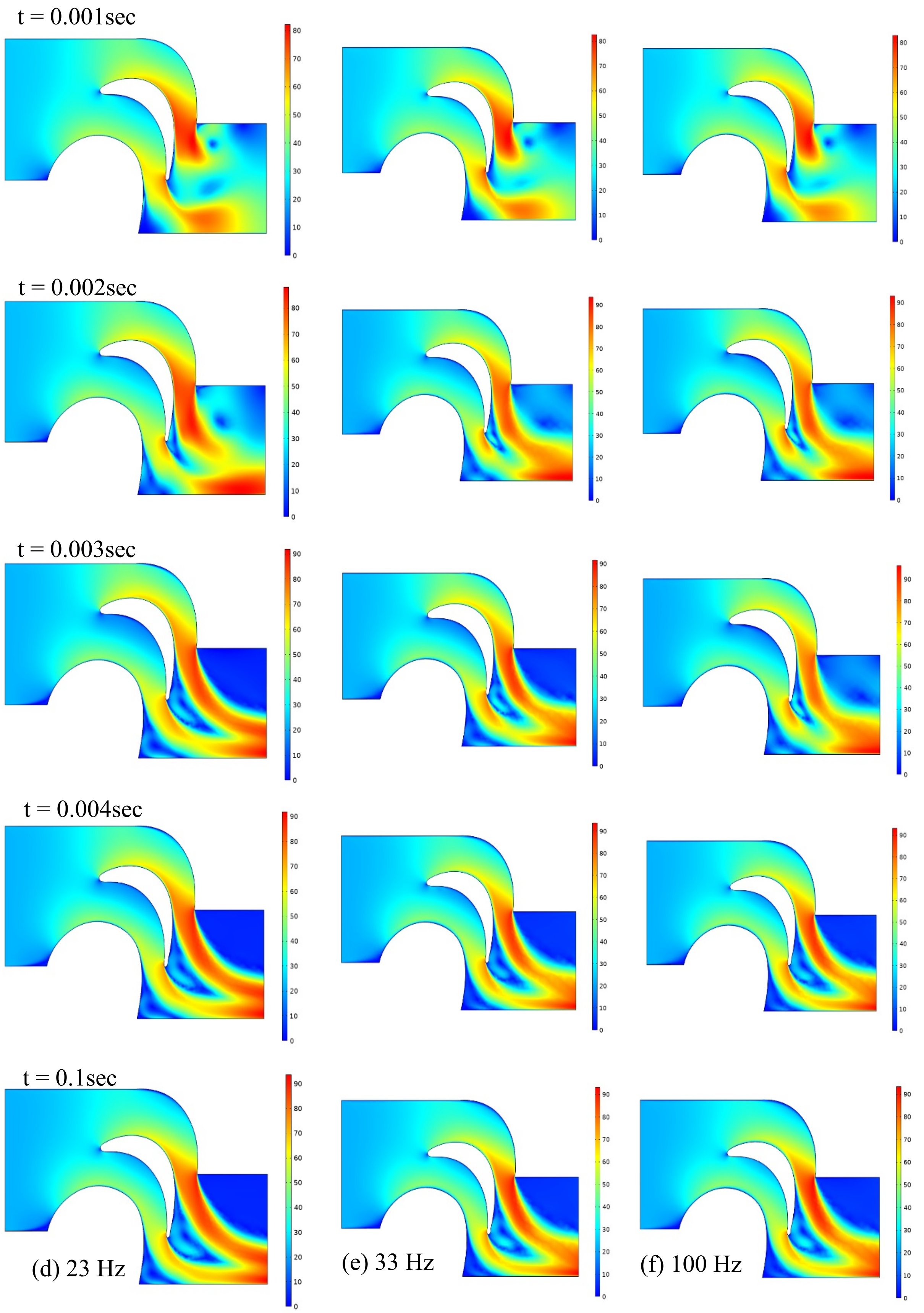

Fig. 5-41: body contour of velocity distribution at last level with frequency (0 to 33) Hz and 22m/s.

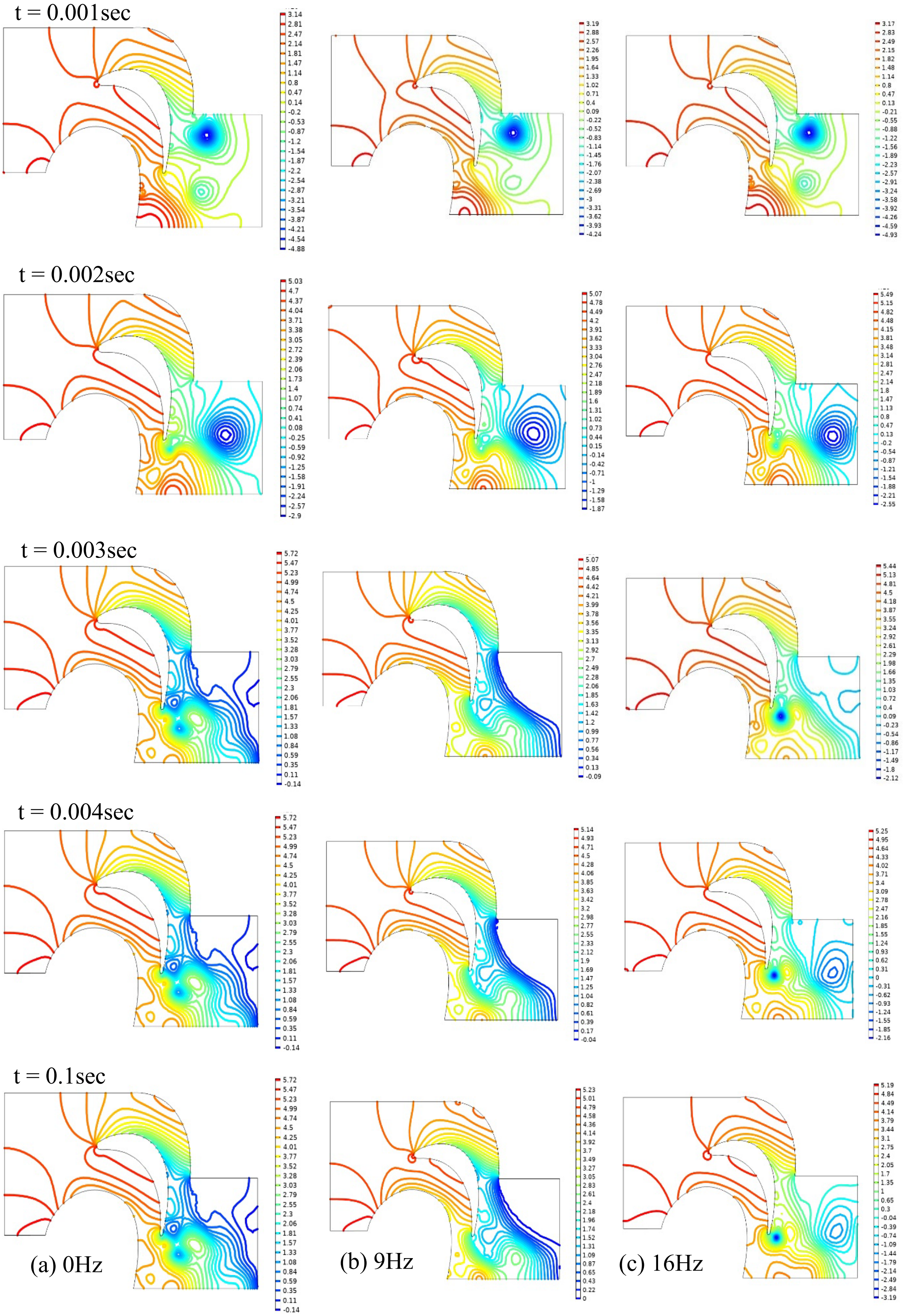

(a) 0Hz (b) 9Hz (c) 16Hz

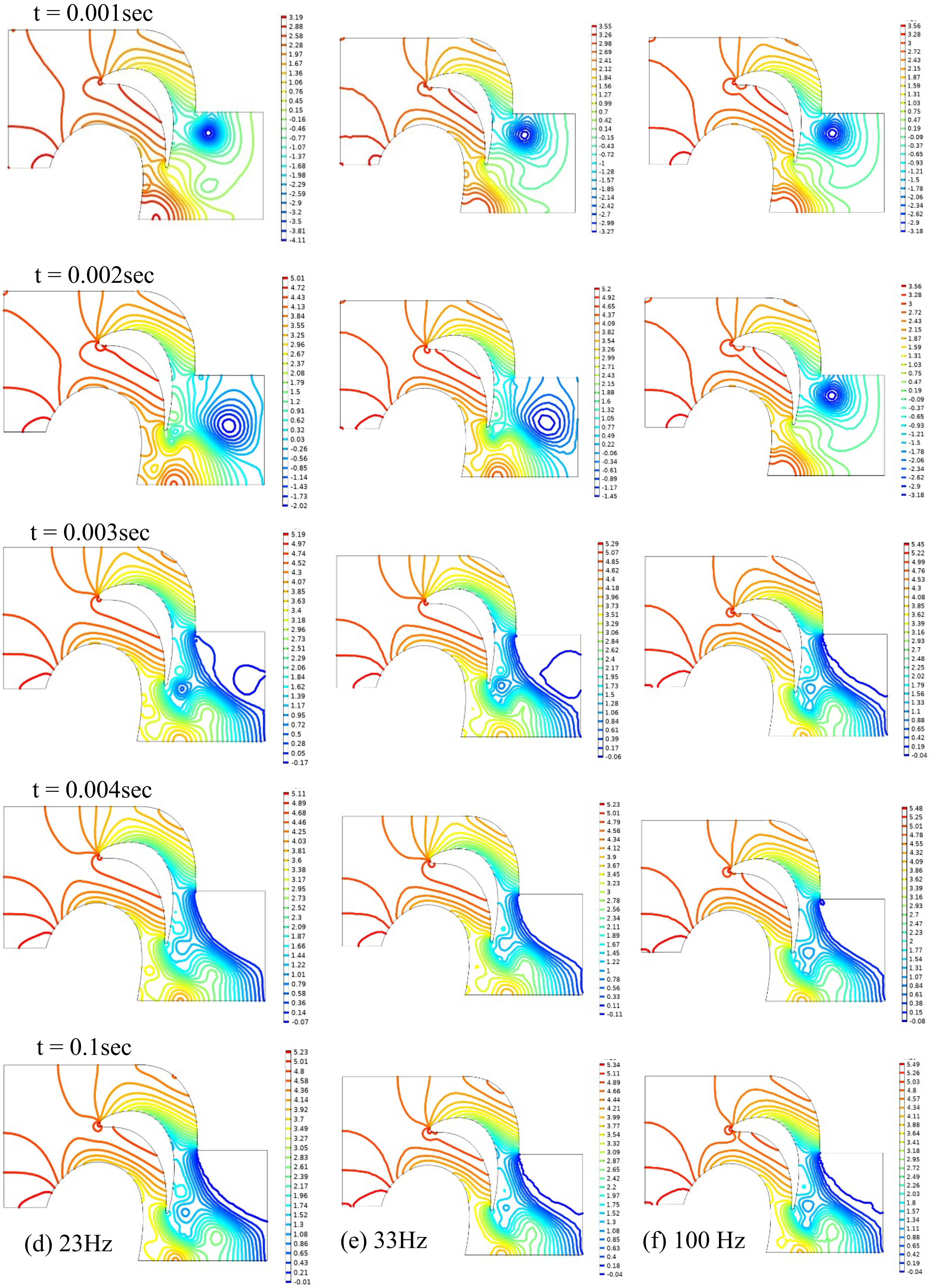

(d) 23Hz (e) 33Hz (f) 100 Hz

Fig. 5-42: body contour of pressure distribution (×10^{3}pa) at last level with frequency (0 to 33) Hz and22m/s.

5.5. Comparison between Numerical and Experimental Results

Fig. 5-43 toFig. 5-45 show the distribution of the pressure coefficient and the ratio of velocity at any point from the surface of the blade to the velocity entering (22m/sec) for three levels of the blade starting from the root with a height from the root of first level, second level, and third level, respectively. For pressure at the suction side, the distribution of the pressure coefficient in the pressure side region is higher than the suction side region affected by the value of the pressure generated by the fluid on the surface of the blade as a result of changing the shape of the section. The bigger value of the velocity ratio is noticed at the suction side and decreases at the pressure side. It is also noticed a good convergence of results between the experimental with numerical work. The reason is that the conditions in which the experimental work was conducted are similar. Variable conditions as a result of changing temperatures and air properties. The errors result from the devices used in experimental work. It can also be seen from the velocity diagrams that vibration reduces the pressure coefficient at the suction region and increase the pressure side for all figures.

Figure 5-46 shows the effect of increasing the vibration on the value of pressure coefficient, which is noted as a gradual increase with the increase of vibration, reaching a value of 23 Hz, after which it tends to decrease slightly with an increase in vibration value relative to the pressure side (P.S.). As for the suction side (S.S), the effect of vibration increases the value of the pressure coefficient at all the vibration values.

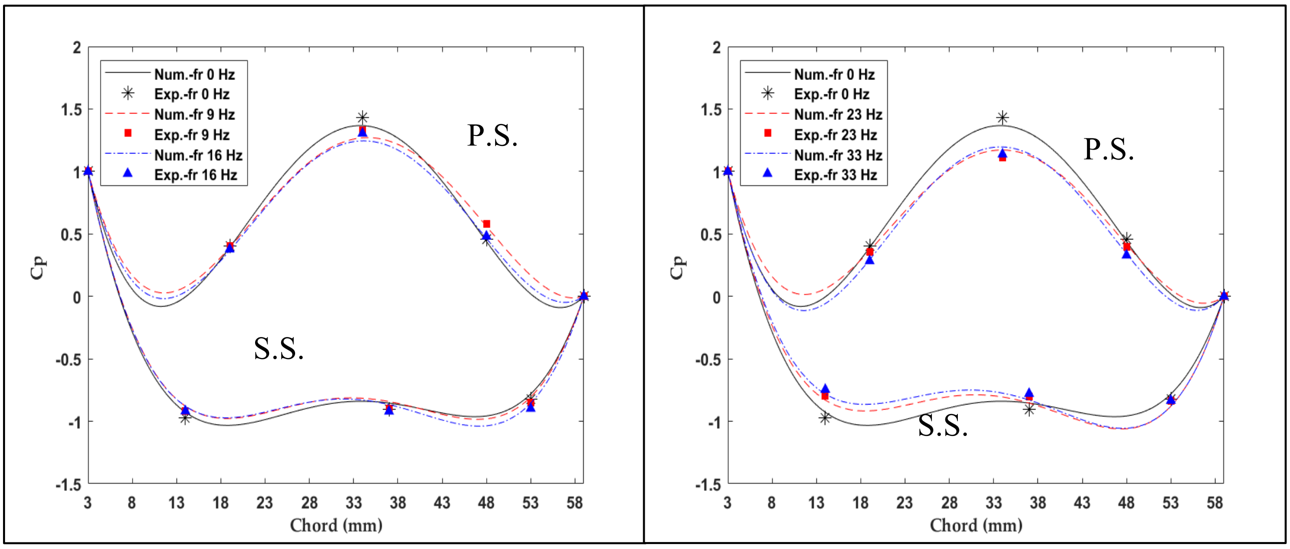

(a) Cp for experiment and simulation

(b) Cp for experiment and simulation

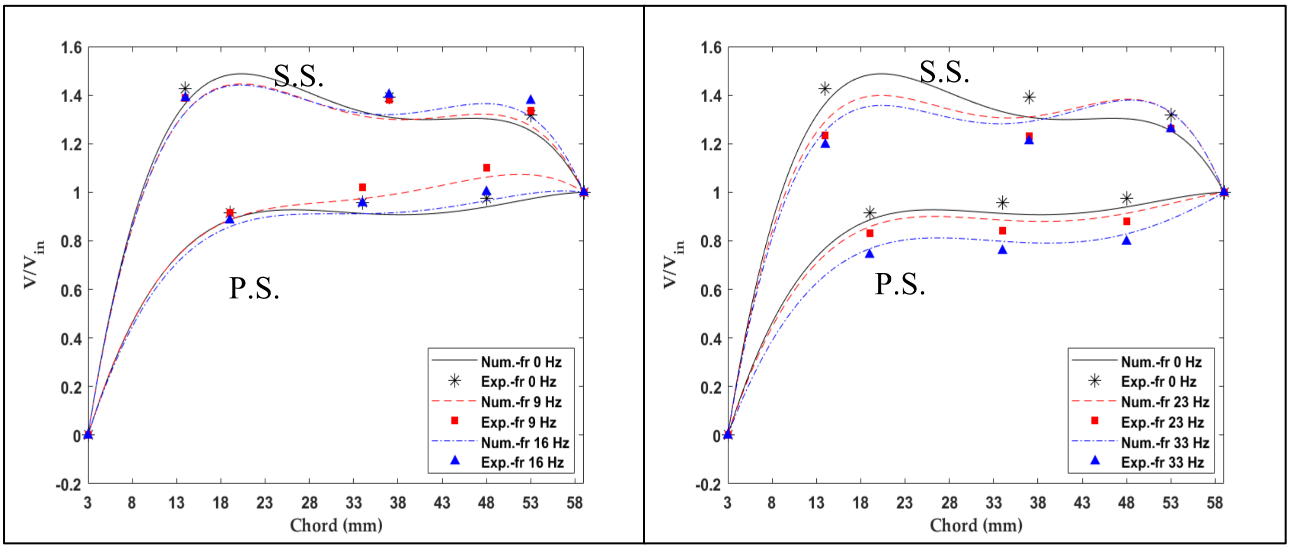

(c) V/V_{in} for experiment and simulation

(d) V/V_{in} for experiment and simulation

Fig. 5-43: Show pressure coefficient and velocity distribution for first level.

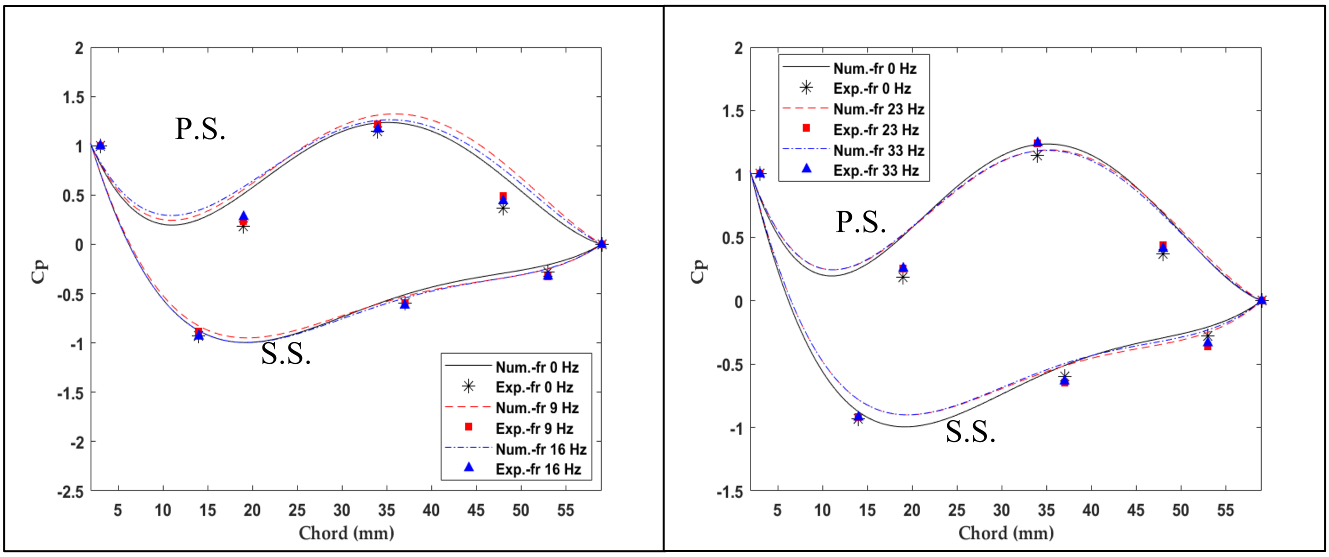

(a) Cp for experiment and simulation (b) Cp for experiment and simulation

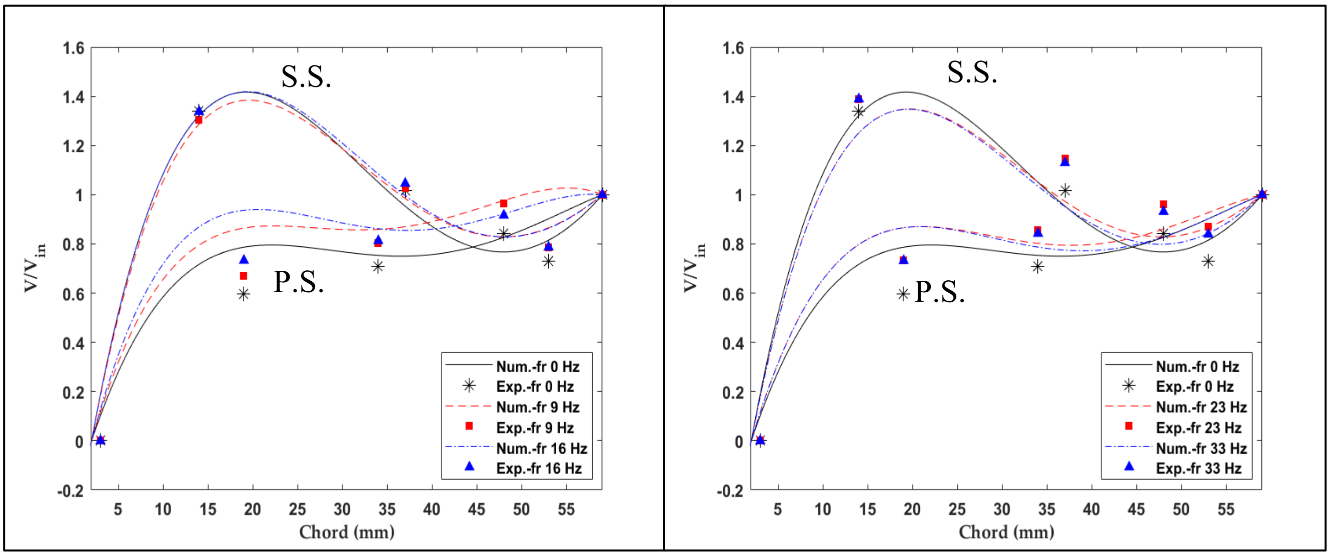

(c) V/V_{in} for experiment and simulation (d) V/V_{in} for experiment and simulation

Fig. 5-44: Show pressure coefficient and velocity distribution for section blade at second level.

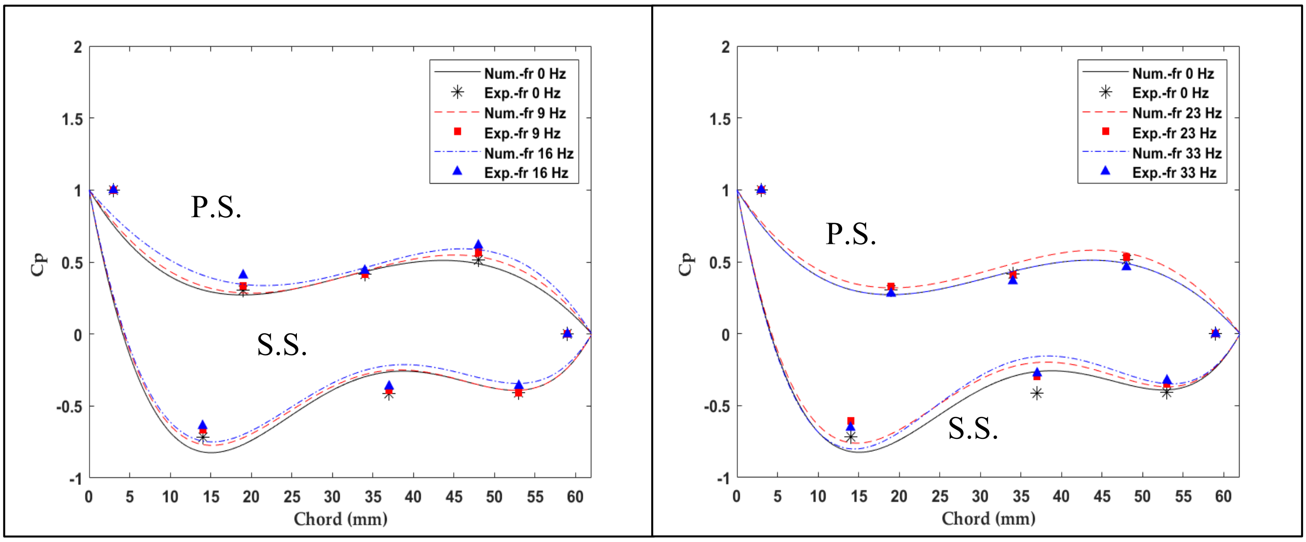

(a) Cp for experiment and simulation

(b) Cp for experiment and simulation

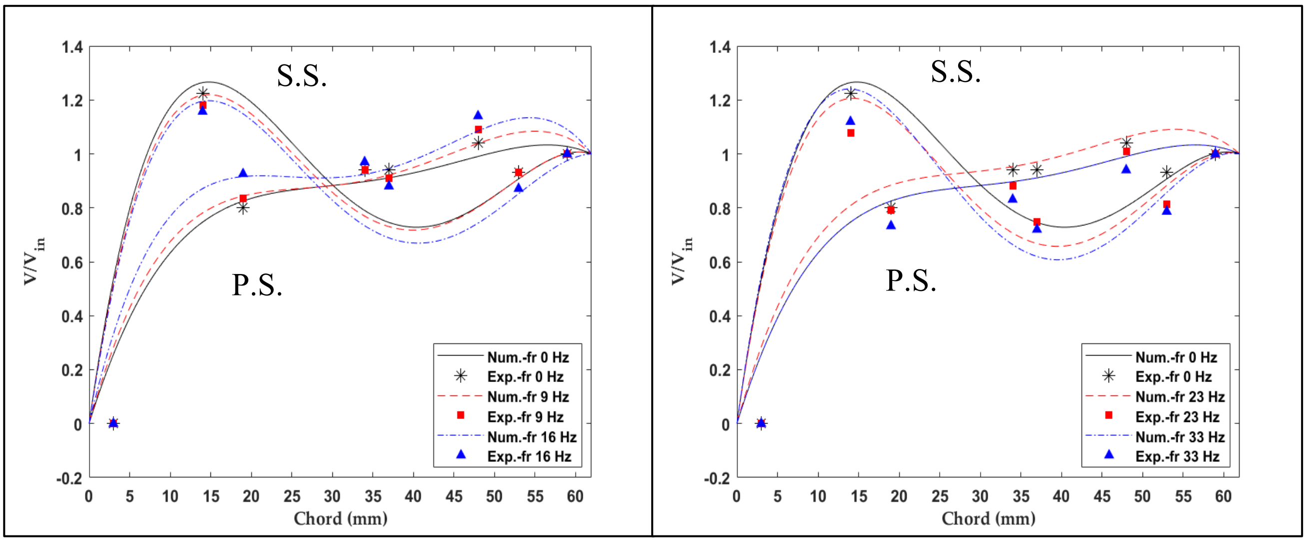

(c) V/V_{in} for experiment and simulation

(d) V/V_{in} for experiment and simulation

Fig. 5-45: Show pressure coefficient and velocity distribution for section blade at last level.

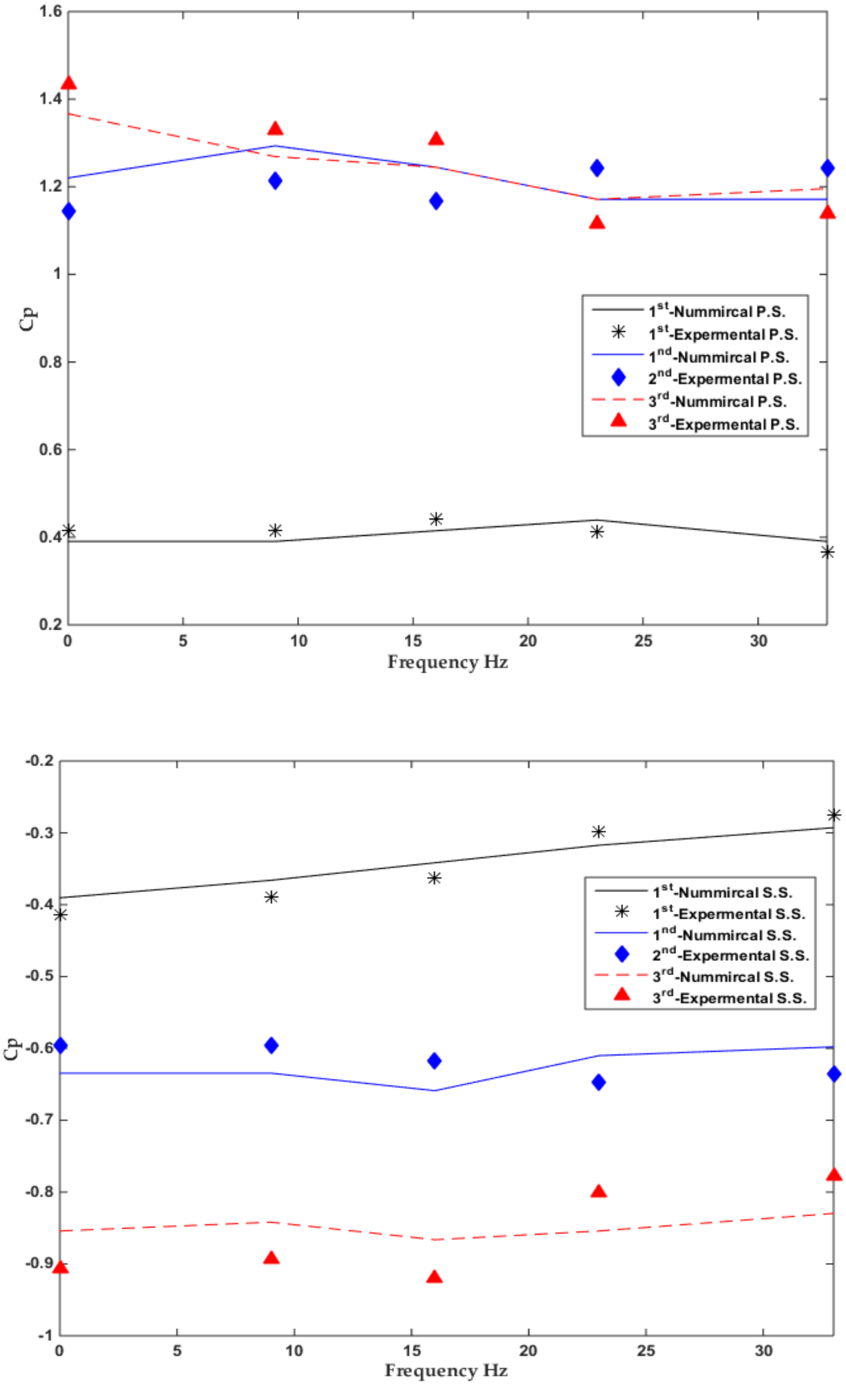

Fig. 5-46: Show effect vibration on pressure coefficient in regions P.S. and S.S. for three levels.

CHAPTER SIX

CONCLUSIONS AND FUTURE WORK

6.1. Conclusion

Turbulent flow is experimentally, and numerically investigated over the cascade blade of a gas turbine with vibration effect. The following points outline the key findings that can be made from this work:

1. Vibration affects the amount of pressure exerted by the fluid on the blade, as its increase in certain ranges leads to an increase in the pressure coefficient by 5% in the pressure side region and the suction side region, but its effect decreases after a frequency of 23 Hz. As for the effect of vibration on velocity, it increases at the pressure side region and decreases velocity in the area of the suction side. The magnitude of this effect increases with increasing vibration to the limit of 23 Hz, and its effect begins to recede.

2. At the S.S. and P.S. sides, the experimental results compared to the numerical simulation show that there is a discrepancy of ±5% and ±6% at first, second, and third level, respectively, from the base in the middle of the chord.

3. The regularity of the scheme in figures is more pronounced when moving away from the root of the blade since the effect of the root on the events of the vortices in the middle of the flow path affects the flow disturbance and pressure.

4. The effect of vibration in the mid-span level is opposite to the pressure side region, where the pressure coefficient decreases by 3-6% with

increasing vibration and the fluid velocity increases in that region, while the behavior is similar to previous levels in the intake side region.

5. There is a change in the velocity distribution, as it increased in regions and decreased in other, because the vertical vibration of the blade works on a change in the airfoil section of the blade when the blade moves upward or a decrease in the cross-sectional area when it moves downward, and by repeating this process periodically leads to an increase in the amount of induced vortices touching the surface of the blade.
6. The deformation in the body contour of the pressure distribution of a fluid as a result of the vibration on the blade, which in turn increases the pressure regions near the pressure side and decreases in the suction side.
7. Without vibration, the velocity of the fluid is higher in the S.S. than its velocity at the P.S., and the gradient in velocity is increasing in P.S. by 66% from near wall to flow passage and decreasing by 22% in the S.S. towards the flow passage region. That is, the velocity of the fluid increases from the surface of the blade in the S.S to the left end, and the velocity increases from the blade surface in the P.S. to the right end.
8. The effect of the vibration is clear on the velocity and pressure distribution when the low range of the frequency and the effect decreases as 6% at 9 and 16 Hz to 5.5% at 23, and 5% at 33Hz.
9. The numerical findings show that effect of the vibration is

insignificant on the velocity and pressure distribution at higher inlet velocity.

10. Compared to the real case, the fluid has a behavior similar to the numerical simulation of the experimental work, but there is an increase in the velocity of the fluid entering the rotating turbine, and there is an increase in the disturbances of the velocity and pressure distribution lines, and this means an increase in the generation of eddies in the flow field generated from near the blade surface.

11. For the vibration effect in the horizontal plane of blade base. By observing the body contours, it can be noted that the effect of the movement of the blade on the distribution of fluid velocity increased the amount of that velocity at the suction region in the case of the rise of the blade towards that region and decreased the area of high velocity at the pressure region, which consequently, results in an increase in pressure at the pressure side and a decrease in it at the suction side. Nevertheless, in the case of the descent of the blade towards the pressure region, the area of high velocity at the pressure region increases, and this leads to a decrease in the pressures applied to the blade. As for the vortices generated behind the blade, they are affected by the up and down position of the blade.

6.2. Future work

1. Repeat this study including compressible flow instead of incompressible flow.
2. Study the effect of vibration on heat transfer the blade.
3. Study the effect of vibration on the tip blade clearance numerically.
4. Study the combined effect of the external vibration along with the flow induced vibration in the cascade blade.
5. Use signal processing for the resulted data of the vibration for assessment gas turbine performance.

References.

[1] M. Arabnia, “Aerodynamic Shape Optimization of Axial Turbines in Three Dimensional Flow,” No. PhD thesis. Concordia University, 2012, [Online]. Available: http://spectrum.library.concordia.ca/973693/4/Mohammad_Arabnia_5792010.pdf.

[2] S. Kaneko et al., Flow-Induced Vibrations: Classifications and Lessons from Practical Experiences: Second Edition. Butterworth-Heinemann, 2013.

[3] D. V. Murthy and M. R. Morel, “Turbine blade forced response prediction using FREPS,” SAE Technical Paper, 1993. doi: 10.4271/931373.

[4] M. Jöcker, “Numerical Investigation of the Aerodynamic Vibration Excitation of High-Pressure Turbine Rotors.” Energiteknik, 2002.

[5] K. J. Pallos, “Gas Turbine Repair Technology,” 2000. [Online]. Available:https://www.ge.com/content/dam/gepower-pgdp/global/en_US/documents/technical/ger/ger-3957b-gas-turbine-repair-technology.pdf.

[6] A. K. Saha, G. I. Mahmood, and S. Acharya, “The role of leading-edge contouring on end-wall flow and heat transfer: Computations and

experiments," in Proceedings of the ASME Turbo Expo, 2006, Vol. 3 PART B, pp. 1105–1118, doi: 10.1115/GT2006-91318.

[7] G. A. Gerolymos, "Numerical integration of the blade-to-blade surface Euler equations in vibrating cascades," AIAA J., Vol. 26, No. 12, pp. 1483–1492, 1988, doi: 10.2514/3.10067.

[8] H. W. D. Chiang and R. E. Kielb, "An analysis system for blade forced response," ASME 1992 Int. Gas Turbine Aeroengine Congr. Expo. GT 1992, Vol. 5, 1992, doi: 10.1115/92GT172.

[9] V. Dedoussis, K. Mathioudakis, and K. D. Papailiou, "Numerical simulation of blade fault signatures from unsteady wall pressure signals," in Proceedings of the ASME Turbo Expo, 1994, Vol. 5, doi: 10.1115/94-GT-289.

[10] J. R. Meneghini and P. W. Bearman, "Numerical simulation of high amplitude oscillatory flow about a circular cylinder," J. Fluids Struct., Vol. 9, No. 4, pp. 435–455, 1995, doi: 10.1006/jfls.1995.1025.

[11] S. The and E. Number, "Kinematics and Dynamics of Sphere," J. Fluids Struct., Vol. 14, pp. 575–585, 2001, doi: 10.1006/j.

[12] C. H. K. Williamson and R. Govardhan, "Vortex-induced vibrations," Annu. Rev. Fluid Mech., Vol. 36, No. 1982, pp. 413–455, 2004, doi: 10.1146/annurev.fluid.36.050802.122128.

[13] S. Moffatt, W. Ning, Y. Li, R. G. Wells, and L. He, “Blade forced response prediction for industrial gas turbines,” J. Propuls. Power, Vol. 21, No. 4, pp. 707–714, 2005, doi: 10.2514/1.6126.

[14] M. Brøns, “Streamline Topology: Patterns in Fluid Flows and their Bifurcations,” Advances in Applied Mechanics, Vol. 41. pp. 1–42, 2007, doi: 10.1016/S0065-2156(07)41001-8.

[15] J. Young and J. C. S. Lai, “Vortex lock-in phenomenon in the wake of a plunging airfoil,” AIAA J., Vol. 45, No. 2, pp. 485–490, 2007, doi: 10.2514/1.23594.

[16] I. McBean, K. Hourigan, M. Thompson, and F. Liu, “Prediction of flutter of turbine blades in a transonic annular cascade,” J. Fluids Eng. Trans. ASME, Vol. 127, No. 6, pp. 1053–1058, 2005, doi: 10.1115/1.2060731.

[17] G. L. Forbes and R. B. Randall, “Simulated Gas Turbine Casing Response to Rotor Blade Pressure Excitation,” 5th Australas. Congr. Appl. Mech. ACAM 2007 10-12 December 2007, No. December, 2007.

[18] G. L. Forbes and R. B. Randall, “Separation of excitation forces from simulated gas turbine casing response measurements,” 2008.

[19] G. L. Forbes and R. B. Randall, “Detection of a blade fault from simulated gas turbine casing response measurements,” in Proceedings of the 4th European Workshop on Structural Health Monitoring, 2008, pp. 882–889.

[20] N. Gourdain et al., “High performance parallel computing of flows in complex geometries: II. Applications,” Comput. Sci. Discov., Vol. 2, No. 1, 2009, doi: 10.1088/1749-4699/2/1/015004.

[21] P. Lampart, “Investigation of endwall flows and losses in axial turbines. Part I. Formation of endwall flows and losses,” J. Theor. Appl. Mech., Vol. 47, No. 2, pp. 321–342, 2009.

[22] Y. Liu, K. Li, J. Zhang, H. Wang, and L. Liu, “Numerical bifurcation analysis of static stall of airfoil and dynamic stall under unsteady perturbation,” Commun. Nonlinear Sci. Numer. Simul., Vol. 17, No. 8, pp. 3427–3434, 2012, doi: 10.1016/j.cnsns.2011.12.007.

[23] M. Moshfeghi, Y. J. Song, and Y. H. Xie, “Effects of near-wall grid spacing on SST-K-ω model using NREL Phase VI horizontal axis wind turbine,” J. Wind Eng. Ind. Aerodyn., Vol. 107–108, pp. 94–105, 2012, doi: 10.1016/j.jweia.2012.03.032.

[24] G. Wang, D. Papadogiannis, F. Duchaine, N. Gourdain, and L. Y. M. Gicquel, “Towards massively parallel large eddy simulation of turbine

stages," in Proceedings of the ASME Turbo Expo, 2013, Vol. 6 C, doi: 10.1115/GT2013-94852.

[25] P. F. Lei, J. Z. Zhang, W. Kang, S. Ren, and L. Wang, "Unsteady flow separation and high performance of airfoil with local flexible structure at low Reynolds number," Commun. Comput. Phys., Vol. 16, No. 3, pp. 699–717, 2014, doi: 10.4208/cicp.111013.090514a.

[26] J. A. Esfahani, E. Barati, and H. R. Karbasian, "Fluid structures of flapping airfoil with elliptical motion trajectory," Comput. Fluids, Vol. 108, pp. 142–155, 2015, doi: 10.1016/j.compfluid.2014.12.002.

[27] P. Šidlof, "CFD simulation of flow-induced vibration of an elastically supported airfoil," EPJ Web Conf., Vol. 114, pp. 1–7, 2016, doi: 10.1051/epjconf/201611402105.

[28] T. A. Khan and L. Wei, "Numerical investigation on the aerodynamic performance of airfoil with local flexible structure," Proc. 2016 13th Int. Bhurban Conf. Appl. Sci. Technol. IBCAST 2016, pp. 428–432, 2016, doi: 10.1109/IBCAST.2016.7429914.

[29] T. A. Khan, W. Li, J. Zhang, and T. I. P. Shih, "Local vibrations and lift performance of low Reynolds number airfoil," Psychol. Learn. Motiv. - Adv. Res. Theory, Vol. 67, pp. 79–90, 2017, doi: 10.1016/j.jppr.2017.05.001.

[30] S.-C. S. Chen, “Axial-Flow Turbine Rotor Discharge-Flow Overexpansion and Limit-Loading Condition Part 1: Computational Fluid Dynamics (CFD) Investigation,” 2017, [Online]. Available: http://www.sti.nasa.gov.

[31] D. Moller, M. Jüngst, F. Holzinger, C. Brandstetter, H. P. Schiffer, and S. Leichtfuß, “Mechanism of nonsynchronous blade vibration in a transonic compressor rig,” J. Turbomach., Vol. 139, No. 1, 2017, doi: 10.1115/1.4034029.

[32] H. Luan, L. Weng, and Y. Luan, “Numerical simulation of unsteady aerodynamic interactions of contra-rotating axial fan,” PLoS One, Vol. 13, No. 7, pp. 1–21, 2018, doi: 10.1371/journal.pone.0200510.

[33] M. R. Rajanna et al., “Optimizing gas-turbine operation using finite-element CFD modeling,” 2018 Jt. Propuls. Conf., No. July, 2018, doi: 10.2514/6.2018-4657.

[34] N. Jain et al., “Towards large eddy simulation of rotating turbomachinery for variable speed gas turbine engine operation,” in Proceedings of the ASME Turbo Expo, 2019, Vol. 2B-2019, doi: 10.1115/GT2019-91592.

[35] Y. Zheng, Q. Gao, H. Yang, and K. Xu, “Aeroelastic vibration analysis of a 1.5 stage compressor,” Propuls. Power Res., Vol. 9, No. 1, pp. 26–36, 2020, doi: 10.1016/j.jppr.2019.11.001.

[36] A. Lifshits, H. R. Simmons, and A. J. Smalley, “More comprehensive vibration limits for rotating machinery,” J. Eng. Gas Turbines Power, Vol. 108, No. 4, pp. 583–590, 1986, doi: 10.1115/1.3239951.

[37] A. Ongoren and D. Rockwell, “Flow structure from an oscillating cylinder Part 2. Mode competition in the near wake,” J. Fluid Mech., Vol. 191, pp. 225–245, 1988, doi: 10.1017/S0022112088001570.

[38] A. Lifson, G. H. Quentin, A. J. Smailey, and C. L. Knauf, “Assessment of gas turbine vibration monitoring,” J. Eng. Gas Turbines Power, Vol. 111, No. 2, pp. 257–263, 1989, doi: 10.1115/1.3240245.

[39] K. Mathioudakis, E. Loukis, and K. D. Papailiou, “Casing vibration and gas turbine operating conditions,” J. Eng. Gas Turbines Power, Vol. 112, No. 4, pp. 478–485, 1990, doi: 10.1115/1.2906192.

[40] D. Greenblatt and I. J. Wygnanski, “Control of flow separation by periodic excitation,” Prog. Aerosp. Sci., Vol. 36, No. 7, pp. 487–545, 2000, doi: 10.1016/S0376-0421(00)00008-7.

[41] R. Govardhan and C. H. K. Williamson, “Resonance forever: Existence of a critical mass and an infinite regime of resonance in

vortex-induced vibration," J. Fluid Mech., Vol. 473, pp. 147–166, 2002, doi: 10.1017/S0022112002002318.

[42] A. Seifert, D. Greenblatt, and I. J. Wygnanski, "Active separation control: An overview of Reynolds and Mach numbers effects," Aerosp. Sci. Technol., Vol. 8, No. 7, pp. 569–582, 2004, doi: 10.1016/j.ast.2004.06.007.

[43] K. M. Lam and M. Y. H. Leung, "Asymmetric vortex shedding flow past an inclined flat plate at high incidence," Eur. J. Mech. B/Fluids, Vol. 24, No. 1, pp. 33–48, 2005, doi: 10.1016/j.euromechflu.2004.05.004.

[44] J. P. Gostelow, M. F. Platzer, and W. E. Carscallen, "On vortex formation in the wake flows of transonic turbine blades and oscillating airfoils," J. Turbomach., Vol. 128, No. 3, pp. 528–535, 2006, doi: 10.1115/1.2184354.

[45] D. J. Cleaver, Z. Wang, and I. Gursul, "Vortex mode bifurcation and lift force of a plunging airfoil at low Reynolds numbers," 48th AIAA Aerosp. Sci. Meet. Incl. New Horizons Forum Aerosp. Expo., No. January, pp. 1–16, 2010, doi: 10.2514/6.2010-390.

[46] Y. M. Tereshchenko, E. V. Doroshenko, A. Tehrani, and J. Abolhassanzade, "Aerodynamic Factors of Influence on the

Resonance Vibration of Gas Turbine Compressor Blades," Strength Mater., Vol. 47, No. 5, pp. 711–718, 2015, doi: 10.1007/s11223-015-9708-1.

[47] S. C. Hsieh, Y. M. Low, and Y. M. Chiew, "Flow characteristics around a circular cylinder undergoing vortex-induced vibration in the initial branch," Ocean Eng., Vol. 129, pp. 265–278, 2017, doi: 10.1016/j.oceaneng.2016.11.019.

[48] X. Qu, Y. Zhang, X. Lu, and J. Zhu, "Unsteady effects of periodic wake passing frequency on aerodynamic performance of ultra-high-lift low pressure turbine cascades," Phys. Fluids, Vol. 31, No. 9, 2019, doi: 10.1063/1.5110782.

[49] D. J. Doorly and M. L. G. Oldfield, "Simulation of wake passing in a stationary turbine rotor cascade," J. Propuls. Power, Vol. 1, No. 4, pp. 316–318, 1985, doi: 10.2514/3.22802.

[50] A. D. Henderson, G. J. Walker, and J. D. Hughes, "The influence of turbulence on wake dispersion and blade row interaction in an axial compressor," J. Turbomach., Vol. 128, No. 1, pp. 150–157, 2006, doi: 10.1115/1.2098809.

[51] G. Persico, A. Mora, P. Gaetani, and M. Savini, "Unsteady Aerodynamics of a Low Aspect Ratio Turbine Stage: Modeling Issues

and Flow Physics," J. Turbomach., Vol. 134, No. 6, 2012, doi: 10.1115/1.4004021.

[52] M. Jüngst, F. Holzinger, H. P. Schiffer, and S. Leichtfuss, "Analysing non-synchronous blade vibrations in a transonic compressor rotor," 2015.

[53] H. Castaing, "The Manufacture of Metal Airscrew Blades," Aircr. Eng. Aerosp. Technol., 1939.

[54] Z. K. Kadhim and H. O. Mery, "Free convection from optimum sinusoidal surface exposed to vertical vibrations," Int. J. Mech. Eng. Technol., Vol. 7, No. 1, pp. 214–224, 2016.

[55] L. J. Clancy, "Aerodynamics, Pitman Publ," Lim., London, 1975.

[56] B. R. Munson, T. H. Okiishi, W. W. Huebsch, and A. P. Rothmayer, "Fluid mechanics (p. 147)." Singapore: Wiley, 2013.

[57] R. S. Figliola and D. E. Beasley, Theory and Design for Mechanical Measurements, Second Edition, Vol. 20, No. 3. John Wiley & Sons, 1995.

[58] Autodesk, "Autocad overview," 2021. .

[59] Dassault Systèmes SolidWorks Corporation, "solidworks overview," 2021. .

[60] W. EIsner, “Transition modelling in turbomachinery,” J. Theor. Appl. Mech., Vol. 45, No. 3, pp. 539–556, 2007, [Online]. Available: http://yadda.icm.edu.pl/baztech/element/bwmeta1.element.baztech-article-BWM2-0068-0020.

[61] G. I. Ilieva, “On Turbulence and its Effects on Aerodynamics of Flow through Turbine Stages,” in Turbulence Modelling Approaches - Current State, Development Prospects, Applications, Vol. 143, K. Volkov, Ed. 2017.

[62] A. R. A. Ali and I. Janajreh, “Numerical Simulation of Turbine Blade Cooling via Jet Impingement,” Energy Procedia, Vol. 75, pp. 3220–3229, 2015, doi: 10.1016/j.egypro.2015.07.683.

[63] M. A. R. Sharif and K. K. Mothe, “Evaluation of turbulence models in the prediction of heat transfer due to slot jet impingement on plane and concave surfaces,” Numer. Heat Transf. Part B Fundam., Vol. 55, No. 4, pp. 273–294, 2009, doi: 10.1080/10407790902724602.

[64] F. Menter, “Turbulence Modeling for Turbomachinery Applications,” in Technology, 2002, No. May.

[65] G. Ilieva, “Modeling, Research and Analysis of 3D Real Flow in Turbine Stages with Complex Geometry,” Thesis, TU-Varna, 2010.

[66] G. I. Ilieva and R. D. Iosifov, “Geometry modeling features for 3D turbine cascade with twisted rotor blade in GAMBIT,” Acta Univ. Pontif. Euxinus, Vol. 5, No. 2, pp. 7–12, 2005.

[67] D. Jošt, A. Škerlavaj, and A. Lipej, “Numerical flow simulation and efficiency prediction for axial turbines by advanced turbulence models,” in IOP Conference Series: Earth and Environmental Science, 2012, Vol. 15, No. PART 6, p. 62016, doi: 10.1088/1755-1315/15/6/062016.

[68] F. R. Menter, “Two-equation eddy-viscosity turbulence models for engineering applications,” AIAA J., Vol. 32, No. 8, pp. 1598–1605, 1994, doi: 10.2514/3.12149.

[69] F. R. Menter, “Zonal two equation κ-ω turbulence models for aerodynamic flows,” in AIAA 23rd Fluid Dynamics, Plasmadynamics, and Lasers Conference, 1993, 1993, p. 2906, doi: 10.2514/6.1993-2906.

[70] J. G. E. Cleak and D. G. Gregory-Smith, “Turbulence modelling for secondary flow prediction in a turbine cascade,” Proc. ASME Turbo Expo, Vol. 1, 1991, doi: 10.1115/91-GT-057.

[71] J. Gimbun, T. G. Chuah, T. S. Y. Choong, and A. Fakhru’l-Razi, “A CFD study on the prediction of cyclone collection efficiency,” Int. J.

Comput. Methods Eng. Sci. Mech., Vol. 6, No. 3, pp. 161–168, 2005, doi: 10.1080/15502280590923649.

$$C_P = \frac{(P - P_\infty)}{{}^1\!/_2\, \rho_{air} U_\infty^2} = \frac{\rho_{water}\, g\, \Delta h}{{}^1\!/_2\, \rho_{air} U_\infty^2}$$

Sample of Calculation **(First Level).**

	X		Cp		Cp		Cp		Cp		Cp
		Δh	W.0 Hz.	Δh	W.9 Hz.	Δh	W.16 Hz.	Δh	W.23 Hz.	Δh	W.33 Hz.
L.E.	3	0.030	1	0.030	1	0.030	1	0.030	1	0.030	1
S.S.P1	14	-0.028	-0.9273	-0.026	-0.8785	-0.026	-0.87851	-0.025	-0.8297	-0.023	-0.7809
S.S.P2	37	-0.025	-0.8541	-0.025	-0.8419	-0.026	-0.86631	-0.025	-0.8541	-0.025	-0.8297
S.S.P3	53	-0.02	-0.7809	-0.024	-0.8053	-0.025	-0.8541	-0.026	-0.87851	-0.026	-0.87851
T.E	58	0	0	0	0	0	0	0	0	0	0

Experimental ***Section side S.S.***

	X		Cp		Cp		Cp		Cp		Cp
		Δh	W.0 vib.	Δh	W.9 vib.	Δh	W.16 vib.	Δh	W.23 vib.	Δh	W.33 vib.
P.Eg	3	0.030	1	0.030	1	0.030	1	0.030	1	0.030	1
P.S.P1	19	0.012	0.390448	0.012	0.390448	0.011	0.366045	0.011	0.366045	0.009	0.292836
P.S.P2	34	0.041	1.366567	0.038	1.268955	0.037	1.244552	0.035	1.171343	0.036	1.195746
P.S.P3	48	0.013	0.439254	0.017	0.561269	0.014	0.463657	0.012	0.414851	0.010	0.341642
P.T	59	0	0	0	0	0	0	0	0	0	0

Pressure side P.S.

Republic of Iraq
Ministry of Higher Education
and Scientific Research
University of Babylon
College of Engineering
Department of Mechanical
Engineering

Aerodynamic Performance of Gas Turbine Blades Due to Excitation of Vibration Effect

A Dissertation

Submitted to the College of Engineering, University of Babylon in Partial Fulfillment of the Requirements for award of Degree of Doctorate of Philosophy in Mechanical Engineering (Power)

By

Mushtaq Faisal Abd Alsadaa

[B.Sc. 2002, M.Sc. 2006]

Supervised By

Prof. Dr. Dhirgham Alkhafaji

Prof. Dr. Riyadh S. Al-Turaihi

2022 A.M **1443 A.H**

جمهورية العراق
وزارة التعليم العالي و البحث العلمي
جامعة بابل
كلية الهندسة
قسم الهندسة الميكانيكية

الأداء الايروديناميكي لريش توربين غازي نتيجة الاهتزازات القسرية

أطروحة مقدمة الى قسم الهندسة الميكانيكية في جامعة بابل كجزء من متطلبات نيل درجة دكتوراه في فلسفة علوم الهندسة الميكانيكية / تخصص حراريات

أعدت من قبل

مشتاق فيصل عبد السادة

[بكالوريوس 2002 ,ماجستير 2006]

باشراف

ا.د ضرغام عبد الحسين الخفاجي

ا.د رياض صباح الطريحي

2022 A.M ***1443 A.H***

بِسْمِ ٱللَّهِ ٱلرَّحْمَٰنِ ٱلرَّحِيمِ

وَمِنْ ءَايَٰتِهِۦٓ أَن يُرْسِلَ ٱلرِّيَاحَ مُبَشِّرَٰتٍ وَلِيُذِيقَكُم
مِّن رَّحْمَتِهِۦ وَلِتَجْرِىَ ٱلْفُلْكُ بِأَمْرِهِۦ وَلِتَبْتَغُوا۟ مِن
فَضْلِهِۦ وَلَعَلَّكُمْ تَشْكُرُونَ

صَدَقَ اللَّهُ الْعَلِيُّ الْعَظِيمُ

SUPERVISOR CERTIFICATION

We certify that the preparation of this Dissertation, entitled “Aerodynamic **Performance of Gas Turbine Blades Due to Excitation of Vibration Effect**"

has been prepared by " **Mushtaq Faisal Abd Alsadaa**" under our supervision at the Department of mechanical Engineering, College of Engineering, University of Babylon, as a partial fulfillment of the requirements for Degree of Doctorate of Philosophy in Mechanical Engineering (Power).

Signature:	**Signature:**
Prof. Dr. Dhirgham Alkhafaji	**Prof. Dr. Riyadh S. Al-Turaihi**
(First supervisor)	**(Second supervisor)**
/ /2022	**/ /2022**

The Committee Certification

We certify that we have read this dissertation, entitled **“Aerodynamic Performance of Gas Turbine Blades Due to Excitation of Vibration Effect"** and as an examining committee, examined the student **" Mushtaq Faisal Abd Alsadaa "** in its content and that in our opinion it meets the standard of dissertation for the Degree of Doctorate of Philosophy in Mechanical Engineering.

Prof. Dr.
Zena Khalefa Kadhim
Title: Member
Date: / /

Prof. Dr.
Qasim Hassen Bader
Title: Member
Date: / /

Prof. Dr.
Ahmed Hashim Yousif
Title: Member
Date: / /

Assist Prof. Dr.
Ahmed Hameed Kaleel
Title: Member
Date: / /

Prof. Dr.
Dhirgham Alkhafaji
Title: First Supervisor
Date: / /

Prof. Dr.
Riyadh S. Al-Turaih
Title: Second Supervisor
Date: / /

Prof. Dr.
Adnan A. Abdulrasool
Title: Chairman
Date: / /

Approval of the Mechanical Engineering Department
Head of the Mechanical Engineering Department

Approval of the College of Engineering
Dean of the College of Engineering

Assist. Prof. Dr.
Samer M. Abdul Haleem
Date: / /

Prof. Dr.
Hatem H. Obeid
Date: / /

Dedication

This Dissertation is dedicated to:

My Family and All People Who Assisted Me with All Gratitude and Love.

ACKNOWLEDGEMENTS

Praise first to Allah for the guidance that has enabled me to complete my research.

I would like to express my deepest thanks and sincere gratitude to my supervisors, **Prof. Dr. Dhirgham Alkhafaji** and **Prof. Dr. Riyadh S. Al-Turaihi**, for their supervision, support, understanding, and encouragement.

I wish to express my thanks to head of mechanical department,

Asst. Prof. Dr. Samer Mohammad Abd - Alhalim, and to my friends and all the staff members of mechanical engineering department. I would like to thank my colleague Dr. Salwan Khafaji for his support.

I would like to thank everyone, who helped me in this study.

Abstract

Gas turbine has been a significantly used in the fields of transportation and power generation. Gas turbines are now one of the most commonly utilized power generation technologies on the planet, and that makes studying gas turbine necessary. Since the vibration is a common phenomenon occurring in a machine, such as vibration of a rotor due to unbalanced mass, the vibration problem must be taken into the consideration.

In this study, effect of vibration on the flow profile of cascade blades of a gas turbine is studied experimentally and numerically. In the experimental part, a full scale-cascade blades of Babylon electric power plant (Hilla-Iraq) is considered as a real test rig in the lab, but the only difference is that the test accomplished for stationary cascade blade.

The blade dimensions are 96 mm full height, 58 mm chord length at the root with maximum camber 17.96 mm, while the chord length at tip is 54.7 mm with maximum camber 11.6 mm. The boundary conditions are harmonic (sinusoidal) blade vibration, inlet air velocity is 22 m/s. Similar working conditions (to some extent) are provided for the rig to achieve a milieu similar to those found in the mentioned power plant for better simulation. A certain shaker is designed and manufactured to provide vibration excitation.

For the numerical results, pressure distribution, pressure values, and velocity profile are calculated and presented with and without vibration effect. For the numerical part, computation fluid dynamic (CFD) along with COMSOL Multiphysics 5.6 is used for the simulation and validation of the experimental part. The dissertation focuses on studying the pressure distribution and velocity profile between blades turbine with effect force vibration for a different frequency (9, 16, 23, and 33 Hz). The pressure distribution is measured using 18 sensors separated into two groups: one on the suction side of the blade and the other on the pressure side.

In the middle of the chord, at the blade pressure and suction sides, compared to the numerical simulation, the experimental results for the pressure coefficient show that there is a 5% increase at the level of 6 mm from the base, a decrease of 6% at the level of 21 mm and an increase of 6% at the level of 36 mm. In addition, the increment in frequency results show that the frequency effect led to an increase in the pressure coefficient that directly increases with frequency increasing from -0.9 without vibration to -0.89 at 9 Hz.

In the numerical part, there is an agreement with the experimental part within error to an order between 4-6% based on the position of investigation sections. Moreover, the actual inlet velocity of rotary cascade turbine is successfully simulated with vibration for (9, 16, 23, 33, and 100 Hz). Finally, effect of vibration decrease with increasing inlet velocity when the vibration frequency is more than 33Hz.

TABLE OF CONTENTS

CHAPTER ONE INTRODUCTION

CHAPTER TWO REVIEW OF LITERATURE

CHAPTER THREE EXPERIMENTAL STUDY

CHAPTER FOUR CFD MODELING STUDY

CHAPTER FIVE RESULTS AND DISCUSSION

CHAPTER SEX CONCLUSION AND FUTRE WORK

NOMENCLATURES

Latin Symbols

Symbol	Description	Unit
p_{static}	Static pressure	Pa
p_{total}	Total pressure	Pa
2D	Two dimensions	m^2
3D	Three dimensions	m^3
A	Amplitude.	m
C	Chord	m
D	Diameter	m
h	plunge amplitude non-dimensional zed by airfoil chord	[-]
Pr	Prandial number	[-]
Rev	Vibration reynold number	[-]
U	Free stream velocity.	m/s
u,v,w	Velocity vectors	m/s
$u_{r.m.s.}$	Root mean square fluctuation velocity in x-direction.	m/s
x,y,z	Cartesian coordinates	[-]
F	Frequency	1/s

Greek Symbols

Symbol	Description	Unit
μ	Dynamic viscosity	kg/ms
ρ	Density of the flow	kg/m^3
ν	kinematic viscosity	m^2/s

ABBREVIATIONS

Abbreviation	Description
CFD	Computational Fluid Dynamics
FEM	Finite Element Method
FIVN	‘flow-induced vibration and noise’
FVM	Finite Volume Method
HS	Horseshoe
LAE	Linear Algebraic Equation
LES	Large eddy simulation
LFS	Local flexible structure
LPT	Low pressure turbine
First level	Height level section blade at (6mm) from the root
Second level	Height level blade section at (21mm) from the root
Third level	Height level blade section at (36mm) from the root
Last level	Height level blade section at (90mm) from the root
N-S	Navier Stokes Equation
P.S.	Pressure side
PDE	Partial Deferential Equation
PV	Passage vortex
RANS	Reynolds-Averaged Navier-Stokes
S.S.	Suction side
VIV	Vortex-induced vibration.
VKI	Von Karman Institute

الخلاصة

يعتبر التوربابين الغازي من الاجهزة التي استخدمت ولا زالت في مجالات النقل وتوليد الطاقة الكهربائية. حيث يعتبر المحطات الغازية واحدة من اكثر التقنيات شيوعا لتوليد الطاقة الكهربائية على سطح الارض وهذا يجعل دراسة المحطات الغازية من الدراسات الضرورية والمهمة. تعتبر مشكلة الاهتزازت من المشاكل المهمة التي يجب ان تؤخذ بنظر الاعتبار وذلك لانها ظاهرة شائعة الحدوث في اغلب المكائن الميكانيكية مثل اهتزاز العمود بسبب انعدام الاتزان الناتج من التوزيع غير المتجانس للكتل وغيرها.

تمت دراسة تأثير الاهتزاز على خصائص الجريان وشكل الجريان للمائع على صف من الريش لتوربين غازي في محطة الحلة الغازية عدديا وعمليا. تم استخدام نموذج مطابق تماما لما موجود من االريش الخاصة بالمحطة الغازية في بابل (محطة الحلة الغازية) مع اختلاف واحد فقط وهو انه تم اجراء الفحوصات العملية لصف من الريش ثابتة (غير دوارة).

ابعاد الريشة المستخدمة هي 96 ملم للارتفاع, 58 ملم لطول الوتر, 17.96 للسمك عند القاعدة, بينما طول الوتر عند االقمة هو 54.5 ملم و اقصى تحدب هو 11.6 ملم .استخدمت موجات حث ترددية (جيبية) كشرط حدودي على الريشة لتمثيل اهتزازها وحددت سرعة الهواء الداخل بقيمة 22 م/ثانية. استخدمت هذه الشروط الحدودية المذكورة وباقي الشروط الاخرى بشكل يشبه الى حد كبير لما موجود في المحطة الغازية المذكورة سابقا. تم حساب قيم الضغط وتوزيعه وشكل توزيع السرعة عمليا مع الاهتزاز وبدونه.

اما بالنسبة للحل العددي, فقد استخدم برنامج الكومسل اصدار 5.6 للتمثيل والمطابقة مع نتائج الجزء العملي. تركز هذه الاطروحة على دراسة توزيع كل من الضغط والسرعه بين الريش تحت تاثير اهتزاز قسري بقيم ترددات مختلفة

(9, 16, 23, 33) هيرتز. استخدم 18 حساس (انبوب قياس الضغط) موزعة على مجموعتين. الاولى تقع على طول جانب السحب والثانية تقع على طول جانب الضغط.

عند مقارنة النتائج الخاصة بمعامل الضغط عند منتصف الوتر ولكل من جانبي السحب والضغط للدراستين العددية والعملية, وجد بان هناك زيادة بمقدار 5% للقراءات عند ارتفاع 6 ملم من قاعدة الريشة, وانخفاض بمقدار 6% عند ارتفاع 21 ملم وزيادة بمقدار 6% عند ارتفاع 36 ملم من القاعدة.بالاضافة الى ذلك, تبين ان الزيادة في التردد ادت الى زيادة بمعامل الضغط والذي يزداد طرديا من قيمة لا بعدية بمقدار 0.9- بدون اهتزاز الى قيمة لا بعدية بمقدار 0.89- عند تردد قيمته 9 هيرتز. هناك تقارب بين النتائج العملية والعددية بنسبة خطأ بمقدار 4-6% لكل من قيم الضغط والسرعة بشكل عام. اضافة الى ذلك, سرعة الهواء الحقيقة الداخلة الى صف الريش قد تم نمذجتها بنجاح تحت تاثير الاهتزاز وبمديات من الترددات تقع بين (9, 16, 23, 33, 100) هيرتز. أخيرا, تبين بان تأثير الاهتزاز يقل كلما زاد تردد الاهتزاز عن 33 هيرتز.